

**GFRP PANELS SUBJECTED TO IMPACT LOADS AT ROOM AND  
ARCTIC TEMPERATURES**

**PANNEAUX EN PRFV SUJETS À DES IMPACTS À TEMPÉRATURE  
AMBIANTE ET TEMPÉRATURE ARCTIQUE**

Thesis submitted to the Division of Graduate Studies  
of the Royal Military College of Canada  
by

Vincent Boivin, RMC  
Captain

In Partial Fulfilment of the Requirements for the Degree of  
Master of Applied Science in Civil Engineering

September 2016

© This thesis may be used within the Department of National Defence, but  
copyright for open publication remains the property of the author.

## **ACKNOWLEDGEMENT**

I wish to thank my supervisor Dr. Gordon Wight as well as my co-supervisor Dr. Pat Heffernan for their continuous support and guidance throughout my two years as a master's student. Your mentorship and expertise have helped me to succeed and I will carry on with my next career step with a significant amount of useful and practical knowledge.

A special thanks to Dr. Yazan Qasrawi who helped me through all the difficulties I encountered in both the testing and the modelling phase. His expertise and experience with impact analysis were key to my success.

I would also like to acknowledge the laboratory technicians, Mr. Dexter Gaskin and Mr. Steve VanVolkingburgh who were instrumental in getting my apparatus set-up in the planning phase, but also for their assistance for the testing phase. Their enthusiasm and flexibility made this experience as smooth as possible.

Finally, I would like to thank my family and friends who have supported me through this very crucial episode of my career. Your words of encouragement and advice did not fall on deaf ears. Especially my girlfriend Valérie, who kept me going for the last two years.

## ABSTRACT

Canada's sovereignty and domestic operations are at the core of Canada's Arctic and Defence policies. These missions warrant the advancement of research in cold temperature environments. Knowledge of cold temperature effects on new infrastructure using innovative materials such as fibre reinforced polymers (FRP) is critical in order to have safe and accurate design procedures. These new structures may be subjected to malicious or accidental threats that can generate extreme dynamic loadings such as blast or impact events.

To investigate extreme loading effects on lightweight infrastructure suitable for Arctic conditions, the impact response of a GFRP multi-cell ribbed structural panel subjected to low-velocity impact loadings was investigated. These panels could be used as primary or secondary structural components. An impact hammer apparatus was used to study the dynamic properties of the panels as well as to investigate the effects of low temperature when the panels were subjected to low-velocity impact. The main varying parameters in the following studies are panels' temperature and imparted kinetic energy. Tests were conducted at two temperatures: 20 °C which represents room temperature and -50 °C for cold Arctic conditions. A total of 52 tests were carried out on 28 panels which had widths of 605 mm, heights of 80 mm and overall lengths of 1500 mm. The kinetic energies imparted to the panels varied from 1300 J to 2970 J by changing the impact hammer drop height. The panels' threshold failure energy for quasi-static 3-point flexure tests at a strain rate of  $6 \times 10^{-5} \text{ s}^{-1}$ , was increased from a value of 960 J to 1590 J by increasing the strain rate to  $1 \text{ s}^{-1}$  using the impact hammer. This energy was increased even higher for cold temperature dynamic tests at similar strain rates to a value of 2090 J showing that the studied panels exhibited a higher energy absorption in cold temperatures under dynamic loads. Similar observations were made for failure displacements which increased not only by increasing the strain rate but also by reducing the temperature for similar strain rates. Residual strength tests were done on dynamically tested panels using a quasi-static 3-point flexural testing frame in order to capture their impact damage resistance. These tests were in good agreement with the threshold energies observed during impact tests. For room temperature tests, panels that were subject to an impact greater than approximately 1500 J would lose up to 80% of their flexural strength, and this threshold value was observed to be approximately 2100 J for cold temperature panels.

To complement the experimental studies, a single degree-of-freedom (SDOF) model was derived in order to simulate the laboratory tests. This model was based on the moment-curvature relations for this particular cross-section. The modelled responses were then created and compared with the observed experimental behaviour of all specimens in the testing schedule. The model generated accurate results under certain conditions. It was however unable to generate accurate results for most specimens that either had failed experimentally or for specimens that did not exhibit the same failure mode in the model and experiments. It is recommended that a more precise evaluation of an appropriate resistance function be determined that could be used for SDOF models or a more complex analysis such as explicit non-linear finite element analysis might be warranted for such brittle materials.

## RÉSUMÉ

La souveraineté du Canada et les opérations domestiques font partie intégrale des politiques canadiennes concernant l'Arctique et la Défense. Ces missions demandent une avancée de recherche pour les conditions arctique. Il est critique de mieux comprendre les effets des températures froides sur les nouvelles infrastructures composées des matériaux légers tels que les polymères renforcés par fibre (PRV). Ces nouvelles structures pourraient être sujettes à des menaces accidentelles ou malicieuses qui résulteraient en force dynamiques extrêmes tels qu'une explosion ou un impact. Afin d'étudier les effets de telles forces dynamiques sur des infrastructures légères en conditions arctiques, la présente thèse étudie le comportement dynamique de panneaux structuraux multicellulaires en PFR de verre (PRFV) sujet à des impacts à faible vitesse. Ces panneaux pourraient être utilisés comme composantes structurales primaires ou secondaires. Un marteau de type pendule a été utilisé afin d'évaluer les propriétés dynamiques de ces panneaux. De plus, ce même appareil a été utilisé pour étudier l'effet des températures froides lorsque les panneaux sont soumis à des impacts à faible vitesse. Les variables principales de la présente thèse sont la température des panneaux et l'énergie cinétique imposée. Deux températures ont été retenues pour cette étude : 20 °C représentant la température ambiante, et -50 °C pour représenter les conditions arctiques. Un total de 52 essais ont été complétés sur 28 panneaux qui avaient 605 mm de largeur, 80 mm de hauteur et une longueur de 1500 mm. L'énergie cinétique transmise aux panneaux varie de 1300 J à 2970 J en changeant la hauteur initiale du marteau. Le seuil critique d'énergie pour les essais quasi statiques à une vitesse de déformation de  $6 \times 10^{-5} \text{ s}^{-1}$  a été augmenté de 960 J à 1590 J en augmentant la vitesse de déformation à  $1 \text{ s}^{-1}$  pour les essais dynamiques. Ce même seuil a été augmenté davantage pour les essais dynamiques à -50 °C ayant une vitesse de déformation similaire avec une valeur de 2090 J. Ceci indique que les panneaux choisis manifestent une plus grande absorption d'énergie lorsque sujets à des forces dynamiques simultanément à des températures froides. Des observations similaires ont pu être constatées avec le seuil critique de déflexion. Ce seuil a été augmenté avec une vitesse de déformation plus rapide, ainsi qu'avec des températures froides pour les essais dynamiques. De plus, des essais de force résiduelle ont été complétés en utilisant un appareil de flexion trois-points afin d'évaluer la résistance des panneaux au dommage générés par les impacts. Ces

essais sont en accord avec les seuils d'énergie et de déflexions au moment de fracture évalués précédemment. Pour les essais à température pièce, les panneaux sujets à des impacts dépassant 1500 J perdaient environ 80% de leur force de flexion. Cette valeur d'impact était plus élevée pour les panneaux à température froide avec un résultat de 2100 J.

Afin de compléter les essais expérimentaux, un modèle à degré de liberté simple a été utilisé pour simuler les résultats observés en laboratoire. Ce modèle a été basé sur la relation moment-courbure. Les relations forces-déflexions simulées ont été comparées avec tous les résultats expérimentaux. Le modèle a généré des comportements adéquats sous certaines conditions : lorsque les panneaux n'ont pas fracturé en laboratoire et lorsqu'ils ont suivi le même mode de rupture dans le modèle et les essais expérimentaux. Les panneaux ne suivant pas ces conditions, soit la majorité, ont présenté des résultats erronés. Il serait alors recommandé d'utiliser une méthode d'évaluation plus précise pour la fonction de résistance d'un modèle à degré de liberté simple ou tout simplement utiliser une autre méthode plus complexe et adéquate pour des matériaux fragiles telle que l'analyse d'éléments finis non-linéaire explicite.

## **CO-AUTHORSHIP STATEMENT**

This document has been written in the manuscript format according to the Royal Military College of Canada thesis preparation guidelines. The entire document was prepared by Capt V. Boivin. It is the intent that revised versions of Chapters 2, 3 and 4 will be submitted for publication in appropriate structural engineering journals. Capt Boivin will be the primary author for all of these publications. Additional individuals, currently listed in acknowledgements who provided significant advice, feedback and input to the individual papers will be appropriately listed as additional authors.

## TABLE OF CONTENTS

ACKNOWLEDGEMENT.....	ii
ABSTRACT .....	iii
RÉSUMÉ.....	v
CO-AUTHORSHIP STATEMENT .....	vii
LIST OF TABLES.....	xii
LIST OF FIGURES .....	xiii
LIST OF ABBREVIATIONS .....	xv
LIST OF SYMBOLS.....	xvi
CHAPTER 1 INTRODUCTION.....	1
1.1 Project Background.....	1
1.2 Aim .....	3
1.3 Scope.....	4
1.4 Thesis Organization .....	8
1.5 References.....	10
CHAPTER 2 IMPACT RESPONSE OF A GFRP MULTI-CELL RIBBED STRUCTURAL PANEL .....	12
2.1 Introduction.....	12
2.1.1 Background.....	13
2.1.2 Dynamic Loading.....	14
2.1.3 Dynamic Properties of GFRPs.....	14
2.1.4 Damage Mechanisms and Tolerance .....	15
2.1.5 Robustness .....	16
2.2 Objective.....	17
2.3 Procedure .....	17
2.3.1 Material Properties.....	17
2.3.2 Quasi-Static 3-point Flexural Test .....	19



2.3.3	Impact Hammer Apparatus .....	20
2.4	Results and Discussion .....	24
2.4.1	Quasi-Static Testing.....	24
2.4.2	Impact Testing .....	25
2.4.3	Comparison of Quasi-Static and Impact testing.....	33
2.4.4	Failure Mechanisms .....	34
2.4.5	Residual Flexural Strength Test.....	39
2.4.6	Robustness Factor .....	40
2.5	Conclusion .....	40
2.6	References.....	41
CHAPTER 3 COLD TEMPERATURE EFFECTS ON A GFRP MULTI-CELL RIBBED STRUCTURAL PANEL SUBJECTED TO IMPACT LOADING .....		46
3.1	Introduction.....	46
3.1.1	Background.....	46
3.1.2	Temperature Effects on FRP Components.....	49
3.1.3	Dynamic Properties of GFRPs.....	50
3.1.4	Damage Mechanisms and Tolerance .....	51
3.2	Objectives .....	52
3.3	Procedure .....	52
3.3.1	Material Properties.....	52
3.3.2	Quasi-Static 3-point Flexural Test .....	53
3.3.3	Impact Hammer Apparatus .....	56
3.3.4	Freezing the Panels .....	59
3.4	Results and Discussions .....	61
3.4.1	Quasi-Static Testing.....	61
3.4.2	Impact Testing .....	64
3.4.3	Comparison of Room Temperature with Cold Temperature ..	68

3.4.4	Failure Mechanisms and Damage Characterization.....	72
3.4.5	Residual Strength.....	75
3.5	Conclusion.....	78
3.6	References.....	78
<b>CHAPTER 4 PREDICTING THE IMPACT RESPONSE OF GFRP MULTI-CELL RIBBED STRUCTURAL PANELS USING A SINGLE DEGREE-OF-FREEDOM MODEL .....</b>		
4.1	Introduction.....	83
4.1.1	Background.....	83
4.1.2	Dynamic Loading.....	83
4.1.3	Single Degree-of-freedom Method .....	84
4.1.4	Failure Model.....	86
4.2	Objective.....	87
4.3	Procedure .....	87
4.3.1	Material Properties.....	87
4.3.2	Quasi-Static 3-point Flexural Test .....	89
4.3.3	Impact Hammer Apparatus .....	89
4.3.4	Modelling the Resistance Function.....	92
4.3.5	SDOF Modelling.....	97
4.4	Results and Discussion .....	98
4.5	Conclusion .....	106
4.6	References.....	107
<b>CHAPTER 5 CONCLUSIONS AND FUTURE WORK.....</b>		
5.1	Summary of Research.....	110
5.2	Conclusions.....	111
5.3	Future Work.....	112
<b>APPENDICES .....</b>		
Appendix A	.....	115

Appendix B.....	121
Appendix C.....	125
Appendix D .....	138
Appendix E.....	144
Appendix F.....	149
Appendix G .....	162
Appendix H .....	175
Appendix I.....	181
Appendix J.....	194
Appendix K .....	200

## LIST OF TABLES

Table 1.1 - Schematic Representation of Testing Schedule.....	7
Table 2.1 - COMPOSOLITE® Mechanical Properties .....	18
Table 2.2 - Impact Testing Schedule .....	23
Table 2.3 - Impact Tests Kinetic Energies.....	25
Table 2.4 - Impact Tests Results.....	30
Table 3.1 - Panel’s Mechanical Properties .....	53
Table 3.2 - Impact Testing Schedule .....	59
Table 3.3 - Quasi-Static Test Results.....	62
Table 3.4 - Flexural Stiffness and Strength Variation .....	63
Table 3.5 - Impact Tests Kinetic Energies.....	64
Table 3.6 - Impact Tests Results for Room and Cold Temperature.....	66
Table 4.1 - Panel’s Mechanical Properties .....	88
Table 4.2 - Impact Testing Schedule .....	92
Table 4.3 - Energy Comparison between Modelled and Experimental Resistance Function .....	97
Table 4.4 - Experimental Results Compared to SDOF Model Results for GFRP Panels’ Impact Response .....	98
Table 4.5 - Quasi-Static tests results.....	101

## LIST OF FIGURES

Figure 1.1 - Use of FRP components in civil infrastructure [10] .....	2
Figure 1.2 - Cross-Section of the GFRP Multi-Cell Ribbed Structural Panel .....	4
Figure 1.3 - Visual Representation of the Impact Hammer Apparatus.....	6
Figure 2.1 - Cross-Section of COMPOSOLITE® Panel [4].....	19
Figure 2.2 - 3-Point Flexural Test Apparatus .....	20
Figure 2.3 - Impact Hammer Apparatus .....	22
Figure 2.4 - Load-Displacement Results of the Quasi-Static 3-point Flexural Tests .....	24
Figure 2.5 - Impact Load and Mid-Span Displacement-Time History, K2-3 .....	26
Figure 2.6 - Impact Load and Mid-Span Displacement-Time History, K4-3 .....	26
Figure 2.7 - Comparison of Support and Impact Load for Panel K2-3.....	28
Figure 2.8 - Comparison of Support and Impact Load for Panel K4-3.....	28
Figure 2.9 - Dynamic Load-Displacement Curve for Panel K2-3 .....	29
Figure 2.10 - Dynamic Load-Displacement Curve for Panel K4-3 .....	29
Figure 2.11 - Energy Conservation for K2-3 .....	31
Figure 2.12 - Energy Conservation for K4-3 .....	31
Figure 2.13 – Strain Energy to Peak Deflection vs. Panel's Peak Deflection .....	32
Figure 2.14 - Strain Energy History vs. Mid-Span Displacement .....	33
Figure 2.15 - Failure Mechanisms for Panel K1-3.....	34
Figure 2.16 - Non-Destructive Failure Characterization of Panels through Thermal Imaging.....	36
Figure 2.17 - Strain Distribution Time History (Panel K2-3).....	37
Figure 2.18 - Strain Distribution Time History (Panel K2-2).....	38
Figure 2.19 - Delamination of the Inside Webs with the Front Face.....	38
Figure 2.20 - Total Strain Energy and Panel Peak Displacement vs. Residual Flexural Strength.....	39
Figure 3.1 - A visitor center in Bristol, UK constructed with COMPOSOLITE® panels [4].....	48
Figure 3.2 - Cross-Section of Panel [4] .....	48
Figure 3.3 - 3-Point Flexural Test Apparatus .....	55
Figure 3.4 - Impact Hammer apparatus .....	57
Figure 3.5 - Temperature-Time History of a Thawing Panel .....	60
Figure 3.6 - Apparent Strain Distribution for a Thawing Panel.....	61
Figure 3.7 - Quasi-Static Results for Room and Cold Temperature.....	62

Figure 3.8 - Comparison of Support and Impact Load for Panel K2-3.....	65
Figure 3.9 - Dynamic Load-Displacement Curve.....	66
Figure 3.10 - Energy Conservation for Panel T2-3.....	68
Figure 3.11 - Strain Energy vs. Peak Impact Deflection for all Panels .....	69
Figure 3.12 - Strain Energy vs. Mid-Span Displacement .....	70
Figure 3.13 - Load-Displacement History Comparison for Panels with Identical Impact Energy.....	71
Figure 3.14 -Thermography of Impacted Panels .....	74
Figure 3.15 - Residual Flexural Test for Panel T2-1 .....	75
Figure 3.16 - Residual Strength vs. Peak Impact Deflection for all Panels .....	76
Figure 3.17 - Residual Strength vs. Strain Energy at Peak Displacement for all Panels .....	77
Figure 4.1 - Panel's Idealization to a SDOF System.....	85
Figure 4.2 - Cross-Section of COMPOSOLITE® Panel [8].....	88
Figure 4.3 - 3-Point Flexural Test Apparatus .....	89
Figure 4.4 - Impact Hammer Apparatus .....	91
Figure 4.5 - Plane Section Analysis.....	93
Figure 4.6 - Modelled Moment-Curvature Relationship of the GFRP Panels for a Quasi-Static Load. ....	94
Figure 4.7 - Strain Gauge Instrumentation of GFRP Panels.....	95
Figure 4.8 - Comparison of Modelled Resistance Function with Experimental Results.....	96
Figure 4.9 - Accurate SDOF Modelled Response. Panel K4-2.....	100
Figure 4.10 - Inaccurate SDOF Modelled Response. Panel K1-2 .....	100
Figure 4.11 - Load-Displacement Histories Showing Variability in the Panels ...	101
Figure 4.12 - SDOF Model Using $K_{LM}=0.49$ for Panel K1-3 .....	102
Figure 4.13 - SDOF Model Using $K_{LM}=0.48$ for Panel K1-3.....	103
Figure 4.14 - Energy Conservation for Panel K1-1 .....	104
Figure 4.15 - Load-Displacement Graphs for Panel T3-2 Using Reaction and Impact Hammer .....	105

## **LIST OF ABBREVIATIONS**

ASTM	American Society for Testing and Materials
APC	Advanced Polymer Composites
CAF	Canadian Armed Force
COG	Center of Gravity
DAQ	Data Acquisition
DIF	Dynamic Increase Factor
EPS	Expanded Polystyrene
FML	Fibre Metal Laminates
FPS	Frames per Second
FRP	Fiber-Reinforced Polymers
GFRP	Glass Fiber-Reinforced Polymers
HSS	Hollow Structural Section
LVDT	Linear Variable Differential Transducer
MTS	Material Testing System
NORAD	North American Aerospace Defense
RMCC	Royal Military College of Canada
SDOF	Single Degree-of-Freedom

## LIST OF SYMBOLS

$A$	Area
$A_{\text{eff}}$	Effective area over which the force is applied
$a_h$	Acceleration of hammer
$a_{\text{ssf}}$	Buckle half-wavelength
$\alpha$	Coefficient of thermal expansion
$b_f$	Flange width
$b_{\text{eff}}$	Web depth for web crushing and buckling calculations
$D_{L_f}$	Flange longitudinal flexural rigidity
$D_{T_f}$	Flange transverse flexural rigidity
$D_{L_{T_f}}$	Flange coupling flexural rigidity
$D_{S_f}$	Flange shear flexural rigidity
$D_{L_w}$	Web longitudinal flexural rigidity
$D_{T_w}$	Web transverse flexural rigidity
$D_{L_{T_w}}$	Web coupling flexural rigidity
$D_{S_w}$	Web shear flexural rigidity
$d_w$	Flange depth
$E$	Elastic modulus
$E_L$	Longitudinal elastic modulus
$E_T$	Transversal elastic modulus
$\varepsilon$	Strain
$F_{\text{crush}}$	Critical crushing force
$F_{\text{local}}$	Critical transverse buckling load
$G_{LT}$	Shear modulus
$h$	Hammer drop height
$I$	Impulse
$I_x$	Moment of inertia about x axis
$k$	Spring constant
$K_M$	Mass factor
$K_{LM}$	Load-mass factor
$KE_p$	Panel's kinetic energy
$KE_h$	Hammer's kinetic energy
$L_{\text{eff}}$	Effective bearing length along the beam in the lengthwise direction
$M_{\text{crush}}$	Crushing moment



$m_e$	Panel's equivalent mass
$m_h$	Hammer's total mass
$m_p$	Panel's total mass
$\mu_{\text{robustness}}$	Robustness factor
$N$	Normal load
$P_b$	Bending load/Support load
$P_t$	Tup load
$R(y)$	Resistance function
$S_{\text{ultimate}}$	Ultimate strength
$S_{\text{serviceability}}$	Serviceability strength
$\sigma$	Stress
$\sigma_{\text{cr}}$	Critical local buckling stress
$\sigma_{\text{crushbending}}$	Flange in-plane compressive stress a crushing load
$\sigma_{\text{ssf}}$	Critical stress in flange
$\sigma_{\text{ylocal}}$	Critical local buckling stress for web crushing and buckling calculations
$t$	Time
$t_{\text{bf}}$	Thickness of bearing under the flange
$t_f$	Flange thickness
$t_w$	Web thickness
$u$	Panel mid-span displacement
$U$	Strain energy
$v$	Panel's velocity at mid-span
$\nu_L$	Longitudinal Poisson ratio
$\nu_T$	Transversal Poisson ratio
$W$	Work done
$w_{\text{ultimate}}$	Ultimate deflection
$w_{\text{serviceability}}$	Serviceability deflection
$y$	Distance to centroid
$\zeta$	Coefficient of restraint

# Chapter 1

## INTRODUCTION

### 1.1 Project Background

International interest in Arctic regions is increasing due to climate change, the requirement for resource development and also the establishment of transportation routes. It is in the interest of Canada to advance the body of knowledge regarding the behaviour of critical infrastructure in Arctic temperatures because it is a northern nation with 40% of its landmass in arctic territories [1]. Resilience is of key importance for any type of construction, especially in remote areas with harsh conditions. In order to have resilient infrastructure, it is critical to take into consideration all types of hazard: malicious, accidental or industrial, and natural hazards [2]. This thesis will focus on impact loading, which covers aspects of the malicious and accidental regions of the hazard spectrum.

Since exercising sovereignty is the most important pillar in Canada's Arctic foreign policy [1], it is anticipated that there will be an increase in Canadian Armed Forces (CAF) in this region. Additionally, conducting daily domestic and continental operations, including in the Arctic, through NORAD is one of the six core missions of the Canadian Forces [3]. This increasing presence could mean the creation of additional permanent or temporary infrastructure to support operations. Also, it is estimated that the Arctic is home to one fifth of the world's petroleum reserves [1]. Claims to the Arctic territories are very complex and some nations such as Russia have increased their military activities in the North in 2014, conducting major military exercises and tests for the first time since the Cold War [4]. Consequently, new and resilient infrastructure is likely to be constructed in the Canadian Arctic to support both economic development and military sovereignty operations. This new infrastructure could potentially be exposed to an extreme event. The probability of a blast or impact event whether it be accidental or intended on critical infrastructure would then be significantly increased in this region. Considering the Arctic as a remote area, the ease of transportation for construction materials and their expedient installation is critical. Lightweight structural components that provide thermal insulation as well as structural capacities are then warranted for such infrastructure.

Fibre-reinforced polymer (FRP) components have been used since the Second World War [5]. However, practitioners did not fully understand their capabilities and use them efficiently in civil infrastructure until the 1970's [5]. Structural applications of FRP products have been increasing since then. This interest in applications in civil infrastructure has led to an increase in research on FRPs in order to better understand the material. Such research is critical and will help civil engineers make more confident decisions while using composite materials. Figure 1.1 illustrates the present use of FRP in civil infrastructure. FRP products have gained a lot of attention due to their high specific strength and stiffness [6]. They also have a much lower thermal conductivity compared to common construction materials such as steel and concrete, which is an attractive property for cold weather application. Different combinations of polymers and fibres as well as their lay-up technique make FRPs very attractive because they can be tailored to the requirements of the application. For example, vinylester as a polymer will increase the durability of structural components in harsh environmental conditions like bridges or marine applications. These characteristics all contribute to a lower life cycle cost compared to other widely used construction materials such as steel or concrete [5]. A large body of research work has been done on FRP rehabilitation for concrete elements and masonry walls against dynamic loadings [7] [8] [9]. Researchers have also studied hybrid components using FRPs and conventional materials such as fibre metal laminates (FML) or sandwich panels which use FRPs as face sheets and energy absorbing materials as core materials.

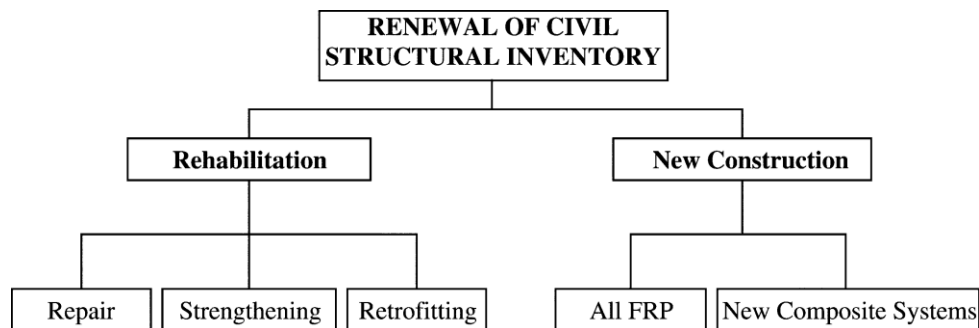


**Figure 1.1 - Use of FRP components in civil infrastructure [10]**

The understanding of cold temperature effects on blast and impact behaviour of FRP materials has been the focus of some studies [11] [12] [13] [14] but is still in need of development and deeper understanding. Most of those studies were done on small-scale specimens, and the variety of FRP composition warrants more research, i.e. type of polymer, type of fibres, fibre orientation, etc. The design philosophy for blast protection states that for a safe design, the absorbed energy must be greater than the kinetic energy imparted to the structure [15]. It is of primary interest in this study to understand the energy absorbing behaviour of the FRP panels under cold temperatures subjected to dynamic impulsive loads. Despite their favourable specific strength and stiffness, FRP components are known to exhibit a brittle failure. The influence of cold temperatures could furthermore hinder that ductility. From the literature, FRP materials are strain rate sensitive as well as temperature sensitive. Combining these properties as part of a single study for a specific type of GFRP panel was the starting point of this thesis. It is important to note the limited scope of this study, and most studies with regards to FRP since there are several possible combinations of polymers, fibres and lay-up methods that can create FRP products with unique properties. The observed conclusions of this study will be most relevant to this particular panel or similar structural components.

## **1.2 Aim**

The main objectives of the research were to:

1. Investigate the impact response and failure mechanisms of the GFRP multi-cell ribbed structural panel and assess the post-failure ductility for energy absorption purposes.
2. Investigate the impact response and failure mechanisms of these panels at sub-zero temperatures when subjected to similar impact loads.
3. Evaluate the residual strength of the panels tested in the prior investigations in order to quantify the damage imparted by these impulsive loads.

4. Determine the effectiveness of a simple Single Degree of Freedom (SDOF) model to accurately predict the dynamic response of the panels.

### 1.3 Scope

The present study evaluates the impact response of a GFRP multi-cell ribbed structural panel, COMPOSOLITE®, tested at room and sub-zero temperatures using a pendulum impact hammer. The intended use of these panels, for the purpose of this project, is as an exterior shell to a structure for retrofit or new construction. The panel's cross-section is shown in Figure 1.2. Each panel had a width of 605 mm, a height of 80 mm and a panel length of 1.50 m and was used for all parts of this investigation. The panel was constructed with a GFRP wall thickness and facing thickness of 2.25 mm to 3.35 mm respectively. All voids were filled with #1 EPS foam.

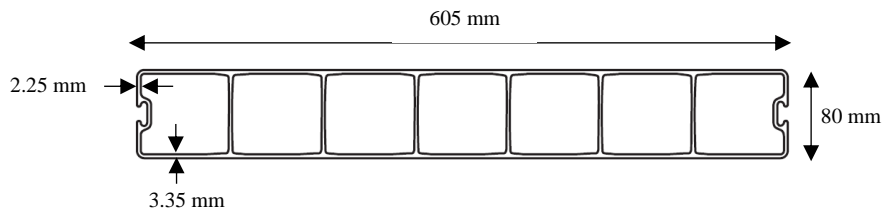
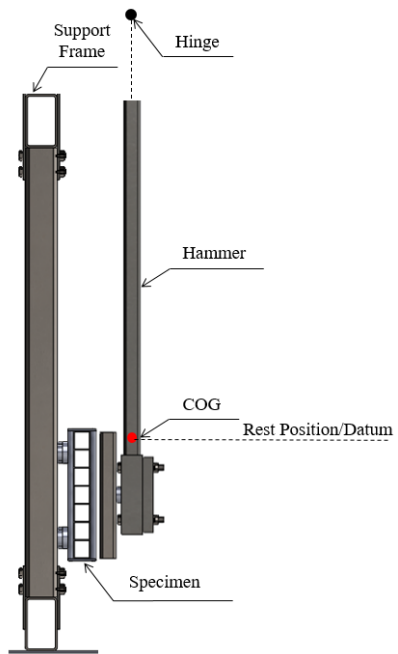
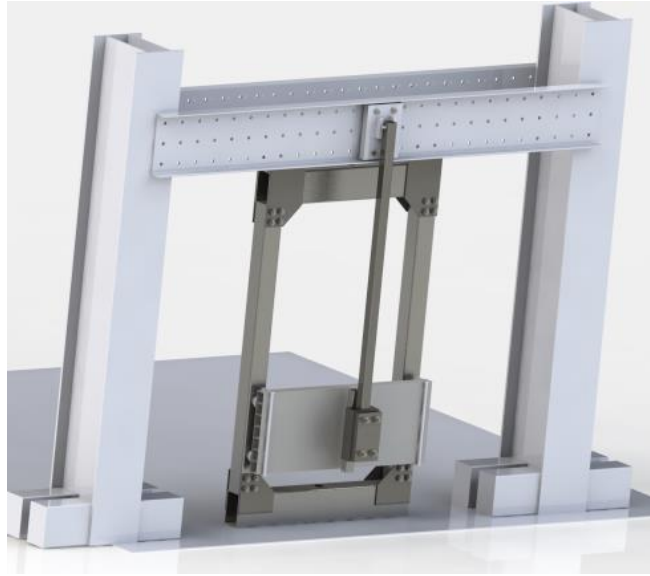


**Figure 1.2 - Cross-Section of the GFRP Multi-Cell Ribbed Structural Panel**

In order to pursue the above objectives, the testing schedule was laid-out as follows:

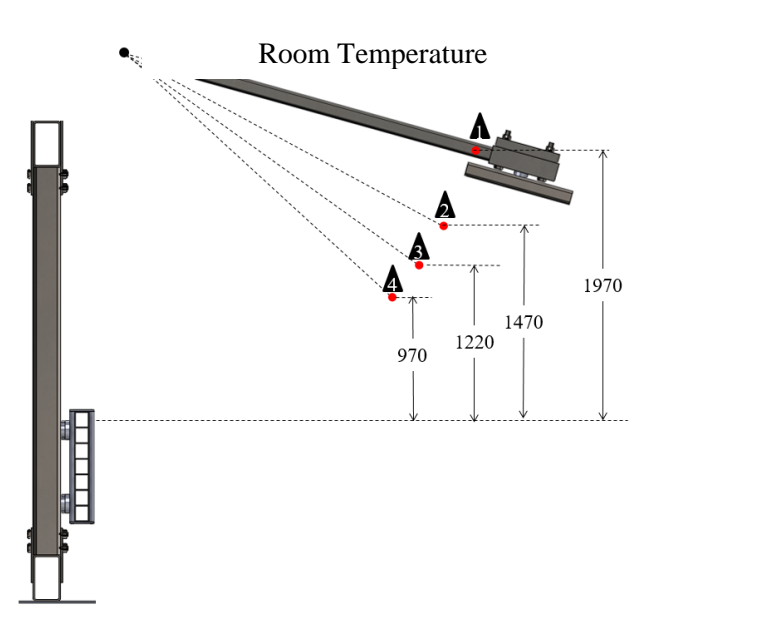
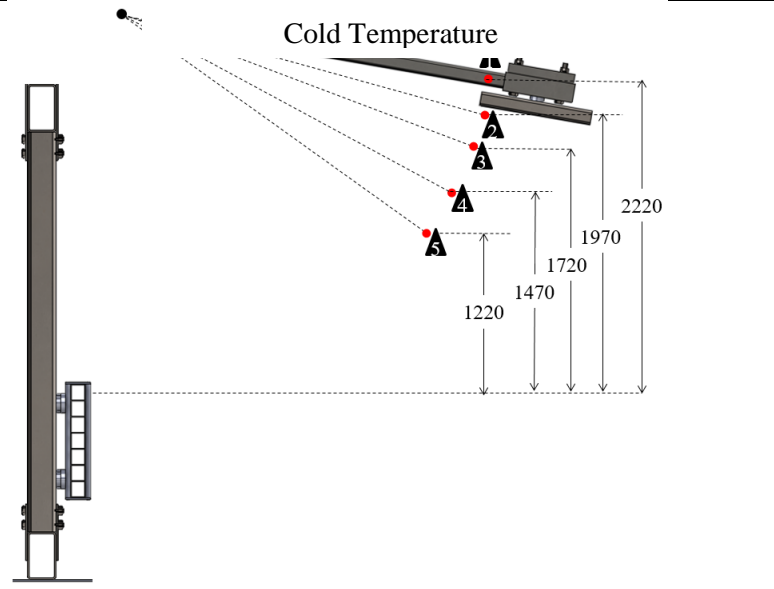
1. 4 × Panels were tested quasi-statically using a three-point flexural apparatus. Two tested at room temperature and two at cold temperatures;
2. 12 × panels were tested dynamically at room temperature using the impact hammer apparatus; and
3. 12 × panels were tested dynamically at -50°C using the same impact hammer apparatus.

The dynamically tested panels were also part of another testing phase, which investigated the residual static flexural strength. It was used to quantify the impact induced damage by using the quasi-static three-point flexural apparatus. Figure 1.3 shows the visual representation of the impact hammer apparatus used in the laboratory. The testing schedule is represented in Table 1.1. The first part of the table shows the impact hammer drop heights for each test series in the first study at room temperature. The second part illustrates the second study at cold temperature. Some drop heights are the same as the first study, while some are higher since the amount of potential energy had to be increased for the cold temperature tests as will be discussed in Chapter 3. The specimens' numbering is as follows: the panels tested at room temperature were labelled starting with the letter 'K', indicating the key variable of the study was the amount of kinetic energy imparted to the structural system and the cold temperature panels with the letter 'T', indicating the key variable was the temperature of the panels.



**Figure 1.3 - Visual Representation of the Impact Hammer Apparatus**

**Table 1.1 - Schematic Representation of Testing Schedule**

Series	Impact Hammer Drop Height	
K1-1, K1-2, K1-3	1	
K2-1, K2-2, K2-3	2	
K3-1, K3-2, K3-3	3	
K4-1, K4-2, K4-3	4	
T1-1, T1-2	1	
T2-1, T2-2, T2-3	2	
T3-1, T3-2, T3-3	3	
T4-1, T4-2, T4-3	4	
T5-1	5	

Note: All measurements in mm.



## 1.4 Thesis Organization

This thesis consists of 5 chapters and is written in the manuscript format according to the Royal Military College of Canada thesis preparation guidelines. Chapter 1 presents a general introduction of the research project. Chapters 2, 3 and 4 consist of research manuscripts and Chapter 5 presents the overarching conclusions and recommendations.

Chapter 2 investigates the behaviour of the GFRP panels subjected to impact loads at room temperature, 20°C. These loads were applied using a pendulum hammer. All the panels tested had the same dimensions and boundary conditions. The varied parameter was the kinetic energy applied on the panel. It was modified by varying the initial drop height of the impact hammer. The hammer weight remained unchanged for all the testing. The maximum displacement during impact was measured as well as the hammer impact load and general strain distribution along the panels. Finally, the residual strength of each tested panel was quantified at room temperature using a standard static flexural test with similar boundary conditions.

Chapter 3 presents the behaviour of the same panels tested at sub-zero temperatures subjected to similar impact energies as the previous chapter. The same instrumentation and apparatus was used as in Chapter 2, in addition to thermocouples in order to monitor the temperature of the panel at the time of testing. The temperature of the panels for the sub-zero tests was kept at approximately -50°C on the outside faces. The varied parameters of this study were panel temperature and imparted kinetic energy, comparing the room temperature impacted panels to the cold temperature ones by varying the height of the impact hammer. Some drop heights were equal for room and cold temperature, but some had to be varied in order to inflict an appropriate extent of damage. Failure mechanisms were also compared to understand the effect of temperature on the brittleness of the panels. Residual strength was tested and compared to Chapter 2 results to better quantify the effects of cold temperature on FRP panels loaded dynamically. All residual capacity tests were performed at room temperature.

Chapter 4 presents a model that can predict the displacement-time history for the panels. An SDOF model was used for that purpose following the Predictor Method presented by Smith and Hetherington (1994) [16]. The model is

temperature and strain-rate dependent since the load-displacement history exhibits different behaviour at colder temperatures and high strain rates. Static flexural tests were performed on undamaged panels at room and sub-zero temperatures to determine a more accurate representation of a baseline resistance function. A resistance function using a modelled moment-curvature relationship was used and different dynamic increase factors (DIF) were used for room and sub-zero temperature impact tests. The results indicated the effectiveness of a SDOF model to accurately predict the behaviour of dynamically loaded GFRP panels.

Finally, Chapter 5 presents general conclusions that were gathered from these three studies. It also presents recommendations for future research on this particular problem.

## 1.5 References

- [1] Government of Canada, "Canada's Arctic Foreign Policy," August 2008. [Online]. Available: [http://www.international.gc.ca/arctic-arctique/arctic\\_policy-canada-politique\\_arctique.aspx?lang=eng](http://www.international.gc.ca/arctic-arctique/arctic_policy-canada-politique_arctique.aspx?lang=eng).
- [2] A. Hay, *Operationnal Survival: Putting Resilience at the Core of Infrastructure Planning*, London: Explora Research, 2013.
- [3] Government of Canada, "Canada First Defence Strategy," August 2013. [Online]. Available: [http://www.forces.gc.ca/assets/FORCES\\_Internet/docs/en/about/CFDS-SDCD-eng.pdf](http://www.forces.gc.ca/assets/FORCES_Internet/docs/en/about/CFDS-SDCD-eng.pdf). [Accessed 2016].
- [4] The Economist, "Frozen Conflict," *The Economist*, 20 Dec 2014.
- [5] L. Hollaway, "A Review of the Present and Future Utilisation of FRP Composite in the Civil Infrastructure with Reference to their Important In-Service Properties," *Construction and Building Materials*, Vol. 24, no. 12, pp. 2419-2445, 2010.
- [6] L. Hollaway, *Advanced Polymer Composites and Polymers in the Civil Structures*, Oxford: Elsevier, 2001.
- [7] M. Arndt, *FRP Rehabilitation of Blast and Impact Damaged Reinforced Concrete*, Kingston: Royal Military College of Canada, 2009.
- [8] J. Crawford and J. Malvar, "Composite Retrofit to Increase the Blast Resistance of RC Buildings," in *Tenth International Symposium on Interaction of the Effects of Munitions with Structures*, Burbank, 2001.
- [9] J. Crawford and et al., "Retrofit of Masonry Walls to Enhance their Blast Resistance," in *Structures Congress: Crossing Borders*, 2008.

- [10] L. Van Den Eide and et al., "Use of FRP Composites in Civil Structural Applications," *Construction and Building Materials*, vol. 17, no. 6-7, pp. 389-403, 2003.
- [11] S. Benli and O. Sayman, "The Effects of Temperature and Thermal Stresses on Impact Damage in Laminated Composites," *Mathematical and Computational Applications*, vol. 16, no. 2, pp. 392-403, 2011.
- [12] M. D. Erickson and et al., "Effect of Temperature on the Low-velocity Impact Behavior of Composite Sandwich Panels," *Journal of Sandwich Structures and Materials*, vol. 7, no.3, pp. 245-264, 2005.
- [13] S. Gupta and A. Shukla, "Blast Performance of Marine Foam Core Sandwich Composites at Extreme Temperatures," *Experimental Mechanics*, vol. 52, no.9, pp. 1521-1534, 2012.
- [14] J. F. Timmerman and et al., "Matrix and Fiber Influences on the Cryogenic Microcracking of Carbon Fiber/Epoxy Composites," *Composites: Part A*, vol. 33, no. 3, pp. 323-329, 2002.
- [15] N. Uddin, *Blast Protection of Civil Infrastructures and Vehicles Using Composites*, Cambridge: Woodhead Publishing Limited, 2010.
- [16] P. Smith and J. Hetherington, *Blast and Ballistic Loading on Structures*, Oxford: Butterworth-Heinemann, 1994.
- [17] A. Bentur and et al., "The Behaviour of Concrete Under Impact Loading: Experimental Porcedures and Method of Analysis," *Matériaux de Construction*, vol. 19, no. 113, pp. 371-378, 1986.

## **Chapter 2**

# **IMPACT RESPONSE OF A GFRP MULTI-CELL RIBBED STRUCTURAL PANEL**

### **2.1 Introduction**

Fibre reinforced polymers (FRP) have gained significant attention over the past few decades, mainly due to their good corrosion resistance, fatigue resistance as well as high specific strength and stiffness [1]. Even though FRPs are more commonly used for rehabilitation of existing structures, all-FRP components for new construction are now more common and require a better understanding of all aspects of their structural behaviour. The panels used in this study are one of many “off the shelf” all-FRP components, more specifically GFRP multi-cell ribbed structural panels called COMPOSOLITE® and are manufactured by Strongwell. These structural panels are made from a pultrusion process and consist of E-Glass continuous strand mat and roving. They present a distinct advantage over traditional building materials, such as structural steel and reinforced concrete, since they exhibit versatility of application and high durability as well as light-weight and ease of construction. They also exhibit a very high strength-to-weight ratio compared to steel. All these factors contribute to overcome the initial high-cost of such materials when compared to more common materials such as steel or concrete for applications in remote areas. It has been demonstrated that FRP products can present a lower life-cycle cost compared to other conventional materials [2] [3]. These modular panels are used in a wide range of applications, including but not restricted to bridges, baffle systems, scaffoldings and small-scale buildings [4]. Very similar panels to the COMPOSOLITE® panels were previously developed by Maunsell Structural Plastics Ltd called Advanced Composite Construction Systems (ACCS). They have been directly used in the construction of the Aberfeldy Bridge in Scotland (1992) and in Gloucestershire for the Bonds Mill Lift Bridge (1994).

### 2.1.1 Background

The types of loadings that these applications may be required to resist include wind, snow, traffic, etc. However, due to malicious or accidental causes, these panels could also be subjected to more impulsive loads such as blast or impact. The analysis of the impact response of the GFRP multi-cell ribbed structural panels subjected to impulsive loads will be the main objective of this investigation. These impulsive loads will be applied using a pendulum hammer. A similar apparatus has been used in previous studies to simulate blast on reinforced concrete members with some success [5]. However, due to the typical low impact strength of composite materials, and because of the high probability of local failure in the impact region, the present study will not try to simulate a blast load, solely generic impulsive loads.

Multiple studies have been made on the resistance of all-FRP components subjected to blast loads. Most of these studies investigated composite laminated plates [6] [7] and composite sandwich panels [8] [9] under such loads. These investigations included parametric studies to better understand the effects of stand-off, explosive weight, ply angle, etc. on the dynamic behaviour of the panels. Other investigations looked at the dynamic response of FRP components subjected to impact loads. Davies [10] looked at the effects of impact on GFRP laminates as well as the damage tolerance from residual strength. A promising damage monitoring method using energy maps was presented. Also, it was found that residual compressive strength was significantly lowered with the increase of damage or incident kinetic energy due to impact induced delamination. The latter conclusion demonstrates the fact that composite materials do not exhibit plastic behaviour past failure. If a certain impact load reaches the threshold resistance of a given composite component, its residual strength will drop significantly, and this damage is irreversible.

In terms of modular building components such as the studied GFRP multi-cell ribbed structural panels, there is limited research into the dynamic response of such structural components when subjected to extreme loads. A number of studies were done on corrugated sandwich panels with different core configurations, but these investigations were mostly done statically [11] [12] [13] [14]. An impact hammer is a suitable device to investigate the dynamic behaviour and impact response of such a component when subjected to rapidly-applied and extreme

loads. Also, because composite materials are very sensitive to impact damage, the impact-induced damage of such complex structural components can be estimated by evaluating their residual flexural strength.

### 2.1.2 Dynamic Loading

In a blast load, the blast wave can be characterized by an almost instantaneous rise in pressure followed by an exponential decay over a very small period of time [15]. The negative phase that normally follows is often neglected in most analyses. An impact load is similar in nature to blast loading, apart from the incident pressure that will usually be lower. Additionally, impact loads are usually identified as low-velocity and will have a longer positive loading phase than a blast event. The response spectrum of a component subjected to a blast or impact load can be either quasi-static, dynamic or impulsive. A quasi-static response happens when the positive phase duration of loading is long compared to the natural period of the structural component. Dynamic response, on the other hand is when the positive phase duration and natural period are similar. An impulsive response occurs when the positive phase duration is much smaller than the natural period [16]. Due to the short duration of the load generated by an impact hammer, the panels are predicted to behave within the dynamic and impulsive response. An important aspect of an impulsive load, unlike static, is time-dependency. This introduces the concept of impulse, which is the product of the force and the time of its duration [17]. Blast and impact loads have two parameters that are of importance and cannot be separated: incident pressure or impact force and impulse.

### 2.1.3 Dynamic Properties of GFRPs

In order to better understand the dynamic behaviour of fibre reinforced polymers, one must take into consideration the effects of strain rate on their material properties. It is known that for common structural materials such as steel, the yield and ultimate strength values increase alongside the strain rate [18]. Consequently, when dealing with dynamic loads such as blast or impact, these strength values are normally multiplied by a dynamic increase factor (DIF) and

strength increase factor (SIF), which varies for different materials and strain rates. Even though static strength values would be more conservative as indicated by CSA S850-12 [19], omitting the DIF in a design procedure will result in over-design. If some part of the design is overly conservative, this might lead to a lack of resources for another critical part in the structure, hence demonstrating the importance for an engineer to understand the dynamic behaviour of the materials used.

The strain rate sensitivity of GFRPs has not been specifically investigated as part of this project. However, these materials are in fact strain rate dependent, and it has been the focus of multiple studies [20] [21] [22]. These studies investigated the strain rate sensitivity of FRPs, including GFRPs, under tensile, compressive, shear and flexural tests. The strain rates investigated were between  $5 \times 10^{-4}$  and  $2500 \text{ s}^{-1}$  and were applied to coupons with different apparatus such as Split Hopkinson Bar and servo-hydraulic tensile tester. It has been demonstrated that ultimate strength, elastic modulus as well as energy absorption are all strain rate dependent, increasing with the strain rate. For example, when a woven glass laminate was tested, it has been showed that there is an increase of 17%, 5.9% and 7.5% for tensile, shear and flexural energy respectively per decade increased in log of strain-rate [21]. Due to these characteristics of GFRPs, it is anticipated that failure strengths of the GFRP multi-cell ribbed structural panels will be higher from a three-point impact hammer test than from a similarly loaded quasi-static three-point flexural test. However, it has also been proven that another important effect of strain rate variation is the change in failure mode experienced by the composites due to material behaviour [22]. This could have an effect on the energy absorption of the panels under static and dynamic loading.

#### 2.1.4 Damage Mechanisms and Tolerance

Impact damage can take multiple forms in a composite panel. These mechanisms include fibre breakage, delamination of adjacent plies, matrix cracking, debonding between the fibre and the matrix and finally fibre pull-out from matrix [23]. These mechanisms are affected by a number of parameters from the composite panel's properties (i.e. types of fibres, matrix, fibre orientation, etc.), but also from the impactor's properties (mass, velocity, shape, etc.). The literature



identifies multiple non-destructive methods of quantifying impact damage such as ultrasonic C-scan, X-Ray radiography as well as destructive methods including cross-sectioning [24]. However, the damage mechanisms on the panels studied in this investigation were evaluated using a qualitative method of infrared thermography. This method was proven to be effective for a wide range of composite components [25]. This method can also be used easily in field applications without the necessity of specialized equipment, which would be very useful for a damage assessment in a remote area such as the Arctic. The damage tolerance, which identifies the capacity of a damaged panel to sustain a subsequent static load, was then quantified using a destructive residual capacity 3-point bending test.

### 2.1.5 Robustness

Since an impulsive load such as an impact hammer or a blast will likely bring a structural component past the elastic regime to the elasto-plastic phase, the behaviour of the component past yield or failure is extremely important. According to Naaman et al. [26], ductility is the ability of a structural component or material to sustain inelastic deformation prior to collapse, without substantial loss in resistance. In a structural system, ductility increases structural safety by allowing the formation of plastic hinges, redirecting the loads from more heavily stressed regions to more lightly stressed ones. However, this definition is inappropriate for all-FRP components, since composite materials exhibit elastic behaviour until a brittle failure. Van Erp [27] introduced the robustness factor that is much more suited for all-FRP components since it takes into account deflection factors and strength factors. The robustness factor can be seen in equation (2.1).

$$\mu_{robustness} = \frac{w_{ultimate}}{w_{serviceability}} * \frac{S_{ultimate}}{S_{serviceability}} \quad (2.1)$$

Where  $\mu$  is the robustness factor,  $w$  is the deflection and  $S$  is the Strength. This concept is ultimately the ratio of the absorbed energy at the ultimate state to the energy at the serviceability limit state. Due to their low stiffness to strength

ratio, FRP components are governed by the serviceability limit state which is accounted for in the robustness concept. This factor may be used to compare the GFRP multi-cell ribbed structural panels to other types of structural components such as steel or reinforced concrete beams from a safety point of view.

## **2.2 Objective**

The objective of this study was to evaluate the impact response of GFRP multi-cell ribbed structural panels. This was done by using varying impact loads with an impact hammer apparatus. The damage resistance of the panels was also evaluated using residual flexural strength tests. This study looks at full-size GFRP panels as opposed to coupons alone. It focuses on a variety of structural failure mechanisms vice material-related failures only.

## **2.3 Procedure**

### **2.3.1 Material Properties**

The materials which comprise the studied panels are a mix of isophthalic polyester fire-retardant resin with E-Glass continuous strand mat and roving. The percentage of fibre to volume ratio is approximately 50% and coupon critical mechanical properties can be found in Table 2.1. Tests have been conducted in the laboratory to confirm the manufacturer's stated mechanical properties. Tensile coupon tests were done as part of this project using an 810 Material Testing System (MTS) monitoring stroke and load as well as strain with 120  $\Omega$ , 10 mm strain gauges from HBM adhesively mounted on the coupon in the lengthwise and cross-width direction. The tests were performed at a constant displacement-rate of 20 mm/min. Results of these tests are shown in Appendix A.

**Table 2.1 - COMPOSOLITE® Mechanical Properties**

<b>Properties</b>	<b>ASTM Test Method</b>	<b>Manufacturer's Value [4]</b>	<b>Laboratory tested at RMCC</b>
<b>Tensile Modulus (Lengthwise) MPa</b>	D638	17,140	19,520
<b>Tensile Strength (Lengthwise) MPa</b>	D638	214	373
<b>Flexural Modulus (Lengthwise) MPa</b>	D790	6,102	N/A
<b>Flexural Strength (Lengthwise) MPa</b>	D790	169	N/A
<b>Flexural Modulus (Cross-Width) MPa</b>	D790	4,454	N/A
<b>Flexural Strength (Cross-Width) MPa</b>	D790	56.5	N/A
<b>Short Beam Shear (Lengthwise) MPa</b>	D2344	22	N/A
<b>Poisson's Ratio (Lengthwise) mm/mm</b>	D3039	0.33	0.34

The properties given by the manufacturer were minimum ultimate values that resulted from a series of tests. The properties that were found in laboratory tests will be used in this study in order to get more accurate predictions of experimental behaviour, instead of the conservative values from the manufacturer, which would be appropriate in a design scenario. Only the modulus and the lengthwise tensile strength were needed for calculations as part of this study. It is important to note that the studied GFRP panel is anisotropic. Coupons were stronger and stiffer in the lengthwise than in the cross-width direction. Even though the literature from the manufacturer states that the compressive strengths are equal or larger in both directions, they were chosen to be equal to the tensile properties for this investigation. The modular panels themselves come in 605 mm wide and 80 mm thick size and were cut to the required lengths, see Figure 2.1.

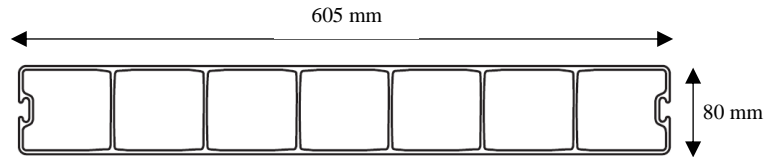
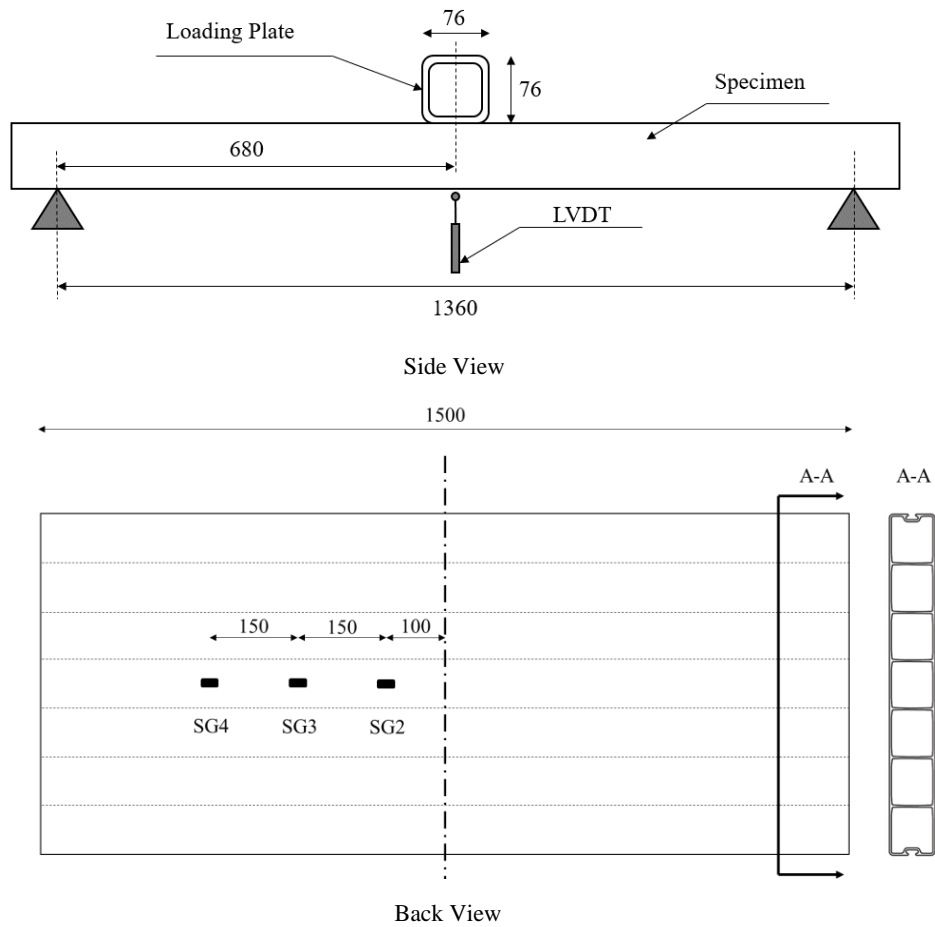


**Figure 2.1 - Cross-Section of COMPOSOLITE® Panel [4]**

The panels used in this study were 1500 mm long and filled with #1 EPS foam. Even though the foam provides thermal insulation, it was deemed to provide no structural benefit to the panel.

### 2.3.2 Quasi-Static 3-point Flexural Test

To understand the flexural behaviour of the panels, a 3-point quasi-static bending simply supported test was performed on the panel as shown in Figure 2.2. This test was done in order to determine the strength and post-failure energy absorption behaviour of the panels. These parameters were then used in order to plan for the magnitude of the impulsive load that would be imparted by the impact hammer. The supports on each end were a triangular pin as can be seen in Figure 2.2, and a 50 mm wide steel plate was placed between the pin and the panel to avoid local crushing of the specimens at the supports. The unsupported span of the specimen was 1360 mm, and the load was applied at the mid-span. The load was applied to the specimens by a 75 mm rectangular Hollow Structural Section (HSS) with a rubber strip between the HSS and the specimens. The HSS had the same width as the panels and was the same one used at the end of the impact hammer. A 322 test frame MTS with a constant head-speed of 20 mm/min was used in this case. The load as well as the stroke were monitored on the MTS as well as the strain distribution using 4 x 120  $\Omega$ , 10 mm strain gauges from HBM adhesively mounted on each specimen. One was placed at the top and the other three were distributed along the length of the bottom face. The location and spacing of the strain gauges can be seen in Figure 2.2. They were used to understand the curvature distribution as well as the shape function of the specimens under a static load. The panels were taken past the point of failure to the maximum stroke of the machine which is approximately 100 mm. Two flexural tests were performed on two panels.



Notes: -All dimensions in mm  
 -SG1 is at the same position as SG2 on the front face

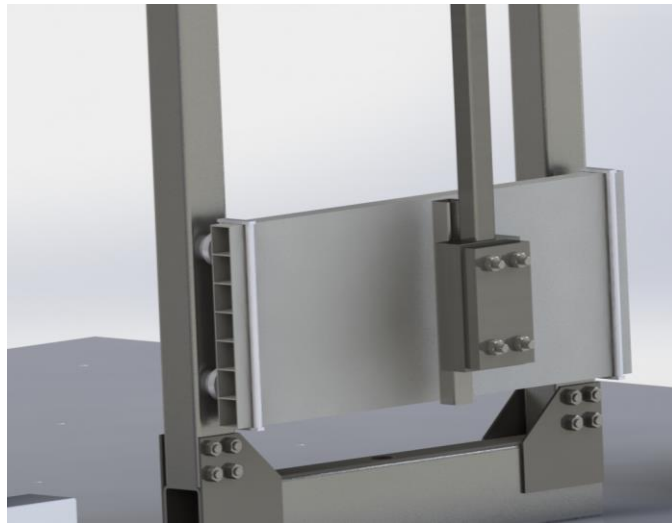
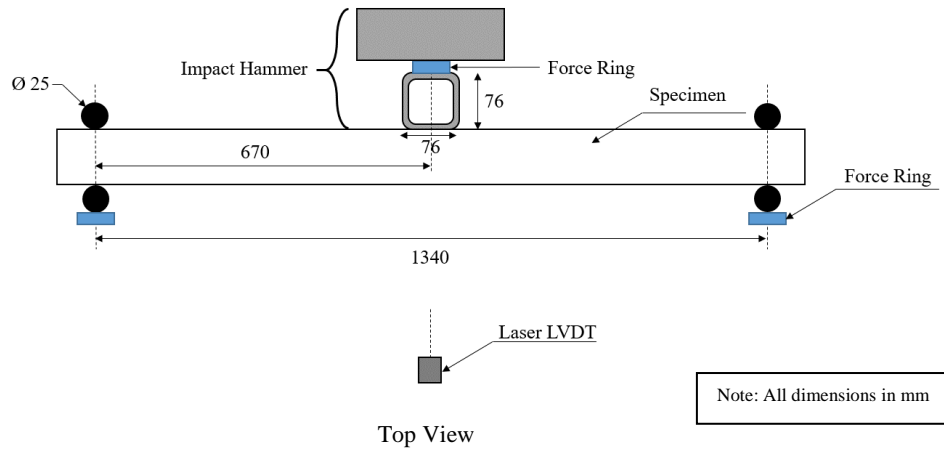
**Figure 2.2 - 3-Point Flexural Test Apparatus**

### 2.3.3 Impact Hammer Apparatus

It is important to note that in the field of impact testing, many different testing configurations are used, and the literature can reflect this [23]. The Izod and Charpy methods could not be used in this case, since the behaviour of the full panel

needed to be assessed. Since the panels were tested in flexure, both statically and dynamically, and because the flexural modulus depends on both mechanical and structural properties [28], the tests had to be done on full-size specimens. Consequently, a 138 kg impact hammer apparatus was used in order to generate a sufficiently large impulsive load onto the composite panels to observe their impact response. This apparatus used the principle of a pendulum with a large mass, transferring a significant amount of energy to the panel over a very short amount of time. The set-up can be seen in Figure 2.3.

The hammer was built using a 100 mm steel HSS as the lever arm, and a rectangular steel section as the head. The head was built so that additional steel plates could be added to the back of it in order to achieve higher potential energies. Also, a 75 mm HSS was attached to the front of the hammer head to distribute the load across the full width of the specimens. These loading conditions were done in order to apply an impulsive impact loading to the panel as opposed to a ballistic loading. The impact response of the panel was sought and not its penetration resistance. The 1500 mm long panels were supported by 25 mm diameter bars on each face of the panels on both supports. This was done so that the panel would be kept in place since the test was done vertically instead of horizontally. The specimens were however allowed to rotate up to approximately 8 degrees at both supports. These support conditions were assessed to be semi-rigid as opposed to simply supported for the quasi-static test. The unsupported span of the panels on the impact apparatus was 1340 mm.



3D View

**Figure 2.3 - Impact Hammer Apparatus**

Instrumentation was used in order to capture the dynamic behaviour of the panels as well as the imparted energy by the impact hammer. A laser LVDT with a range of 600 mm was used to measure the mid-span deflection of the specimens. Also, strain gauges along the front and back face of the panels were used to capture the curvature as well as the shape function of the dynamically loaded GFRP panels. Two hundred mm spring LVDTs were also used at the supports to measure the specimens' displacements in the supports. A 207C ICP® 445 KN compression

piezo-electric force ring was used behind one of the supports to measure the dynamic reaction generated by the hammer. As for the hammer, a similar force ring was placed just between the HSS and the head to measure the applied dynamic load to the specimens. Additionally, a shock ICP® 1000 g piezo-electric accelerometer was placed just above the head to measure acceleration and estimate the hammer’s velocity. Lastly, a high-speed camera was set-up just above the specimens to capture the hammer’s velocity before the impact as well as the dynamic response of the specimens. All these instruments, except for the camera, were connected to an MGC plus DAQ system and recorded in the software Catman Pro. The sampling rate of the piezo-electric instruments (i.e. accelerometer and force rings) as well as the laser LVDT was set at 2400 Hz. All the other instruments were sampled at 1200 Hz. The camera recorded images at 1000 fps. The load imparted to the specimens by the hammer was well-distributed along the width of the panel with the HSS and this has been checked by placing strain gauges along the width of specimen K1-1, as shown in Appendix B. One-way bending was observed between the two supports.

In total, twelve (12) specimens were tested dynamically. The testing schedule consisted of four groups of three specimens that were imparted with different kinetic energies (K1 to K4). The mass of the hammer remained constant while the drop height was changed for all four series, resulting in a change of impact velocity. However, to predict the applied energies for each series, the potential energy was used from known drop height values. The complete testing schedule can be seen in Table 2.2.

**Table 2.2 - Impact Testing Schedule**

<b>Test Series</b>	<b>Drop Height of the Hammer from rest (mm)</b>	<b>Resulting Potential Energy (J)</b>
<b>K1-1, K1-2, K1-3</b>	1970	2630
<b>K2-1, K2-2, K2-3</b>	1470	1970
<b>K3-1, K3-2, K3-3</b>	1220	1630
<b>K4-1, K4-2, K4-3</b>	970	1300



## 2.4 Results and Discussion

### 2.4.1 Quasi-Static Testing

The load-displacement results of the two quasi-static tests can be seen in Figure 2.4. The mid-span displacement as shown is the deflection of the back face measured using the LVDT.

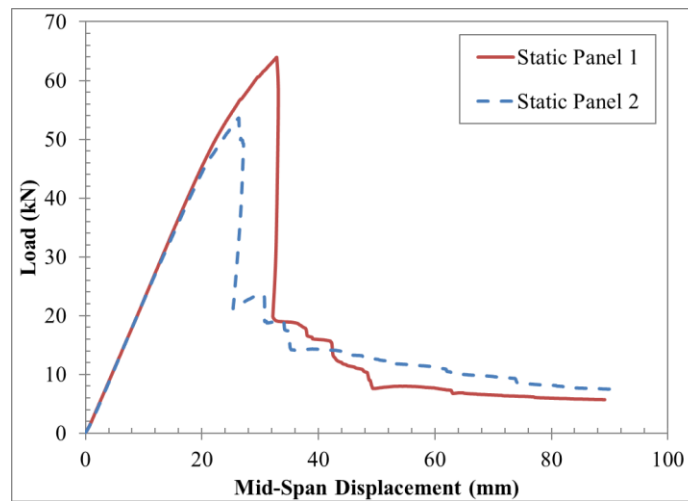


**Figure 2.4 - Load-Displacement Results of the Quasi-Static 3-point Flexural Tests**

These results were used in order to identify the residual strength of the panels post-impact by comparing the peak load as well as strain energy up to a key mid-span displacement (i.e. failure and peak). The peak strength of the panels under 3-point bending was found to be 58.8 kN and a strain energy of 1604 J for a 90.0 mm mid-span deflection. The energy and displacement threshold values to failure were found to be 964 J and 29.6 mm respectively. These values were taken from the average of the two tests. Failure in these panels was observed by the sudden drop in strength at displacements greater than the elastic behaviour as seen in Figure 2.4. While the panel still carried loads past that failure, the strength was significantly reduced at that point. However, the behaviour past failure is still important in order to estimate the total strain energy that can be absorbed by these panels. The total quasi-static strain energy was used in order to estimate the imparted kinetic energy for the dynamic tests.

## 2.4.2 Impact Testing

As mentioned in the procedure, each test series was completed by testing three panels at the same drop height. The resolution of the high-speed footage was not accurate enough to determine the exact velocities of the hammer and therefore were not used in order to determine the kinetic energy provided by the hammer. Consequently, a method suggested by Banthia [29] was used following the impulse-momentum relationship. The resulting averaged kinetic energy values can be seen in Table 2.3 for all four series as calculated from equation (2.2).

$$KE(t) = \frac{1}{2} m_h \left[ 2a_h h - \left( \sqrt{2a_h h} - \frac{1}{m_h} \int P_t(t) dt \right)^2 \right] \quad (2.2)$$

**Table 2.3 - Impact Tests Kinetic Energies**

Series	Predicted Potential Energy (J)	Measured Kinetic Energy (J)
K1	2630	2440
K2	1970	1959
K3	1630	1630
K4	1300	1296

Where,  $m_h$  is the mass of the hammer,  $a_h$  is the acceleration of the hammer,  $h$  is the drop height, and  $P_t$  is the recorded hammer tup load. Also, the hammer's acceleration used in the latter equation is the acceleration pre-impact. The chosen acceleration was  $9.81 \text{ m/s}^2$  assuming there was no friction in the apparatus. This assumption was made knowing that the resulting kinetic energy would be a more conservative representation of reality. Potential energy calculations were performed by measuring the difference of the at-rest height of the center of gravity (COG) of the hammer and arm and the drop height of the same COG. The discrepancy between the measured kinetic energies and the projected potential energies can be due to loss of energy in the rotating pin, air friction, etc.

An example of a hammer impact load and specimen mid-span displacement time-history are shown in Figure 2.5 and Figure 2.6.

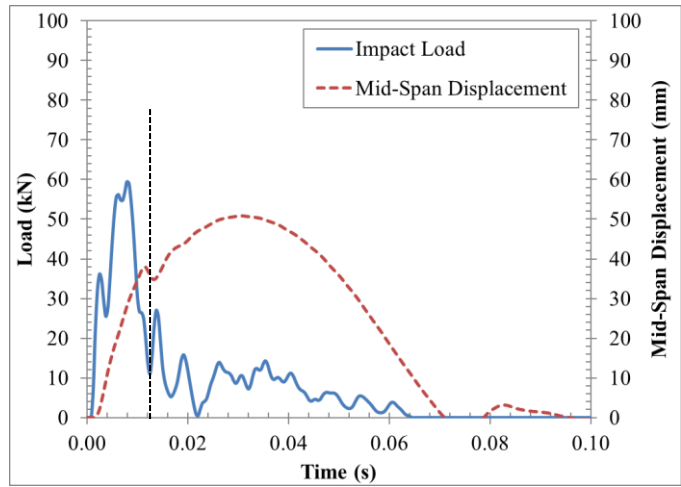


Figure 2.5 - Impact Load and Mid-Span Displacement-Time History, K2-3

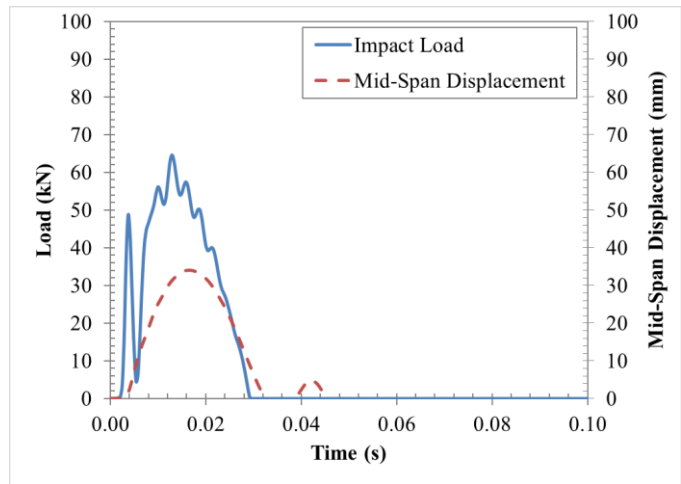
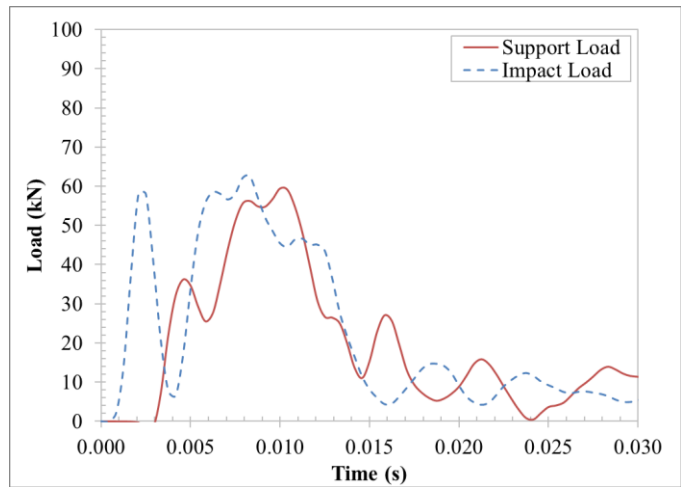


Figure 2.6 - Impact Load and Mid-Span Displacement-Time History, K4-3

The initial peak followed by a drop in the impact load time-history can be observed in most of the impact events. This phenomenon represents the loss of contact between the specimen and the hammer for a short time duration following the initial impulse. This was confirmed by looking at velocity data from the panel and the hammer, gathered from the laser LVDT and accelerometer respectively. Also, the sudden reduction of load occurring simultaneously with a short drop in the mid-span deflection represents the initial failure of the specimens, similar to the

failure of the quasi-static static tests as seen in Figure 2.4. These failures were also confirmed using the high-speed camera. The specimens that did not exhibit these sudden reductions in the displacement-time history were considered to be damaged without having failed as shown in Figure 2.6. Notwithstanding the fact that failure is not observed in Figure 2.6, another clue to see if the panel had failed or not is to look at the way the load and the panel's displacement behaved just before the panel rebounded back to its starting position. The failed panel's impact load sharply dropped following failure and stayed relatively low until the panel went back to rest. While the non-failed panel's impact load stayed high until it suddenly dropped when the panel rebounded back to a rest position. The impact load and mid-span deflection time-histories for all 12 dynamic tests on the specimens are shown in Appendix C.

An important consideration in the case of an impact hammer apparatus is the load recorded from the piezo-electric force ring. It had to be corrected to obtain the actual bending load applied on the panel because some of the impact load is in fact used to maintain the balance with the inertial force during loading [30]. If the hammer load is used, a correction including the effects of the inertial load must be applied using a method such as is prescribed by Banthia et al. [29]. Alternatively, the reaction from the support force ring may be used. Using the support load has been used successfully by Soleimani et al. [31]. This method has been used during this study because it is a direct way to measure the loading that is applied directly to the specimen. The support load acquired was multiplied by four since the supports rods were anchored at two points to the testing frame on each side. The comparison of the impact load and the support reaction for a failed panel can be seen in Figure 2.7 (Specimen K2-3) and a non-failed panel is shown in Figure 2.8 (Specimen K4-3).



**Figure 2.7 - Comparison of Support and Impact Load for Panel K2-3**

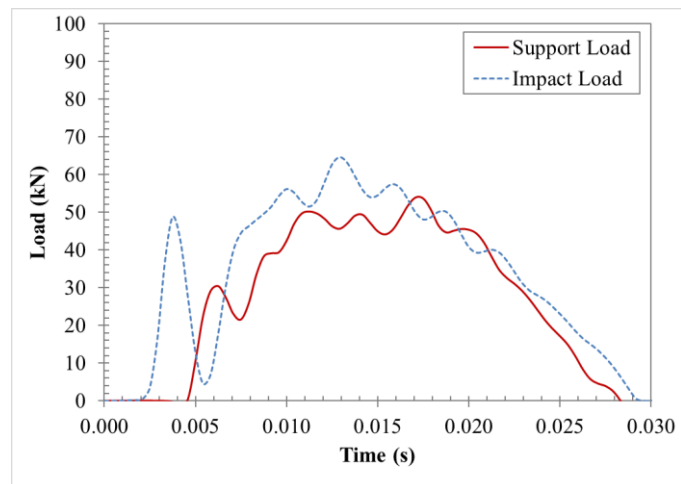


**Figure 2.8 - Comparison of Support and Impact Load for Panel K4-3**

It is important to note that the start of both loads is offset by a 2ms delay. This delay has been observed in previous investigations [30] [29] [31]. It is mainly due to the fact that the rise time of the initial load is so sudden that the stress wave takes time to propagate from the point of impact to the support. This delay can also be observed by looking at the strain values along the length of the specimens. The strain gauges closer to the impact point will show variations faster than the ones closer to the supports. The delay was then accounted for, as was successfully done in previous work [30] [31], by shifting the support reaction 2 ms earlier. The load-

displacement curve of the specimens could then be plotted and two examples (failed specimen K2-3 and non-failed specimen K4-3) are shown in Figure 2.9 and Figure 2.10 respectively. The static load-deflection behaviour of a similar panel is also shown in the figure. Dynamic load-deflection plots are shown in Appendix D. Again, the load used for these graphs was the support reaction multiplied by four and not the impact load as explained previously.

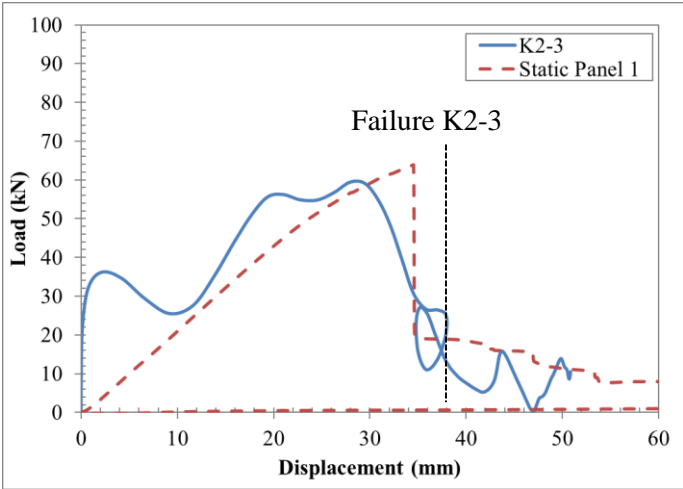


Figure 2.9 - Dynamic Load-Displacement Curve for Panel K2-3

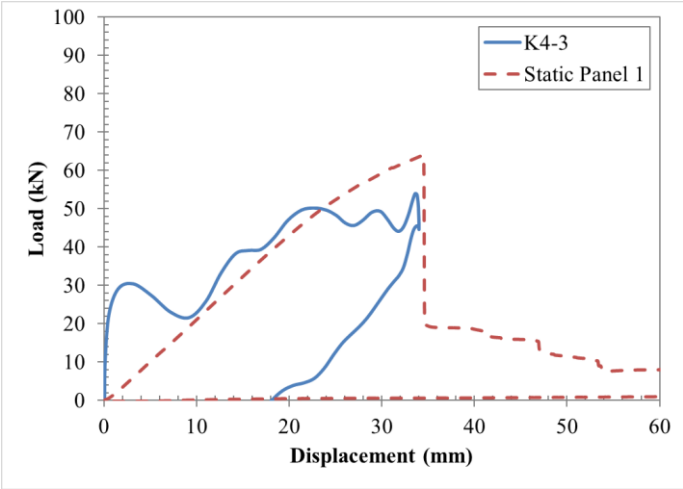


Figure 2.10 - Dynamic Load-Displacement Curve for Panel K4-3

The abnormal behaviour past failure is mainly due to the back-face rebounding towards the front face following crushing of the inside webs. The strain energy of the panel was calculated using the area under the dynamic load-displacement curve. Table 2.4 shows the gathered results for all the panels tested. Sample calculations for these results can be found in Appendix E.

**Table 2.4 - Impact Tests Results**

Test Series	Potential Energy (J)	Total Work Done (J)	Failure Displacement (mm)	Peak Displacement (mm)	Strain Energy Prior Initial Failure (J)	Strain Energy at Peak Deflection (J)
<b>K1-1</b>	2630	1805	36.3	64.0	1730	2077
<b>K1-2</b>	2630	2050	39.4	94.6	1612	2045
<b>K1-3</b>	2630	2036	39.5	92.8	1608	2108
<b>K2-1</b>	1970	1580	36.2	47.4	1612	1771
<b>K2-2</b>	1970	1561	34.9	54.1	1332	1530
<b>K2-3</b>	1970	1616	37.9	50.9	1580	1709
<b>K3-1</b>	1630	1613	38.6	38.6	1667	1667
<b>K3-2</b>	1630	1531	36.9	36.9	1544	1544
<b>K3-3</b>	1630	1684	No failure	35.9	No failure	1710
<b>K4-1</b>	1300	1291	No failure	33.9	No failure	1147
<b>K4-2</b>	1300	1308	No failure	31.8	No failure	1270
<b>K4-3</b>	1300	1345	No failure	34.0	No failure	1299

The total work done can be expressed as the impact energy and was calculated from the area under the impact load-displacement curve. The potential energy should be very similar to the work done. The reason why they differ with higher energy level impacts might be because of where the panel's displacement was measured. If the displacement was measured at the front and the back of the panels as opposed to the back only, the total work done might be more accurate by taking into account local crushing at the point of impact. The work done should be equal to the summation of the panel's kinetic energy and its strain energy. The kinetic energy of the panel was calculated by using its velocity, which was differentiated from the laser measurements, and the factored mass of the panel, assuming a sinusoidal shape. As mentioned before, the panel's strain energy was calculated using the area under the load-displacement curve from the support reaction multiplied by four and the mid-span displacement. The summation of the panel's kinetic and strain energy is called the total absorbed energy and should

correspond very closely to the work done by the hammer. Table 2.4 shows that the panels were able to withstand an average strain energy of 1586 J before failure. Figure 2.11 and Figure 2.12 show the energy conservation graph. The remainder of these graphs for all panels are shown in Appendix F.

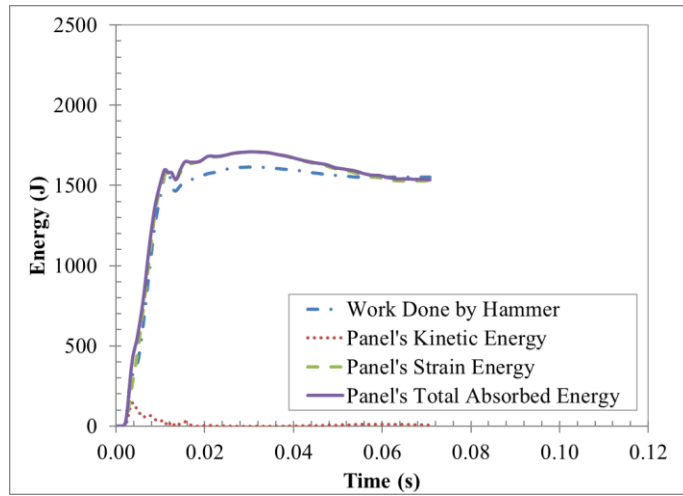


**Figure 2.11 - Energy Conservation for K2-3**

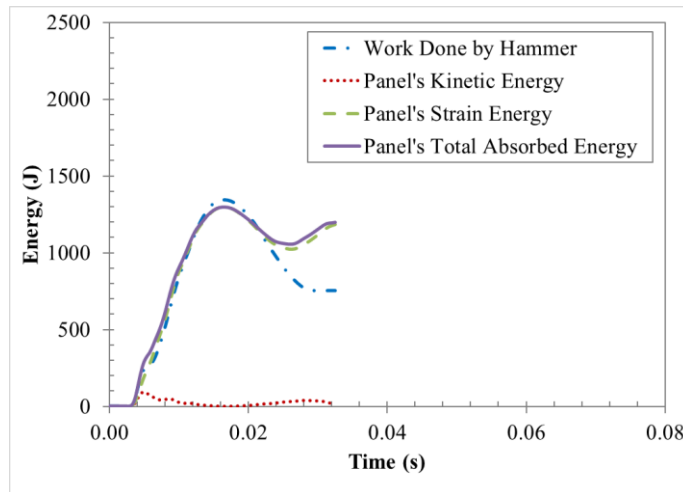


**Figure 2.12 - Energy Conservation for K4-3**



The failure energy can also be seen in this graph as the change of slope at approximately 1600 J which matches the value in Table 2.4 for panel K2-3. The total energy, which is characterized as the total energy transferred to the panel, is higher than the work done by the hammer slightly after impact. This could be due to an overestimation of the panel's kinetic energy, or maybe the support's reaction. Shifting the load in time might have had an effect on these energy conservations. Also, the reason why the total energy does not match the work done by the hammer following failure is because some of the energy is lost in the system. This energy could be transferred to the hammer or support vibrations. In the following sections, the threshold energy will reference to the amount of energy needed to bring the panels to failure, which could be work done or strain energy since they are very similar up to failure.

Figure 2.13 presents the strain energy of all the tested panels as a function of peak dynamic deflection. There seems to be a plateau energy that the panels can absorb around 2100 J. However, this cannot be confirmed since the panels have not been taken to ultimate failure or fracture, meaning the back face would fail as well creating two new fracture surfaces. A second order polynomial relation was used for this graph in order to estimate the plateau. However, the energy capacity at higher displacements would likely stay constant at or increase slightly from the 2100 J level.

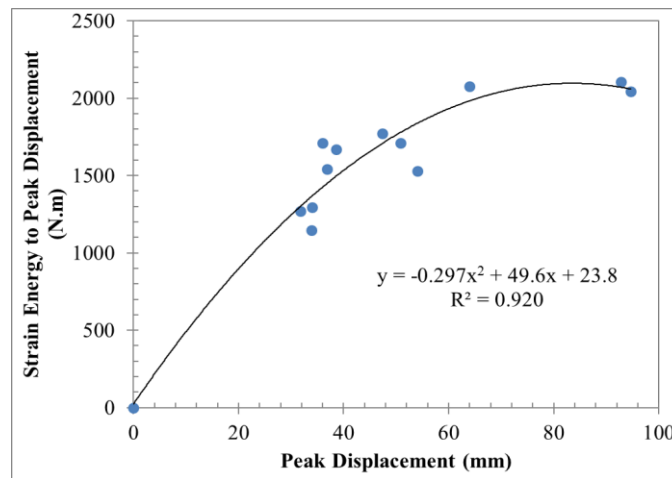


Figure 2.13 - Strain Energy to Peak Deflection vs. Panel's Peak Deflection

### 2.4.3 Comparison of Quasi-Static and Impact testing

As mentioned in the introduction, GFRP materials are strain rate dependent. The strain rate measured in the quasi-static tests were of  $6 \times 10^{-5} \text{ s}^{-1}$  while the dynamic strain rate was observed to be as high as  $1 \text{ s}^{-1}$  for the highest kinetic energy hits (i.e. K1 series). These strain rates were measured using SG2, i.e. closest to the mid-span. It is then expected that there will be a higher flexural capacity for the panels under impact than during the quasi-static tests. The threshold values discussed in further discussions are simply the values the panels were able to withstand prior to failure, i.e. the failure displacement and failure energy. The failure threshold mid-span deflections for the quasi-static tests, 29.6 mm, have increased by 26.7% in the impact tests, which averaged 37.5 mm. However, the difference is much more noticeable with the threshold failure energies. In fact, with an average value of 1586 J, the dynamic threshold failure energy is 64.5% higher than the quasi-static case, 964 J. Figure 2.14 shows the history of the strain energy in the panels as a function of mid-span displacement. An example of each series is presented and compared with the strain energy history for one of the static tests. This shows that the panels absorbed more energy dynamically than they did statically.

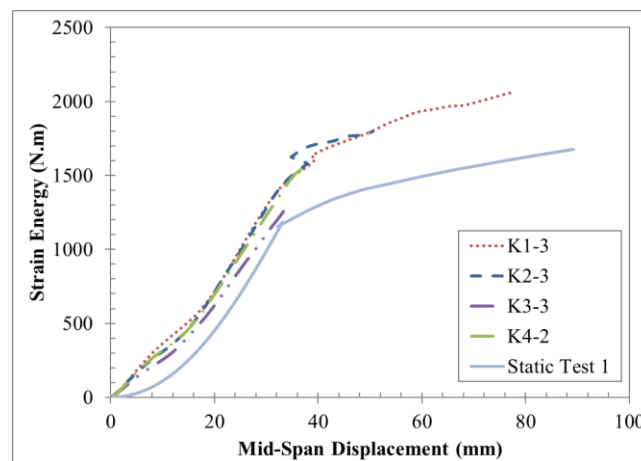


Figure 2.14 - Strain Energy History vs. Mid-Span Displacement

Therefore, the studied GFRP multi-cell ribbed structural panels' material properties are strain rate dependent, and the strain energy is the most sensitive

parameter observed in this study. No significant increase has been observed in the actual bending load for the dynamic and quasi-static case.

#### 2.4.4 Failure Mechanisms

Throughout all of the tests from this study, all of the cracks were present in the vicinity of the point of impact. In larger potential energy impacts such as K1, cracks would be most prominent along the connection between the top face and the side webs of the panels. In these cases, cracks were also visible between the back face and the side webs. This can be seen in Figure 2.15, and the remainder of the damaged panels' images can be seen in Appendix G. Major cracks were also visible across the width of the panels, indicating that parts of the front face completely delaminated from the inside webs and failed in tension or compression, which can be observed in some of the strain-time history graphs. In the K2 series, panels exhibited failure along the edges of the front face with the side webs, but not the back. Some cracking was also visible along the front face but were mostly localised around the areas where the front face meets the inside webs. K3 panels exhibited similar failures as the K2 series. For K4 panels, where major failure did not occur, only minor cracks were visible in along the side of the core and front face, and some micro-cracking where the front face meets the inside webs. Apart from the connection between the back face and the side webs, no visible failure was present on the back face of the panels during any of the impact tests.

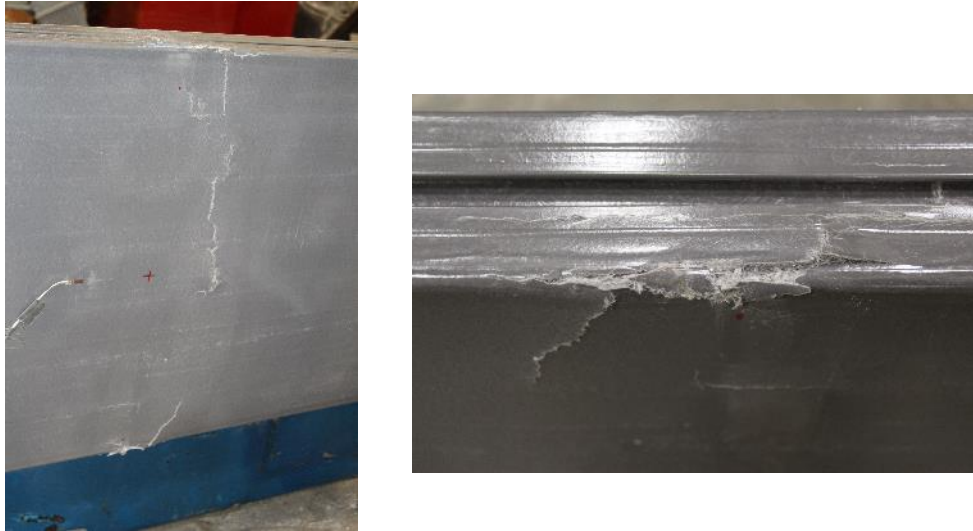


**Figure 2.15 - Failure Mechanisms Observed for Panel K1-3**

Figure 2.16 shows the infrared thermography captured with a FLIR thermographic camera. The damaged panels were frozen to  $-80^{\circ}\text{C}$  and quickly taken out of the freezer so that the infrared thermography could be done in the first few minutes of thawing, in order to get clearer characterization of damage areas. The darker colours represent the colder areas and the lighter ones represent the warmer areas. For example, the webs of the panels are clearly seen as the dark areas. Damage can be seen in the lighter colours with the use of IR thermography. These images clearly depict the areas where cracks occurred in the case of K1-3 and K2-3. K4-3 shows no major damage from the thermal imaging, nor the visual inspection except micro-cracks. However, in the K3-2 analysis, where no visible cracking occurred on the front face, the thermal imaging was able to identify a delamination between the front face and the inside web. This phenomenon is more apparent in the top portion of the image. These concentrated failures in the web-face connection makes sense from the known behaviour of web-core sandwich panels. Romanoff and Varsta [32] have studied the bending response of these types of panels and have identified through FEA that normal stresses are higher in the face plates where they connect with the webs. This has also been observed in one of the quasi-static flexural tests performed in this study.

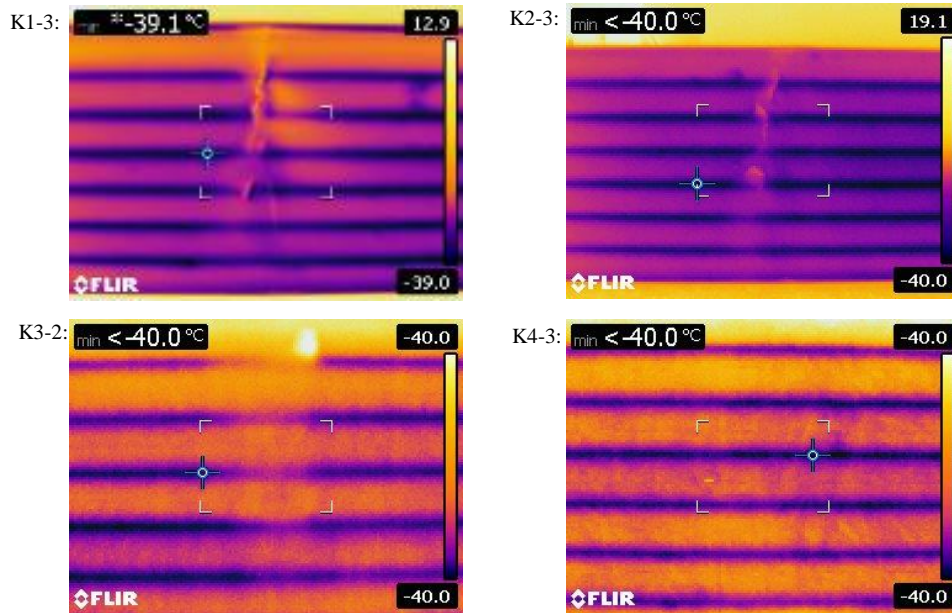


**Figure 2.16 - Non-Destructive Failure Characterization of Panels through Thermal Imaging**

Looking at the strain distribution in the front and back face of the panels for different tests can provide additional information regarding the failure mechanisms from a structural component point of view. An example can be seen in Figure 2.17, where SG1 and SG2 are strains at the front and back face respectively 100 mm away from the mid-span (see Figure 2.2 for strain gauges labelling). SG2, SG3 and SG4 represent the strain distribution in the longitudinal direction on the back face and those strain gauges were 150 mm apart. Before failure, the strains and their slopes on the front and back face are similar, demonstrating composite action in the panel. However, when the slope of the strains on the front face start to differ from the back face, this could very well illustrate the buckling of the front face. Also, it can be seen that there is a sudden drop in the strain on the back face following failure. This failure marks the end of the composite action in the panel, and this is very likely due to the delamination between the front face and the inside webs, as can be seen in Figure 2.19. The ultimate limit state was checked to see if these observations matched the theoretical failure [33], and the local buckling of the flange due to in-plane stresses governed for flexural behaviour. The calculated

critical buckling stress was  $-75.4$  MPa, which is significantly lower than the ultimate stress prescribed by the manufacturer for a coupon. This stress in the flange would correspond to a strain of  $-4400$   $\mu\text{m}/\text{m}$  using the manufacturer's modulus. Some panels exhibited failure in the vicinity of those strains, K2-3 for example as shown in Figure 2.17, more likely exhibiting a failure due to in-plane compression buckling of the front face. However, some panels showed compressive strains much higher than  $-4400$   $\mu\text{m}/\text{m}$ , as seen in Figure 2.18 with panel K2-2. This may be due to the fact that the buckling of the front face did not develop sufficiently to fail certain panels, and the local crushing of the web would then govern failure. The concentrated load needed for this failure mode was  $67$  kN according to the ultimate state calculations performed, which is similar to the peak load recorded experimentally. Sample calculations of these can be found in Appendix H.

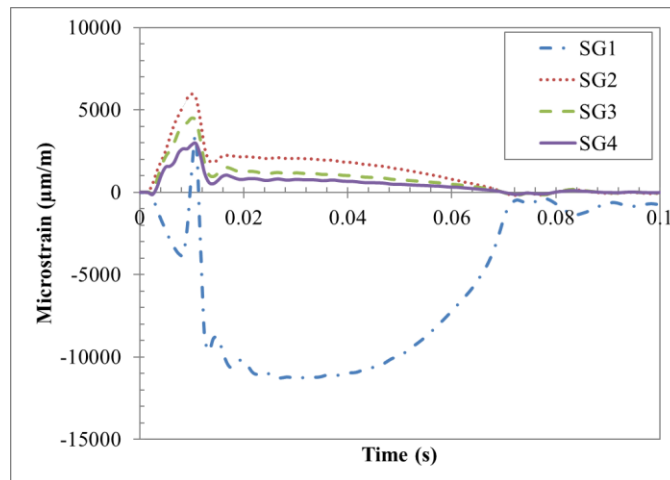
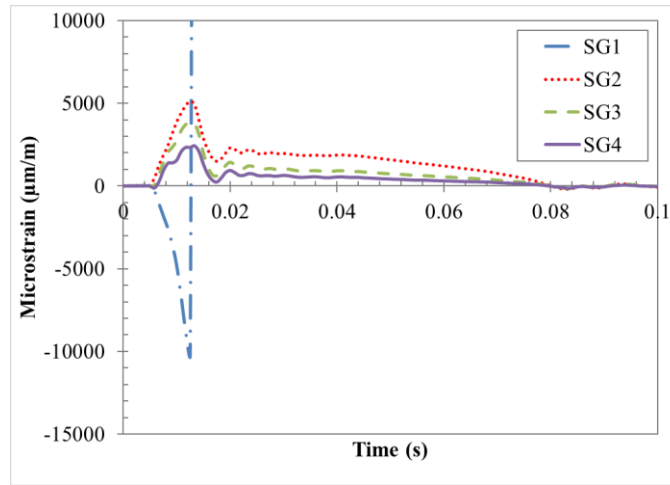
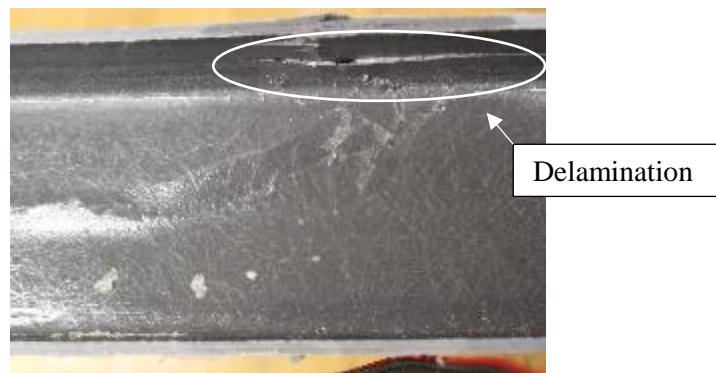


Figure 2.17 - Strain Distribution Time History (Panel K2-3)



**Figure 2.18 - Strain Distribution Time History (Panel K2-2)**

It can also be observed that the strains along the length of the panel do not follow the same trend before and after failure. Before failure, the strains of SG2 were approximately 1.5 times the ones in SG3 and the latter were 1.5 times of SG4. However, after failure, the strains in SG3 were similar to SG4 while it was observed that SG2 registered strains twice the values of SG3 and SG4. This could demonstrate the formation of a hinge at the mid-span of the panel. Therefore, the panel has a pseudo-ductile behaviour, by redistributing the stresses to less loaded areas of the panel. This phenomenon can also be demonstrated by looking at Figure 2.17, where there is a drop in strains on the back face following failure, while the strains in other areas are dramatically increasing.



**Figure 2.19 - Delamination of the Inside Webs with the Front Face**

## 2.4.5 Residual Flexural Strength Test

Once the panels had been loaded dynamically in the impact hammer apparatus, they were tested with the same procedure as the static flexural specimens. However, the only acquired data during these tests were the mid-span deflection and applied load. The results of the residual flexural strength tests are shown in Figure 2.20.

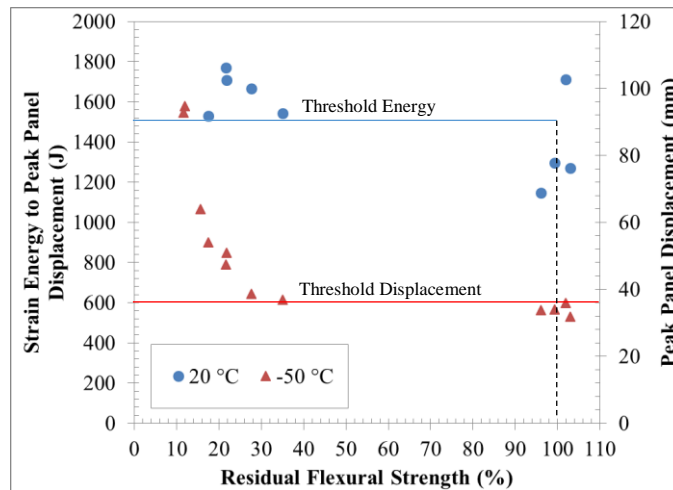


**Figure 2.20 - Total Strain Energy and Panel Peak Displacement vs. Residual Flexural Strength**

An approximate threshold failure energy and failure displacement, as defined earlier, can be estimated from the residual strength results. Looking at Figure 2.20, these values can be approximated to be 1500 J and 35 mm respectively. The dots on the extreme right of the graph represent the panels that did not fail during the impact tests and the ones on the left-hand side are the panels that did fail, hence having the least residual flexural strength. Once the threshold values are exceeded in a dynamic event, the panels will fail and lose up to 80% of their initial flexural strength. These estimated threshold energy and displacement are similar to the ones shown in Table 2.4, which averages to 1586 J and 37.5 mm respectively. The load-displacement graphs for the residual flexural strength tests can be seen in Appendix I.



#### 2.4.6 Robustness Factor

As explained in the introduction, the robustness factor is the ratio of the absorbed energy at the ultimate state to the energy at the serviceability limit state. Due to their known low stiffness to strength ratio, FRP components are governed by the serviceability limit state. This fact is accounted for in this factor and it allows all-FRP structural components to be compared to other well-known materials used in civil infrastructure structural components such as steel and reinforced concrete (RC). According to Van Erp [27], RC and steel beams typically have a robustness factor around 20 as a result of a deformation factor of 8 and strength factor around 2.5 for both cases. These values will depend on the design standard used for the serviceability state of course. On the other hand, the robustness factor of the studied GFRP panels was found using the following method. The serviceability limit state was calculated using the Cl. 8.3.2 of CSA S806-12 [34]. The allowable deflection that was chosen for these components was  $l_n/240$ , assuming the panels would be attached or supporting non-structural elements not likely to be damaged by large deflection. This gives an allowable deflection of 5.67 mm for a span of 1360 mm. From the experimental static load-deflection curve, knowing the failure displacement of 29.8 mm, the resulting deformation factor was found to be 5.26. Due to their linear-elastic behaviour, FRP components have the same strength factor as the deformation one. Consequently, the overall robustness factor of the GRFP ribbed panels was calculated at 27.6. This value can either increase or decrease depending on the choice of allowable deflection. The calculated robustness factor for the studied panels showed that even though they do not exhibit textbook ductility unlike steel or RC, they do have the ability to carry excess loading and will exhibit large deflections when doing so to warn of this unreasonably high load. The large “reserve” strength between the serviceability and the ultimate deflection is a great advantage for these FRP components.

### 2.5 Conclusion

The following conclusions were determined from this investigation:

1. The GFRP multi-cell ribbed structural panels are strain-rate dependent. The most sensitive parameters are failure energy threshold and also failure displacement.
2. The panels were able to withstand a strain energy averaging 1500 J.
3. Even though GFRP panels are light compared to the impact hammer, inertial effects are not negligible for dynamic behaviour analysis. The time lag that affects the support reaction also has to be accounted for if using this load for actual bending load. An alternative to using acquired data from the supports would be to use the inertial equations for specific support conditions [29] and subtracting the inertial load from the recorded impact load of the hammer.
4. Thermal imagery could be an adequate tool to evaluate the residual serviceability of these specific panels, even though more work is needed on the specific failure mechanisms.
5. Residual strength tests were in good agreement with the failure energy and displacements gathered from impact tests.
6. The conservation of energy graph is a good indication of how much energy is lost in the system. This specific apparatus showed a good conservation of energy with minor losses.
7. The work done by the hammer can differ from the predicted potential energy even though the correct hammer mass and drop height are used. Dynamic instrumentation is required to accurately estimate impact and strain energy.

## 2.6 References

- 1] L. Hollaway, *Advanced Polymer Composites and Polymers in the Civil Structures*, Oxford: Elsevier, 2001.
- 2] L. Hollaway, "A Review of the Present and Future Utilisation of FRP Composite in the Civil Infrastructure with Reference to their Important In-Service Properties," *Construction and Building Materials*, vol. 24, no. 12, pp. 2419-2445, 2010.
- 3] P. Buchan and J. Chen, "Blast Protection of Buildings Using Fibre-Reinforced Polymer (FRP) Composites," in *Blast Protection of Civil Infrastructures and Vehicles using Composites*, Cambridge, Woodhead Publishing, 2010, pp.

269-297.

- Strongwell, "COMPOSOLITE: Fiberglass Building Panel System," 2015.
- 4] [Online]. Available: [www.strongwell.com/tools/product-literature/](http://www.strongwell.com/tools/product-literature/). [Accessed 20 October 2015].
- M. Arndt, "FRP Rehabilitation of Blast and Impact Damaged Reinforced Concrete," in *6th International Conference on Advanced Materials in Bridges and Structures*, Kingston, 2012.
- 5] S. Mehmet and Z. Kazanci, "Non-Linear Dynamic Analysis of a Laminated Hybrid Composite Plate Subjected to Time-Dependent External Pulses," *Acta Mechanica Solida Sinica*, vol. 25, no. 6, pp. 586-597, 2012.
- 6] H. Turkmen and Z. Mecitoglu, "Dynamic Response of a Stiffened Laminated Composite Plate Subjected to Blast Load," *Journal of Sound and Vibration*, vol. 221, no. 3, pp. 371-389, 1998.
- 7] J. Hoemann, H. Salim and R. Dinan, "Fibre Reinforced Polymer (FRP) Panels for Blast and Fragmentation Mitigation," in *78th Shock and Vibration Symposium*, Philadelphia, 2008.
- 8] L. Librescu, S. Oh and J. Hohe, "Linear and Non-Linear Dynamic Response of Sandwich Panels to Blast Loading," *Composites: Part B*, vol. 35, no. 6-8, pp. 673-683, 2004.
- 9] G. Davies, D. Hitchings and G. Zhou, "Impact Damage and residual strengths of woven fabric glass/polyester laminates," *Composites: Part A*, vol. 27A, no. 12, pp. 1147-1156, 1996.
- 10] H. Ji and et al., "Design, Test and Field Application of a GFRP Corrugated-Core Sandwich Bridge," *Engineering Structures*, vol. 32, no. 9, pp. 2814-2824, 2010.
- 11] S. Davey and et al., "Fibre Composite Bridge Deck - an Alternative Approach," *Composites Part A*, vol. 32, no. 9, pp. 1339-1343, 2001.
- 12] F. Jin and et al., "Failure Mechanisms of Sandwich Composites with

- 13] Orthotropic Integrated Woven Corrugated Cores: Experiments," *Composites Structures*, vol. 98, pp. 53-58, 2013.
- J. Zhang and et al., "Improving the Bending Strength and Energy Absorption  
14] of Corrugated Sandwich Composite Structure," *Materials and Design*, vol. 52, pp. 767-773, 2013.
- D. Dusenberry, *Handbook for Blast-Resistant Design of Buildings*, Hoboken:  
15] John Wiley & Sons , 2010.
- D. Cormie, G. Mays and P. Smith, *Blast Effects on Buildings*, London:  
16] Institution of Civil Engineers, 2009.
- M. Paz and W. Leigh, *Structural Dynamics: Theory and Computation*, Boston:  
17] Kluwer Academic Publishers, 2004.
- M. Iqbal and et al, "The Characterization and Ballistic Evaluation of Mild  
18] Steel," *International Journal of Impact Engineering*, vol. 78, pp. 98-113, 2015.
- CSA Group, S850-12: Design and Assessment of Buildings Subjected to Blast  
19] Loads, Mississauga: CSA Group, 2012.
- T. Tay, "An Empirical Strain Rate-Dependent Constitutive Relationship for  
20] Glass-Fibre Reinforced Epoxy and Pure Epoxy," *Composite Structures*, vol. 33, no.4, pp. 201-210, 1995.
- O. Okoli, "The Effects of Strain Rate and Failure Modes on the Failure  
21] Energy of Fibre Reinforced Composites," *Composite Structures*, vol. 54, no. 2-3, pp. 299-203, 2001.
- R. Ochola, "Mechanical Behaviour of Glass and Carbon Fibre Reinforced  
22] Composites at Varying Rates," *Composite Structures*, vol. 63, no. 3-4, pp. 455-467, 2004.
- N. Hancox, "An Overview of the Impact Behaviour of Fibre-Reinforced  
23] Composites," in *Impact Behaviour of Fibre-Reinforced Composite Materials*

*and Structures*, Cambridge, Woodhead Publishing, 2000, pp. 1-32.

G. Zhou, "The Use of Experimentally-Determined Impact Force as a Damage  
24] Measure in Impact Damage Resistance and Tolerance of Composite  
Structures," *Composite Structures*, vol. 42, no.4, pp. 375-382, 1998.

J. Kim, "Recent Developments in Impact Damage Assessment of Fibre  
25] Composites," in *Impact Behaviour of Fibre-Reinforced Composite Materials  
and Structures*, Cambridge, Woodhead Publishing, 2000, pp. 33-74.

A. Naaman and et al., "Analysis of Ductility in Partially Prestressed Concrete  
26] Flexural Members," *PCI Journal*, vol. 31, no. 3, pp. 64-87, 1986.

G. Van Erp, "Robustness of Fibre Composite Structures Loaded in Flexure,"  
27] in *FRP Composites in Civil Engineering*, Amsterdam, 2001.

J. De Castro San Roman, *System Ductility and Redundancy of FRP Structures  
28] with Ductile Adhesively-Bonded Joints*, Lausanne: Ecole Polytechnique  
Federale de Lausanne, 2005.

N. Banthia and et. al. , "Impact Testing of Concrete Using a Drop-Weight  
29] Impact Machine," *Experimental Mechanics*, vol. 29, no. 1, pp. 63-69, 1989.

X. X. Zhang and et. al., "A New Drop-Weight Impact Machine for Studying  
30] Fracture Processes in Structural Concrete," *An International Journal of  
Experimental Mechanics*, vol. 46, no. 3, pp. 252-257, 2010.

S. Soleimani and et. al., "Behavior of RC Beams Under Impact Loading:  
31] Some New Findings," in *Sixth International Conference on Fracture  
Mechanics of Concrete and Concrete Structures*, Catania, 2007.

J. Romanoff and P. Varsta, "Bending Response of web-core sandwich plates,"  
32] *Composite Structures*, vol. 81, no. 2, pp. 292-302, 2007.

L. Bank, *Composites for Construction: Structural Design with FRP Materials*,  
33] Hoboken: John Wiley & Sons, Inc., 2006.

CSA Group, S806-12: Design and Construction of Building Structures with

34] Fibre-Reinforced Polymers, Mississauga: CSA Group, 2012.

P. Smith and J. Hetherington, Blast and Ballistic Loading on Structures,  
35] Oxford: Butterworth-Heinemann, 1994.

N. Uddin, Blast Protection of Civil Infrastructures and Vehicles Using  
36] Composites, Cambridge: Woodhead Publishing Limited, 2010.

A. Bentur and et al., "The Behaviour of Concrete Under Impact Loading:  
37] Experimental Porcedures and Method of Analysis," *Matériaux de  
Construction*, vol. 19, no. 5, pp. 371-378, 1986.

L. Van Den Einde and et al., "Use of FRP Composites in Civil Structural  
38] Applications," *Construction and Building Materials*, vol. 17, no. 6-7, pp. 389-  
403, 2003.

## **Chapter 3**

# **COLD TEMPERATURE EFFECTS ON A GFRP MULTI-CELL RIBBED STRUCTURAL PANEL SUBJECTED TO IMPACT LOADING**

### **3.1 Introduction**

#### **3.1.1 Background**

Remote areas such as the Arctic have been gaining more and more attention from governments, industries and concerned individuals during the past decade. This is mainly due to the newly acquired knowledge of the presence of critical resources such as petroleum. In fact, it has been estimated that almost a fifth of the world's petroleum reserve exists in the Arctic region [1]. This increasing interest will result in new permanent or temporary infrastructure in such remote areas. Important factors to take into consideration in infrastructure planning for such applications are cost, effectiveness in cold-temperatures and resilience to extreme loads. In the earlier stages of planning, cost analysis is critical and will shape the entire operation. The cost analysis must look beyond the up-front cost of the building materials. The cost of transportation, which is a function of weight, distance and means of shipping is critical for remote area construction projects. Also, labour is another very important part of cost analysis. The level of construction expertise required on-site, the requirement for heavy equipment as well as the availability of labour on-site or the requirement to fly in crews need to be considered. Certainly, any reductions associated with transportation, labour and equipment costs such as the use of light-weight material and modular construction can be significant. Furthermore, materials used in Arctic construction should be durable and effective insulators. The use of appropriate products can significantly reduce the operating and maintenance costs during the lifespan of a structure. Finally, when construction materials may be used to support industrial or military

use in Arctic conditions, the products should be resilient and able to resist rapidly applied and extreme loads.

Previous investigations have proven that composite materials such as GFRP, even though they might present a higher purchase cost than more common materials, have a lower life-cycle cost if factors such as transportation, ease of construction and maintenance are taken into consideration [2] [3]. Furthermore, thermal conductivity of FRP materials is low [2], making such components very attractive for construction in a cold environment. Employing these concepts, the following investigation was pursued on an all-FRP component that could be used as a primary or a secondary structural component of a building design in a remote region. Since remote areas such as the Arctic present very harsh environmental conditions, the behaviour of FRP panels subjected to extremely cold temperatures was investigated.

All-FRP components such as modular building panels fit the criteria of low specific weight and ease of construction suitable for buildings in remote Arctic Regions. Maunsell Structural Plastics Ltd developed such components that were called Advanced Composite Construction Systems (ACCS). This system consists of GFRP multi-cell ribbed structural panels that can be assembled in a variety of shapes and configurations by bonding and inserting mechanical toggles. They have been directly used in the construction of the Aberfeldy Bridge in Scotland (1992) and in Gloucestershire for the Bonds Mill Lift Bridge (1994). Strongwell Corporation now markets this system and the GFRP multi-cell ribbed structural panels known commercially as COMPOSOLITE®. Such modular panels can be used in a wide range of applications, including but not restricted to bridges, baffles systems, scaffoldings and small-scale buildings as seen in Figure 3.1 [4].





**Figure 3.1 - A visitor center in Bristol, UK constructed with COMPOSOLITE® panels [4]**

As seen in Figure 3.1, the panels are very versatile, and, in this case, no supporting frame was needed. The panels are supporting all of the loads. This sort of application would then be an option for an expedient and light construction in Arctic regions. For larger scale structures, the panels could be employed as secondary elements mounted on a structural frame. According to National Building Code of Canada (NBCC) 2015 Volume 2 [5], the coldest design temperature in the Canadian Arctic for January (1%) is  $-53^{\circ}\text{C}$ , for a town called Snag, in Yukon Territory. This town is in the climatic zone 8 ( $\geq 7000$ ) and the minimum required RSI value for this type of small building application would be  $5.02 \text{ m}^2\text{K/W}$ .

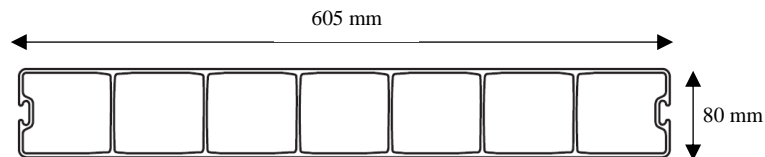


**Figure 3.2 – Cross-Section of Panel [4]**

Taking into consideration the EPS foam insulation, located in the panel's voids as shown in Figure 3.2, as well as the thermal-bridges provided by the webs, the panels would provide an RSI value of approximately  $1.42 \text{ m}^2\text{K/W}$ . Hence, for Arctic applications, an additional thermal insulation barrier would be needed.

However, these added materials would not hold add any structural capacity, nor add a significant dead load to the structure.

The types of loadings that these applications would have to resist could be wind, snow, traffic, etc. However, due to malicious or accidental causes or the use of these components in military structures, these panels could be subjected to more impulsive loads such as blast or impact. This study investigated this type of panel's impact response when also subjected to sub-zero temperatures. The dynamic load was imparted using a large impact hammer on full-scale panels. A similar apparatus was used in previous studies to simulate blast on reinforced concrete members with some success [6]. Although the nature of blast and hammer load differ the impulsive loads associated with a hammer, the experiment provided an opportunity to investigate the effect of rapidly-applied, short-duration load on the strength and energy-absorption capacity of the panels.

### 3.1.2 Temperature Effects on FRP Components

Since the coldest design temperature according to the National Building Code of Canada 2015 [5] was  $-53\text{ }^{\circ}\text{C}$ , the panels were tested at temperatures that exceeded this temperature,  $-50\text{ }^{\circ}\text{C}$ . Extensive studies have been made on the effects of temperatures on FRP as a material. Because all FRP components have different matrices and fibre materials, the temperature effects are inherently different for most composites. In fact, temperature effects will depend on the type of polymer, fibre and specimen geometry [7]. Multiple studies have looked at the effects of temperature on different polymers and have shown that the yield stress and Young's modulus usually decrease with temperature increase, with tested temperatures ranging from  $-180$  to  $20\text{ }^{\circ}\text{C}$  [8] [9]. Also, Wagner et al. [7] looked at the effects of temperature on unidirectional GFRP and came up with similar results as with pure polymers, i.e. the Young's modulus and yield stress are higher for colder temperatures, i.e.  $-200\text{ }^{\circ}\text{C}$  compared to  $140\text{ }^{\circ}\text{C}$ . The yield stress at the lowest temperature could increase up to four times when compared to the yield at the highest temperature. Despite these increases in performance for colder temperatures, Timmerman et al. [10] showed that cryogenic cycling creates significant micro-cracks in FRP which consequently affects the fracture strength of

the composites. The density of cracks was dependent on many factors including fibre and matrix properties.

Other studies also looked at the effect of temperatures of FRP components subjected to dynamic loadings. Gupta and Shukla [11] looked at the blast behaviour of sandwich panels at extreme temperatures. This study concluded that specimens exhibited larger deflection and in-plane strains at  $-40\text{ }^{\circ}\text{C}$  than at room temperature. Erickson et al. [12] also looked at the effect of temperature on composite sandwich panels but subjected to low-velocity impact instead of blast loads. This investigation concluded that energy absorption as well as impact peak loads were temperature dependent. These observations were also observed by Benli [13]. All these studies show that the behaviour of FRP composites subjected to both static and dynamic loading is temperature dependent. However, this study will not look at a broad range of temperatures but will rather compare the behaviour of GFRP multi-cell ribbed structural panels subjected to impact at extreme cold temperatures with similar panels impacted at room temperatures.

### 3.1.3 Dynamic Properties of GFRPs

In order to better understand the dynamic behaviour and impact response of fibre reinforced polymers, one must take into consideration the effects of strain rate on their material properties. It is known that for common structural materials such as steel, the yield and ultimate strength values increase alongside the strain rate [14]. Consequently, when dealing with dynamic loads such as blast or impact, these strength values are normally multiplied by a dynamic increase factor (DIF) and strength increase factor (SIF), which vary for different materials and strain rates. Static strength values typically used for design would be more conservative than actual material strengths and hence a SIF is recommended by the CSA S850-12 [15]. Furthermore, omitting the DIF in a design procedure to account for the material strengths associated with a rapidly applied load will result in over-design. If some part of the design is overly conservative, this might lead to a lack of resources for another critical part in the structure, hence demonstrating the importance for an engineer to understand the dynamic behaviour of the materials used.

The strain rate sensitivity of GFRPs has not been specifically investigated as part of this project. However, these materials are in fact strain rate dependent, and it has been the focus of multiple studies [16] [17] [18]. These studies investigated the strain rate sensitivity of FRPs, including GFRPs, under tensile, compressive, shear and flexural loading. It has been demonstrated that ultimate strength, elastic modulus as well as energy absorption are all strain rate dependent, increasing with the strain rate. Due to these characteristics of GFRPs, it is anticipated that failure strengths of the GFRP panels investigated will be higher from the impact hammer test than the static three-point flexural test. However, it has also been proven that another important effect of strain rate variation is the change in failure mode experienced by the composites [18]. This could have an effect on the energy absorption characteristics of the panels under static and dynamic loading.

#### 3.1.4 Damage Mechanisms and Tolerance

Impact damage can take multiple forms in a composite panel. These mechanisms include fibre breakage, delamination of adjacent plies, matrix cracking, debonding between the fibre and the matrix and finally fibre pull-out from the matrix [19]. These mechanisms are affected by a number of parameters from the composite panel's properties (i.e. types of fibres, matrix, fibre orientation, etc.), but also from the impactor's properties (mass, velocity, shape, etc.). Multiple studies [11] [12] [13], showed that failure mechanisms differ at different impact temperatures. These differences will be investigated as part of this study. The literature identifies multiple non-destructive methods of quantifying impact damage such as ultrasonic C-scan, X-Ray radiography as well as destructive methods including but not restricted to cross-sectioning [20]. However, the damage mechanisms on the panels studied in this investigation were evaluated using a qualitative method of infrared thermography. This method was proven to be effective for a wide range of composite components [21]. This method can also be used easily in field applications without the necessity of specialized equipment, which would be very useful for a damage assessment in a remote area such as the Arctic. The damage tolerance, which identifies the capacity of a damaged panel to sustain a subsequent static load, was then quantified using a destructive residual 3-point bending test.

## **3.2 Objectives**

The main objective of this study was to investigate the impact response of the GFRP multi-cell ribbed structural panels subjected to varying low-velocity impact loads at Arctic and room temperatures. This was done by comparing the results of this Chapter to the results of Chapter 2. Qualitative damage comparison also done to identify major differences between cold and room temperature impacted panels. This study looks at full-size GFRP panels as opposed to coupons alone. It focuses on a variety of structural failure mechanisms vice material-related failures only.

## **3.3 Procedure**

### **3.3.1 Material Properties**

The materials which make up the GFRP multi-cell ribbed structural panels are a mix of isophthalic polyester fire-retardant resin with E-Glass continuous strand mat and roving. The percentage of fibre to volume ratio is of 50% and the key coupon mechanical properties can be found in Table 3.1. Tests have been conducted to confirm the manufacturer's stated mechanical properties. Tensile coupon tests were done as part of this project using an MTS 810 Material System, monitoring stroke and load as well as strain with 120  $\Omega$ , 10 mm strain gauges from HBM adhesively mounted in the lengthwise and cross-width direction. The tests were performed at a constant displacement-rate of 20 mm/min.

The properties given by the manufacturer were minimum ultimate values that resulted from a series of tests. The properties that were found in laboratory tests were used in this study in order to more accurately predict experimental results instead of the conservative values from Strongwell, which would be appropriate for a design scenario. It is important to note that the GFRP panel is anisotropic. Even though the literature states that the compressive strengths are

equal or larger in both directions, they were chosen to be equal to the tensile properties for this investigation. The panel's dimensions are shown in Figure 3.2.

**Table 3.1 – Panel's Mechanical Properties**

<b>Properties</b>	<b>ASTM Test Method</b>	<b>Manufacturer's Values [4]</b>	<b>Laboratory tested at RMCC 20°C</b>
<b>Tensile Modulus (Lengthwise) MPa</b>	D638	17,140	19,520
<b>Tensile Strength (Lengthwise) MPa</b>	D638	214	373
<b>Flexural Modulus (Lengthwise) MPa</b>	D790	6,102	N/A
<b>Flexural Strength (Lengthwise) MPa</b>	D790	169	N/A
<b>Flexural Modulus (Cross-Width) MPa</b>	D790	4,454	N/A
<b>Flexural Strength (Cross-Width) MPa</b>	D790	56.5	N/A
<b>Short Beam Shear (Lengthwise) MPa</b>	D2344	22	N/A
<b>Poisson's Ratio (Lengthwise) mm/mm</b>	D3039	0.33	0.34

The panels used in this study were 1500 mm long and filled with #1 EPS foam. Even though the foam provides thermal insulation, it was deemed to provide no structural benefit to the panel.

### 3.3.2 Quasi-Static 3-point Flexural Test

In order to understand the flexural behaviour of the panels, a 3-point bending simply-supported test was performed on the panel, see Figure 3.3. This test was done in order to determine the strength and post-failure energy absorption behaviour of the panels. These parameters were then used to plan for the magnitude of the impulsive load that would be imparted by the impact hammer. The supports on each end were a triangular pin as can be seen in Figure 3.3, and a 50 mm wide steel plate was placed between the pin and the panel to avoid local crushing of the specimens at the supports. The unsupported span of the specimen was 1360 mm, and the load was applied at the mid-span. The load was imparted to the specimens by a 75 mm rectangular HSS with a rubber strip between the HSS and the specimens. The HSS had the same width as the panels and was the same one used at the end of the impact hammer.

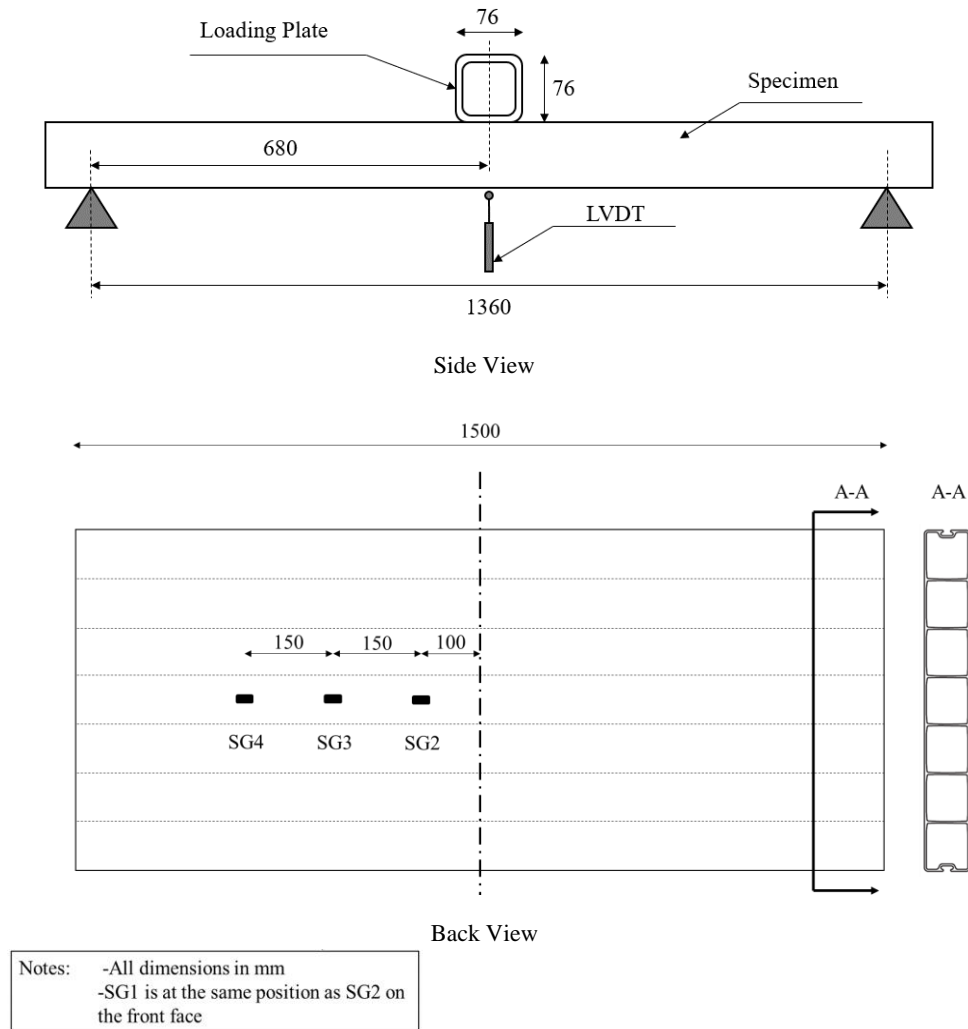


**Figure 3.3 - 3-Point Flexural Test Apparatus**

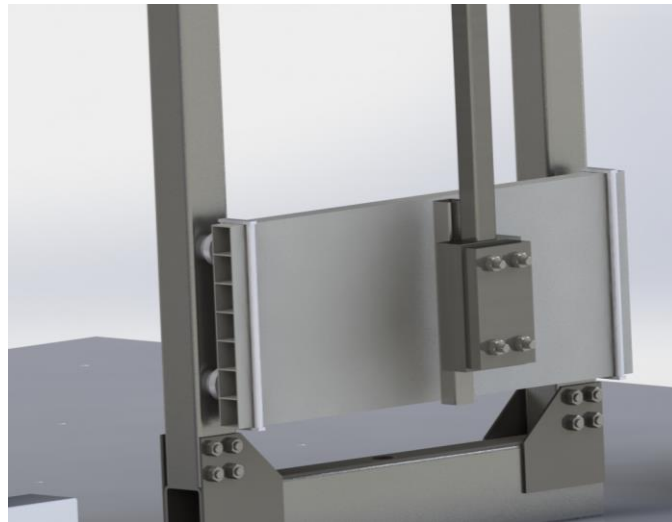
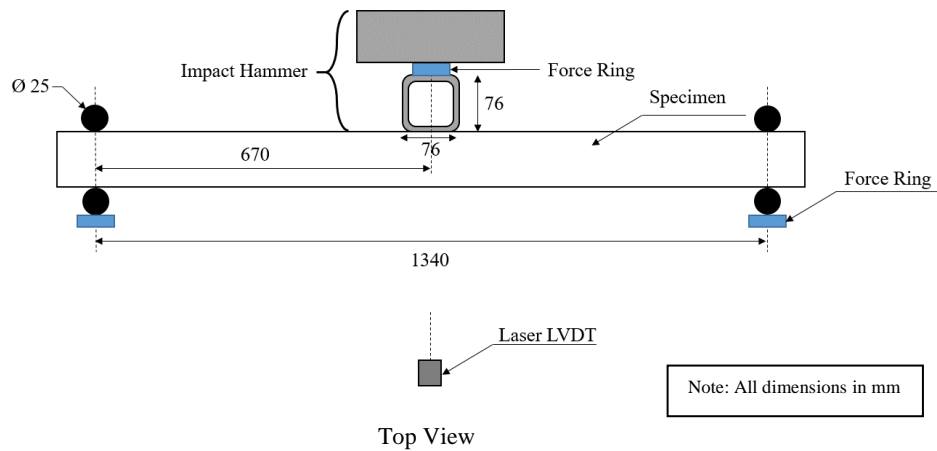
A MTS 322 Test Frame with a constant head-speed of 20 mm/min was used in this case. The load and the stroke were monitored on the MTS as well as the strain distribution using 4 x 120 Ω 10 mm strain gauges on each specimen. The room temperature specimens were instrumented with Showa's N11-FA-10-120-11 strain gauges rated for -30 to 80 °C while the cold temperature tested panels used HBM's 1-LY11-10/120 strain gauges rated from -200 to 200 °C. For all the tests, one strain gauge was placed on the front face and the other three were distributed



along the length of the back face. They were used to understand the curvature distribution as well as the shape function of the specimens under a static load. The panels were taken past the point of failure to the maximum stroke of the machine which is approximately 100 mm. Two flexural tests were performed at room temperature (20 °C) and two were done at cold temperatures (-40 °C). The time required to move the panels from the freezer and install them into the quasi-static testing apparatus dictated the temperature of -40 °C. This apparatus was also used in order to perform the residual flexural strength tests on the panels post-impact. All those residual tests were completed at room temperature. This was done in order to have a constant temperature for damage assessment for a more consistent and accurate comparison.

### 3.3.3 Impact Hammer Apparatus

Before the apparatus is described, it is important to note that in the field of impact testing, many different testing configurations are used, and the literature can reflect this [19]. The Izod and Charpy method could not be used in this case, since the behaviour of the full panel needed to be assessed. Since the panels were tested in flexure, both statically and dynamically, and because the flexural modulus depends on both mechanical and structural properties of a component [22], the tests were done on full-size specimens. Consequently, a 138 kg impact hammer apparatus was used in order to generate a sufficiently large impulsive load onto the composite panels to observe their impact response. This apparatus used the principle of a pendulum with a large mass, essentially transferring a significant potential energy into kinetic energy and work on the panel in a very short amount of time. The set-up can be seen in Figure 3.4.



3D View

**Figure 3.4 - Impact Hammer apparatus**

The hammer was built using a 100 mm square steel HSS as the lever arm, and a rectangular steel section as the head. The head was built so that additional steel plates could be added to the back of it in order to achieve higher potential energies. Also, a 76.2 mm square HSS was attached to the front of the hammer

head to distribute the load across the full width of the specimens. These loading conditions were designed in order to apply an impulsive impact loading to the panel as opposed to a ballistic loading. The impact response of the panel was sought and not its penetration resistance. The 1500 mm long panels were supported by 25 mm diameter bars on each face of the panels on both supports to ensure that the panel remained in contact with the support when loaded and when rebounding. The specimens were however allowed to rotate up to approximately 8 degrees on both supports. These support conditions were assessed to be semi-rigid as opposed to simply supported. The unsupported span of the panels on the impact apparatus was 1340 mm.

Instrumentation was used in order to capture the dynamic behaviour of the panels as well as the imparted energy by the impact hammer. A laser LVDT with a range of 600 mm was used to measure the mid-span deflection of the specimens. Also, LVDTs along the front and back face of the panels were used to capture the curvature as well as the shape function of the dynamically loaded GFRP panels. Two hundred mm spring LVDTs were also used at the supports to measure the specimens' displacements in the supports. Also, a 207C ICP® 445 kN compression piezo-electric force ring was used behind one of the supports to measure the dynamic reaction generated by the hammer. As for the hammer, another identical force ring was placed just between the HSS and the head to measure the applied dynamic load to the specimens. Additionally, a shock ICP® 1000 g piezo-electric accelerometer was placed just above the head to measure the hammer's acceleration, estimate its velocity and could also be used to estimate a force reading. Lastly, a high-speed camera was set-up just above the specimens to capture the hammer's velocity moments before the impact as well as the dynamic response of the specimens. All these instruments, except for the camera, were connected to an MGC plus DAQ system and recorded in Catman Pro. The sampling rate of the piezo-electric instruments (i.e. accelerometer and force rings) as well as the laser LVDT was set at 2400 Hz. All the other instruments were sampled at 1200 Hz. The camera recorded images at 1000 fps. The only difference in instrumentation for the cold and room temperature tested panels were the strain gauges used, as discussed in the previous section.

In total, 24 specimens were tested dynamically. Half of them were tested at room temperature while the remainder were tested in cold temperature. The mass of the hammer remained constant while the drop height was changed for different series, resulting in a change of impact velocity. However, to predict the applied

energies for each series, the potential energy was used from known drop height values. The same drop heights were used for the room and cold temperature tests for comparison purposes, except for two series and the reason will be discussed in the results section. The complete testing schedule can be seen in Table 3.2.

**Table 3.2 - Impact Testing Schedule**

<b>Test Series</b>	<b>Temperature (°C)</b>	<b>Drop Height of the Hammer from rest (mm)</b>	<b>Resulting Potential Energy (J)</b>
<b>K1-1, K1-2, K1-3</b>	20	1970	2630
<b>K2-1, K2-2, K2-3</b>	20	1470	1970
<b>K3-1, K3-2, K3-3</b>	20	1220	1630
<b>K4-1, K4-2, K4-3</b>	20	970	1300
<b>T1-1, T1-2</b>	-50	2220	2970
<b>T2-1, T2-2, T2-3</b>	-50	1970	2630
<b>T3-1, T3-2, T3-3</b>	-50	1720	2300
<b>T4-1, T4-2, T4-3</b>	-50	1470	1970
<b>T5-1</b>	-50	1220	1630

### 3.3.4 Freezing the Panels

In order to achieve a temperature of -50 °C for the panel, a Panasonic MDF-794-PE ultra-low freezer was used, since an environmentally controlled room that could hold the impact hammer apparatus was not available. This freezer could reduce the temperature of the entire specimens down to -80 °C. Because the room temperature was around 20 °C, the panels, once removed from the freezer, would warm up at a rapid rate. On average, it took 3 min for the specimen to warm-up from -80 to -50 °C. Type T thermocouples were used to monitor the temperature of the panels at all times. A thermocouple was placed on the face of the panels while another one was on the inside web. It is important to note that for all the tests, there was foam in the panel's voids, meaning that the faces were warming up much quicker than the webs. An example of a temperature-time history of a panel that has been taken out of the freezer can be seen in Figure 3.5.

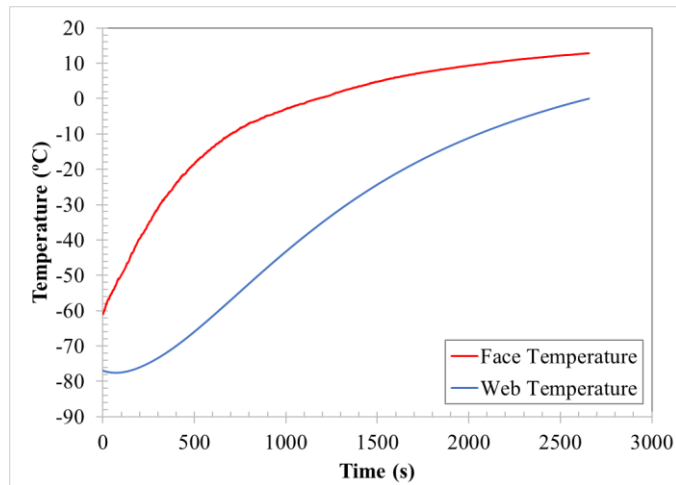


**Figure 3.5 - Temperature-Time History of a Thawing Panel**

The face and web temperature do not start at the same temperature in Figure 3.5 only because the data recording started one minute after taking the panel out of the freezer. The temperature that will be documented in the present study will be that of the face. For the impact tests, the panels were carried to the apparatus and tested within 3 minutes. The face temperature at the time of testing was at approximately -50 °C for all the cold panels. The quasi-static test apparatus was a little more complex in terms of placing the panel, and the face temperature was approximately -40 °C at the beginning of the tests. A variation in temperature existed through the depth of the panels at the time of testing. It is possible that the entire panel will be at a cold temperature for a building scenario, since it will most likely be used as an outside wall, while additional insulating layers would be used on the inside of the building. However, it would be more precise to have a temperature gradient going from the inside to the outside face of the panel. A controlled variation in temperature through the depth of the panel was not studied in this investigation.

An important aspect to consider during cold tests was the instrumentation. Extreme temperature rated strain gauges (-200 to 200 °C) were used. These strain gauges were calibrated for steel, with a coefficient of thermal expansion of  $\alpha = 10.8 \times 10^{-6}/K$  while the panels had a coefficient of  $\alpha = 12.6 \times 10^{-6}/K$ . However, there was still apparent strain in the values due to thermal strains in the panel with temperature variations. Compensation formulas had to be derived by reviewing the apparent strains on a thawing panel with no loads applied on it. This provided an

apparent strain distribution that could be used to compensate for temperature induced strains in the panels during testing. Figure 3.6 shows the apparent strain distribution that was used to calibrate the measured strains for cold temperature.

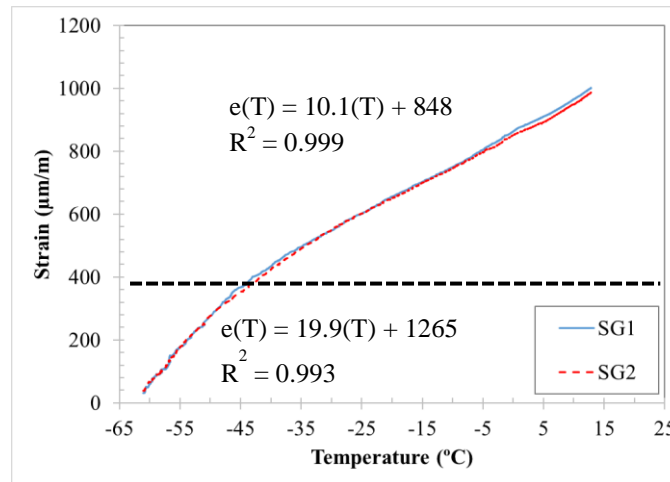


Figure 3.6 - Apparent Strain Distribution for a Thawing Panel

It can be seen that the apparent strain is a bi-linear function. The apparent strain functions for temperatures below and above  $-45\text{ }^{\circ}\text{C}$  can be seen in Figure 3.6. The lower equation was used for impact tests since the temperatures for these tests were in the vicinity of  $-50\text{ }^{\circ}\text{C}$ . On the other hand, the upper equation was used to compensate strains acquired during the quasi-static tests.

### 3.4 Results and Discussions

#### 3.4.1 Quasi-Static Testing

As mentioned previously, two panels were tested at room temperature and two at sub-zero temperatures. The results of those four tests are shown in Figure 3.7.

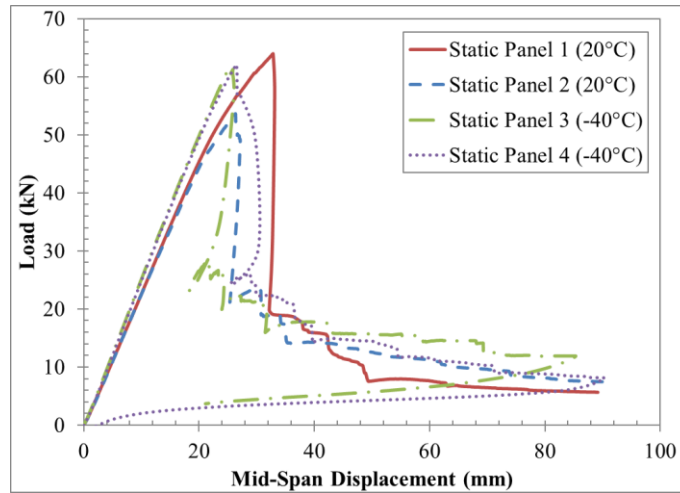


**Figure 3.7 - Quasi-Static Results for Room and Cold Temperature**

The only changing parameter in these tests was the temperature. The first two tests were done at room temperature (20 °C) while the last two were done in sub-zero temperature (~ -40 °C) by freezing the panels in a freezer prior to the test. Because this was a quasi-static test and because the temperature of the laboratory was not maintained below zero, the panels would warm-up significantly during the tests. Type T thermocouples were used on those tests to monitor the temperature of the panel's face and webs at all times during testing. Test 3 started with an unknown face temperature due to a thermocouple malfunction, but it was started approximately 5 minutes after it had been taken out of the freezer. The same time was taken for Test 4 and the face temperature at the beginning of the test was at -43 °C. It was then assumed that the face temperature was approximately the same for Test 3. The quasi-static tests had an average duration of four minutes, showing a total temperature variation of approximately 20 °C during the tests. Table 3.3 shows the results for the four flexural tests.

**Table 3.3 - Quasi-Static Test Results**

Test #	Face Temperature (°C)	Failure Displacement (mm)	Flexural Stiffness (kN/m)	Peak Load (kN)	Fracture Energy (J)
1	20	32.9	2175	64.0	1170
2	20	26.3	2163	53.6	757
3	~ -40	25.9	2416	61.3	831
4	~ -40	26.5	2341	62.1	858

Even though the variation in the quasi-static test results might appear to be temperature related, they may be due to panel variation. Table 3.4 shows the flexural results of all the flexural tests that were done, including the residual strength tests done on panels that were deemed to have not failed on impact.

**Table 3.4 - Flexural Stiffness and Strength Variation**

	<b>Flexural Stiffness (kN/m)</b>	<b>Peak Load (kN)</b>
<b><u>Quasi-Static Room Temperature</u></b>		
<b>Quasi-Static 1</b>	2175	64.0
<b>Quasi-Static 2</b>	2163	53.6
<b><u>Quasi-Static Cold Temperature</u></b>		
<b>Quasi-Static 3</b>	2416	61.3
<b>Quasi-Static 4</b>	2341	62.1
<b><u>Residual Strength of non-failed impacted Specimens (All tested at room temperature)</u></b>		
<b>K3-3</b>	2575	59.6
<b>K4-1</b>	2239	56.2
<b>K4-2</b>	2456	60.6
<b>K4-3</b>	2218	58.4
<b>T4-1</b>	2484	59.2
<b>T4-3</b>	2194	55.8
<b>T5-1</b>	2475	55.9
<b>Average for All Room Temperature Flexural Tests</b>	2331	58.1
<b>Standard Variation for All Room Temperature Flexural Tests</b>	163	3.13
<b>Average for All Cold Temperature Flexural Tests</b>	2379	61.7
<b>Standard Variation for All Cold Temperature Flexural Tests</b>	53.0	0.566
<b>Average for All Flexural Tests</b>	2340	58.8
<b>Standard Variation for All Flexural Tests</b>	148	3.16

Looking at the average values for flexural stiffness of room temperature and cold temperature tested panels, there is only a 2% difference. The same observation can be made for the peak load with only a 6% difference. The standard variation



for the flexural stiffness's and peak loads of the room temperature panels are sufficiently large to reach the average value for the cold temperature tested panels. Even though the coupon tensile tests performed in the laboratory exhibited an increase of tensile modulus for colder coupons, no similar observation can be clearly made for full-size panels. It is possible that the panels that were investigated came from two different construction batches resulting in some discrepancies. For this reason, no significant difference can be concluded from the cold and room temperature panels subjected to quasi-static loads.

### 3.4.2 Impact Testing

The panels were tested dynamically by applying kinetic energy provided by the impact hammer. The high-speed camera did not have sufficient resolution to accurately measure the hammer's velocity and consequently its kinetic energy. An alternative was used, suggested by Banthia [23], and this method was used successfully in previous experiments related to this study. The resulting measured kinetic energies can be seen in Table 3.5.

**Table 3.5 - Impact Tests Kinetic Energies**

<b>Series</b>	<b>Predicted Potential Energy(J)</b>	<b>Kinetic Energy (J)</b>
<b>K1</b>	2630	2440
<b>K2</b>	1970	1959
<b>K3</b>	1630	1630
<b>K4</b>	1300	1296
<b>T1</b>	2970	2967
<b>T2</b>	2630	2616
<b>T3</b>	2300	2296
<b>T4</b>	1970	1965
<b>T5</b>	1630	1630

The reason why these kinetic energy values do not match the projected potential energies presented earlier may be due to loss of energies through friction in the system.

An important consideration in the case of an impact hammer apparatus is the load recorded from the piezo-electric force ring. It had to be corrected to obtain the

actual bending load applied on the panel, because some of the impact load is in fact used to maintain the balance with the inertial force during loading [24]. Using the support load has been used successfully by Soleimani et al. [25] to find this bending load. The support load acquired had to be multiplied by four since the supports rods were anchored at two points on each side of the testing frame four at total of four support reactions. The comparison of the impact load and the support reaction can be seen in Figure 3.8.

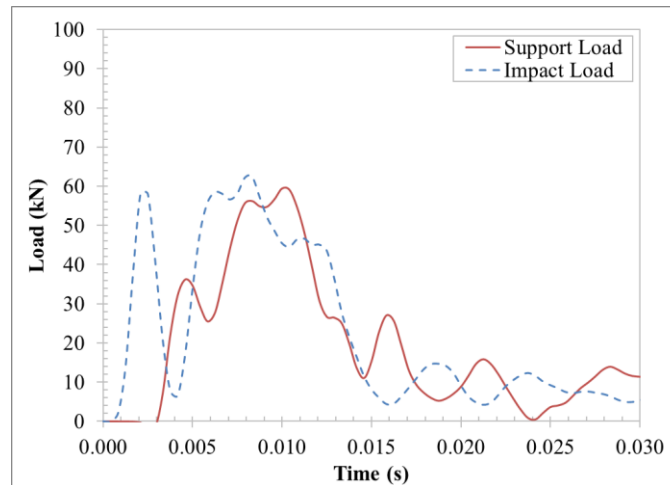


**Figure 3.8 - Comparison of Support and Impact Load for Panel K2-3**

It is important to note that the start of both loads is offset by a 2 ms delay. The same delay was observed in all the tests regardless of the imparted energy or temperature of the specimens. This delay has also been observed in previous investigations [24] [23] [25]. It is mainly due to the fact that the rise time of the initial load is so sudden that the stress wave takes time to propagate from the point of impact to the support. This delay can also be confirmed by looking at the strain values along the length of the specimens. The strain gauges closer to the impact point will show variations faster than the ones closer to the supports. The delay was then accounted for, as was successfully done in previous work [24] [25], by shifting the support reaction 2 ms earlier. The load-displacement curve of the specimens could then be built, and an example is shown in Figure 3.9. It shows the load-displacement functions of room temperature and cold temperature impact tested panels at the same hammer potential energy compared with their quasi-static counterparts.

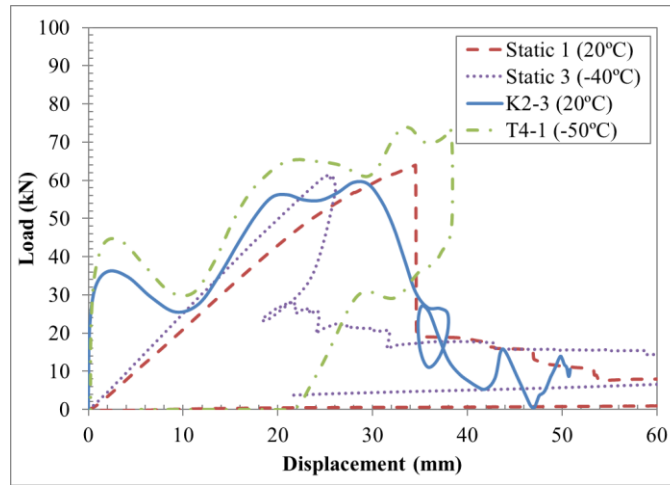


**Figure 3.9 - Dynamic Load-Displacement Curve**

The abnormal behaviour past failure for panel K2-3 is mainly due to the back-face rebounding towards the front face following failure. The strain energy of the panel could then be calculated using the area under the dynamic load-displacement curve.

The analyzed data for all the panels can be seen in Table 3.6. The top part of the table shows the results for the room temperature panels while the bottom part shows the cold panel results.

**Table 3.6 - Impact Tests Results for Room and Cold Temperature**

Test Series	Potential Energy (J)	Total Work Done (J)	Failure Displacement (mm)	Peak Displacement (mm)	Strain Energy Prior Initial Failure (J)	Strain Energy at Peak Deflection (J)
<b>K series tested with a face temperature of 20 °C</b>						
<b>K1-1</b>	2630	1805	36.3	64.0	1730	2077
<b>K1-2</b>	2630	2050	39.4	94.6	1612	2045
<b>K1-3</b>	2630	2036	39.5	92.8	1608	2108
<b>K2-1</b>	1970	1580	36.2	47.4	1612	1771
<b>K2-2</b>	1970	1561	34.9	54.1	1332	1530
<b>K2-3</b>	1970	1616	37.9	50.9	1580	1709
<b>K3-1</b>	1630	1613	38.6	38.6	1667	1667
<b>K3-2</b>	1630	1531	36.9	36.9	1544	1544
<b>K3-3</b>	1630	1684	No failure	35.9	No failure	1710

<b>K4-1</b>	1300	1291	No failure	33.9	No failure	1147
<b>K4-2</b>	1300	1308	No failure	31.8	No failure	1270
<b>K4-3</b>	1300	1345	No failure	34.0	No failure	1299
<b>T series tested with a face temperature of approximately -50 °C</b>						
<b>T1-1</b>	2970	2777	40.2	82.2	1997	2655
<b>T1-2</b>	2970	2551	40.4	105	1809	2366
<b>T2-1</b>	2630	2316	45.1	50.2	2140	2126
<b>T2-2</b>	2630	2347	43.4	61.6	2197	2289
<b>T2-3</b>	2630	2423	41.8	65.3	2089	2411
<b>T3-1</b>	2300	1845	40.0	49.2	1987	2137
<b>T3-2</b>	2300	2286	40.3	40.3	2343	2343
<b>T3-3</b>	2300	2141	42.2	42.2	2194	2194
<b>T4-1</b>	1970	1995	No failure	38.4	No failure	2066
<b>T4-2*</b>	1970	1469	31.5	47.4	1369	1762
<b>T4-3</b>	1970	1995	No failure	40.0	No failure	1944
<b>T5-1</b>	1630	1662	No failure	34.9	No failure	1763

\*This panel's results were omitted for in this study since they were because they were likely affected by specimen defects and did not follow the trends of the rest of the population.

The reason why not all the same hammer drop-heights were used for the room and cold temperature test is the response of the panels. At cold temperatures, the panels were observed to be stronger and capable of absorbing more energy than the room temperature ones. The cold panels did not seem to fail at the 1965 J potential energy hits or lower and this is why it was decided to carry on with higher energy impacts. The total work done as shown in the previous table was taken as the area under the impact load-displacement curve up to the panel's peak displacement. An important observation that can be made looking at Table 3.6 is energy conservation. The total work done at the peak displacement is very similar to the absorbed strain energy. An example of an energy conservation time history is shown in Figure 3.10.

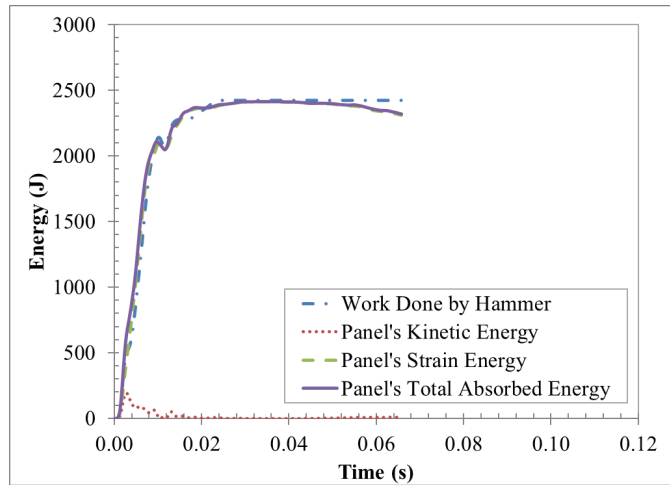


**Figure 3.10 - Energy Conservation for Panel T2-3**

Not all the panel's energy conservation looked as realistic as this one. Some panels, especially almost all of the T3/T4/T5 series, exhibited a larger strain energy than work done at peak displacement. This could not be true since the absorbed energy cannot be larger than the imparted energy. This may be due to the fact that the support load was shifted to the left as explained earlier. This may overestimate the applied bending load on the specimens. For the panels where the strain energy is lower than the work done by the hammer, this loss of energy could very well have been lost in the apparatus through sound and vibrations. The remainder of the energy conservation graphs can be seen in Appendix F.

### 3.4.3 Comparison of Room Temperature with Cold Temperature

One important difference between the behaviour of room and cold temperature panels is the energy absorption through strain energy. It can be observed in Table 3.6 that for the similar imparted energy levels, the cold temperature panels absorbed more strain energy than the room temperature ones. Figure 3.11 shows the strain energy as a function of peak displacement for all of the testing schedule.

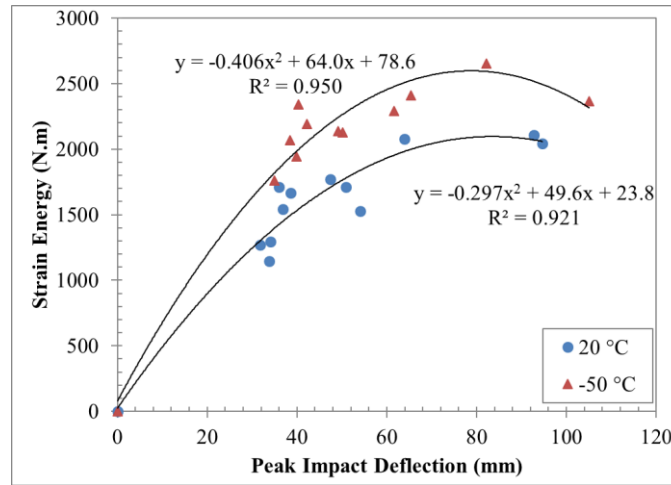
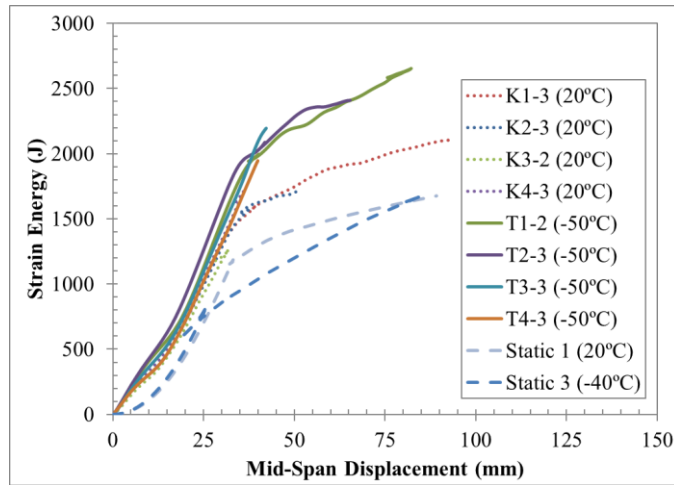


Figure 3.11 - Strain Energy vs. Peak Impact Deflection for all Panels

The same observation can be made that cold panels seem to absorb more energy for the same peak displacements as the room temperature panels. These observations are similar to the ones made by Erickson et al. [12]. They found that energy absorption in cold temperature could be higher than room temperatures for FRP sandwich panels tested with increasing impact energies. This correlates with Figure 3.11 where the difference between the two curves becomes larger at higher energy impacts and peak deflections, which are the data points further to the right on the graph. A second order polynomial relationship was used in this case to best estimate the plateau. However, past the peak of these equations, one should assume a constant or slightly increasing strain energy.

Figure 3.12 shows the difference in strain energies with respect to panel's displacement for quasi-static tests as well as dynamic cold and room temperature tests. It can be seen that the strain energies are much larger for dynamic tests compared to quasi-static. Also, the energy values are larger for cold temperature panels than room temperature ones. However, for the same temperature, the strain energy absorption behaviour is similar. In fact, strain-rate values for all of the impact series were of the same order, from  $0.5 \text{ s}^{-1}$  to  $1 \text{ s}^{-1}$ . In order to get a better understanding of the strain-rate effect, much higher strain-rates would need to be achieved by using a different dynamic loading apparatus. The difference in behaviour is much more significant looking at the quasi-static tests where measured strain rates were of  $6 \times 10^{-5} \text{ s}^{-1}$ .



**Figure 3.12 - Strain Energy vs. Mid-Span Displacement**

In addition to having higher failure displacements, the cold panels also exhibited a larger resistance for similar displacements when compared to room temperature panels, as can be seen graphically in Figure 3.9 and numerically in Table 3.6. With an average failure displacement of 41.7 mm and fracture energy of 2094 J, cold panel's values were increased by 11.3% and 32.1% respectively from room temperature. In this study's case, it can then be concluded that most of this increase in strain energy occurs prior to failure. Figure 3.13 shows the comparison of the load-displacement history for both room and cold temperature panels that were tested at the same impact energy. The room temperature panels are shown with the full lines and the cold ones with dotted lines. It can be observed that the strain energy prior to failure (area under the load-displacement curve) is noticeably larger for the cold panels than the room temperature ones. Failure is represented in Figure 3.13 by the end of each load-displacement curves, except for the panels that did not fail. The latter show a closed-loop in the load-displacement curves. This energy increase seems to be larger for higher energy hits as shown in a. and b. as opposed to lower impact energy shown in c. The higher absorbed energy can be due to the fact that the damage area is typically higher in cold temperatures, therefore the energy is dissipated over a larger area. However, even though literature shows an increase of total absorbed energy by decreasing the panels temperature, the energy required to cause failure should normally decrease proportionally with temperature since there are higher in-plane thermal stresses at

lower-temperature [13]. This was not the case in this study as can be seen in Figure 3.13 where the strain energy is higher before failure for cold panels.

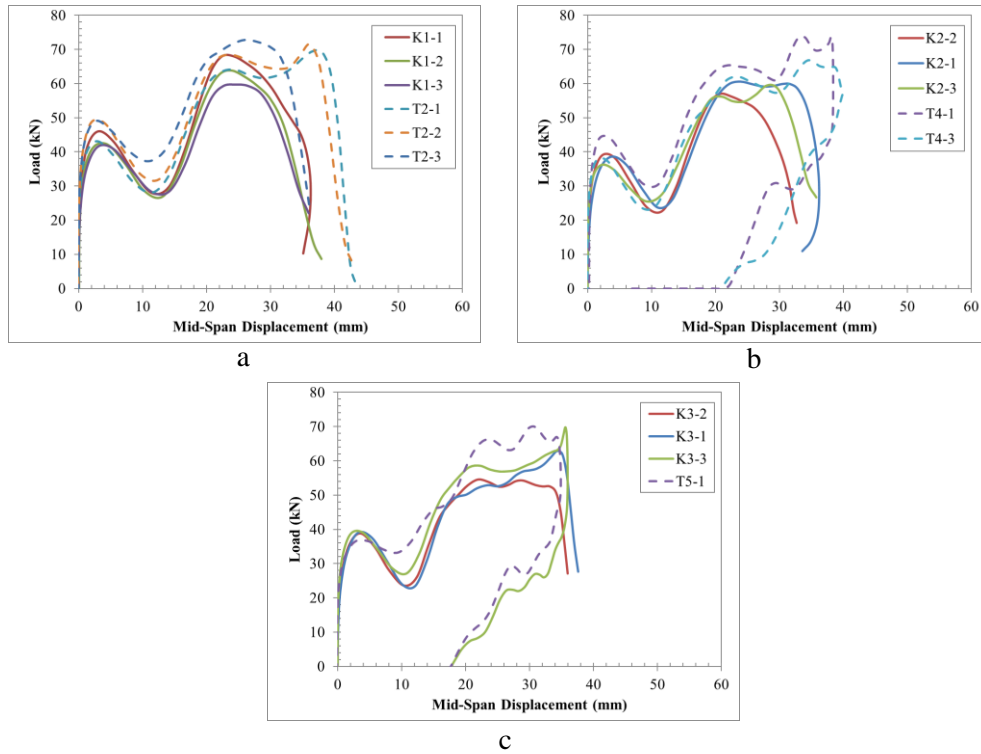


**Figure 3.13 - Load-Displacement History Comparison for Panels with Identical Impact Energy. a: 2634 J, b: 1965 J, c: 1631 J**

Referring back to the previous comment where it appears that temperature did not have a major impact on quasi-static behaviour, it can be seen that temperature is a significant factor for the impact response of these particular panels. They are more affected by strain-rate at lower temperatures than at room temperature. Consequently, dynamic increase factors (DIF) used as part of design should be temperature dependent for these panels. However, more extensive studies would have to be done in order to come up with an accurate design DIF value.



### 3.4.4 Failure Mechanisms and Damage Characterization

One panel per testing series was evaluated using infrared thermography in order to characterize the impact damage using a non-destructive method. This method was used in order to evaluate its effectiveness, since it would be a promising field procedure in order to assess damage expediently. In this investigation, the damaged panels were brought to  $-80\text{ }^{\circ}\text{C}$  by placing them in the freezer. Then, thermal imagery was taken while the panels were thawing after taking them out and exposing them to room temperatures. The darker colours in the pictures represent the colder temperatures while the higher temperatures are shown in lighter colours. The webs appear as dark areas on the images. The damaged areas can be clearly shown by observing the lighter colours for the damaged panels. Figure 3.14 shows one infrared picture per test series except T5 since there was no damage and it was very similar to that of series T4.

Thermal imaging proved to be very useful in assessing the damage resulting from impact on the panels. For example, the main failure mechanism for these panels is the delamination of the front face from the inside webs. This delamination is probably a result of buckling failure due to in-plane stresses in the front face of the panel, as discovered in another experiment related to this study. This failure is represented by the large loss of strength in the quasi-static and dynamic load-displacement time histories. Originally, the delamination was only observed by cutting open the panel and examining the damage. However, the infrared images were able to identify if the front face was still attached to the webs by taking IR imagery of the cold panels. The transversal cracks in K1-2 and K2-3 are a clear indication that the bond between the front face and the webs have been lost, and this could be observed with the naked eye. However, for the case of K3-2 where no visible large cracks were observable, the IR images were very helpful in identifying a delamination invisible without this method. IR thermography could then be very useful in the field where other more complex monitoring instruments are available. One could assume that if a loss of bond between any face from the webs is observed, the panel would be deemed to have failed and need to be replaced. Any large cracks along the width across the webs visible to the naked eye would also be an indicator of failure.

Now looking at the comparison between the room temperature impacted panels and the cold ones, there is an observable difference in failure mechanisms

from the IR thermography. Series K1 with T2, K2 with T4 as well as K3 with T5 were impacted with the same potential energy. There was an evident quantitative difference looking at the results in the previous section, and Figure 3.14 can also help us to see this difference qualitatively. Quantitatively, for the case of K1 and T2, for the same imparted potential energy, K1 panels exhibited a larger peak deflection but a lower total absorbed energy than T2 panels. A difference that could be explained by looking at the IR images. Panel T2-3 seems to exhibit a much different cracking pattern than K1-2. The delamination in the front face of the cold panel seems to be spread over a larger area than the room temperature one. The larger absorbed energy for the cold panels may be due to the hypothesis that more of the energy is spent by cracking the matrix and spreading the cracks in the front face than actually debonding the face from the webs. Even though this hypothesis could not be verified, an observable difference in failure mechanisms can still be identified between an impacted panel at 20 °C and -50 °C.

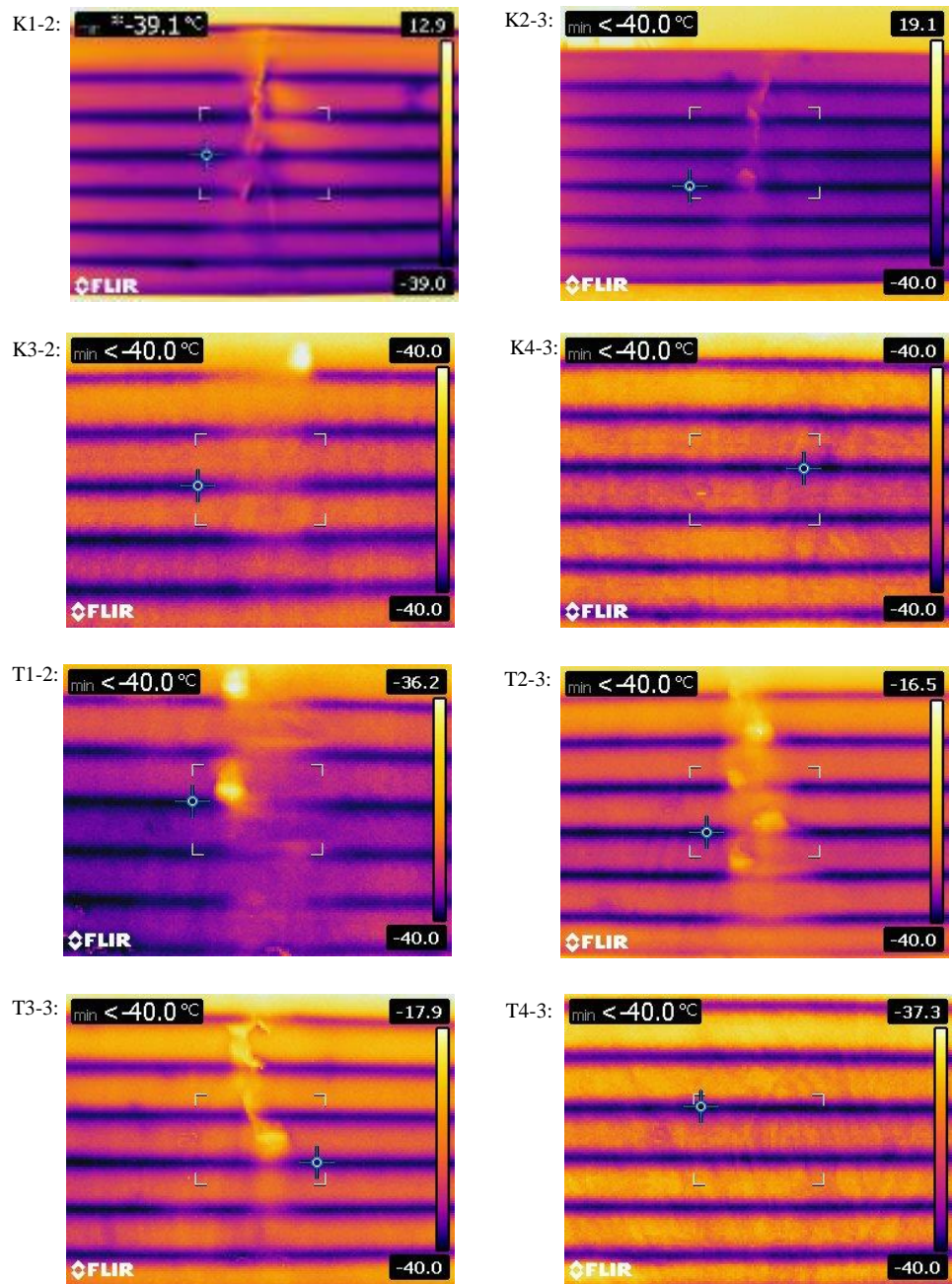
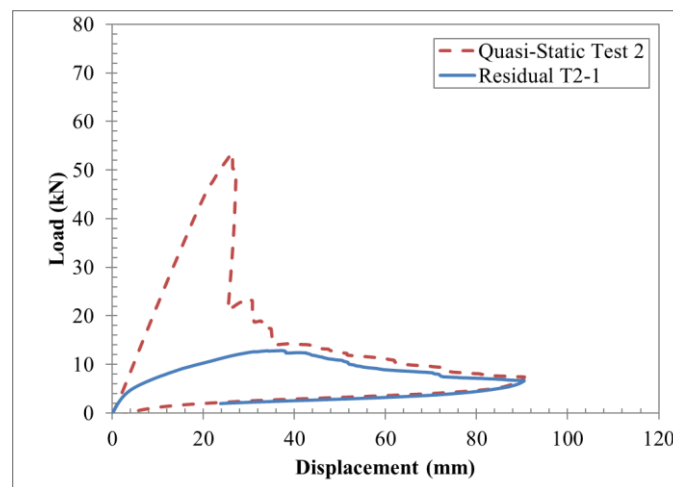


Figure 3.14 -Thermography of Impacted Panels

### 3.4.5 Residual Strength

Each impact test was followed by a residual flexural test in order to assess the damage imparted by the hammer at different drop heights. It was quantified by looking at the magnitude of the loads that the panels could support following an impact event compared to the undamaged panels. The cold panels were thawed to room temperature before the residual strength tests in order to get an appropriate comparison. The residual tests were done at room temperature instead of cold temperature, because no significant temperature dependency was observed for quasi-static tests. For these tests, only the applied load and mid-span deflection were recorded. An example of the residual test load-displacement time history can be seen in Figure 3.15 compared with the baseline quasi-static load-displacement.



**Figure 3.15 - Residual Flexural Test for Panel T2-1**

The residual strength was calculated using the peak recorded load for all the panels. These results as a function of the maximum mid-span displacement on impact were compared and these are shown in Figure 3.16.

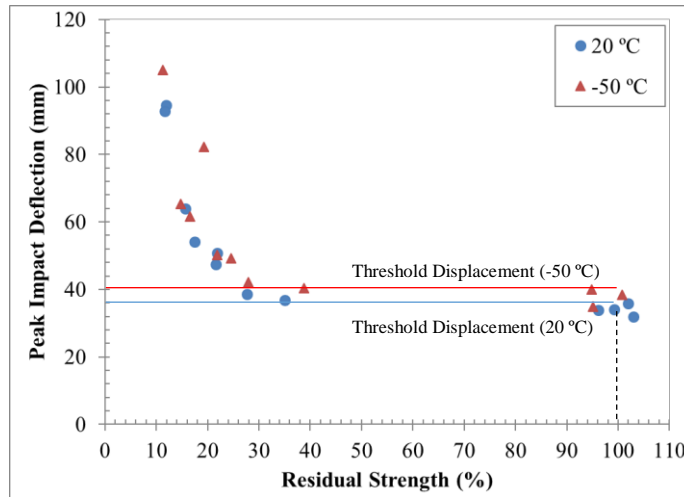


**Figure 3.16 - Residual Strength vs. Peak Impact Deflection for all Panels**

It can be observed that for similar impact deflections, the room and temperature panels exhibited a similar level of damage. From this figure, an approximate threshold mid-span deflection can be found of 36 mm and 40 mm for room and cold temperature panels respectively. These values are similar to the ones yielded from Table 3.6. Both room and cold temperature panels suffer a significant loss of residual strength (~80%) past these threshold deflections.

As observed earlier, the cold temperature panels seemed to have a much higher energy absorption capacity than their room temperature counterpart. It is then expected that for a similar absorbed energy or imparted energy, the cold panels would have a higher residual strength. This can in fact be observed in Figure 3.17.

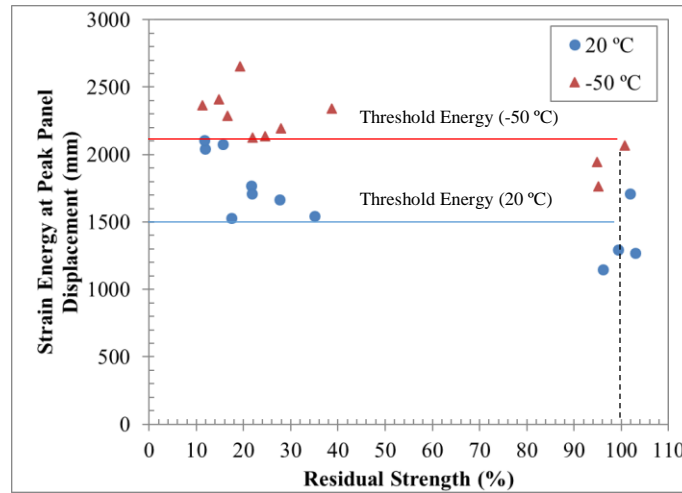


**Figure 3.17 - Residual Strength vs. Strain Energy at Peak Displacement for all Panels**

Even though both room and cold temperature tested panels showed similar behaviour, i.e. a sudden drop in residual strength past a threshold strain energy, that energy is quite different for both cases. Looking at Figure 3.17, room temperature panels exhibited a threshold failure energy of approximately 1500 J while this value was 2100 J for cold temperature series. Again, these values are in agreement with the strain energy results at maximum displacements from Table 3.6.

Even though the residual strength is reduced by almost 80% when the threshold displacement or energy are exceeded, the residual strain energy is reduced by approximately 60%. The reason for this can be explained by looking at the energy absorption behaviour past failure for the quasi-static panels. It seems to plateau with a very gradual loss in strength as seen in Figure 3.7. The panels that reached failure in the impact test showed a similar behaviour following their peak residual strength.

### 3.5 Conclusion

The aim of this study was to compare the impact response of GFRP multi-cell ribbed structural panels subjected to different temperatures. More precisely, room temperature (20 °C) and Arctic temperature (-50 °C) were investigated. As a result of this investigation, the following conclusions could be made for these particular panels.

1. Even though the tensile tests on coupons showed an increase in tensile modulus for cold temperature compared with room temperature, no similar observations could be noted for the quasi-static tests on full-size panels.
2. However, when subjected to dynamic loads by an impact hammer, the panels exhibited a significant difference in behaviour at different temperatures. The absorbed total energy as well as the failure displacements were increased by 32.1% and 11.3% respectively for panels tested at cold temperature compared to room temperature.
3. The panels tested at cold temperatures absorbed more energy than the room temperature tested specimens with a threshold failure energy of 2100 J.
4. Infrared thermography has been proven to be useful in order to assess damaged panels. This method was able to identify a loss of bond between the outside faces and the inside webs as well as identify a difference in failure mechanisms for room and cold temperature panels.
5. This study showed that the panels exhibited strain-rate sensitivity at temperatures of -50 °C and 20 °C. However, a more in-depth study is required with a larger strain-rate and temperature range to more precisely quantify the relationship between strain rate and temperature effects on the panels.

### 3.6 References

- [1] Government of Canada, "Canada's Arctic Foreign Policy," August 2008. [Online]. Available: [http://www.international.gc.ca/arctic-arctique/arctic\\_policy-canada-politique\\_arctique.aspx?lang=eng](http://www.international.gc.ca/arctic-arctique/arctic_policy-canada-politique_arctique.aspx?lang=eng).
- [2] L. Hollaway, "A Review of the Present and Future Utilisation of FRP

Composite in the Civil Infrastructure with Reference to their Important In-Service Properties," *Construction and Building Materials*, vol. 24, no.12, pp. 2419-2445, 2010.

- [3] P. Buchan and J. Chen, "Blast Protection of Buildings Using Fibre-Reinforced Polymer (FRP) Composites," in *Blast Protection of Civil Infrastructures and Vehicles using Composites*, Cambridge, Woodhead Publishing, 2010, pp. 269-297.
- [4] Strongwell, "COMPOSOLITE: Fiberglass Building Panel System," 2015. [Online]. Available: [www.strongwell.com/tools/product-literature/](http://www.strongwell.com/tools/product-literature/). [Accessed 20 October 2015].
- [5] Canadian Commission on Building and Fire Codes and National Research Council of Canada, National Building Code of Canada, Ottawa: National Research Council of Canada, 2010.
- [6] M. Arndt, FRP Rehabilitation of Blast and Impact Damaged Reinforced Concrete, Kingston: Royal Military College of Canada, 2009.
- [7] H. Wagner and et. al., "Time and Temperature Dependence of Fracture in a Unidirectional glass-reinforced epoxy," *Polymer*, vol. 20, no. 5, pp. 653-658, 1979.
- [8] Y. W. Mai and J. G. Williams, "The effects of temperature on the fracture of two partially crystalline polymers; polypropylene and nylon," *Journal of Materials Science*, vol. 12, no. 7, pp. 1376-1382, 1977.
- [9] M. Parvin and J. G. Williams, "The Effect of Temperature on the Fracture of polycarbonate," *Journal of Materials Science*, vol. 10, no. 11, pp. 1883-1888, 1975.
- [10] J. F. Timmerman and et al., "Matrix and Fiber Influences on the Cryogenic Microcracking of Carbon Fiber/Epoxy Composites," *Composites: Part A*, vol. 33, no. 3, pp. 323-329, 2002.



- [11] S. Gupta and A. Shukla, "Blast Performance of Marine Foam Core Sandwich Composites at Extreme Temperatures," *Experimental Mechanics*, vol. 52, no. 9, pp. 1521-1534, 2012.
- [12] M. D. Erickson and et al., "Effect of Temperature on the Low-velocity Impact Behavior of Composite Sandwich Panels," *Journal of Sandwich Structures and Materials*, vol. 7, no.3, pp. 245-264, 2005.
- [13] S. Benli and O. Sayman, "The Effects of Temperature and Thermal Stresses on Impact Damage in Laminated Composites," *Mathematical and Computational Applications*, vol. 16, no. 2, pp. 392-403, 2011.
- [14] M. Iqbal and et al, "The Characterization and Ballistic Evaluation of Mild Steel," *International Journal of Impact Engineering*, vol. 78, pp. 98-113, 2015.
- [15] CSA Group, S850-12: Design and Assessment of Buildings Subjected to Blast Loads, Mississauga: CSA Group, 2012.
- [16] T. Tay, "An Empirical Strain Rate-Dependent Constitutive Relationship for Glass-Fibre Reinforced Epoxy and Pure Epoxy," *Composite Structures*, vol. 33, no. 4, pp. 201-210, 1995.
- [17] O. Okoli, "The Effects of Strain Rate and Failure Modes on the Failure Energy of Fibre Reinforced Composites," *Composite Structures*, vol. 54, no. 2-3, pp. 299-203, 2001.
- [18] R. Ochola, "Mechanical Behaviour of Glass and Carbon Fibre Reinforced Composites at Varying Rates," *Composite Structures*, vol. 63, no. 3-4, pp. 455-467, 2004.
- [19] N. Hancox, "An Overview of the Impact Behaviour of Fibre-Reinforced Composites," in *Impact Behaviour of Fibre-Reinforced Composite Materials and Structures*, Cambridge, Woodhead Publishing, 2000, pp. 1-32.
- [20] G. Zhou, "The Use of Experimentally-Determined Impact Force as a Damage Measure in Impact Damage Resistance and Tolerance of

Composite Structures," *Composite Structures*, vol. 42, no. 4, pp. 375-382, 1998.

- [21] J. Kim, "Recent Developments in Impact Damage Assessment of Fibre Composites," in *Impact Behaviour of Fibre-Reinforced Composite Materials and Structures*, Cambridge, Woodhead Publishing, 2000, pp. 33-74.
- [22] J. De Castro San Roman, *System Ductility and Redundancy of FRP Structures with Ductile Adhesively-Bonded Joints*, Lausanne: Ecole Polytechnique Federale de Lausanne, 2005.
- [23] N. Banthia and et. al. , "Impact Testing of Concrete Using a Drop-Weight Impact Machine," *Experimental Mechanics*, vol. 29, no. 1, pp. 63-69, 1989.
- [24] X. X. Zhang and et. al., "A New Drop-Weight Impact Machine for Studying Fracture Processes in Structural Concrete," *An International Journal of Experimental Mechanics*, vol. 46, no. 3, pp. 252-257, 2010.
- [25] S. Soleimani and et. al., "Behavior of RC Beams Under Impact Loading: Some New Findings," in *Sixth International Conference on Fracture Mechanics of Concrete and Concrete Structures*, Catania, 2007.
- [26] A. Hay, *Operationnal Survival: Putting Resilience at the Core of Infrastructure Planning.*, London: Explora Research, 2013.
- [27] L. Hollaway, *Advanced Polymer Composites and Polymers in the Civil Structures*, Oxford: Elsevier, 2001.
- [28] J. Crawford and et al., "Retrofit of Masonry Walls to Enhance their Blast Resistance," in *Structures Congress: Crossing Borders*, 2008.
- [29] J. Crawford and J. Malvar, "Composite Retrofit to Increase the Blast Resistance of RC Buildings," in *Tenth International Symposium on Interaction of the Effects of Munitions with Structures*, Burbank, 2001.

- [30] P. Smith and J. Hetherington, Blast and Ballistic Loading on Structures, Oxford: Butterworth-Heinemann, 1994.
- [31] N. Uddin, Blast Protection of Civil Infrastructures and Vehicles Using Composites, Cambridge: Woodhead Publishing Limited, 2010.
- [32] S. Fuller, "Life-Cycle Cost Analysis (LCCA)," 28 06 2010. [Online]. Available: <https://www.wbdg.org/resources/lcca.php>. [Accessed 14 03 2016].

## **Chapter 4**

# **PREDICTING THE IMPACT RESPONSE OF GFRP MULTI-CELL RIBBED STRUCTURAL PANELS USING A SINGLE DEGREE-OF-FREEDOM MODEL**

### **4.1 Introduction**

#### 4.1.1 Background

Dynamic events such as blast or impact are types of loads that should be considered in today's new construction. With the very present threat of terrorism or even accidental catastrophes, significant progress has been made to better understand the behaviour of structures and structural components subjected to dynamic loads. Multiple references and books present how to analyse a structural component under a dynamic load such as a blast [1] [2] [3]. Although several analysis approaches are possible, all of these references present a practical method for analysing a structural component dynamically, and this method is single degree-of-freedom modelling (SDOF). This study will focus on the SDOF modelling of GFRP multi-cell ribbed structural panels subjected to a low-velocity impulsive load. Experimental results will then be compared to the SDOF model in order to validate its outputs.

#### 4.1.2 Dynamic Loading

In a blast load, the blast wave can be characterized by an almost instantaneous rise in pressure followed by an exponential decay over a very short period of time [4]. The negative pressure phase that normally follows is often neglected in most analyses. An impact load is similar in nature, apart from the incident pressure that will be usually lower. Additionally, impact loads are usually identified as low-velocity and will have a longer positive loading phase than most

blast events. The response spectrum of a component subjected to a blast or impact load can be either quasi-static, dynamic or impulsive. Quasi-static response happens when the positive phase duration of loading is long compared to the natural period of the structural component. Dynamic response, on the other hand is when the positive phase duration and natural period are similar. And impulsive response happens when the positive phase duration is much smaller than the natural period [1]. Due to the short duration of the load generated by an impact hammer, the panels are predicted to behave within the dynamic and impulsive range. An important aspect of an impulsive load, unlike a static load, is time-dependency. This introduces the concept of impulse, which is the product of the force and the time of its duration [2]. Blast and impact loads have two parameters that are of importance and cannot be separated: incident pressure or impact force and impulse. These parameters are of interest in the present study. Even though blast wave parameters can be predicted by using empirical equations [5], predicting an impact load is much more complex. Studies have shown that using a measured load-time history results in much more accurate responses for a SDOF approach [6].

#### 4.1.3 Single Degree-of-freedom Method

As mentioned previously, analysing the dynamic behaviour of a structural component is a complex task, because a dynamic load is time-dependent. The response of the component is then equally time-dependent in addition to being space dependent. A common method used to simplify these analyses is a single degree-of-freedom system. The complex structural system is conceptually idealized with a much simpler mathematical model following three main assumptions. Firstly, a material assumption must be made regarding the material properties like homogeneity, isotropy or anisotropy and material behaviour such as elasticity or plasticity. Secondly, loading assumptions must be made to represent the geometric location for distributed or concentrated loads, and also their time dependency such as constant or suddenly applied/removed loads. Finally, geometric assumptions must be made for structures, whether they are beams, frames or trusses. An assumption is that they consist of a finite number of unidirectional elements. The displacement of these elements or nodes that form these continuous structures will describe its overall dynamic behaviour [2]. For certain structures, such as the

panels studied in the present research, a single unidirectional element and a single node moving a specified direction may be used to represent the dynamic response of the overall structure. For this present study, the main assumptions will be material homogeneity, elasto-plastic behaviour, the load applied by the hammer will be represented as a point load applied at the center node of the beam, and the panel or beam will be represented by a single element that follows a specific shape function,  $\psi$ . The chosen shape function for this study will be a sinusoidal shape generated by a simply supported beam.

The continuous component that is the GFRP panel is idealized into a SDOF system in order to have a simpler mathematical or numerical model to solve. Basically, the panel's mass, stiffness and applied load are idealized by a simple SDOF system as can be seen in Figure 4.1. It is important to note that damping will be omitted for this study, as it is for most blast and impulsive loading analyses. This omission is acceptable since the maximum displacement occurring during the first displacement peak is of most interest as opposed to the full dynamic response.

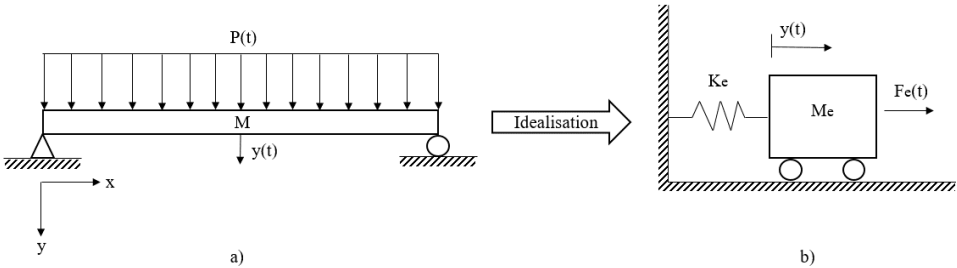


**Figure 4.1 - Panel's Idealization to a SDOF System. a) Simply Supported Panel. b) Equivalent SDOF System.**

For an equivalent system, the appropriate equivalency parameters,  $F_e$ ,  $M_e$  and  $K_e$ , must be used. These will depend on the shape function of the panel, which is dependent on the boundary and loading conditions as well as mass distribution. Following the generalized coordinates method and assuming a general shape function for the structural component, one can derive the equivalent parameters used in a SDOF system. Further simplification can also be done by assuming that the equivalent factor for stiffness and load are the same, consequently yielding only one equivalent load-mass factor,  $K_{LM}$ , that will be applied to the total mass of the

panel in order to get an equivalent system. These equivalent parameters have also been derived for generic cases [1] [2]. The equivalent load-mass factors found in Cormie et al. [1] will be used for this study. The equation of motion, as seen in equation (4.1), can then be used to obtain the displacement history of the SDOF equivalent model.

$$MK_{LM}\ddot{y}(t) + ky(t) = F(t) \quad (4.1)$$

Where  $M$  is the total mass of the component,  $ky(t)$  is the resistance function and  $F(t)$  the load time-history. Using a numerical method presented by Smith and Hetherington [3], by knowing the forcing function time-history, the resistance function of the structural component, its mass and equivalent load-mass factor,  $K_{LM}$ , one could find the displacement-time history for most structures based on the correct assumptions mentioned previously. It is important to note however, that this method also assumes constant acceleration throughout each time-step, which can add error to the model. If the time-steps are sufficiently small, this approximation should be acceptable. SDOF models have been used successfully for ductile structural components such as reinforced-concrete [6]. However, they are not often used for brittle components such as FRP panels.

#### 4.1.4 Failure Model

Thin wall structures such as the studied GFRP multi-cell ribbed structural panels are particularly susceptible to local buckling because of their low in-plane moduli and their high slenderness ratio. Ultimate limit state checks have to be done in order to identify the critical local buckling stresses. These limiting stresses were calculated using the equations for a rectangular box beam according to Bank [7], since the equations for stiffened panels such as those studied were not available in the literature. As part of this study, the following buckling failures were taken into consideration. Firstly, local buckling of walls due to in-plane compression was checked. Secondly, local buckling of the webs due to in-plane shear was monitored for the critical shear stress. Thirdly, web crushing and web buckling in the transverse direction at concentrated loads and supports was checked in order to monitor the critical crushing load and critical transverse buckling load at the

supports and at the loading point. The calculations for these stresses can be found in Appendix H. This failure model was incorporated in the moment-curvature predictive model that was used to model the resistance function of the panels.

## **4.2 Objective**

The objective of this study was to evaluate the accuracy of a SDOF model to predict the behaviour of GFRP multi-cell ribbed structural panels subjected to low-velocity impact. This model also considered the effects of temperature variations. The SDOF model will be compared to experimental impact results from Chapter 2 and Chapter 3.

## **4.3 Procedure**

### **4.3.1 Material Properties**

The materials which make up the GFRP multi-cell ribbed structural panels are a mix of isophthalic polyester fire retardant resin with E-Glass continuous strand mat and roving. The exact composition of the lay-ups is however unknown. The percentage of fibre to volume ratio is of 50% and the key coupon mechanical properties can be found in Table 4.1. Tests were conducted in the laboratory to confirm the manufacturer's listed mechanical properties. Tensile coupons in the longitudinal direction were tested as part of this project using an MTS 810 Material System, monitoring stroke and load as well as strain with 120  $\Omega$ , 10 mm long foil strain gauges from HBM adhesively bonded in the lengthwise and cross-width direction. The tests were performed at a constant displacement-rate of 20 mm/min.

The properties given by the manufacturer, Strongwell, were minimum ultimate values that resulted from a series of tests. The ultimate strength that was found in laboratory tests were used in this study in order to predict results consistent with experimental testing instead of the conservative values from the manufacturer. It is important to note that the GFRP panel is orthotropic. The



literature states that the compressive strengths are equal or larger to the transverse tensile strength in both directions, hence they were then chosen to be equal to the tested tensile strength property of 373 MPa.

**Table 4.1 – Panel’s Mechanical Properties**

Properties	ASTM Test Method	Manufacturer’s Values [8]	Laboratory tested at RMCC 20°C
Tensile Modulus (Lengthwise) MPa	D638	17,140	19,520
Tensile Strength (Lengthwise) MPa	D638	214	373
Flexural Modulus (Lengthwise) MPa	D790	6,102	N/A
Flexural Strength (Lengthwise) MPa	D790	169	N/A
Flexural Modulus (Cross-Width) MPa	D790	4,454	N/A
Flexural Strength (Cross-Width) MPa	D790	56.5	N/A
Short Beam Shear (Lengthwise) MPa	D2344	22	N/A
Poisson’s Ratio (Lengthwise) mm/mm	D3039	0.33	0.34

The panel’s cross-section dimensions are shown in Figure 4.2. The panels used in this study were 1500 mm long and filled with #1 EPS foam. Even though the foam provides thermal insulation, it was deemed to offer no significant structural benefit to the panel.

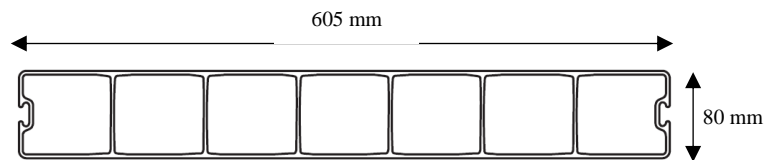


**Figure 4.2 – Cross-Section of COMPOSOLITE® Panel [8]**

### 4.3.2 Quasi-Static 3-point Flexural Test

In order to understand the flexural behaviour of the panels, a 3-point bending simply supported test was performed on the panel, see Figure 4.3. This test was done in order to obtain a static resistance function that would be used to calibrate the modelled resistance function. The unsupported span of the specimen was 1360 mm, and the load was applied at the mid-span. The panels were taken past the point of failure to the maximum stroke of the machine which is approximately 100 mm. Two flexural tests were performed at room temperature (20 °C) and two were done at cold temperatures (-40 °C). (It is the same testing frame as seen in previous studies Chapters 2 and 3.)

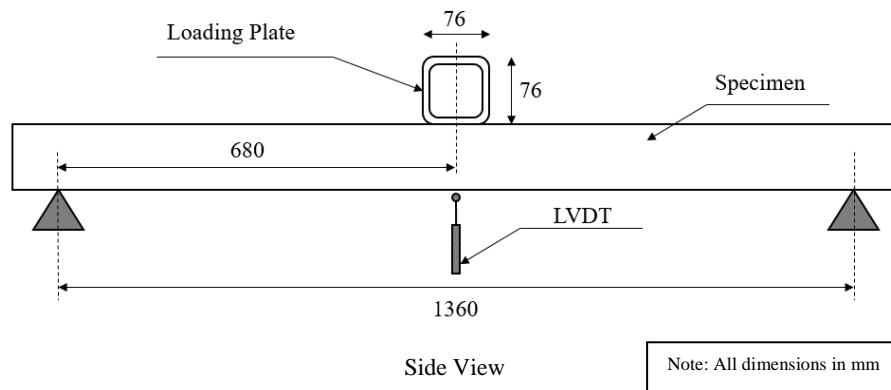
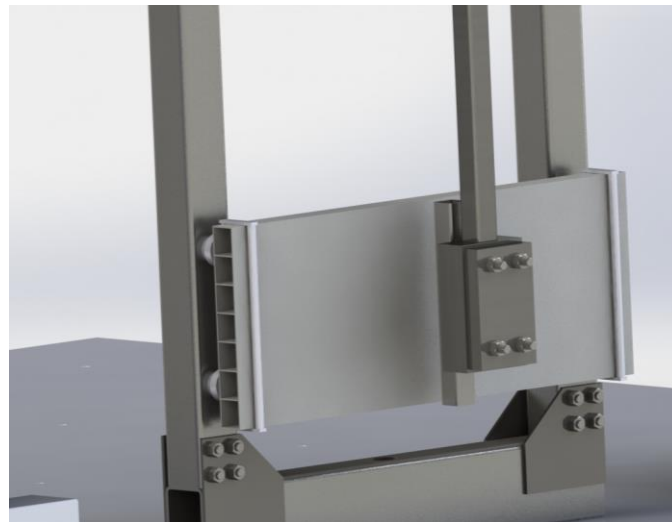
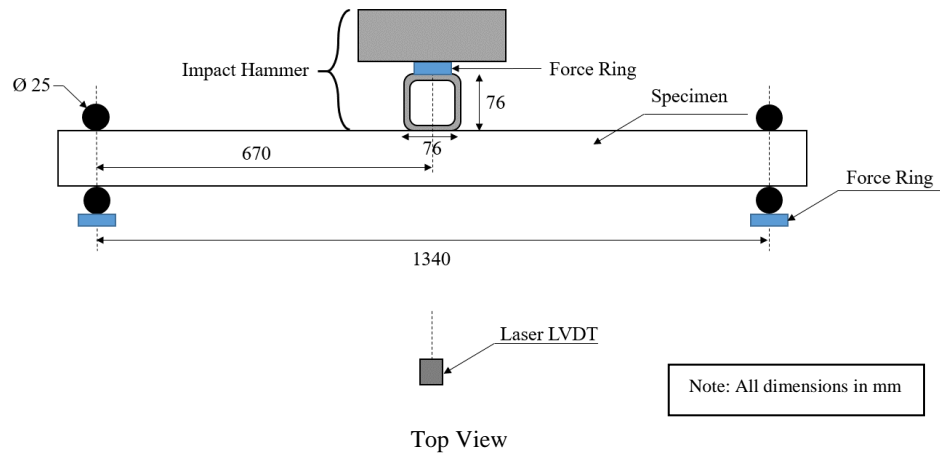


Figure 4.3 - 3-Point Flexural Test Apparatus

### 4.3.3 Impact Hammer Apparatus

Since the panels were tested in flexure, both statically and dynamically, and because the flexural modulus depends on both mechanical and structural properties of a component [9], the tests were conducted on full-size specimens. Consequently, a 138 kg impact hammer apparatus was used in order to generate a sufficiently large impulsive load onto the composite panels to observe their impact response.

This apparatus used the principle of a pendulum with a large mass, projecting a significant potential energy over a very short amount of time. The set-up can be seen in Figure 4.4. It is also the same apparatus as seen in Chapter 2 and 3. The impact response of the panel was sought and not its penetration resistance. These support conditions were assessed to be semi-rigid as opposed to simply supported. The unsupported span of the panels on the impact apparatus was 1340 mm.



3D View

**Figure 4.4 - Impact Hammer Apparatus**

Instrumentation was used in order to capture the dynamic behaviour of the panels as well as the imparted energy by the impact hammer. A laser LVDT with a range of 600 mm was used to measure the mid-span deflection of the specimens. A 207C ICP® 445 kN compression piezo-electric force ring was used on the hammer head to measure the applied dynamic load to the specimens. All these instruments

were connected to an MGC plus DAQ system and recorded in Catman Pro. The sampling rate of the piezo-electric instruments and laser LVDT was set at 2400 Hz. In addition, a high-speed camera was used to monitor the panel's behaviour using a frame rate of 1000 fps.

In total, 24 specimens were tested dynamically (as outlined earlier in Chapter 2 and 3) and herein will be compared to the SDOF model. Half of them were tested at room temperature while the remainder were tested in cold temperature. The mass of the hammer remained constant while the drop height was changed for different series, resulting in a change of impact velocity. Potential energy was used to predict the applied energy onto the panel since the drop height and hammer's mass were calculated with more certainty than the impact velocity. The complete testing schedule can be seen in Table 4.2. The labelling of the panels was done by looking at the main variable in each study. For the first study (chapter 2), the kinetic energy was the main variable, hence the K, while the temperature, T, was of interest in the second study (chapter 3). In Table 4.2, the measured dropped height of the impact hammer is presented for each testing series, and the predicted potential energy was then calculated using the latter measurement in conjunction with the total mass of the hammer.

**Table 4.2 - Impact Testing Schedule**

Test Series	Drop Height of the Hammer from rest (mm)	Resulting Potential Energy (J)
K1-1, K1-2, K1-3	1970	2630
K2-1, K2-2, K2-3	1470	1970
K3-1, K3-2, K3-3	1220	1630
K4-1, K4-2, K4-3	970	1300
T1-1, T1-2	2220	2970
T2-1, T2-2, T2-3	1970	2630
T3-1, T3-2, T3-3	1720	2300
T4-1, T4-2, T4-3	1470	1970
T5-1	1220	1630

#### 4.3.4 Modelling the Resistance Function

The resistance function for the GFRP panels could be built using the panel's material and geometric properties, as well as some assumptions regarding the failure mechanisms. A predictive moment-curvature model was used for this

purpose, similar to the one presented by Collins and Mitchell [10]. This model uses sectional analyses of component's cross sections subjected to flexure, see Figure 4.5. By using the principles of strain compatibility, force equilibrium and known material properties, this method can yield the moment-curvature diagram for the studied panels.

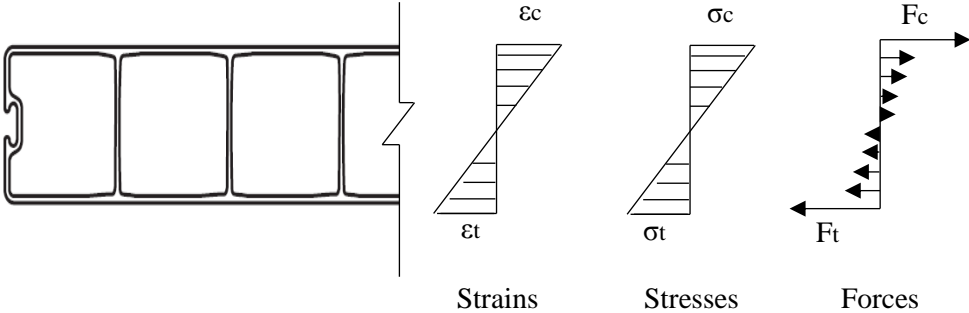
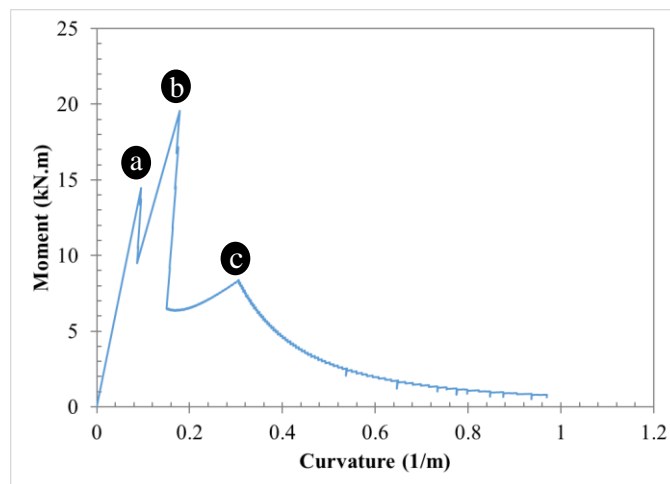


Figure 4.5 - Plane Section Analysis

The moment-curvature model was built using a spreadsheet by dividing the panel's cross-section into a finite number of layers. By assuming a strain at the top of the section at every strain-step, using strain compatibility and force equilibrium, the total strain, stress and force distribution could be found for every strain-step. Some alterations had to be made to the material model for this particular case and the material properties given by the manufacturer alone were not sufficient. This was done by assuming a certain failure mode and sequence for these panels. This particular sequence is illustrated in Figure 4.6. The significant changes in the moment-curvature relationship are labelled in Figure 4.6 and will be explained in the following paragraph.

The ultimate limit state was checked [7], and the local buckling of the flange due to in-plane stresses governed the capacity when considering flexural behaviour. The model was designed so that only the compressive portion of the cross-section would fail following the critical buckling stress of -75 MPa, which is significantly lower than the ultimate stress prescribed by the manufacturer. However, since these ultimate stresses were calculated for a box section and that structure could be seen as multiple box beam sections, it was assumed that a certain redundancy occurred when local buckling failure occurred in the flange. This was taken into consideration in the model by reducing resisting stresses by 50% in the

flange following local buckling failure (a). Then, local crushing of the web would occur at a concentrated load of approximately 67 kN according to ultimate state calculations. The bending stress resulting in that critical point load was then approximated for the top fibre of the cross-section, -171 MPa, and the top flange was assumed to lose all resistance following crushing of the web (b). This would result in catastrophic failure of the panel following the loss of the main compression area. However, the same assumption for redundancy was taken for the web's stresses and were reduced by 50% following local crushing stress. The remainder of the cross-section failed when it achieved ultimate axial stress, i.e. 373 MPa for tension and -373 MPa for compression (c).



**Figure 4.6 - Modelled Moment-Curvature Relationship of the GFRP Panels for a Quasi-Static Load. a) Top flange local buckling failure due to in-plane compressive stresses, b) Local crushing of the webs resulting in catastrophic panel failure, c) Secondary failure following ultimate axial stresses and resulting in softening behaviour**

Once the moment-curvature relationship has been modelled for the panels, the resistance function (load-displacement) could then be determined. Boundary conditions as well as loading conditions had to be assumed in order to obtain the resistance function. Simply supported boundary conditions as well as a concentrated load at the middle were assumed. Moreover, a plastic hinge was created at the mid-span of the panel following its failure. This would result in a constant moment in the plastic hinge region. The hinge would be taken past the failure curvature while the rest of the panel would be unloaded following the elastic portion of the moment-curvature [11] and would be subjected to softening.

Another assumption was made as to the size of the hinge along the length of the panel. It was assumed for this case that the hinge would be 200 mm in length. This assumption is based on the strain distribution determined from the experimental results during the previous studies outlined in Chapter 2 and 3. Strain gauges were placed along the panel as seen in Figure 4.7. Before failure, the strain variation is constant between SG2, 3 and 4. However, post-failure, the strain variation between SG3 and 4 is much smaller than between SG2 and 3, which would indicate that SG2 is in or very close to the hinge portion of the beam. From observation of the tested specimens the heavily damaged section did not appear to exceed a 200 mm length. Therefore 200 mm was chosen for the length of the plastic hinge for the load-displacement model.

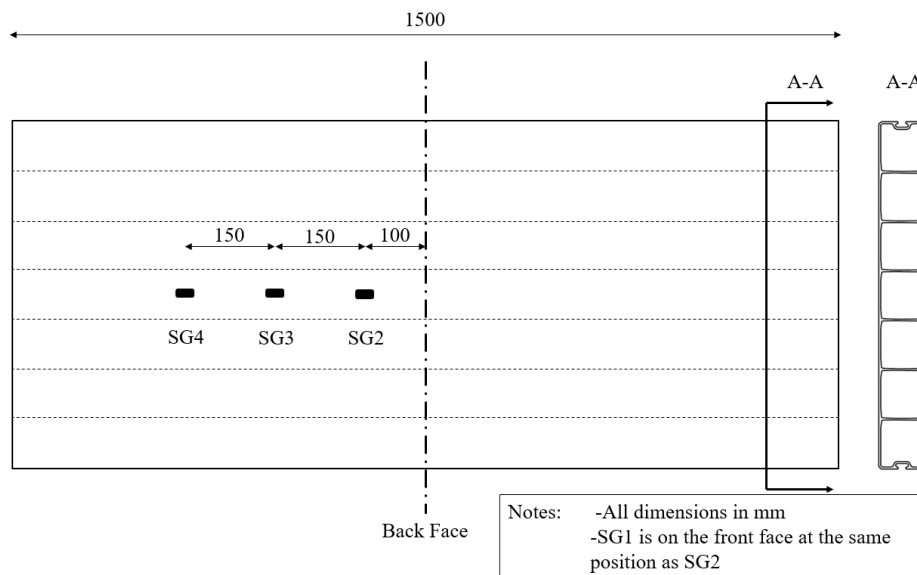


**Figure 4.7 - Strain Gauge Instrumentation of GFRP Panels**

The obtained resistance function was the quasi-static case, but it has been determined in previous studies (Chapter 2 and 3) that the absorbed energy differed from dynamic to quasi-static loading. Additionally, energy varied with different temperatures, absorbing more energy at sub-zero temperatures for these specific panels. Consequently, a dynamic increase factor (DIF) was estimated for the dynamic loading at room and sub-zero temperatures. These DIF were chosen by calibrating the resistance function to the experimental results, in order to obtain similar absorbed energies prior to failure. Figure 4.8 shows an experimental quasi-static resistance function compared to the modelled resistance functions. The



modelled quasi-static as well as the modelled dynamic room temperature and cold temperature resistance functions are presented. Table 4.3 shows a quantitative comparison of the experimental and modelled resistance functions looking mainly at the strain energy and failure displacements. Ultimately, a DIF of 1.35 was chosen for the dynamic resistance function at room temperature and a value of 1.55 for the sub-zero case. This was determined from the strain energy as seen in Table 4.3.

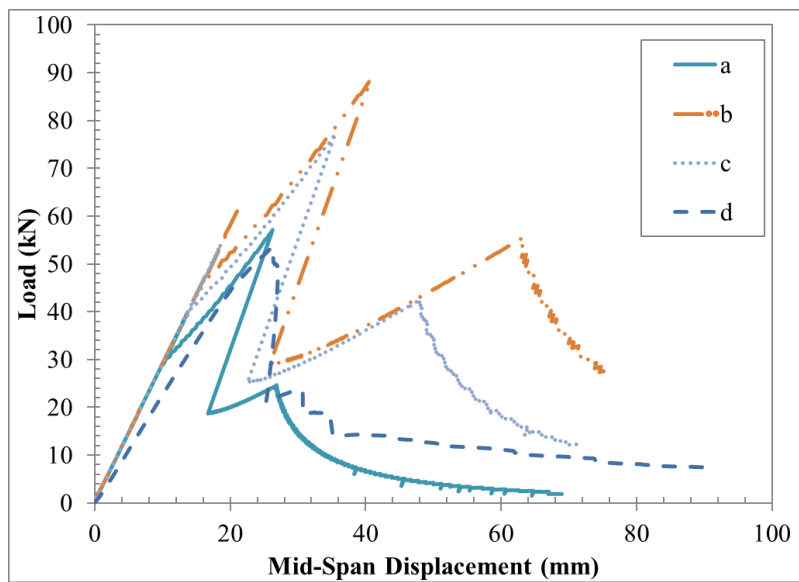


**Figure 4.8 - Comparison of Modelled Resistance Function with Experimental Results.**  
a) Modelled quasi-static, b) Modelled dynamic (-50°C), c) Modelled dynamic (20°C), d) Quasi-static experimental test 2 (20°C)

**Table 4.3 - Energy Comparison between Modelled and Experimental Resistance Function**

Testing method	Experimental Strain Energy at failure* (J)	Modelled Strain Energy at failure (J)	Experimental failure mid-span displacement* (mm)	Modelled failure mid-span displacement (mm)	Dynamic increase factor (DIF)
Quasi-Static	967	840	27.9	26.2	1.0
Dynamic (20°C)	1586	1531	37.5	35.5	1.35
Dynamic (-50°C)	2094	2021	41.7	40.8	1.55

\*Average of all tests, both room and sub-zero temperatures for quasi-static case

The dynamic loading function was not theoretically modelled for this study. In fact, unlike blast wave parameters, impact hammers do not have empirical data available to estimate the peak load, impulse and duration. Also, it has been demonstrated that using known experimental forcing functions are more accurate than predicted ones, even for blast [6]. For this reason, the experimental load time-history from the hammer load-cell was used as the loading function for the SDOF model.

#### 4.3.5 SDOF Modelling

As mentioned earlier, the SDOF model according to Smith and Hetherington [3] was used to predict the peak displacement of the panels. Ultimately, only the peak displacement was of interest here, as it is for most blast or impact analyses, in order to see if the panels reach the failure displacements and lose most residual strength. The chosen SDOF model is an iterative numerical approach that uses constant acceleration throughout time-steps. Typically, the time-step should be less than one tenth of the natural period of the beam. This is recommended in order to capture the sudden variations in the forcing and resistance function. Using the beam's stiffness and equivalent mass, the panel's natural period,  $T$ , was found to be 0.012 s using simply supported boundary conditions. The model's time-step was driven by the sampling rate of the hammer load-cell, which was 2400 Hz that yielded a time-step of 0.000417 s. This value was approximately three times smaller than the required 0.0012 s.

The model also takes into consideration the change of load-mass factor pre- and post-failure of the panel. In fact, prior to failure, the assumed simply supported boundary conditions would generate a shape function resembling half a sinusoidal function, parabolic in shape. This yields a load-mass factor,  $K_{LM}=0.49$ . Post-failure, the formation of a plastic hinge changes the shape function of the panel. The portion of the panel between the hinge and the supports will be quasi-linear, while the hinge portion will continue to have a parabolic shape until ultimate curvature is reached. This second shape function results in  $K_{LM}=0.33$ . These factors were taken from Cormie et al. [1], even though more accurate factors could have been generated using a more complex method such as the generalized coordinates method [2]. The latter method would have taken into consideration the actual shape function of the panel without assuming the boundary conditions. However, in order to get an accurate shape function, more strain gauges would have been needed along the full length of the panels, especially closer to the supports. An example of calculations made for the SDOF model can be seen in Appendix J.

#### 4.4 Results and Discussion

The experimental results to which the SDOF model will be compared with are the impacted GFRP panels discussed in detail in Chapters 2 and 3. The experimental impact load recorded by a force ring on an impact hammer was used as the forcing function and was inputted into the SDOF model. Table 4.4 shows the results that were acquired experimentally and compares the experimental peak displacements with the modelled ones.

**Table 4.4 - Experimental Results Compared to SDOF Model Results for GFRP Panels' Impact Response**

Test Series	Potential Energy (J)	Total Work Done (J)	Measured Peak Displacement (mm)	Did Failure Occur Experimentally	SDOF Modelled Peak Displacements (mm)	Did Failure Occur in the Model	Displacement Error (%)
<b>K series tested with a face temperature of 20°C</b>							
<b>K1-1</b>	2630	1805	64.0	Yes	1322	Yes	>200%
<b>K1-2</b>	2630	2050	94.6	Yes	936	Yes	>200%
<b>K1-3</b>	2630	2036	92.8	Yes	177	Yes	90.6
<b>K2-1</b>	1970	1580	47.4	Yes	35.1	No*	25.9

<b>K2-2</b>	1970	1561	54.1	Yes	32.6	No*	39.7
<b>K2-3</b>	1970	1616	50.9	Yes	46.1	Yes	9.5
<b>K3-1</b>	1630	1613	38.6	Yes	31.2	No*	19.2
<b>K3-2</b>	1630	1531	36.9	Yes	31.0	No*	15.9
<b>K3-3</b>	1630	1684	35.9	No	5872	Yes*	>200%
<b>K4-1</b>	1300	1291	33.9	No	26.6	No	21.4
<b>K4-2</b>	1300	1308	31.8	No	31.6	No	0.8
<b>K4-3</b>	1300	1345	34.0	No	28.5	No	16.2
<b>T series tested with a face temperature of approximately -50°C</b>							
<b>T1-1</b>	2970	2777	82.2	Yes	4044	Yes	>200%
<b>T1-2</b>	2970	2551	105	Yes	213	Yes	103.1
<b>T2-1</b>	2630	2316	50.2	Yes	579	Yes	>200%
<b>T2-2</b>	2630	2347	61.6	Yes	1145	Yes	>200%
<b>T2-3</b>	2630	2423	65.3	Yes	743	Yes	>200%
<b>T3-1</b>	2300	1845	49.2	Yes	101	Yes	106.1
<b>T3-2</b>	2300	2286	40.3	Yes	3654	Yes	>200%
<b>T3-3</b>	2300	2141	42.2	Yes	845	Yes	>200%
<b>T4-1</b>	1970	1995	38.4	No	2726	Yes*	>200%
<b>T4-2</b>	1970	1469	47.4	Yes	34.0	No*	28.2
<b>T4-3</b>	1970	1995	40.0	No	39.02	No	2.3
<b>T5-1</b>	1630	1662	34.9	No	38.82	No	11.1

\*These panels' modelled and experimental failure mode did not match. They failed in the model and not the experiment or vice-versa.

The compared results are only peak displacements, since it is the most critical value to predict if the panels will survive the imparted impact or forcing function. An example of an accurate predicted response from the model is shown in Figure 4.9 and an inaccurate prediction of response is shown in Figure 4.10. The remainder of the graphs comparing the SDOF modelled response with the experimental response in the time domain can be found in Appendix K. The appendix presents the modelled response using the room temperature resistance function for the K series and the sub-zero resistance function for the T series. The forcing functions are also presented in the same appendix which are taken directly from the experimentally acquired data.

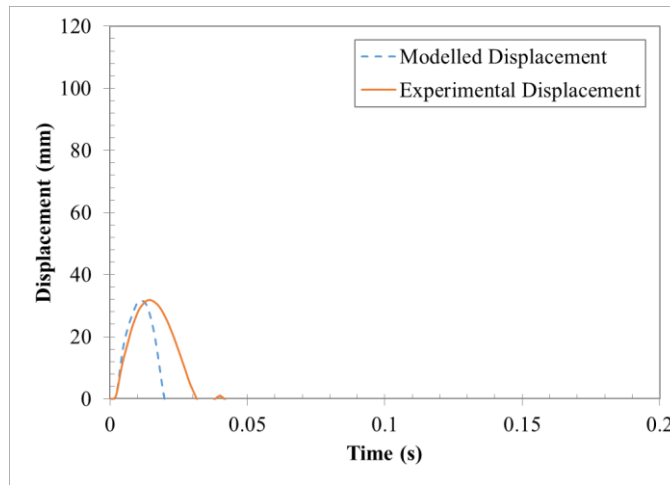


**Figure 4.9 - Accurate SDOF Modelled Response. Panel K4-2**

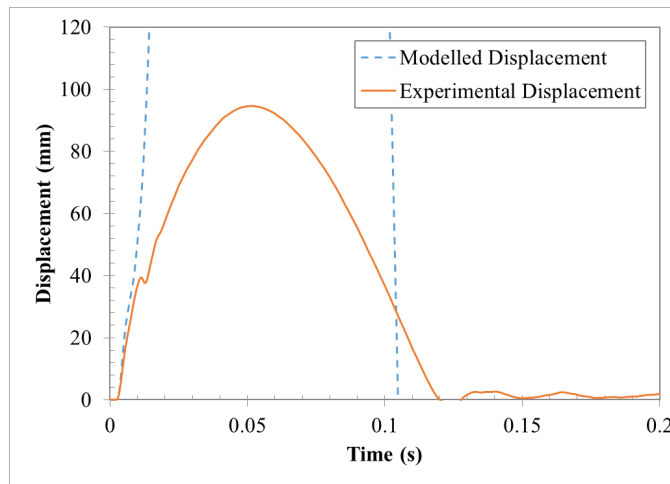


**Figure 4.10 - Inaccurate SDOF Modelled Response. Panel K1-2**

It can be observed by looking at Figure 4.9 and Figure 4.10 as well as the numerical values in Table 4.4 that the model was not capable of accurately representing the experimental observations for all the tests. The abnormally large displacements and percentage of error shown in Table 4.4 for some of the impact series is due to instability of the model following failure. The resistance functions that were generated were built on assumptions made following experimental observations. Different panels showed different behaviour and there was a certain degree of variability within the panel's population. A variability was observed in

panel properties such as modulus and peak strength as well as peak displacements. This can be seen graphically in Figure 4.11 where the quasi-static load-displacement histories are shown and are represented in Table 4.5. Since the panels do not behave as typical ductile members past failure, a different failure displacement may translate to a significant difference in strain energy prior failure. By using the same resistance function for all the panels, some panels' failure strain energy might be overestimated and some underestimated. This could be part of the issue where the modelled peak displacements are significantly lower or higher than the experimental displacements. In the cases where failure occurred in the model but not in the experiment, the error in modelled displacements would be very important since the experimental forcing function of a non-fractured panel was used. Consequently, as observed for panel K3-3 and T4-1, the forcing function values post-failure in the model were largely over-estimated. Thus, resulting in extremely large displacements.

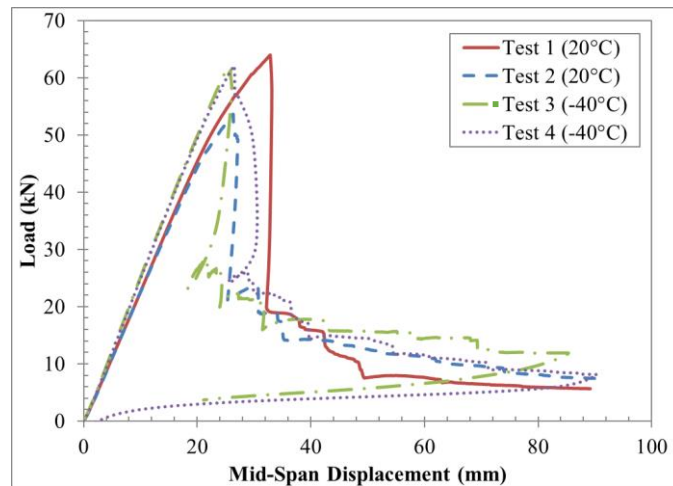


Figure 4.11 - Load-Displacement Histories Showing Variability in the Panels

Table 4.5 - Quasi-Static tests results

Test #	Face Temperature (°C)	Failure Displacement (mm)	Flexural Stiffness (kN/m)	Peak Load (kN)	Fracture Energy (J)
1	~ 20	32.9	2175	64.0	1170
2	~ 20	26.3	2163	53.6	757
3	~ -40	25.9	2416	61.3	831

Also, it was observed that the SDOF model is very sensitive to the assumptions that were originally made. The assumption that the panels were perfectly simply-supported is not correct. Since there was some rotational stiffness at the supports due to the apparatus set-up, the load-mass factor would in theory have to be adjusted to account for semi-rigid supports, between simply supported and rigid. It was observed that by reducing the load-mass factor,  $K_{LM}$ , before failure would reduce the modelled peak displacement closer to the experimental values. Figure 4.12 and Figure 4.13 show the difference in modelled displacements for panel K1-3 by reducing  $K_{LM}$  from 0.49 to 0.48. The difference in peak displacements went from 176.86 mm to 87.31 mm respectively. This 50% difference was not observed for all panels, but it shows the sensitivity of the model for these particular panels and support conditions.

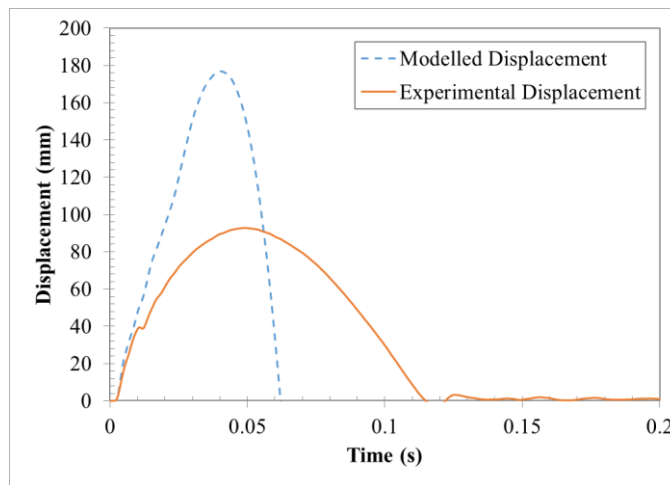
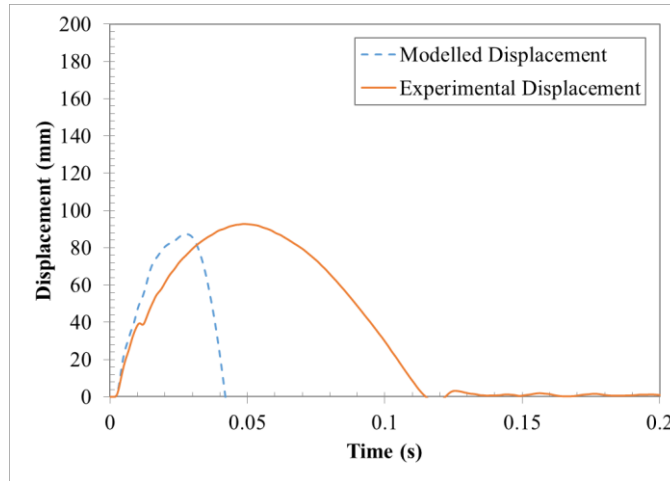


Figure 4.12 - SDOF Model Using  $K_{LM}=0.49$  for Panel K1-3



**Figure 4.13 - SDOF Model Using  $K_{LM}=0.48$  for Panel K1-3**

For some cases, the applied experimental load was also deemed to be erroneous and not representative of the actual impact load. The piezo-electric force ring might have given false data for some of the tests. In fact, by looking at the experimental energy conservation graphs, discrepancies were observed for some tests. For example, panel K1-1's energy conservation graph showed a large discrepancy at peak displacement as shown in Figure 4.14. The work done by the hammer, which is the area under the load-displacement curve using the hammer force ring, is much different from the panel's absorbed energy, which is the summation of the panel's strain energy and kinetic energy. This should not be the case. The strain energy was calculated using the force ring at the supports in order to subtract the inertial forces from the hammer's force ring. This shows a discrepancy between the support reaction and the impact load. It is difficult to determine which one shows erroneous data, but since the SDOF model for these cases outputs unreliable results, it is likely that the less reliable instrumentation would be the hammer's force ring for these specific cases, since it is used as the input forcing function for the models. It was observed that the error between the panel's total absorbed energy and the work done by the hammer at peak displacement was 13.08% for panel K1-1. Errors of more than 10% were also observed for panel K2-1, T3-1 and T4-2. The forcing function for those cases was deemed unreliable and the SDOF would likely output inaccurate results. However,



the magnitude of error was observed to be more important when the panel fractured in the model, i.e. K1-1 and T3-1.

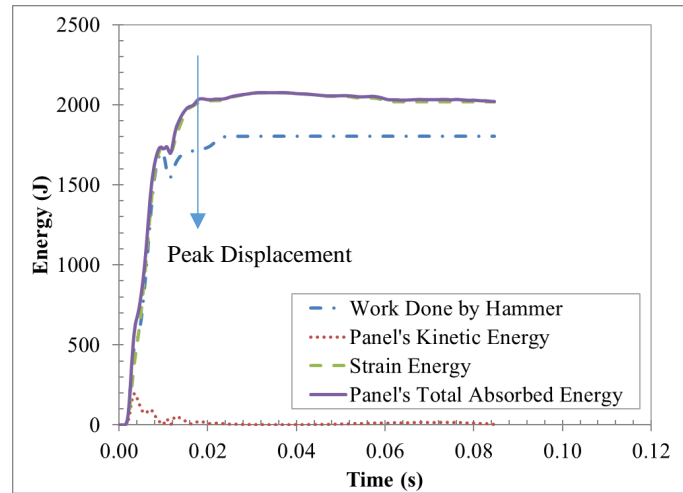


**Figure 4.14 - Energy Conservation for Panel K1-1**

It is important to note that there could be an error associated with the way the work done by the hammer was calculated. The displacement used for the work was the panel's back face displacement and not the hammer, due to instrumentation constraints where during the experiment it was difficult to monitor the front face of the specimen. In the short instance where the panel's back face displacement decreased just moments after failure, the hammer could be moving forward. Consequently, instead of observing a decrease in work following failure, as observed in Figure 4.14, the work could be increasing, and the energy error could then be decreased. However, there was no way of confirming that hypothesis accurately, so the panel's displacement was used instead.

Another observation that could conclude erroneous readings from the hammer's force ring is the impact load behaviour at the time of fracture. For example, in panel T3-2, a high load peak occurred post-failure, which would be inconsistent since failure brings an important loss in resistance. If one would plot the impact load vs. panel's displacement for this particular panel, see Figure 4.15, this increase in load following failure is clearly represented by a backwards loop.

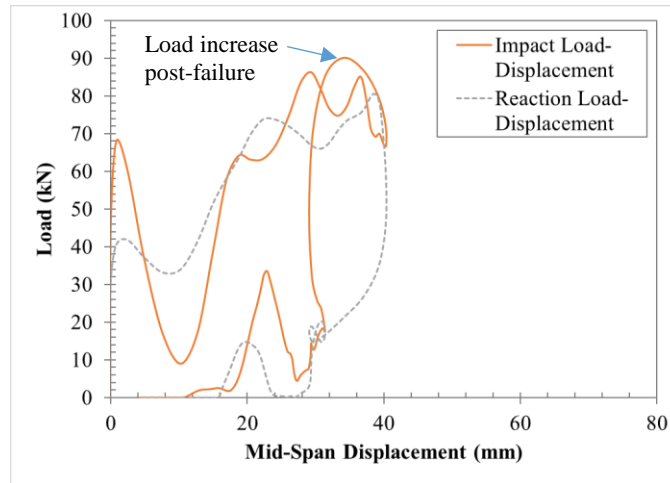


**Figure 4.15 - Load-Displacement Graphs for Panel T3-2 Using Reaction and Impact Hammer**

This increase was not observed by looking at the supports reaction as shown by the dotted line in Figure 4.15. By eliminating this peak, the maximum modelled displacement was reduced from 3654.21 mm to 994.92 mm. This value is still greater than the experimental results, but it has been reduced significantly from the original modelled displacement. Similar behaviour at time of failure was also observed for panel T3-3. This implies that a quick review of the energy conservation graph as well as the impact load-displacement graphs may indicate if the load from the force ring was sufficiently accurate. The predicted modelled response of panels with an inaccurate forcing function would then have to be discarded since the forcing function used would likely be wrong.

The SDOF for the room temperature impacted panels appeared to yield more accurate peak displacements than the cold temperature hits. This can be due to the way the resistance functions were obtained, by only applying the DIF to the ultimate stresses and not the elastic modulus. If the DIF were to be applied to the modulus, then it would generate more strain energy prior failure. However, if an increased failure displacement was desired from the dynamic response, as was observed experimentally, a lower DIF would be necessary for the modulus than the ultimate stresses. Further work would need to be completed to determine different DIF for different properties.

## 4.5 Conclusion

To conclude, SDOF models have been proven accurate for previous studies, but they have certain limitations. As shown in this study, brittle structural components such as GFRP modular panels do not exhibit simple ductile resistance functions as are usually observed in components made of steel or reinforced-concrete. Their resistance functions are very difficult to predict and have to be based on certain failure assumptions. For this case, these assumptions were made using ultimate limit state stresses, but were also based on experimental knowledge. The SDOF used, was acceptable for the panels where failure was neither predicted by the model nor observed in the experiments, displaying a maximum error for displacements of 21.4%. Where the model predicted a panel failure, but an experimental failure was not observed in the panels, the error could go as high as 160 times the observed displacement. For the remainder of the modelled impacted panels, the predicted displacement varied from a 9.5% error to 90 times the observed displacements. The source of errors for these cases were likely inaccuracies in the assumed shape function, calculated resistance functions and readings in the impact hammer force ring.

It is recommended that a more precise evaluation of an appropriate resistance function be determined that could be used for SDOF models. Alternative methods such as variable equivalent SDOF parameters as prescribed by Krauthammer et al. [6] could be used for more accuracy. Also, a more in-depth analysis on DIF using both temperature and strain-rate as parametric studies would be needed for these panels.

Finally, SDOF models might not be the best approach for structural components displaying sudden large loss of resistance and softening past failure. Maybe more complex analyses using finite element method (FEM) may generate more accurate results.

Furthermore, any efforts to improve the post-failure load-carrying capacity and energy absorption in the panel would improve both its structural behaviour and the ability of any model to accurately predict its behaviour.

## 4.6 References

- [1] D. Cormie, G. Mays and P. Smith, *Blast Effects on Buildings*, London: Institution of Civil Engineers, 2009.
- [2] M. Paz and W. Leigh, *Structural Dynamics: Theory and Computation*, Boston: Kluwer Academic Publishers, 2004.
- [3] P. Smith and J. Hetherington, *Blast and Ballistic Loading on Structures*, Oxford: Butterworth-Heinemann, 1994.
- [4] D. Dusenberry, *Handbook for Blast-Resistant Design of Buildings*, Hoboken: John Wiley & Sons , 2010.
- [5] US Army Corps of Engineers, Naval Facilities Engineering Command and Air Force Civil Engineer Support Agency, *Structures to Resist the Effects of Accidental Explosions. UFC 3-340-02*, Washington, DC: US Department of Defense, 2008.
- [6] T. Krauthammer and et al. , "Response of Reinforced Concrete Elements to Severe Impulsive Loads," *Journal of Structural Engineering*, vol. 116, no. 4, pp. 1061-1079, 1990.
- [7] L. Bank, *Composites for Construction: Structural Design with FRP Materials*, Hoboken: John Wiley & Sons, Inc., 2006.
- [8] Strongwell, "COMPOSOLITE: Fiberglass Building Panel System," 2015. [Online]. Available: [www.strongwell.com/tools/product-literature/](http://www.strongwell.com/tools/product-literature/). [Accessed 20 October 2015].
- [9] J. De Castro San Roman, *System Ductility and Redundancy of FRP Structures with Ductile Adhesively-Bonded Joints*, Lausanne: Ecole Polytechnique Federale de Lausanne, 2005.
- [10] M. Collins and D. Mitchell, *Prestressed Concrete Structures*, Response Publications, 1997.

- [11] M. Jirasek and Z. Bazant, *Inelastic Analysis of Structures*, West Sussex: John Wiley and Sons, Ltd., 2002.
- [12] Government of Canada, "Canada's Arctic Foreign Policy," August 2008. [Online]. Available: [http://www.international.gc.ca/arctic-arctique/arctic\\_policy-canada-politique\\_arctique.aspx?lang=eng](http://www.international.gc.ca/arctic-arctique/arctic_policy-canada-politique_arctique.aspx?lang=eng).
- [13] M. Arndt, *FRP Rehabilitation of Blast and Impact Damaged Reinforced Concrete*, Kingston: Royal Military College of Canada, 2009.
- [14] A. Hay, *Operational Survival: Putting Resilience at the Core of Infrastructure Planning*, London: Explora Research, 2013.
- [15] L. Hollaway, "A Review of the Present and Future Utilisation of FRP Composite in the Civil Infrastructure with Reference to their Important In-Service Properties," *Construction and Building Materials*, vol. 24, no. 12, pp. 2419-2445, 2010.
- [16] L. Hollaway, *Advanced Polymer Composites and Polymers in the Civil Structures*, Oxford: Elsevier, 2001.
- [17] J. Crawford and et al., "Retrofit of Masonry Walls to Enhance their Blast Resistance," in *Structures Congress: Crossing Borders*, 2008.
- [18] J. Crawford and J. Malvar, "Composite Retrofit to Increase the Blast Resistance of RC Buildings," in *Tenth International Symposium on Interaction of the Effects of Munitions with Structures*, Burbank, 2001.
- [19] N. Uddin, *Blast Protection of Civil Infrastructures and Vehicles Using Composites*, Cambridge: Woodhead Publishing Limited, 2010.
- [20] A. Nassr and et al., "Single and Multi Degree of Freedom Analysis of Steel Beams Under Blast Loading," *Nuclear Engineering and Design*, vol. 242, pp. 63-77, 2012.
- [21] N. Hancox, "An Overview of the Impact Behaviour of Fibre-Reinforced Composites," in *Impact Behaviour of Fibre-Reinforced Composite Materials and Structures*, Cambridge, Woodhead Publishing, 2000, pp.

1-32.

## Chapter 5

### CONCLUSIONS AND FUTURE WORK

#### 5.1 Summary of Research

The main objectives for the research presented in this document were to: evaluate the response of a particular GFRP stiffened panel when it is subjected to low-velocity impact loadings; compare the effects of sub-zero temperature on the previously analyzed panels subjected to similar low-velocity impact; and create a single degree-of-freedom (SDOF) model that could take into account the strain and temperature sensitivity of the panels in order to accurately simulate the laboratory tests. As a first study, the impact response of the GFRP panels was studied by using a pendulum impact hammer apparatus that was built to apply an impulse of up to 3000 J to the full-size panel. The panels were monitored with multiple instruments measuring the applied load, panel's mid-span displacements and longitudinal strain. The amount of damage was also quantified by observing the residual flexural strength of the impacted panels. As a second study, another set of panels were exposed to a low temperature environment consistent with extreme Arctic conditions and were impacted at approximately  $-50^{\circ}\text{C}$  using the same apparatus as the first study. The goal was to compare the dynamic properties of the panels by varying the temperature parameter. The amount of damage was also measured and compared to the room temperature panels. To complement the experimental studies, a SDOF model was derived in order to simulate the laboratory tests. This model was based on the moment-curvature relations for this particular cross-section. It uses the material and geometry properties of the GFRP panels to create a moment-curvature diagram, which was used to generate a resistance function that was used in the model. Then, the load-time history of the impact hammer was used as input for the model. The modelled responses were then created and compared with the observed experimental behaviour of all specimen in the testing schedule.

## 5.2 Conclusions

The following conclusions were determined from the experimental studies and predictive modelling.

1. The GFRP multi-cell ribbed structural panels are strain-rate dependent. The most sensitive parameters are failure energy threshold and also failure displacement.
2. The panels could be used as a main structural component for small scale buildings and would provide safety as well as robustness comparable to steel or RC components for quasi-static loading conditions.
3. For quasi-static loading conditions of full-size panels, temperature variation did not seem to have a significant impact.
4. When subjected to dynamic loads by an impact hammer, the panels exhibited a significant difference in behaviour at different temperatures. For cold temperature impacted panels, the absorbed total energy as well as the failure displacements were increased by 32.1% and 11.3% respectively when compared to room temperature panels.
5. The panels were able to withstand a strain energy averaging 1586 J at room temperature and 2094 J at cold temperature before failure. Many blast or impact events would easily surpass this amount of energy.
6. The work done by the hammer on the panel can differ from the predicted potential energy even though the correct hammer mass and drop height are used. Dynamic instrumentation is required in order to accurately estimate impact and strain energy.
7. Even though GFRP panels are light compared to the impact hammer, inertial effects are not negligible for dynamic behaviour analysis. The time lag that affects the support reaction also has to be accounted for if using this load for actual bending load. An alternative to using acquired data from the supports would be to use the inertial equations for specific support conditions and subtracting the inertial load from the recorded impact load of the hammer.
8. Infrared thermography has been proven to be useful in order to assess damaged panels. This method was able to identify a loss of bond between the outside faces and the inside webs as well as identify a difference in failure mechanisms for room and cold temperature panels.
9. Residual strength tests were in good agreement with the failure energy and displacements gathered from impact tests for both temperature ranges.



10. The conservation of energy graph is a good indication of how much energy is lost in the system. This specific apparatus showed a good conservation of energy with minor losses.
11. SDOF models have been proven accurate for previous studies, but they have certain limitations. Brittle structural components such as GFRP multi-cell ribbed structural panels do not exhibit simple ductile resistance functions as is usually observed in components made of steel or reinforced-concrete. Their resistance functions are very difficult to predict and have to be based on certain failure assumptions.
12. The SDOF predictive model used, was acceptable for the panels that were impacted with low kinetic energies where failure did not happen, displaying a maximum error for displacements of 21.4%.

### **5.3 Future Work**

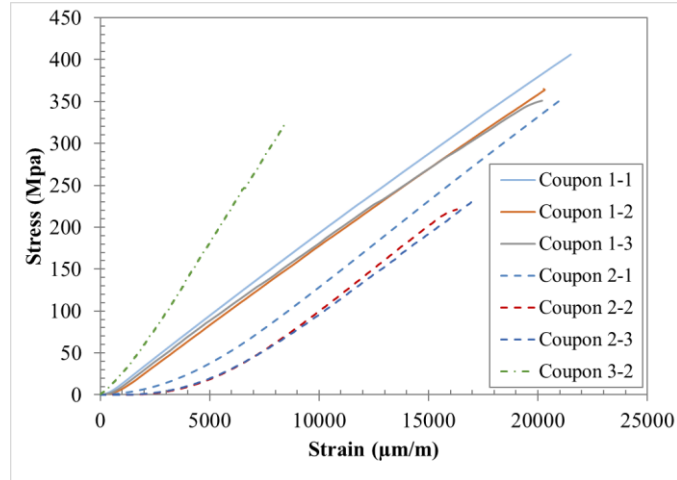
1. Further testing could be done using energy absorbing anchors in order to increase the resistance of the panels subjected to larger dynamic events. Other alternatives could also be studied using the panels in conjunction with sacrificial cladding or ballistic resistant panels.
2. This study showed that the panels exhibited a difference in strain-rate sensitivity with different temperatures. A more in-depth study is required with a faster strain-rate and additional specimens in the investigated temperature range to more precisely quantify the relationship between strain rate and temperature effects on the panels. This could then be used for design purposes using the correct DIF for the specific panels.
3. Both dynamic and quasi-static apparatus could be modified in order to record the behaviour of the panels at larger mid-span displacements. The potential catenary action of these panels when appropriately anchored should be investigated.
4. Finally, a more detailed SDOF model using more complex methods to predict the behaviour of the panels should be investigated, e.g. a variable coefficients method, may generate more accurate results for these types of materials with brittle failure behaviour. An FEA using explicit analysis may be a suitable technique for predicting the overall behaviour of the panels when subjected to an impulsive load.



## **APPENDICES**

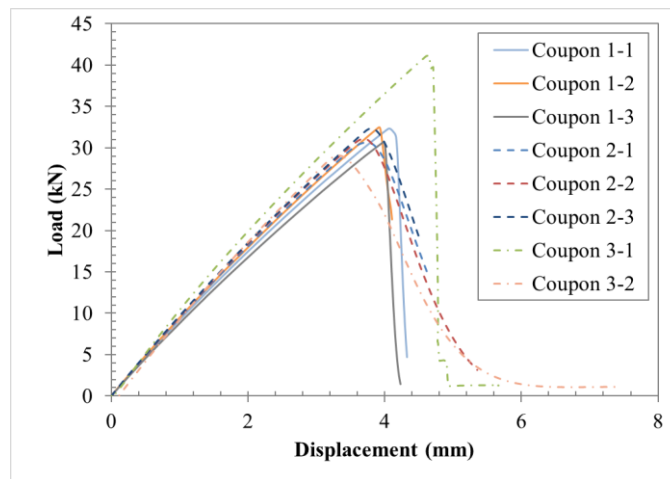
**Appendix A**  
**Coupon Experimental Tension Testing**

**Stress-Strain Relationship for All Tested Coupons\*:**

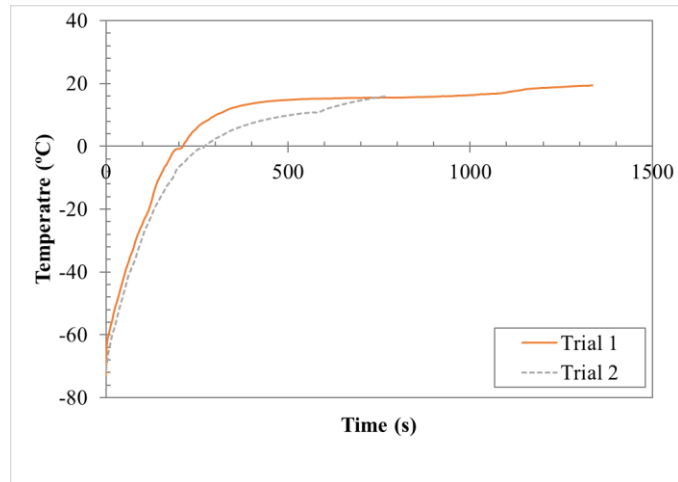


\*The longitudinal strain gauge was faulty for Coupon 3-1. Therefore, the stress strain relationship for this test was not possible to evaluate.

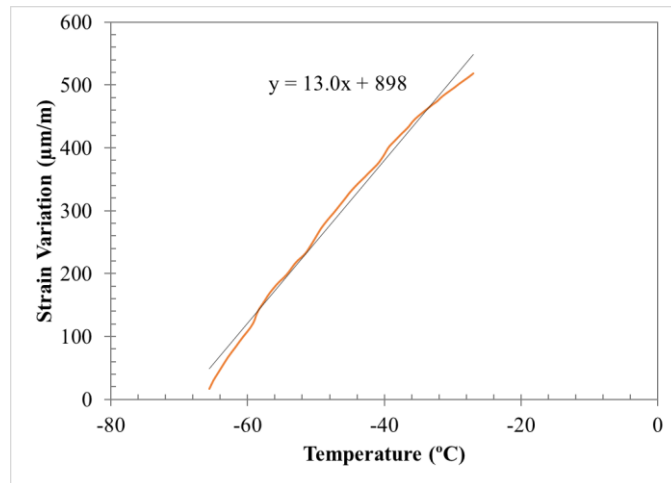
**Load-Displacement Relationship for All Tested Coupons:**



**Coupons' Temperature Variation When Taken Out of the Freezer (-80 °C to 20 °C):**



**Apparent Strain Calibration Curve for Cold Coupons:**



This calibration curve was used in order to account for apparent strain due to temperature change during the tensile tests. Cold temperature coupons were taken out of the freezer and directly to the MTS machine for tensile tests, which was at room temperature. The coupons' temperature variation was significantly higher than full-size panels when taken out of the freezer, seen in Chapter 3.

Tensile Coupon Data Analysis:

Coupon Serials 1: Head Speed of 2mm/min (Room Temperature)

Coupon 1-1:

$$A := 79.0951 \text{ mm}^2$$

$$N_{max} := 32.353 \text{ kN}$$

$$\sigma_{max} := \frac{N_{max}}{A} = 409 \text{ MPa}$$

$$E := \frac{(341.2814 \text{ MPa} - 100.9885 \text{ MPa})}{(0.01785579 - 0.005311384)} = 19155 \text{ MPa}$$

Coupon 1-2:

$$A := 89.06061 \text{ mm}^2$$

$$N_{max} := 32.499 \text{ kN}$$

$$\sigma_{max} := \frac{N_{max}}{A} = 365 \text{ MPa}$$

$$E := \frac{(268.2542 \text{ MPa} - 62.85221 \text{ MPa})}{(0.01493207 - 0.003951117)} = 18705 \text{ MPa}$$

Coupon 1-1:

$$A := 80.938 \text{ mm}^2$$

$$N_{max} := 30.718 \text{ kN}$$

$$\sigma_{max} := \frac{N_{max}}{A} = 380 \text{ MPa}$$

$$E := \frac{(280.2774 \text{ MPa} - 100.2777 \text{ MPa})}{(0.01560607 - 0.005631259)} = 18045 \text{ MPa}$$

Average Values:

$$N_{max} := \frac{30.718 \text{ kN} + 32.499 \text{ kN} + 32.353 \text{ kN}}{3} = 31.9 \text{ kN}$$

$$\sigma_{max} := \frac{409 \text{ MPa} + 365 \text{ MPa} + 380 \text{ MPa}}{3} = 385 \text{ MPa}$$

$$E := \frac{19155.383 \text{ MPa} + 18705.297 \text{ MPa} + 18045.425 \text{ MPa}}{3} = 18635.368 \text{ MPa}$$

Coupon Serials 2: Head Speed of 20mm/min (Room Temperature)

Coupon 2-1:

$$A := 81.7668 \text{ mm}^2$$

$$N_{max} := 30.596 \text{ kN}$$

$$\sigma_{max} := \frac{N_{max}}{A} = 374 \text{ MPa}$$

$$E := \frac{(292.6259 \text{ MPa} - 52.13394 \text{ MPa})}{(0.01804821 - 0.005982134)} = 19931 \text{ MPa}$$

Coupon 2-2:

$$A := 84.34283 \text{ mm}^2$$

$$N_{max} := 31.090 \text{ kN}$$

$$\sigma_{max} := \frac{N_{max}}{A} = 369 \text{ MPa}$$

$$E := \frac{(194.3125 \text{ MPa} - 59.03485 \text{ MPa})}{(0.01464207 - 0.007814892)} = 19815 \text{ MPa}$$

Coupon 2-3:

$$A := 86.03303 \text{ mm}^2$$

$$N_{max} := 32.372 \text{ kN}$$

$$\sigma_{max} := \frac{N_{max}}{A} = 376 \text{ MPa}$$

$$E := \frac{(195.7407 \text{ MPa} - 60.98373 \text{ MPa})}{(0.01519994 - 0.008036375)} = 18811 \text{ MPa}$$

Average Values:

$$N_{max} := \frac{30.596 \text{ kN} + 31.090 \text{ kN} + 32.372 \text{ kN}}{3} = 31.4 \text{ kN}$$

$$\sigma_{max} := \frac{374 \text{ MPa} + 369 \text{ MPa} + 376 \text{ MPa}}{3} = 373 \text{ MPa}$$

$$E := \frac{19931 \text{ MPa} + 19815 \text{ MPa} + 18811 \text{ MPa}}{3} = 19519 \text{ MPa}$$



Coupon 3-1: Head Speed of 20mm/min (Cold Temperature)

Temperature: -40 to 30 C during test

$$A := 99.7 \text{ mm}^2$$

$$N_{max} := 41.2 \text{ kN}$$

$$\sigma_{max} := \frac{N_{max}}{A} = 413 \text{ MPa}$$

E: Longitudinal strain gauge failed to measure data.

Coupon 3-2: Head Speed of 20mm/min (Cold Temperature)

Temperature: -40 to 30 C during test

$$A := 87.256 \text{ mm}^2$$

$$N_{max} := 29.108 \text{ kN}$$

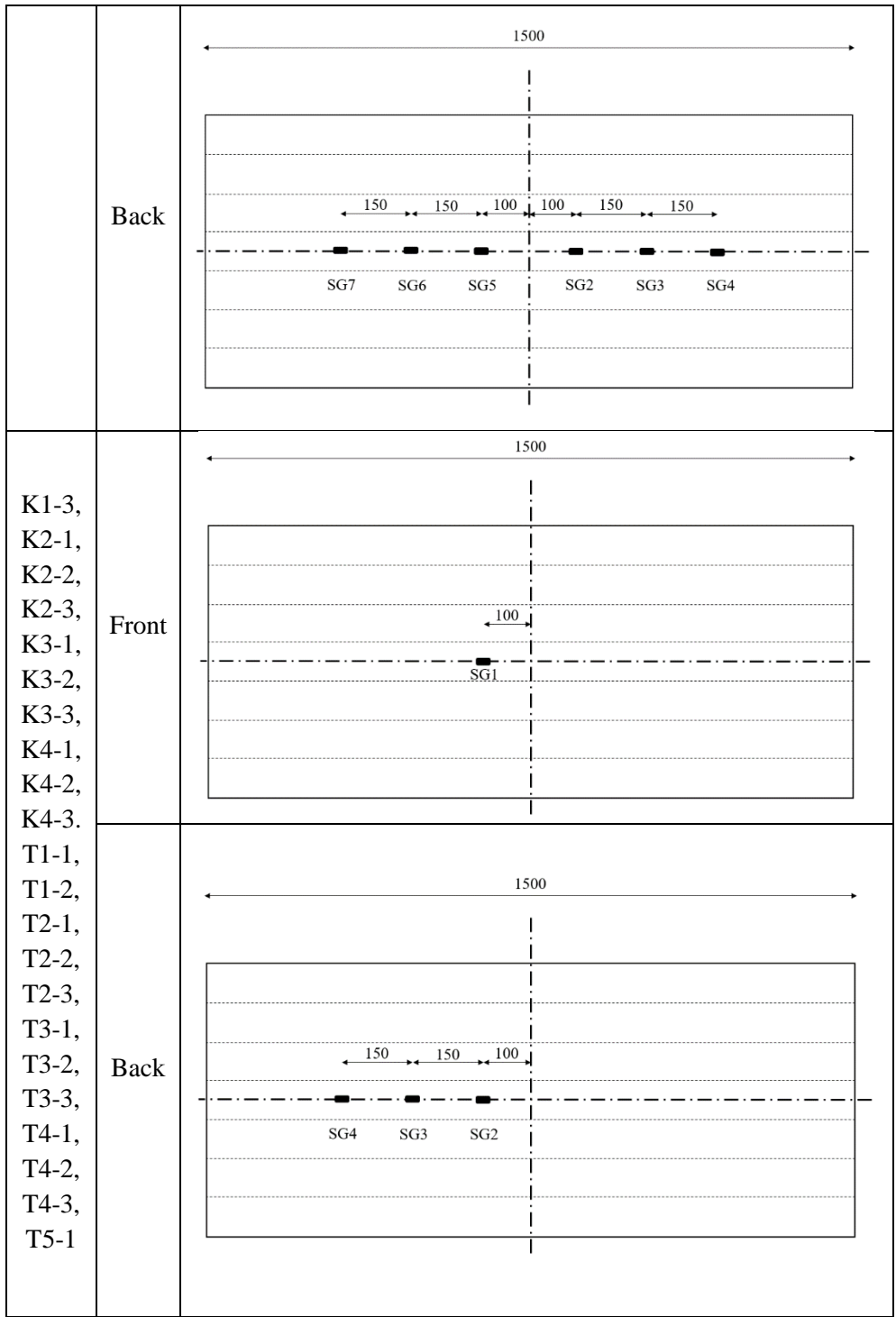
$$\sigma_{max} := \frac{N_{max}}{A} = 333.593 \text{ MPa}$$

$$E := \frac{(240.2958 \text{ MPa} - 71.71934 \text{ MPa})}{(0.008591138 - 0.00453115)} = 41521.418 \text{ MPa}$$

The calculated values of Coupon 2 series will be used in this thesis for the modulus and ultimate tensile strength. The reason why Coupon 1 series is disregarded is because a head speed of 2 mm/min was used. Coupon 2 had the same head velocity as the 3-point flexural tests on full-size panels: 20 mm/min. The data gathered with Coupon 3 series was not sufficiently reliable to make accurate conclusions. However, even though the longitudinal strain gauge failed for Coupon 3-1, observations from Coupon 3-2 shows a potentially higher modulus for cold temperature. More tests would need to be done in order to verify these observations.

**Appendix B**  
**Testing Schedule and Strain Gauge Layout**

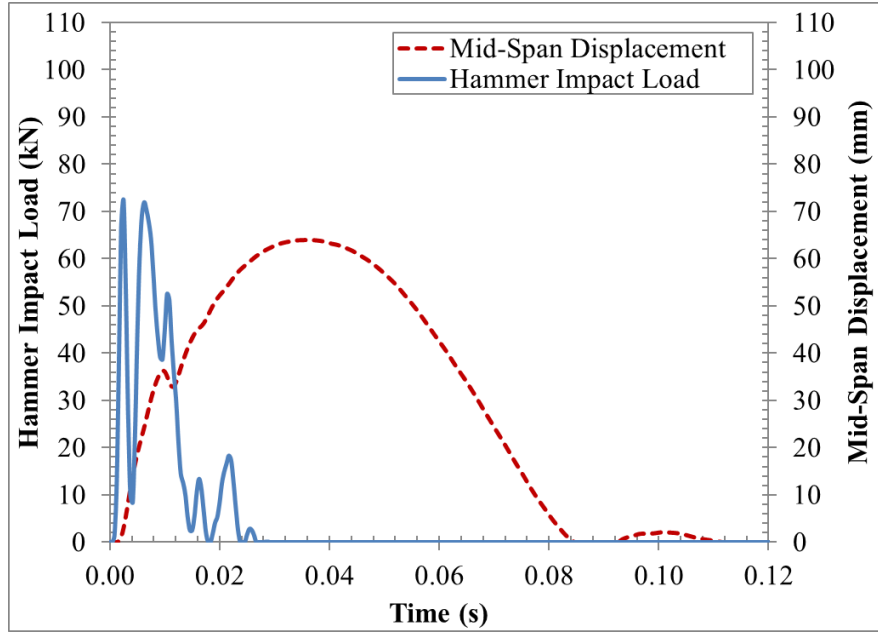
Series	Strain Gauges Lay-Out	
K1-1	Front	
	Back	
K1-2	Front	



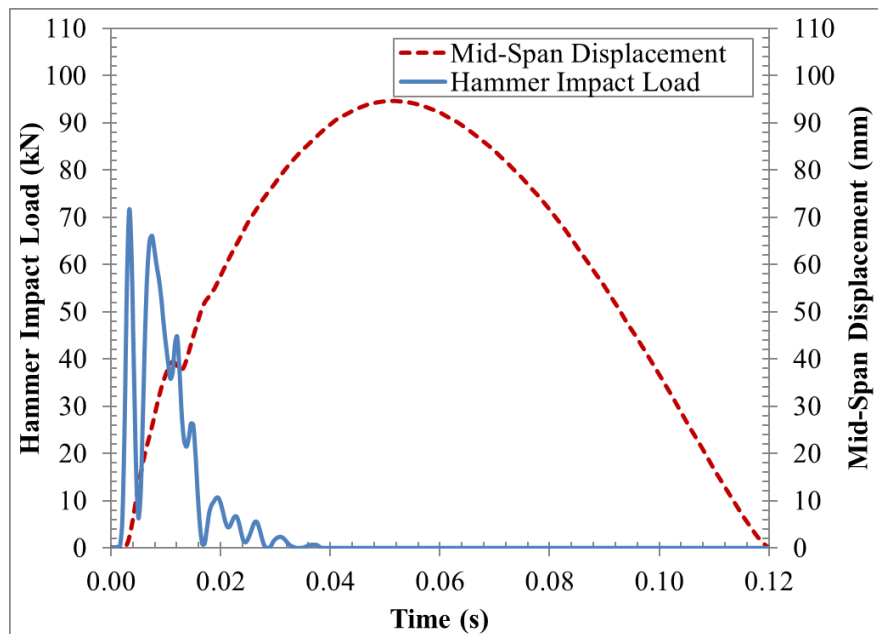
Series	Impact Hammer Drop Height	
K1-1, K1-2, K1-3	<b>1</b>	
K2-1, K2-2, K2-3	<b>2</b>	
K3-1, K3-2, K3-3	<b>3</b>	
K4-1, K4-2, K4-3	<b>4</b>	
T1-1, T1-2	<b>1</b>	
T2-1, T2-2, T2-3	<b>2</b>	
T3-1, T3-2, T3-3	<b>3</b>	
T4-1, T4-2, T4-3	<b>4</b>	
T5-1	<b>5</b>	
Notes: -All measurements are in mm.		

**Appendix C**  
**Hammer Impact Load and Panels Mid-Span Displacement-  
Time Histories**

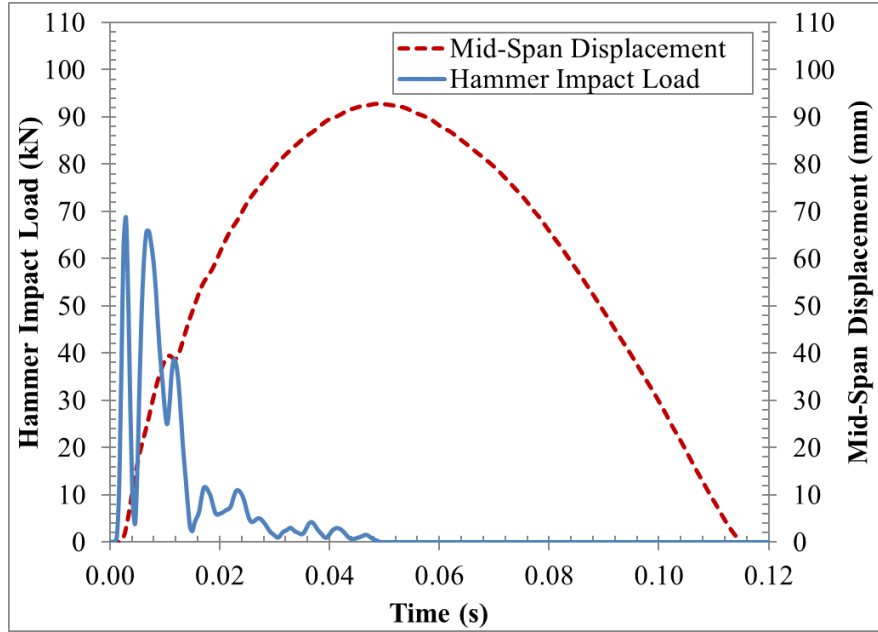
**Panel K1-1:**



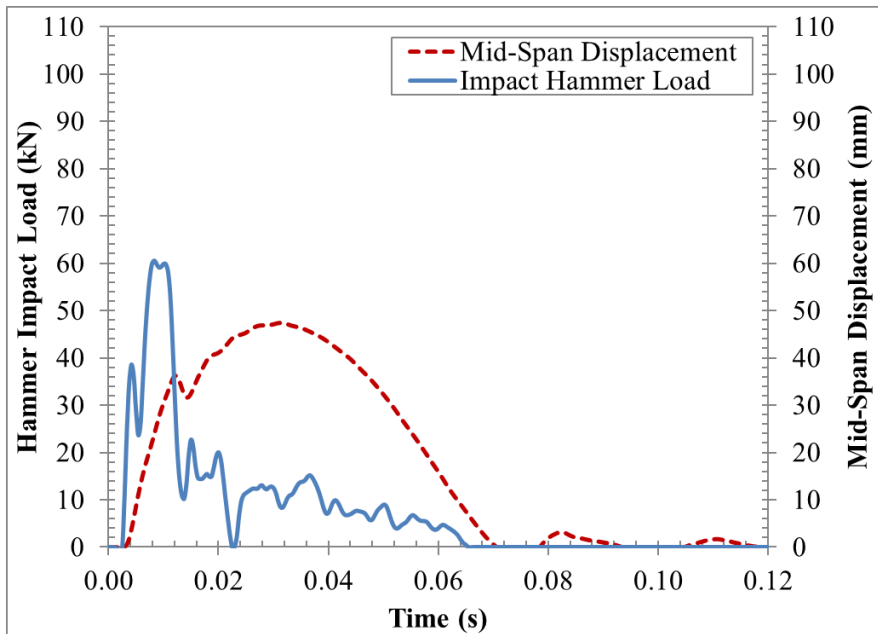
**Panel K1-2:**



**Panel K1-3:**

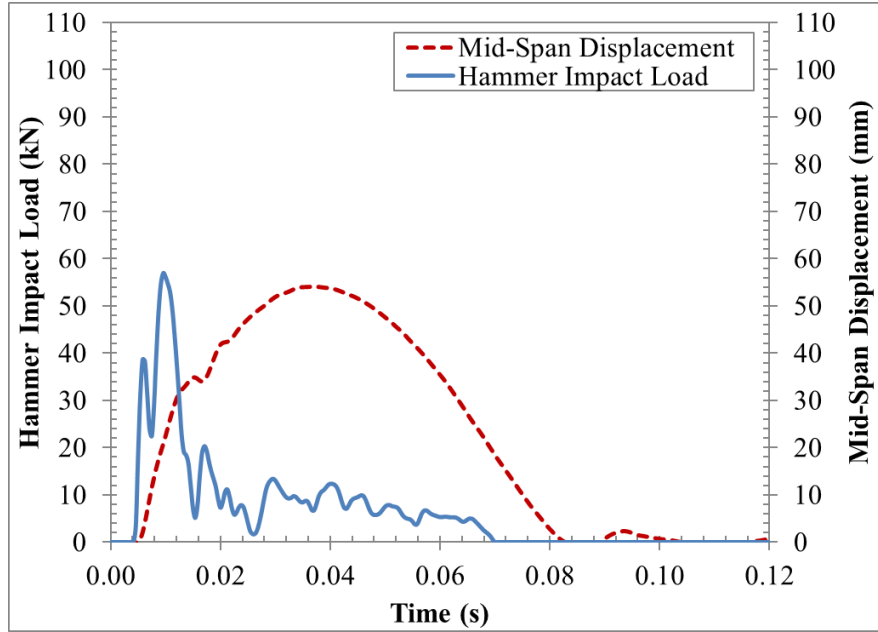


**Panel K2-1:**

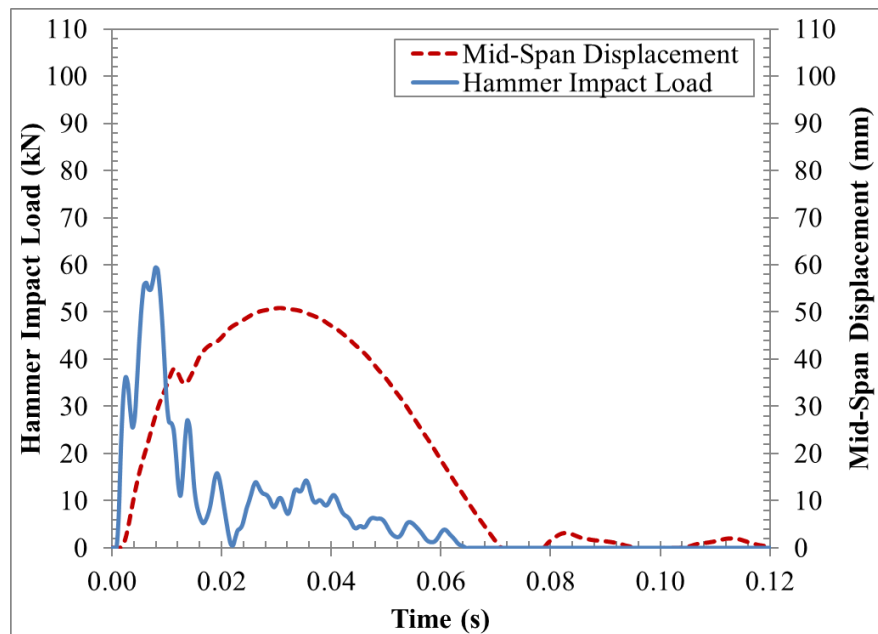




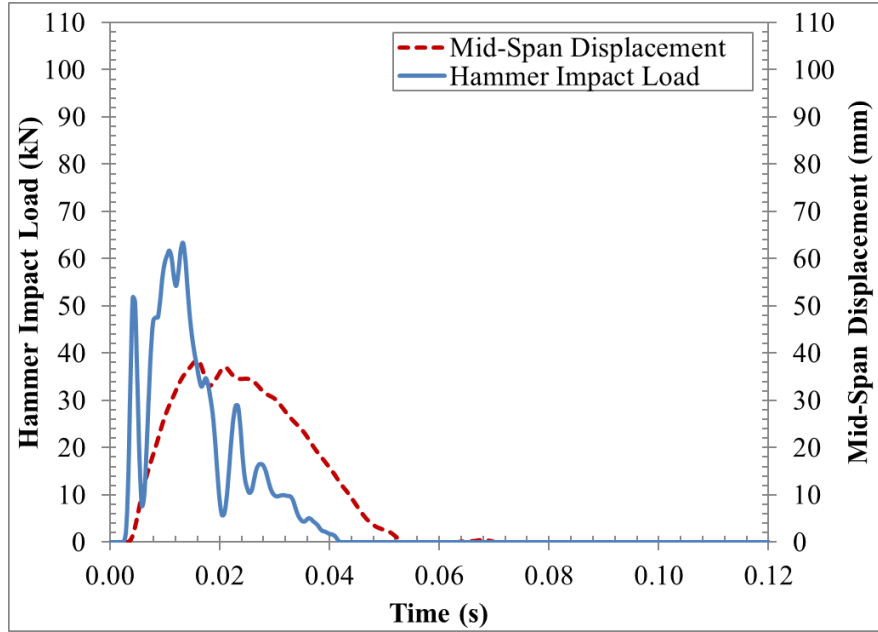
**Panel K2-2:**



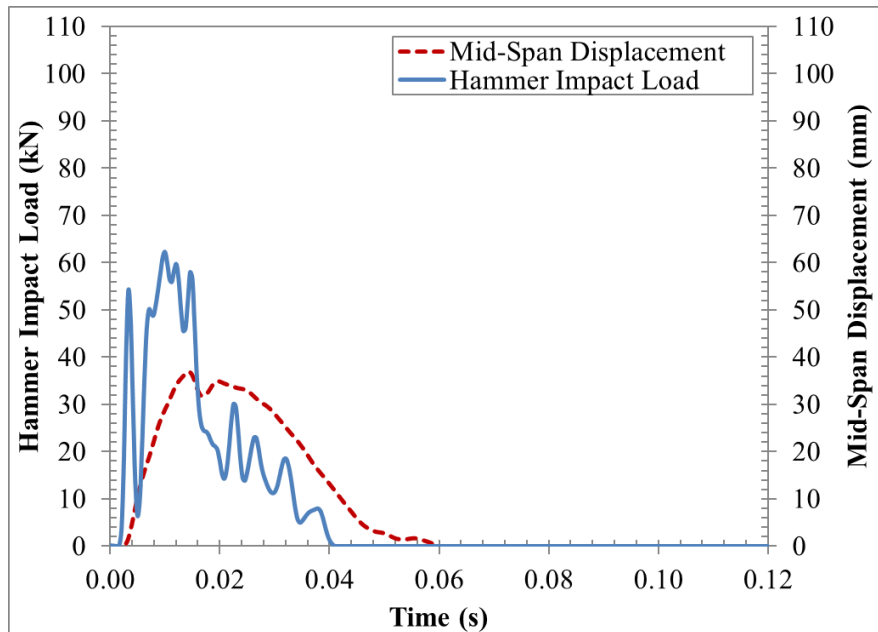
**Panel K2-3:**



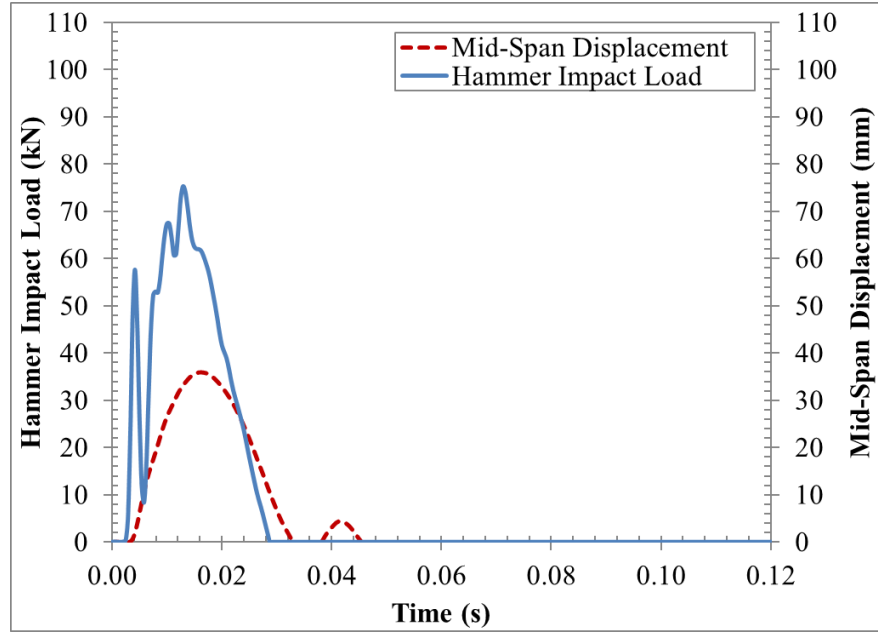
**Panel K3-1:**



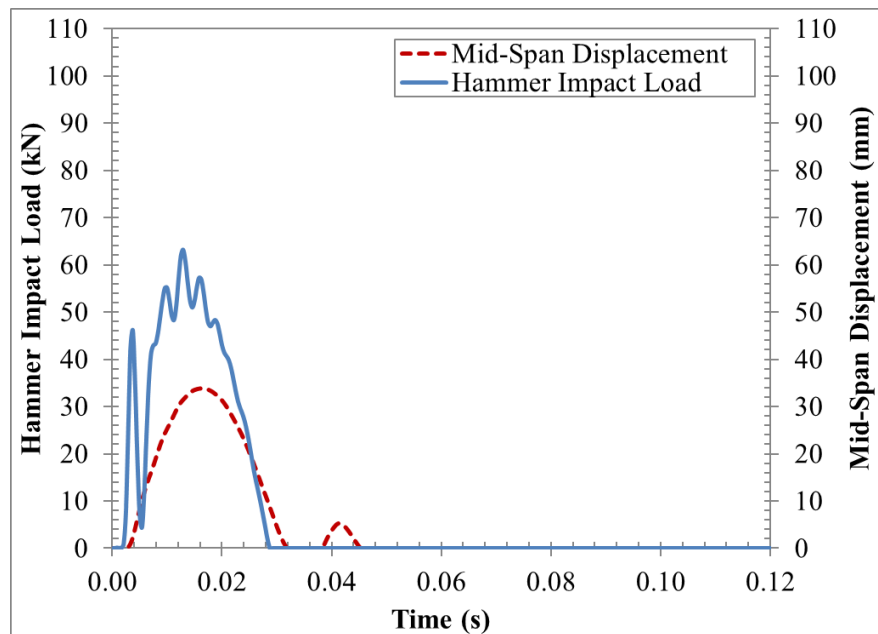
**Panel K3-2:**



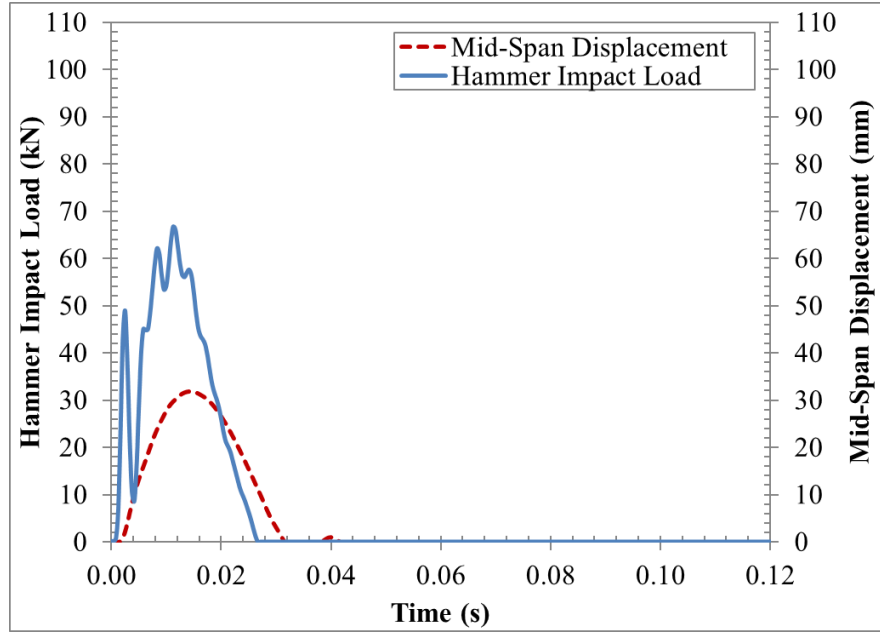
**Panel K3-3:**



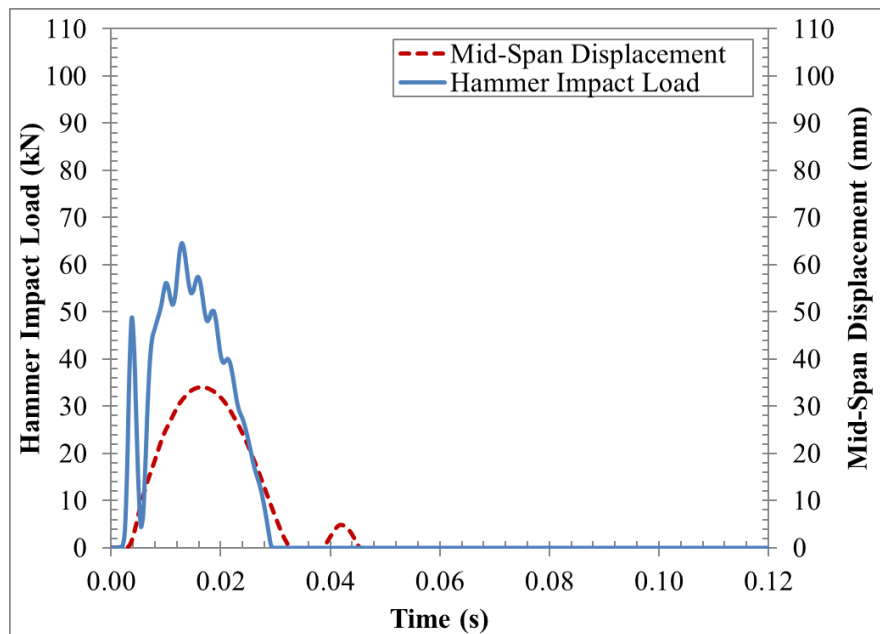
**Panel K4-1:**



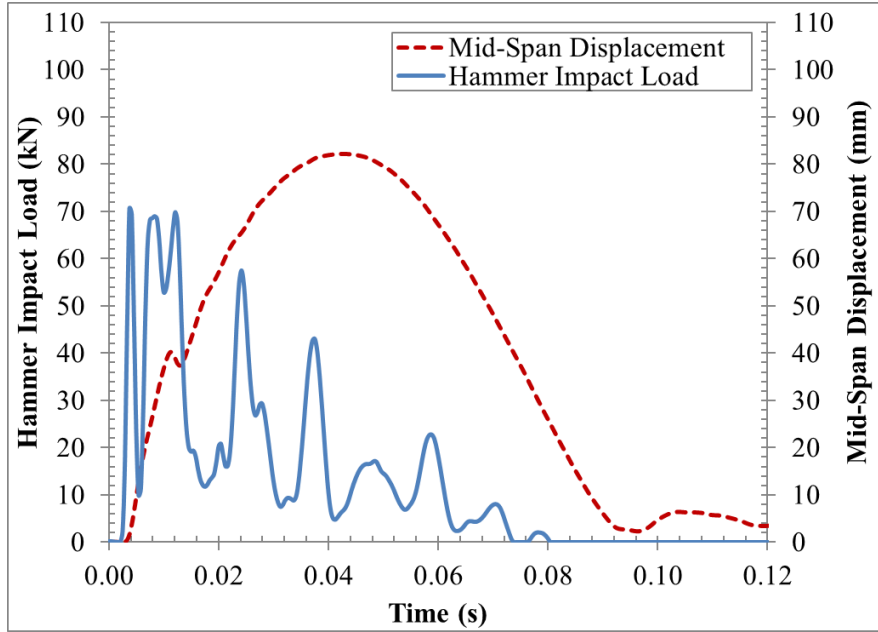
**Panel K4-2:**



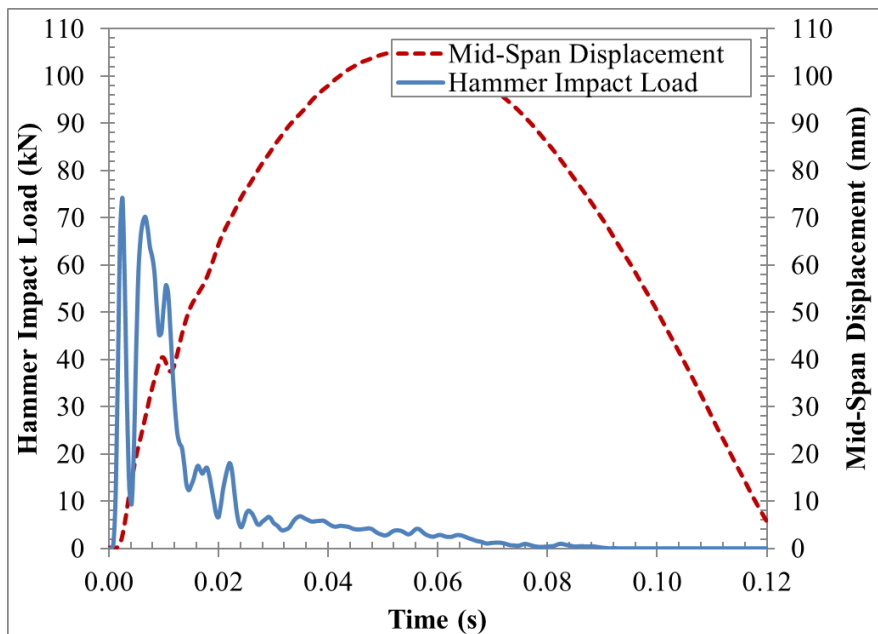
**Panel K4-3:**



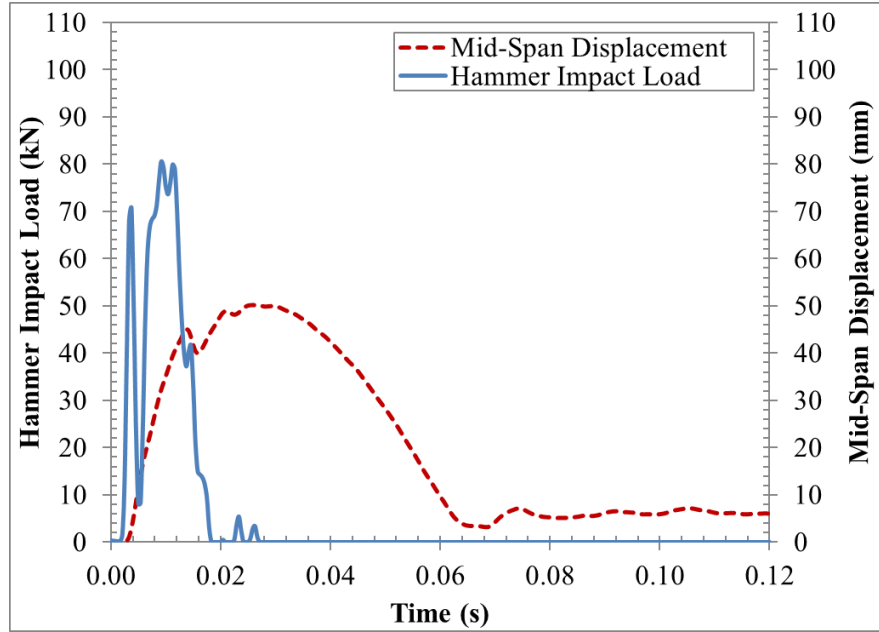
**Panel T1-1:**



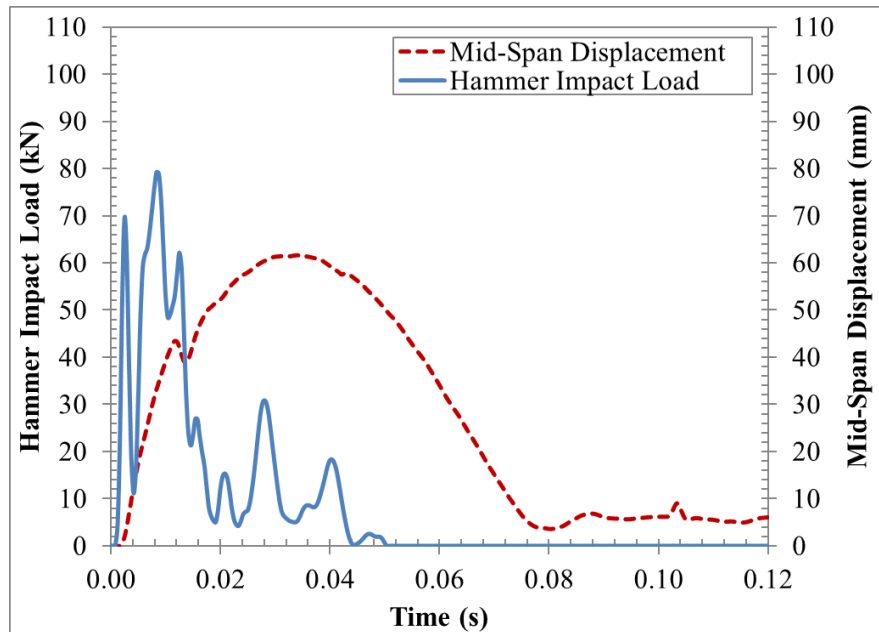
**Panel T1-2:**



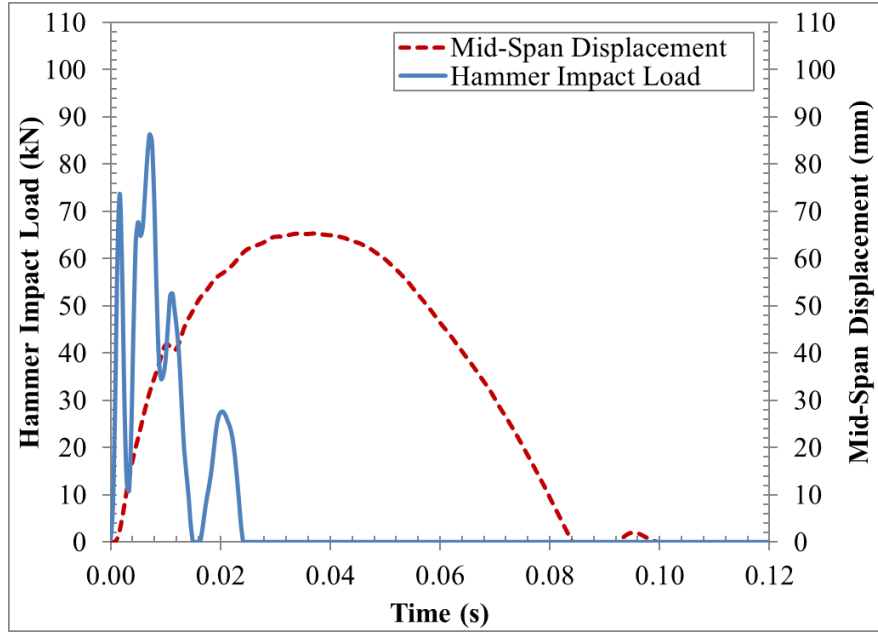
**Panel T2-1:**



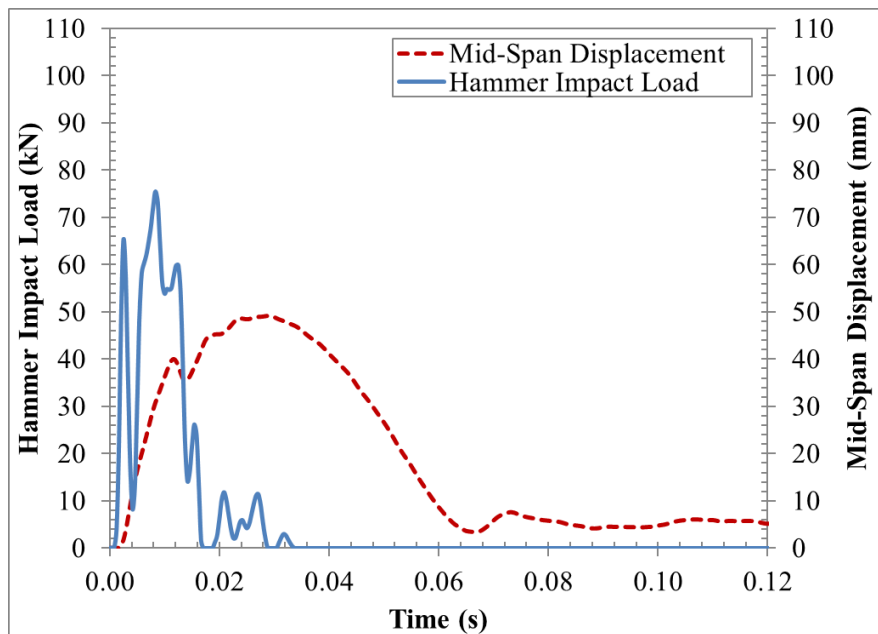
**Panel T2-2:**



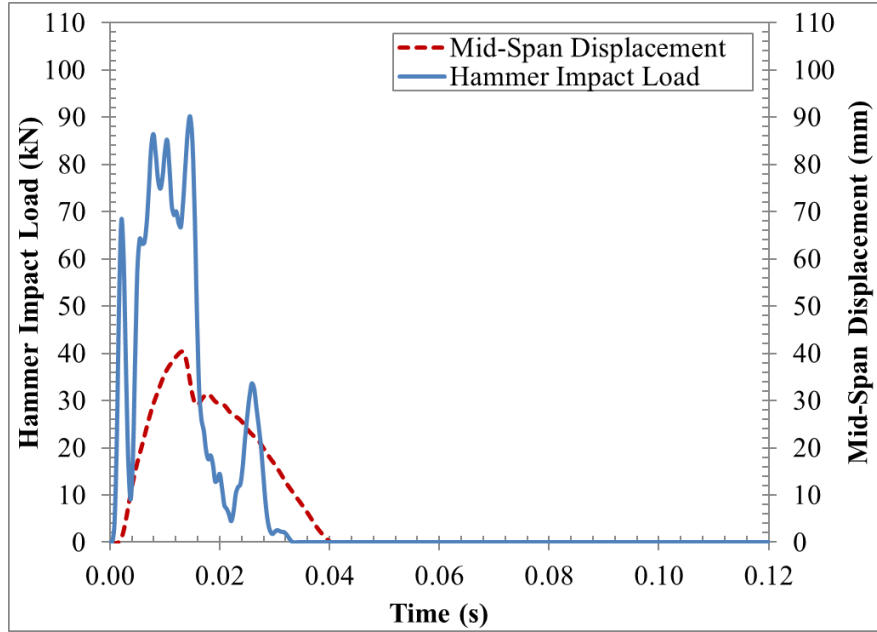
**Panel T2-3:**



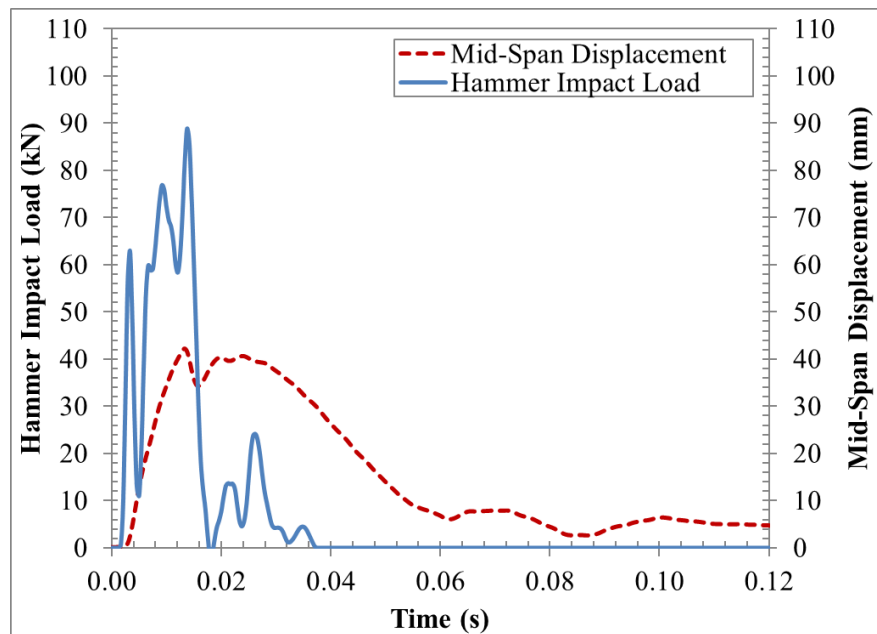
**Panel T3-1:**



**Panel T3-2:**

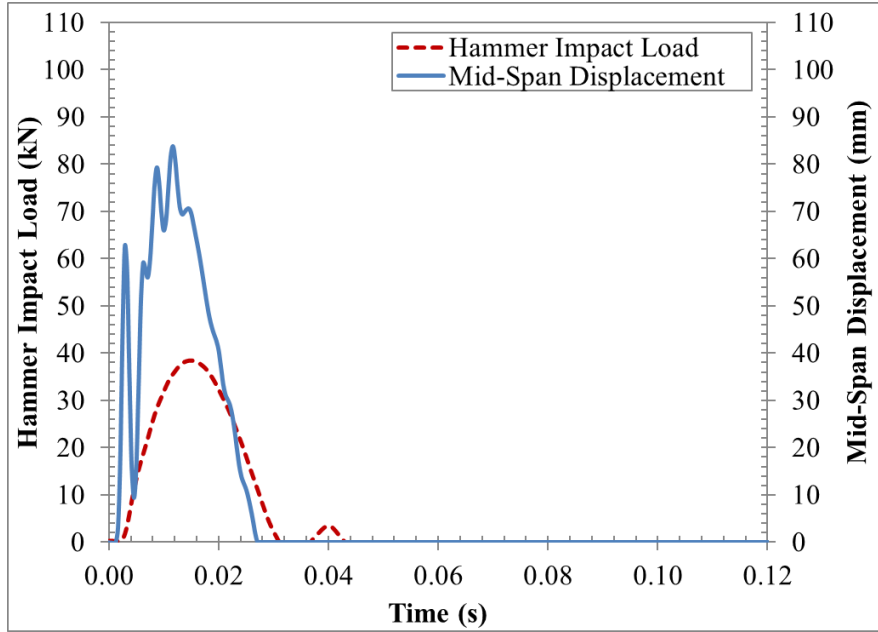


**Panel T3-3:**

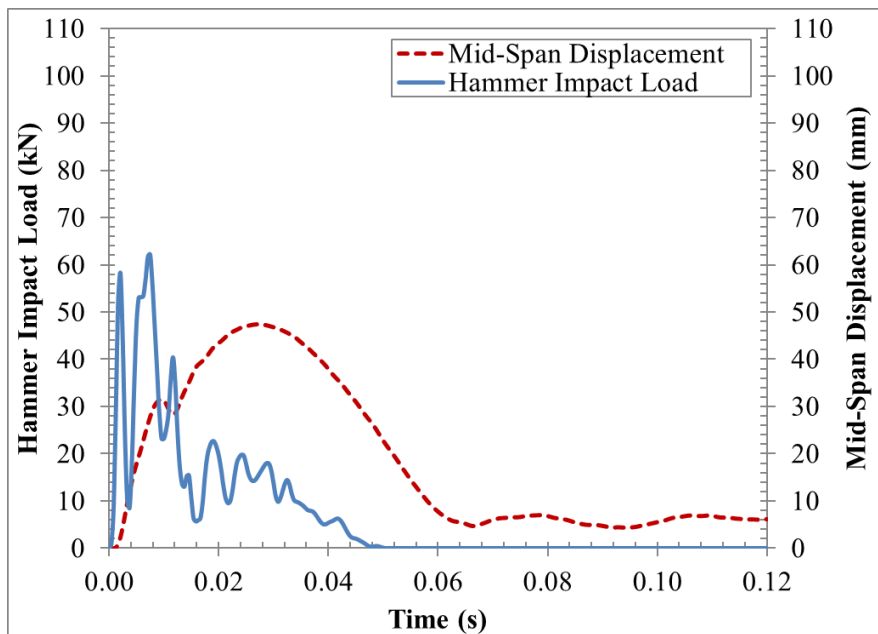




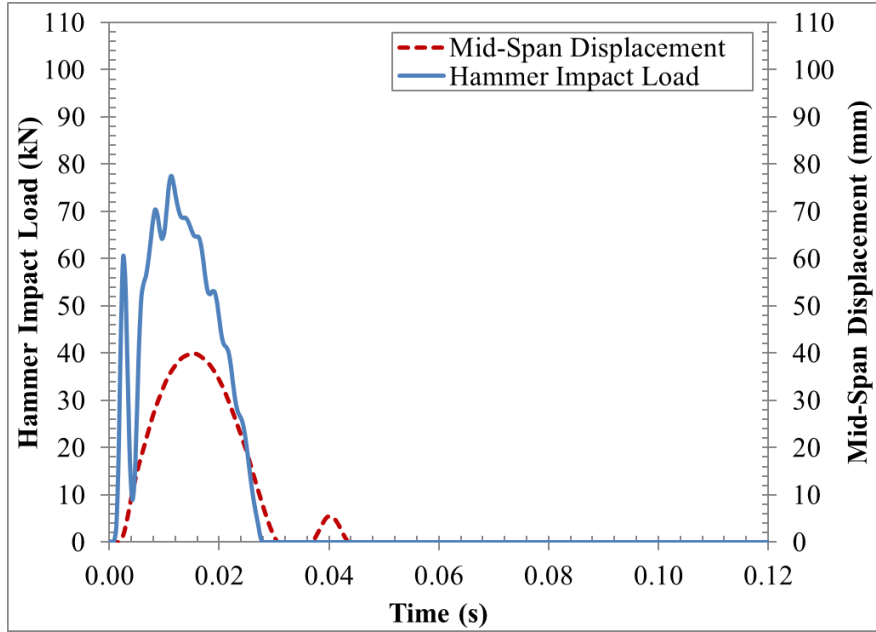
**Panel T4-1:**



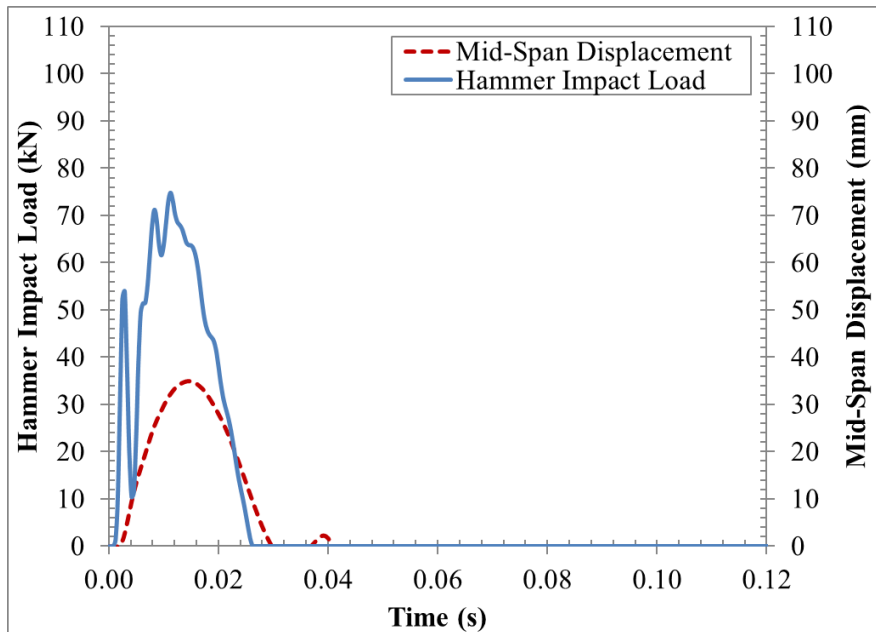
**Panel T4-2:**



**Panel T4-3:**

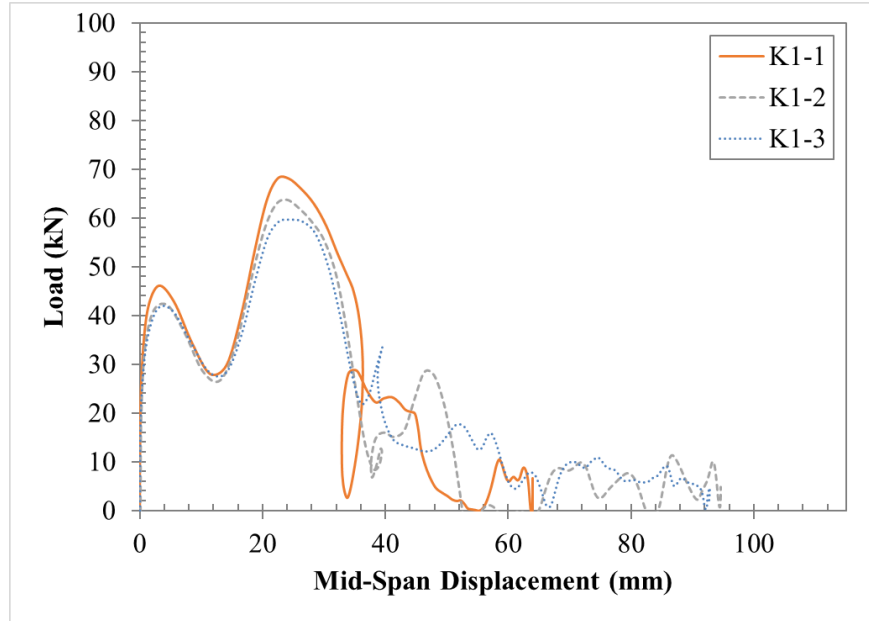


**Panel T5-1:**

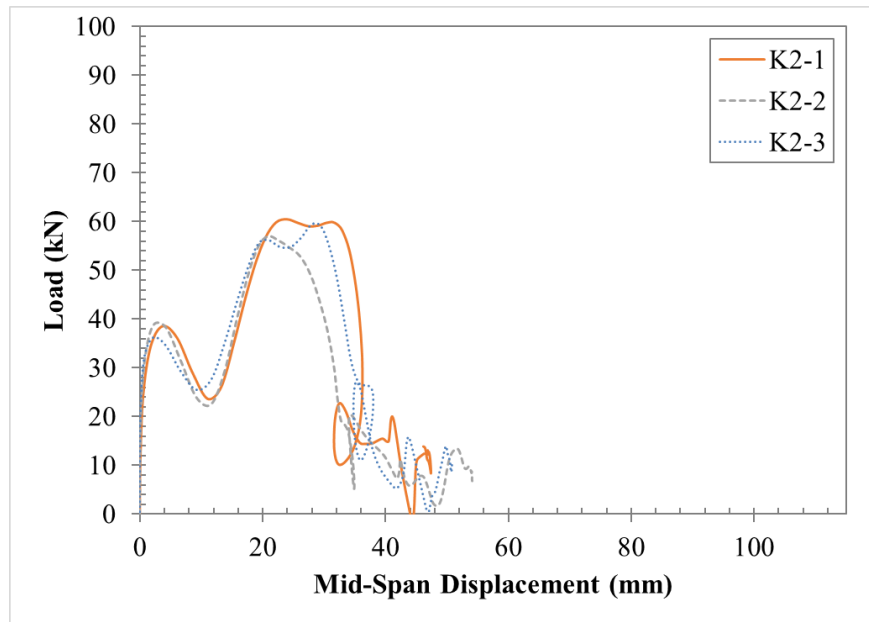


**Appendix D**  
**Load-Displacement Histories Using the Reaction Force Ring**

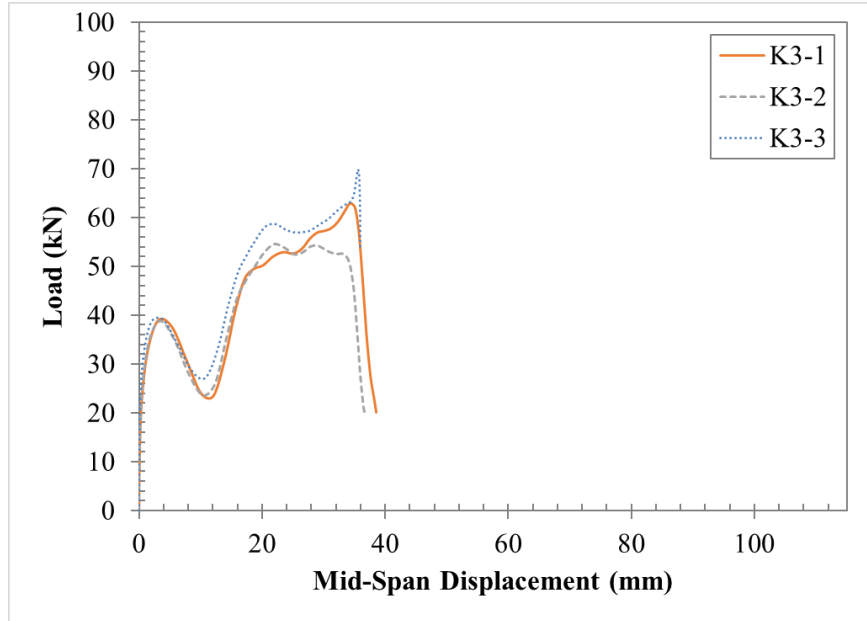
**Panels K1:**



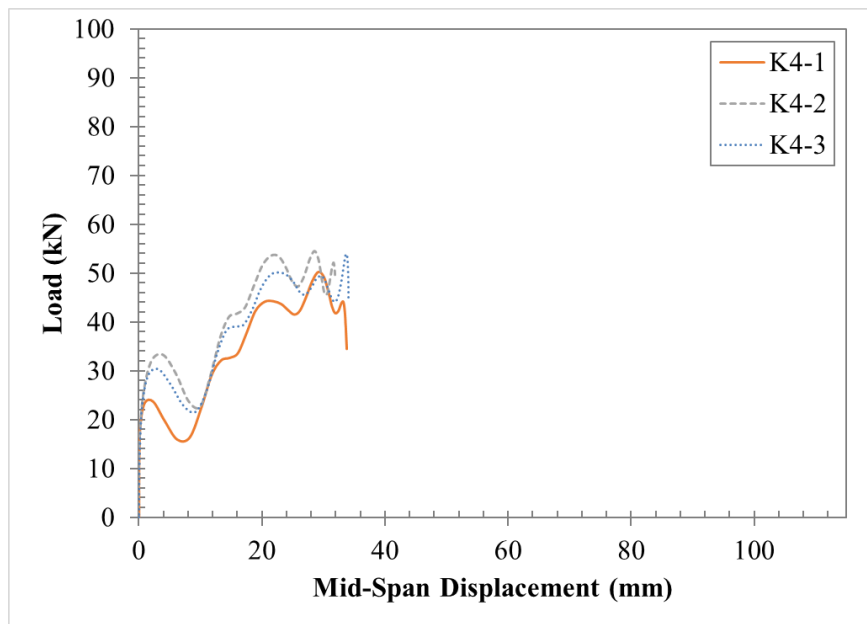
**Panels K2:**



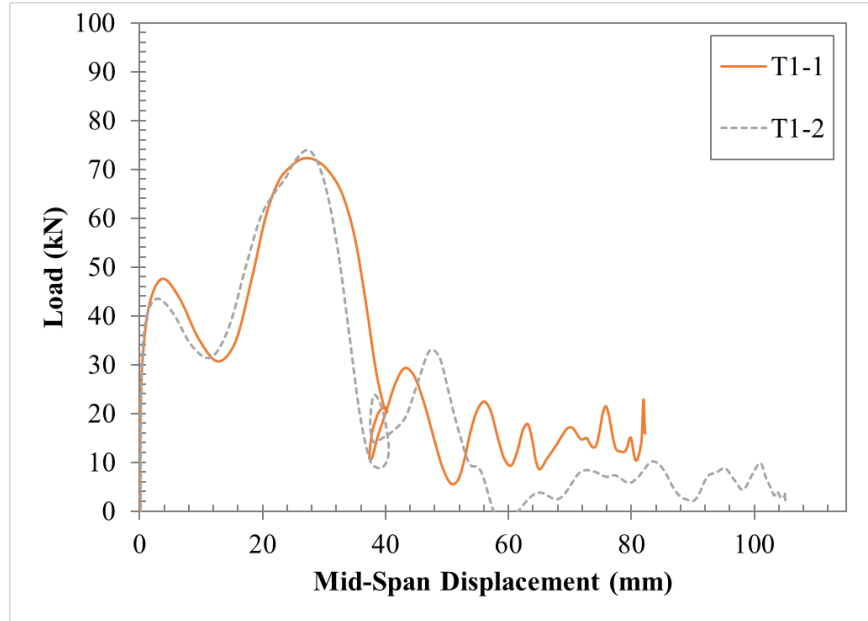
**Panels K3:**



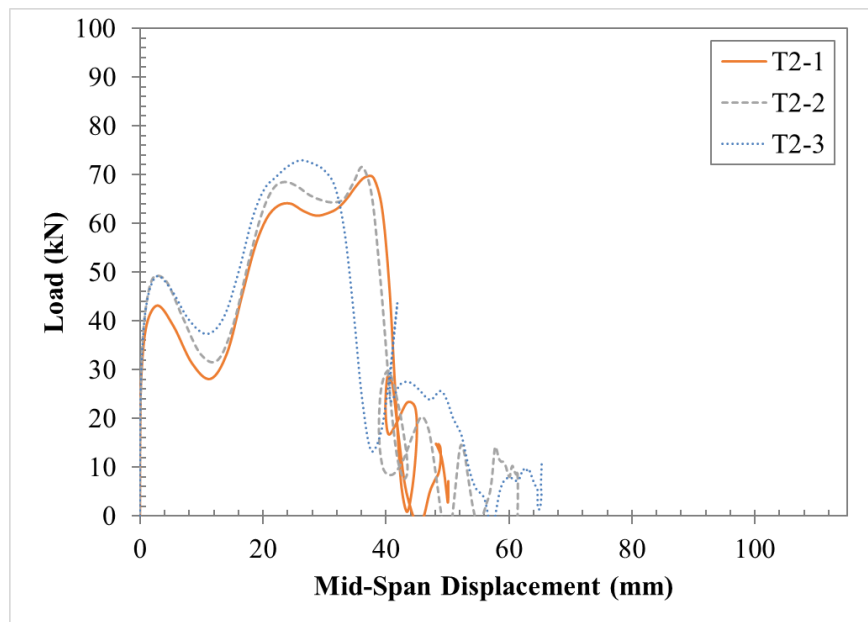
**Panels K4:**



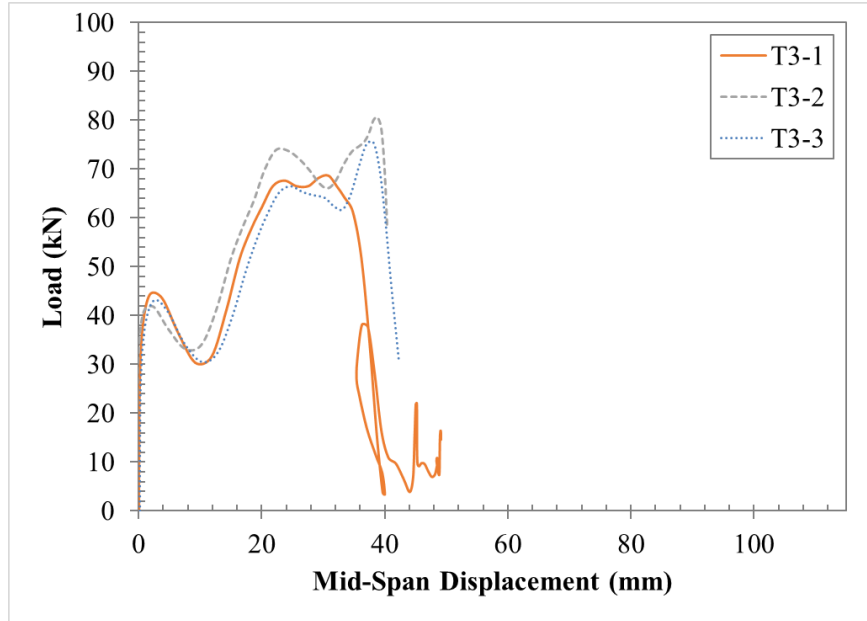
**Panels T1:**



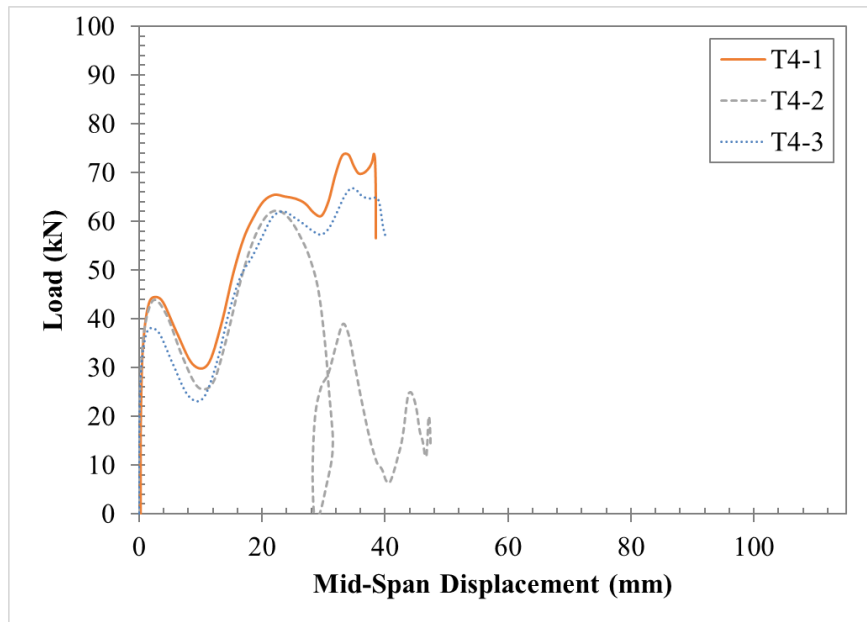
**Panels T2:**



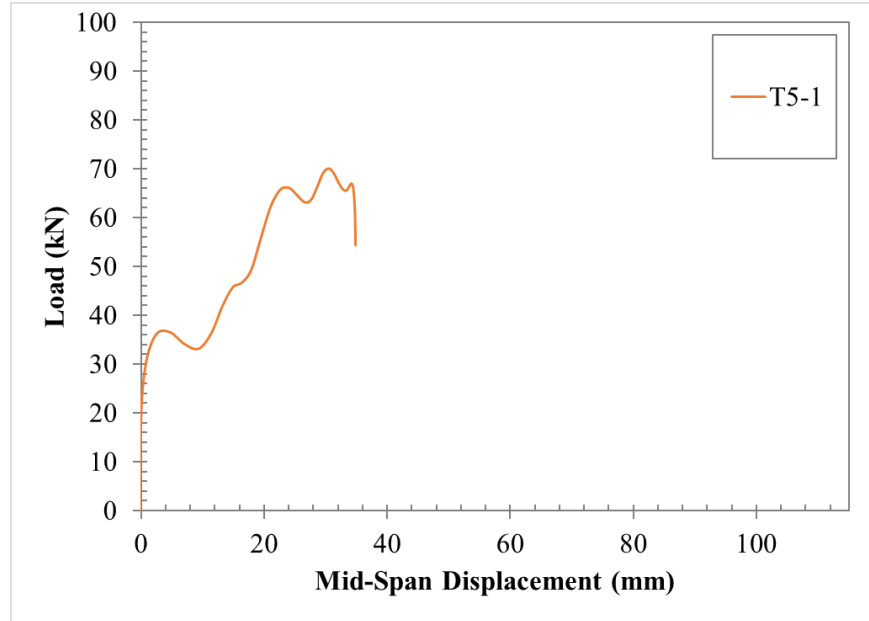
**Panels T3:**



**Panels T4:**



**Panel T5:**





**Appendix E**  
**Energy Sample Calculations**

**Sample Calculations for K1-1:**

Kinetic Energy Lost by the Hammer:

$KE_h$  = Hammer's lost kinetic energy

$P_t$  = Hammer tup load

$I$  = Impulse

$a_h$  = Hammer's acceleration

$m_h$  = Total mass of the hammer

$h$  = Hammer drop height

$t$  = Time

$$a_h := 9.81 \frac{m}{s^2}$$

$$m_h := 136.27 \text{ kg}$$

$$h := 1970 \text{ mm}$$

$$I(t_i) = \int P_t(t) dt = (I(t_{i-1})) + \frac{P_t(t_{i-1}) + P_t(t_i)}{2} \cdot ((t_i) - (t_{i-1}))$$

$$KE_h(t_i) := \frac{1}{2} \cdot m_h \cdot \left[ 2 \cdot a_h \cdot h - \left( \sqrt{2 \cdot a_h \cdot h} - \frac{1}{m_h} \cdot I(t_i) \right)^2 \right]$$

$t$ (s)	$P_t$ (N)	$I$ (N·s)	$KE_h$ (J)
0	0	0	0
0.00042	1064	0.222	1.378
0.00083	11373	2.813	17.458
0.00125	36713	12.831	79.166
0.00167	63272	33.661	205.116
0.00208	68670	61.149	366.447
0.00250	51341	86.152	508.373
0.00292	26646	102.399	598.143
0.00333	797	109.612	637.375
.	.	.	.
0.0475	264	619.334	2441.792

At maximum panel displacement

Strain energy absorbed by the panel:

$U$  = Strain energy

$P_b$  = Panel bending load (from support force ring)

$u$  = Panel's mid-span displacement

$$U(t_i) := (U(t_{i-1})) + \frac{P_b(t_{i-1}) + P_b(t_i)}{2} \cdot (u(t_i) - u(t_{i-1}))$$

$t$ (s)	$P_b$ (N)	$u$ (m)	$U$ (J)
0	0	0	0
0.00042	44.5	0.0000259	0.00108
0.00083	8778	0.0000425	0.0741
0.00125	22692	0.000270	3.656
0.00167	34485	0.001153	28.904
0.00208	41414	0.002928	96.258
0.00250	40912	0.005421	198.871
0.00292	34595	0.008297	307.448
0.00333	28457	0.011270	401.179
.	.	.	.
0.0475	4599	0.092801	2107.563

Work done by the hammer:

$W$  = Work done by the hammer

$$W(t_i) = (W(t_{i-1})) + \frac{P_t(t_{i-1}) + P_t(t_i)}{2} \cdot (u(t_i) - u(t_{i-1}))$$

$t$ (s)	$P_t$ (N)	$u$ (m)	$W$ (J)
0	0	0	0
0.00042	1064	0.0000259	0.0138
0.00083	11373	0.0000425	0.117
0.00125	36713	0.000270	5.590
0.00167	63272	0.001153	49.740
0.00208	68670	0.002928	166.829
0.00250	51341	0.005421	316.411
0.00292	26646	0.008297	428.554
0.00333	7970	0.011270	480.022
.	.	.	.
0.0475	264	0.092801	2036.480

Panel's Kinetic Energy:

$KE_p$  = Panel's kinetic energy

$M_p$  = Panel's total mass

$K_M$  = Mass factor

$M_e$  = Equivalent mass of panel (since only one know velocity location)

$v$  = Panel's velocity

$$M_p := 15.9 \text{ kg}$$

$$K_M := 0.49$$

$$M_e := M_p \cdot K_M = 7.791 \text{ kg}$$

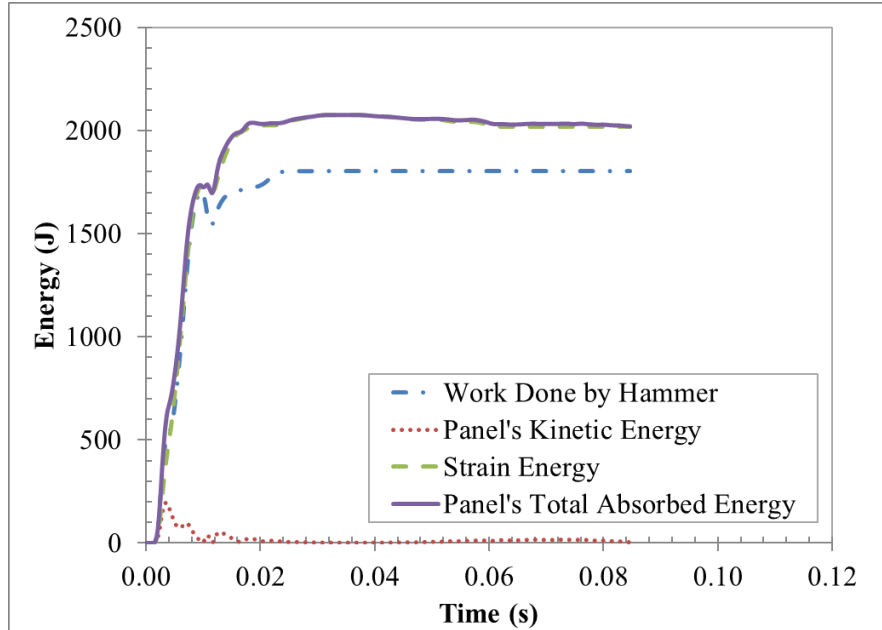
$$v(t_i) := \frac{u(t_i) - u(t_i - \Delta t)}{\Delta t}$$

$$KE_p(t_i) := \frac{M_e \cdot (v(t_i))^2}{2}$$

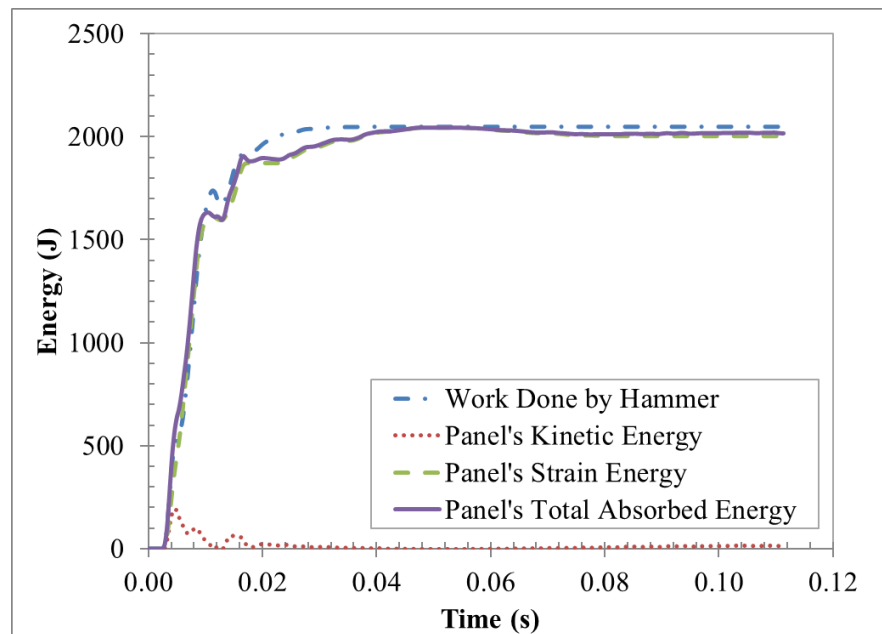
$t$	$u$	$v$	$KE_p$
(s)	(m)	$\left(\frac{m}{s}\right)$	(J)
0	0	0	0
0.00042	0.0000259	0.0623	0.0000443
0.00083	0.0000425	0.0398	0.0175
0.00125	0.000270	0.546	0.0151
0.00167	0.001153	2.120	0.00615
0.00208	0.002928	4.260	1.162
0.00250	0.005421	5.983	17.482
0.00292	0.008297	6.902	70.611
0.00333	0.011270	7.136	139.294
.	.	.	.
0.0475	0.092801	0.057	0.0126

**Appendix F**  
**Energy Conservation Graphs**

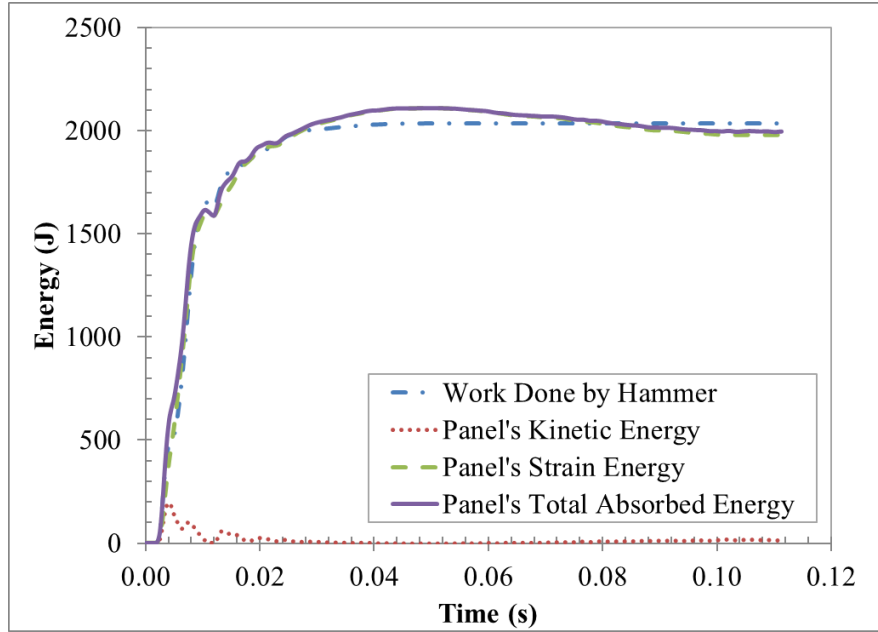
**Panel K1-1:**



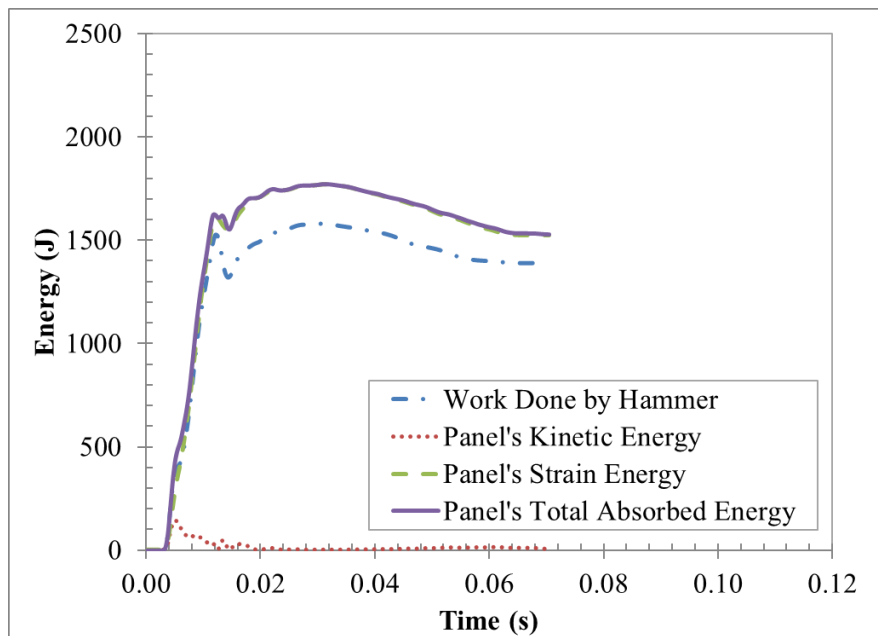
**Panel K1-2:**



**Panel K1-3:**

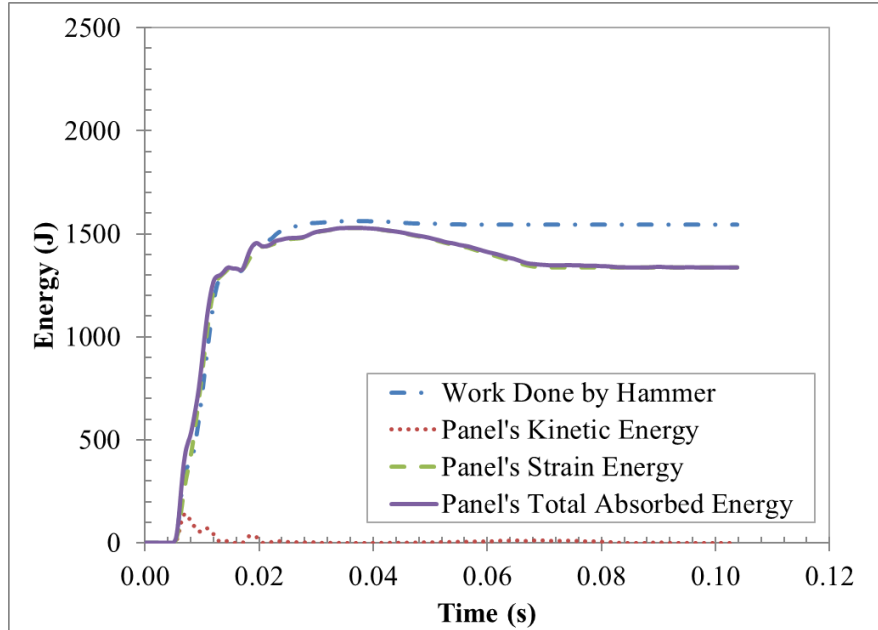


**Panel K2-1:**

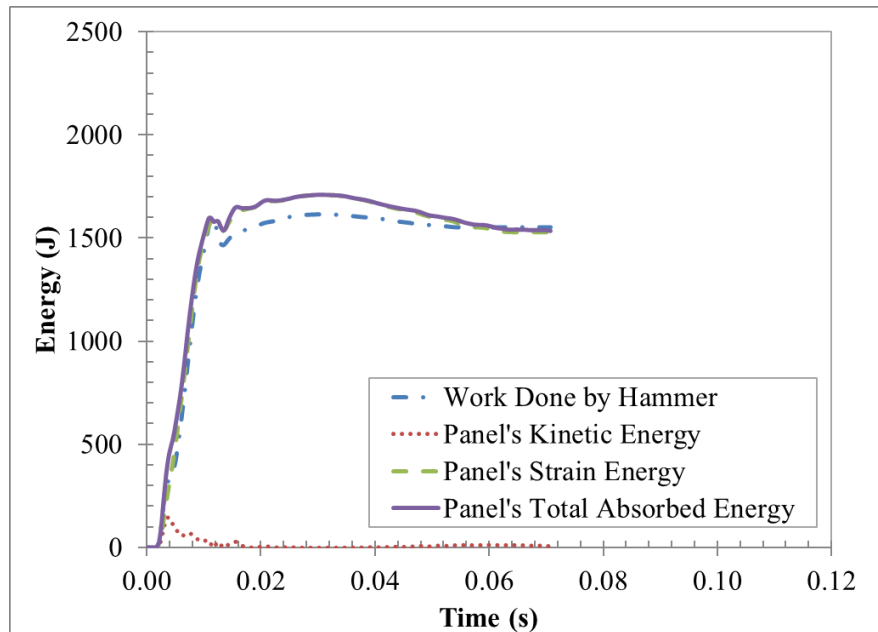




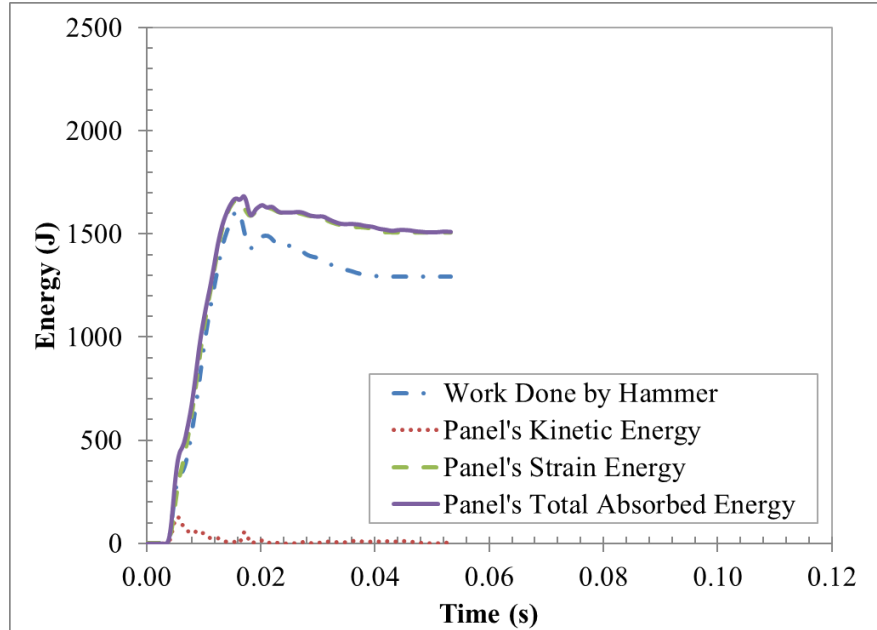
**Panel K2-2:**



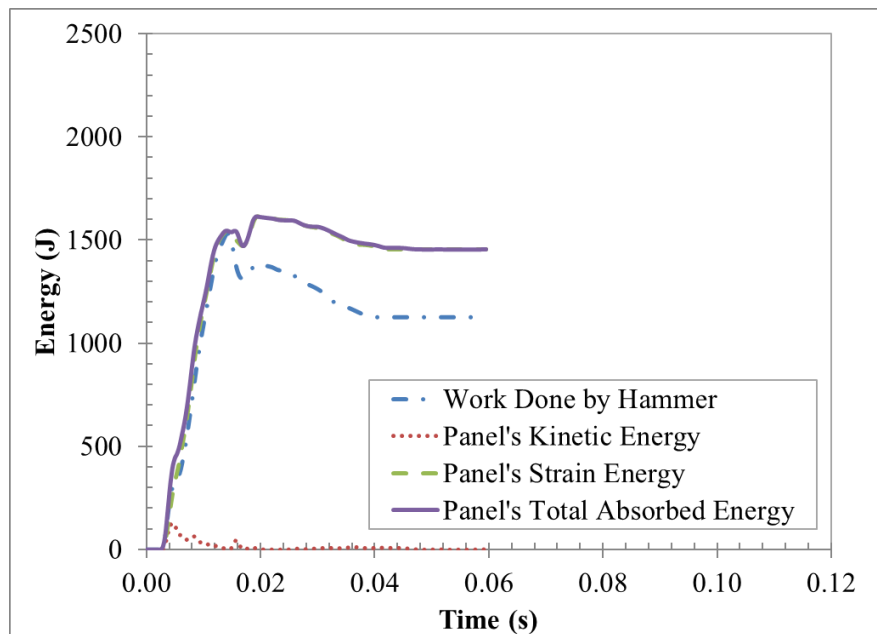
**Panel K2-3:**



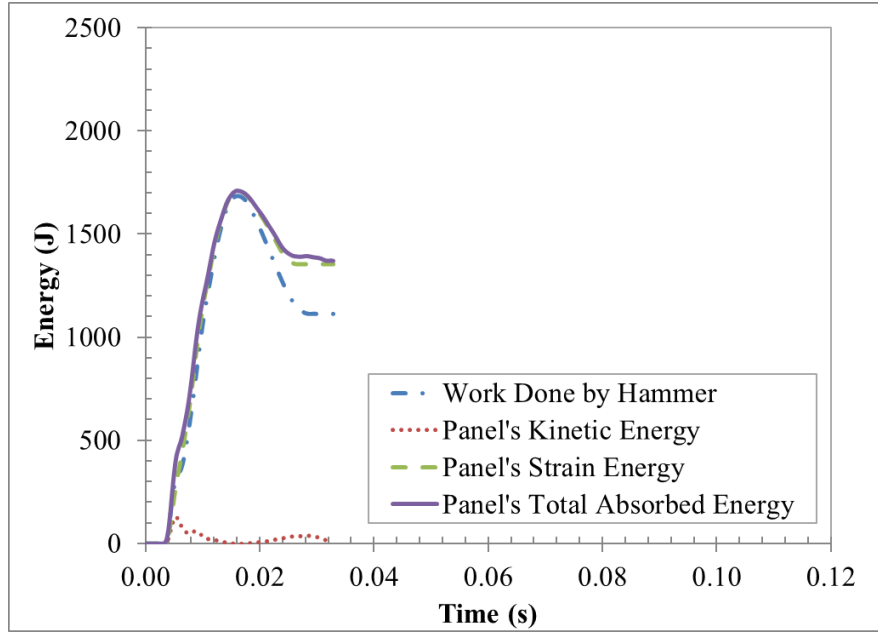
**Panel K3-1:**



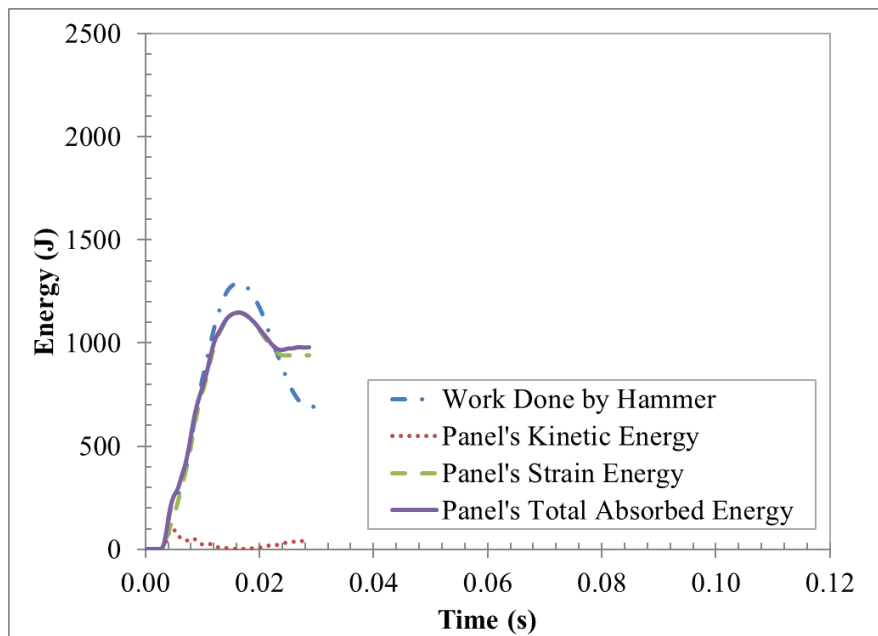
**Panel K3-2:**



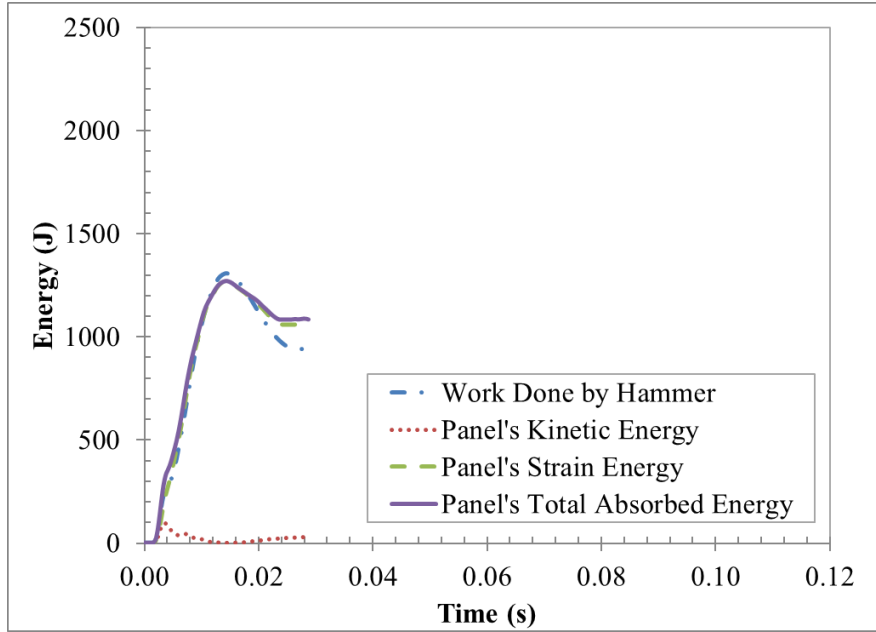
**Panel K3-3:**



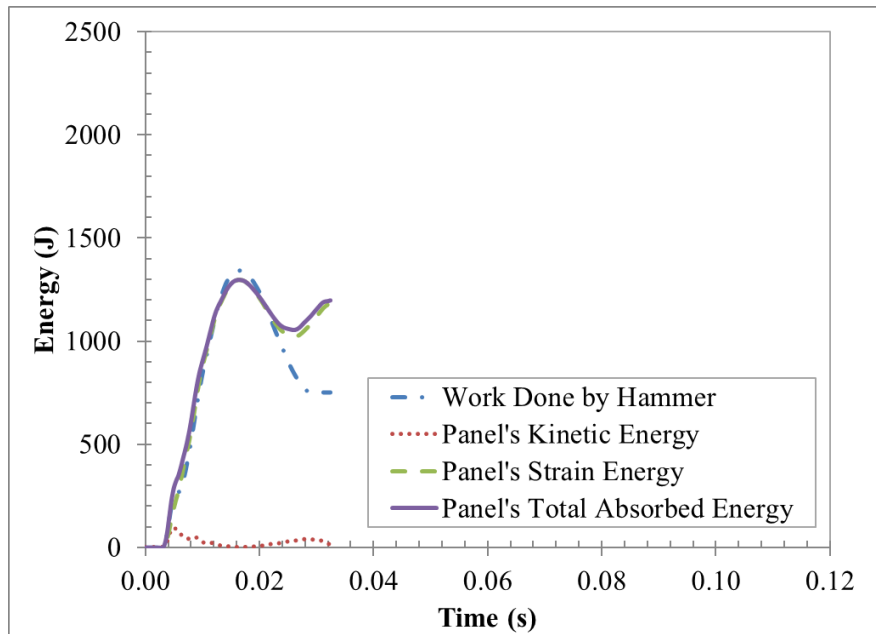
**Panel K4-1:**



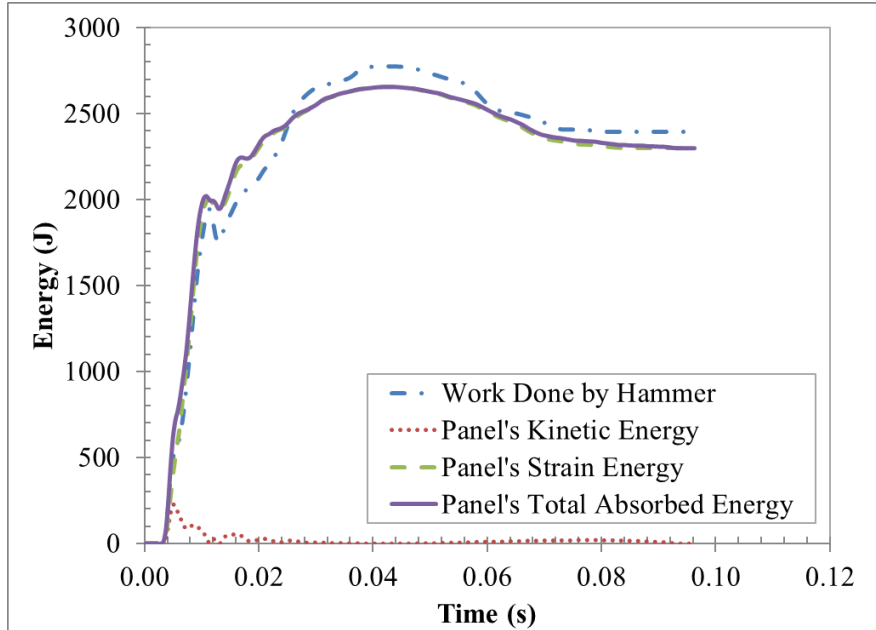
**Panel K4-2:**



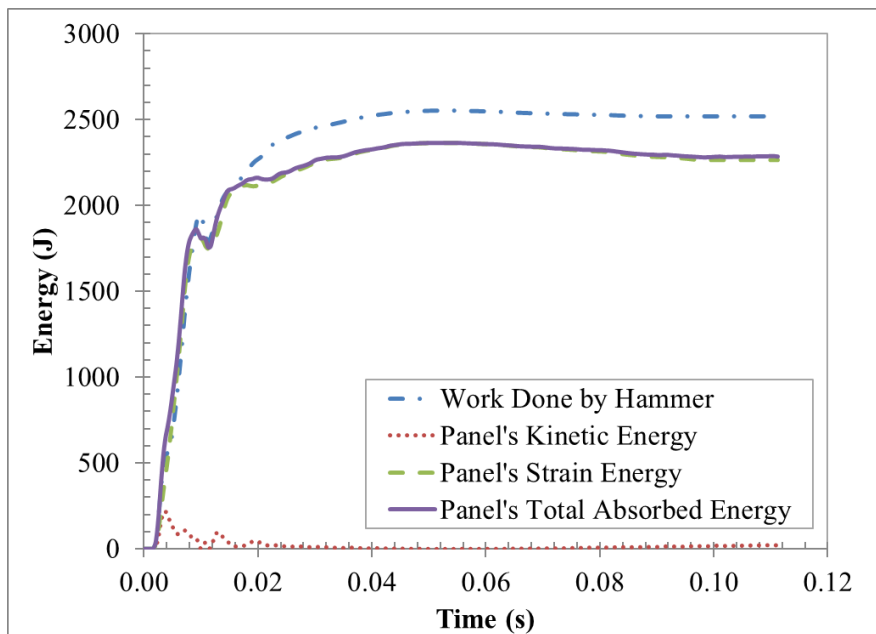
**Panel K4-3:**



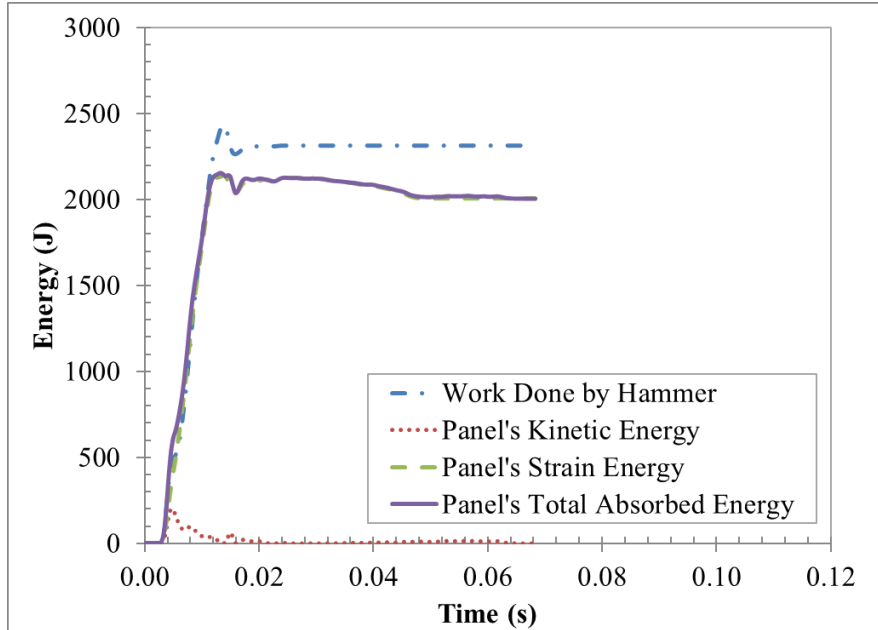
**Panel T1-1:**



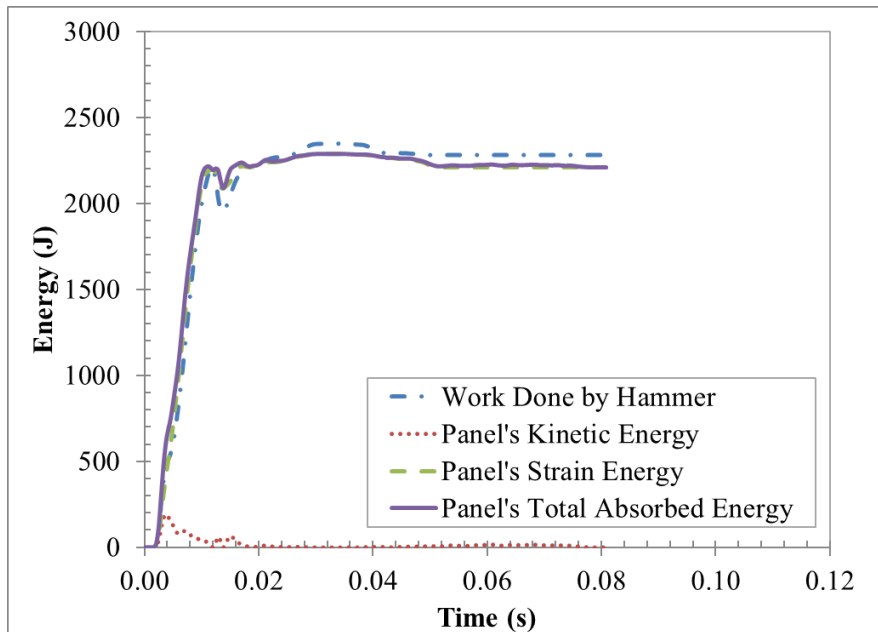
**Panel T1-2:**



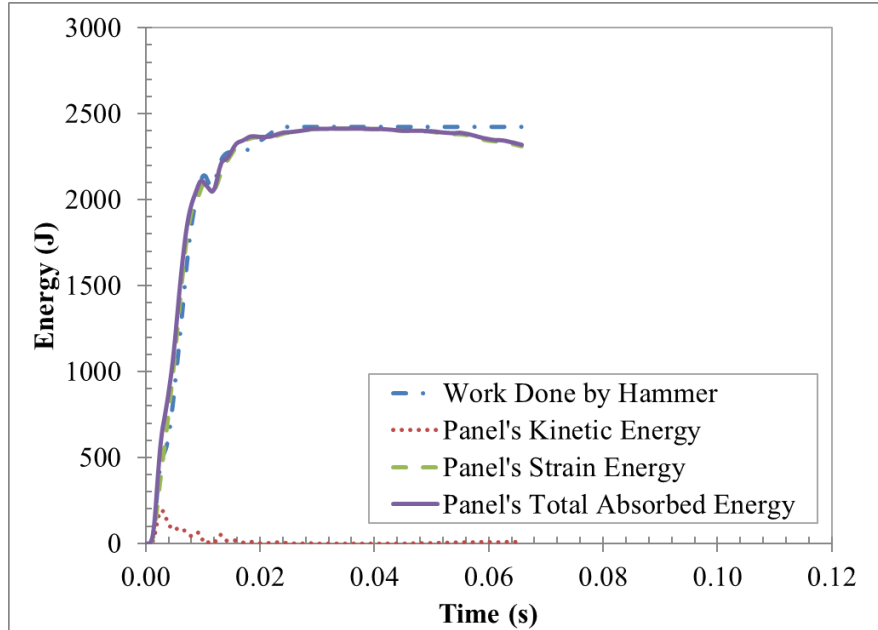
**Panel T2-1:**



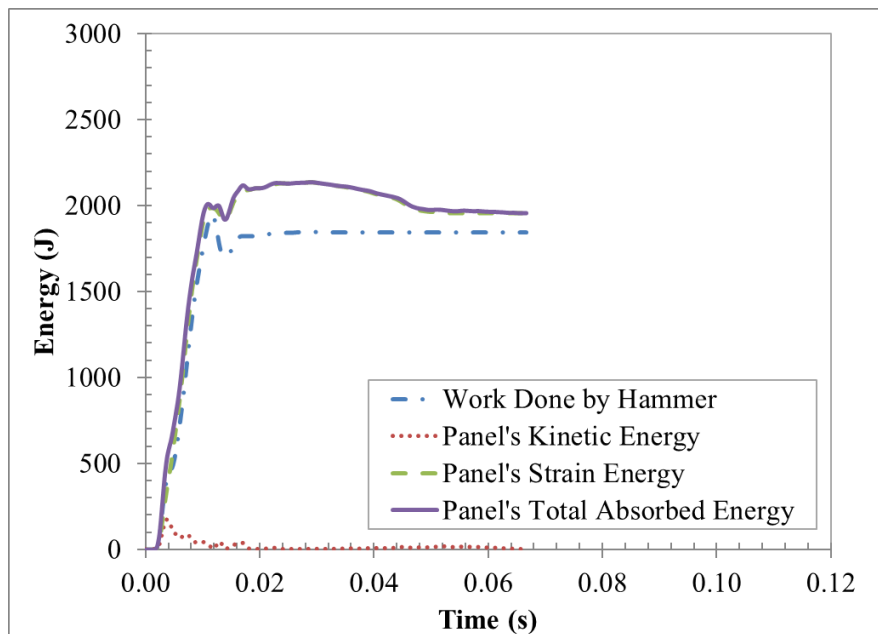
**Panel T2-2:**



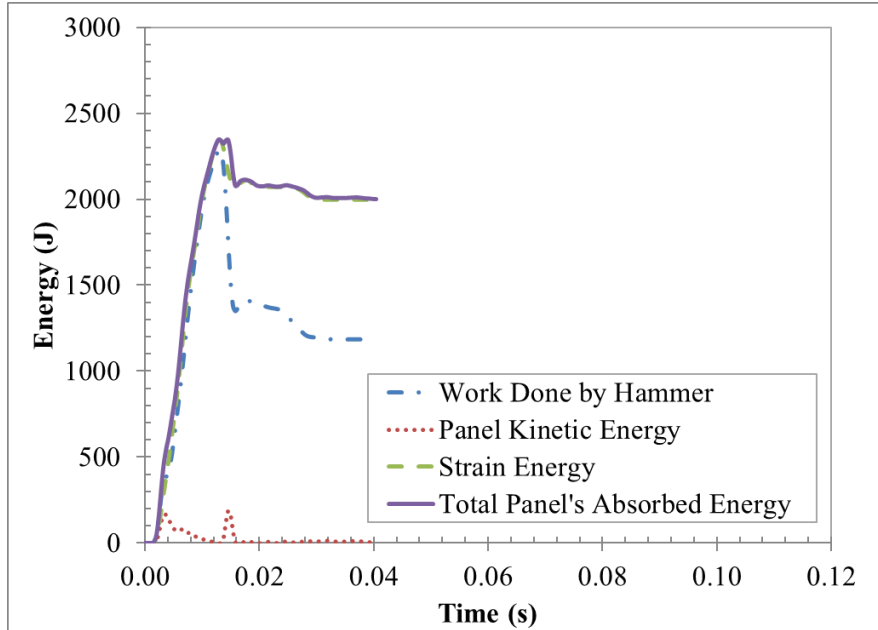
**Panel T2-3:**



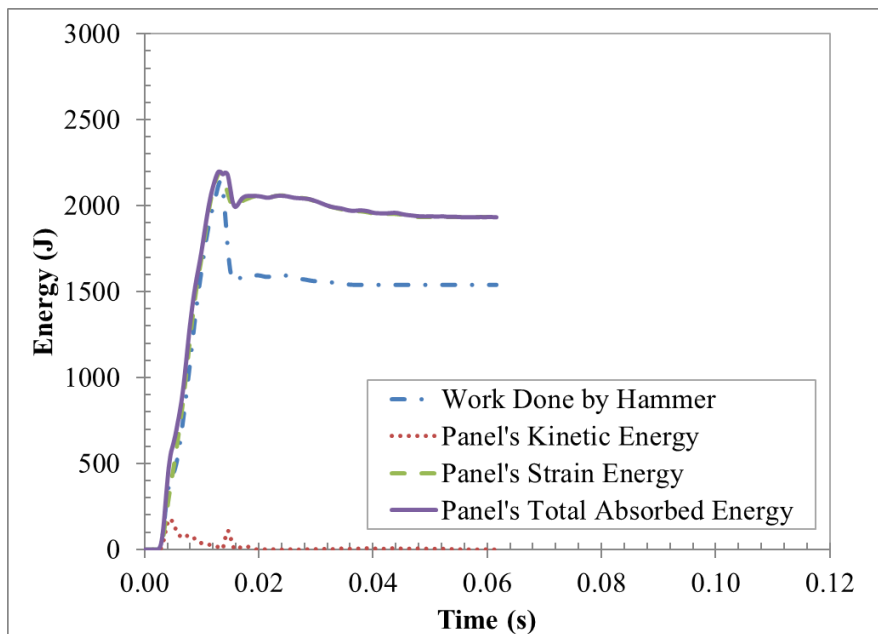
**Panel T3-1:**



**Panel T3-2:**

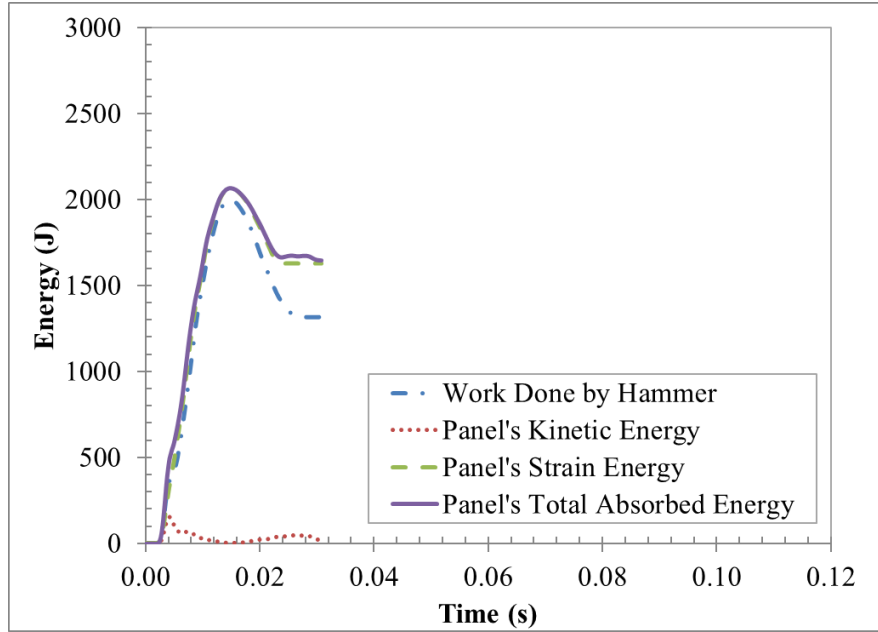


**Panel T3-3:**

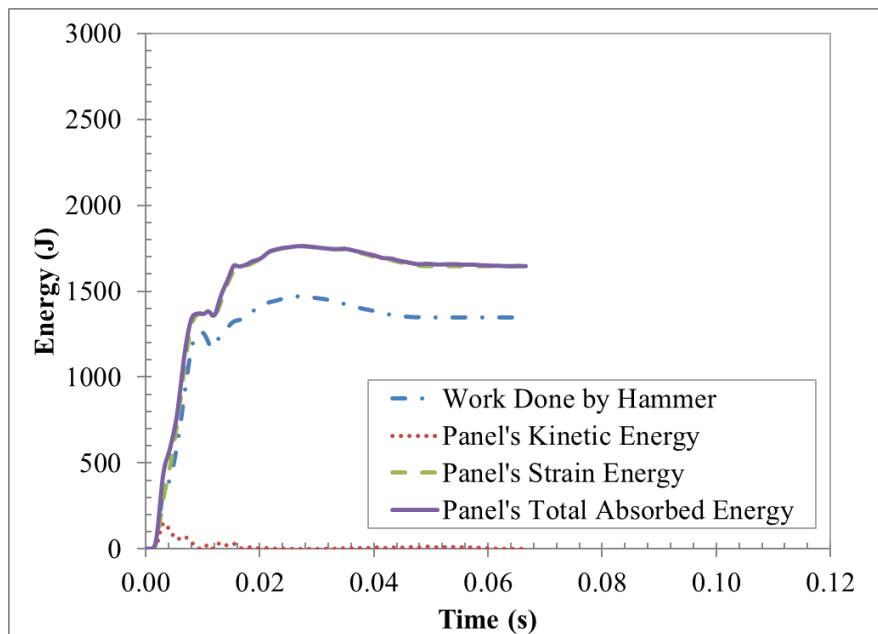




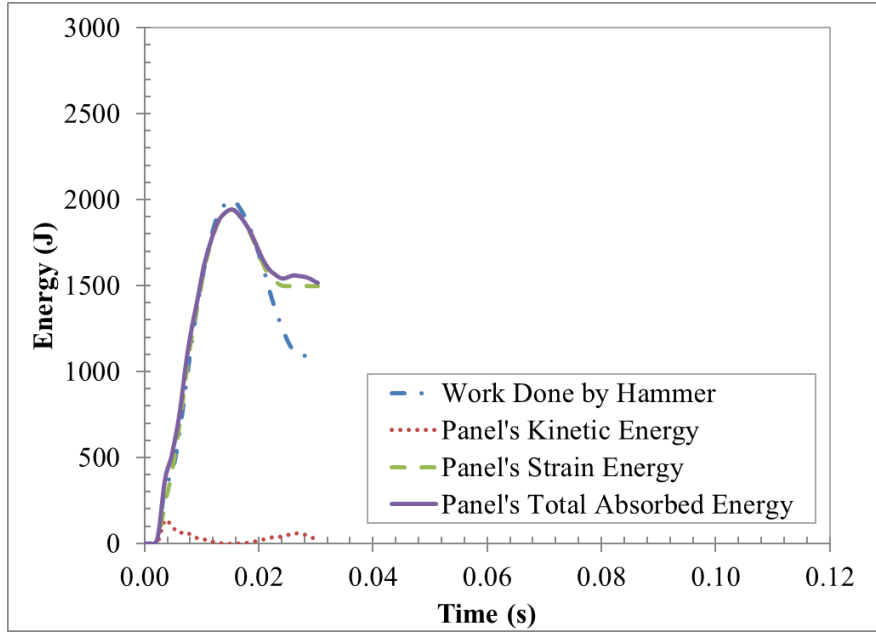
**Panel T4-1:**



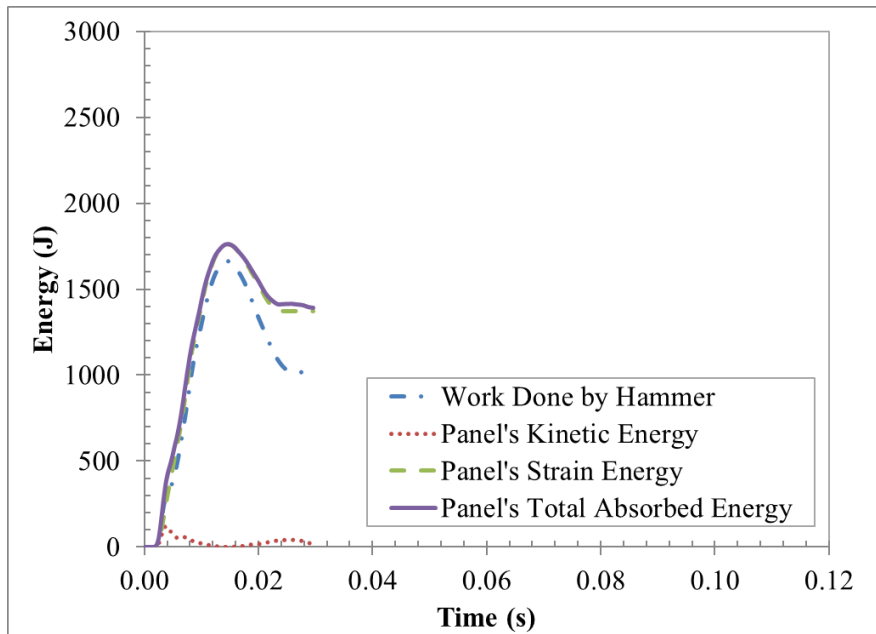
**Panel T4-2:**



**Panel T4-3:**



**Panel T5-1:**

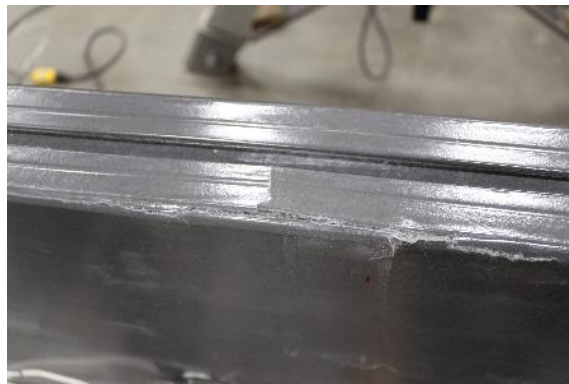


**Appendix G**  
**Pictures of Panels Post-Impact**

**Panel K1-1:**



Front View



Top View

**Panel K1-2:**



Front View



Top View

**Panel K1-3:**

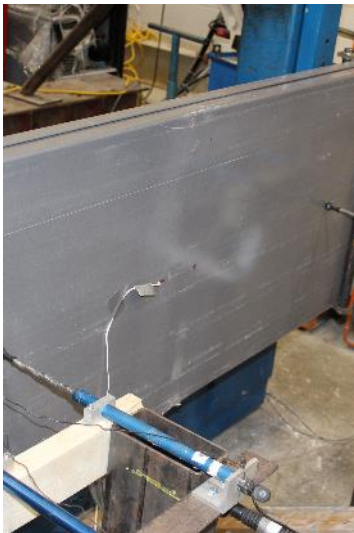


Front View



Top View

**Panel K2-1:**



Front View

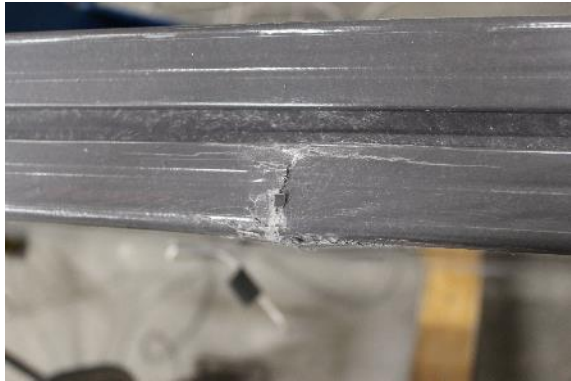


Top View

**Panel K2-2:**



Front View

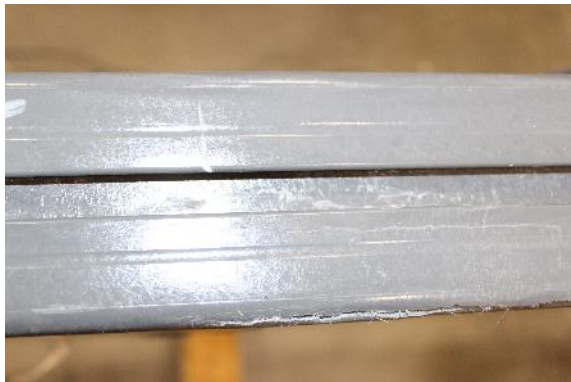


Top View

**Panel K2-3:**



Front View

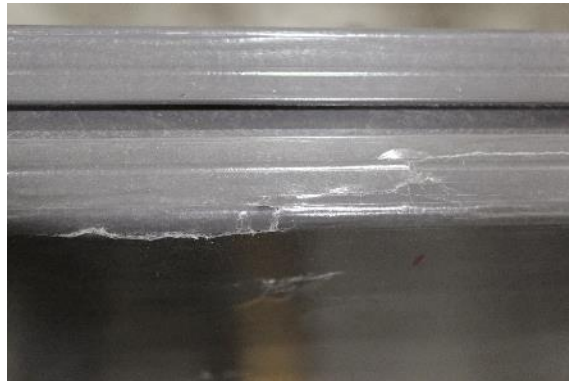


Top View

**Panel K3-1:**



Front View



Top View

**Panel K3-2:**



Front View

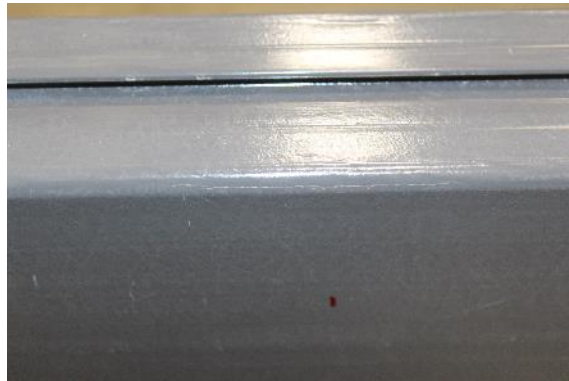


Top View

**Panel K3-3:**



Front View

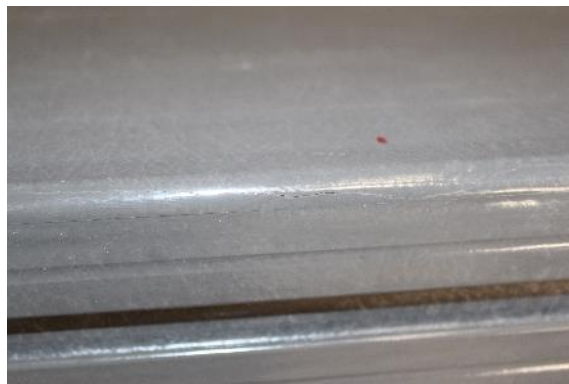


Top View

**Panel K4-1:**



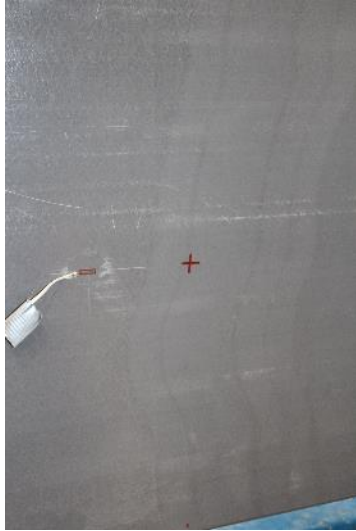
Front View



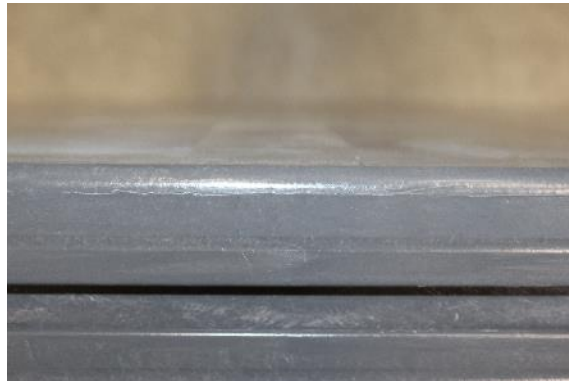
Top View



**Panel K4-2:**



Front View

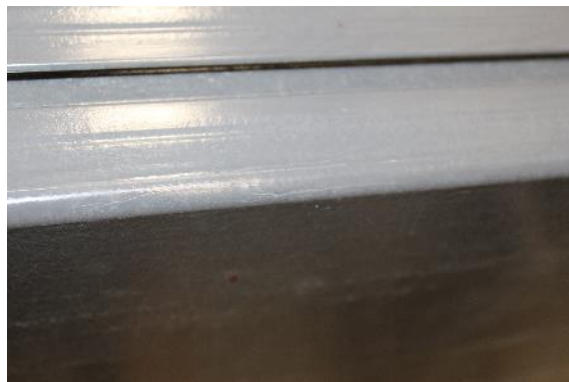


Top View

**Panel K4-3:**



Front View

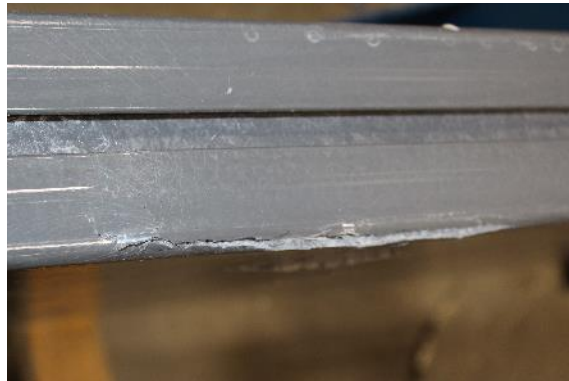


Top View

**Panel T1-1:**



Front View

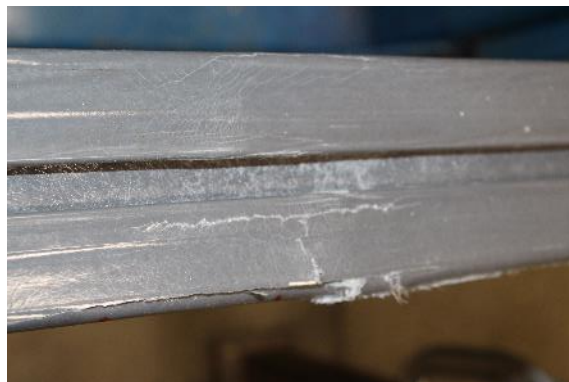


Top View

**Panel T1-2:**



Front View

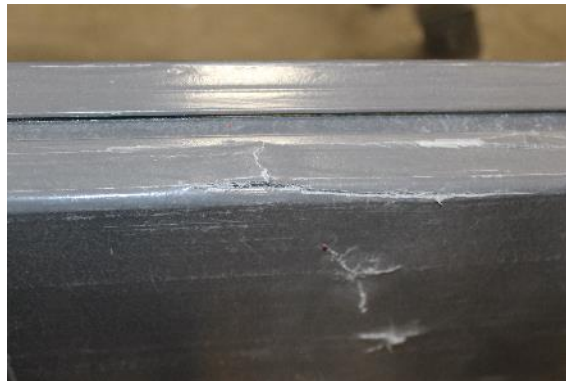


Top View

**Panel T2-1:**



Front View



Top View

**Panel T2-2:**



Front View



Top View

**Panel T2-3:**



Front View

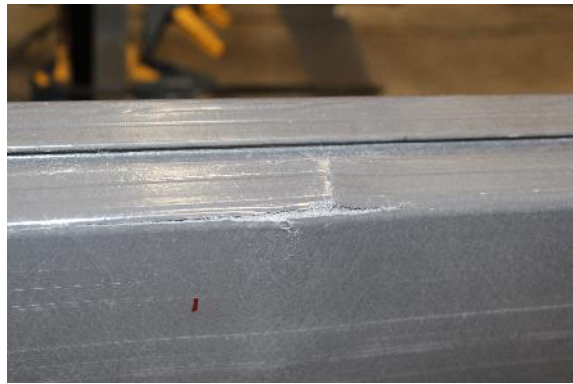


Top View

**Panel T3-1:**



Front View

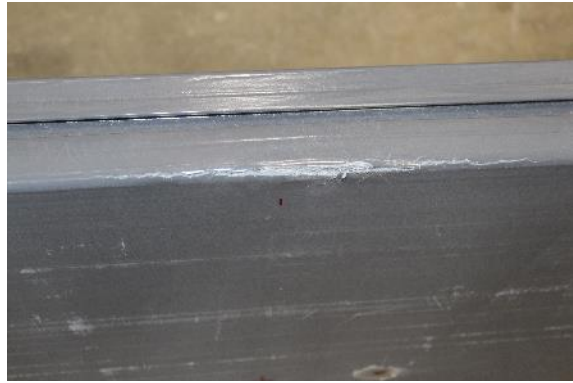


Top View

**Panel T3-2:**



Front View

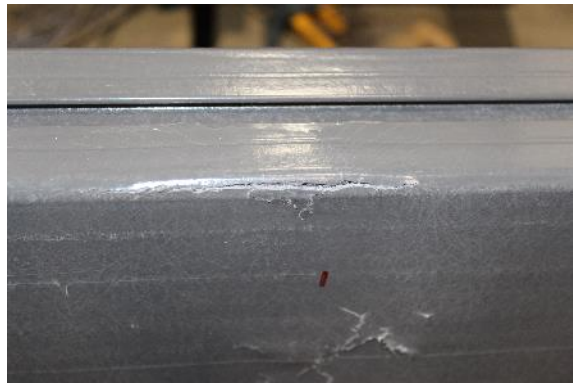


Top View

**Panel T3-3:**



Front View



Top View

**Panel T4-1:**



Front View

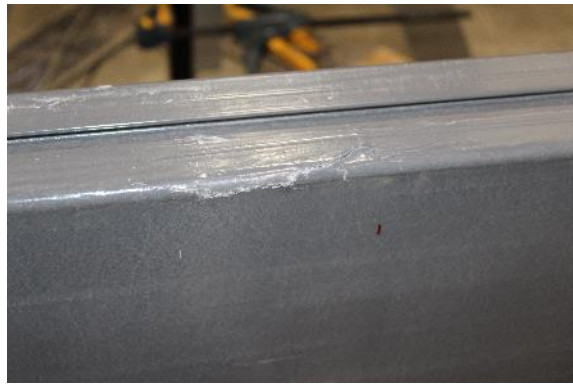


Top View

**Panel T4-2:**



Front View



Top View

**Panel T4-3:**



Front View



Top View

**Panel T5-1:**



Front View



Top View

**Appendix H**  
**Ultimate Limit State Sample Calculations**



### Ultimate Limit State Calculations:



Panel  
(3.16' x 23.80' nominal size — 80.26mm x 604.52mm actual) 7.48 lbs/ft (11.13 kg/m)

(Strongwell, 2016)

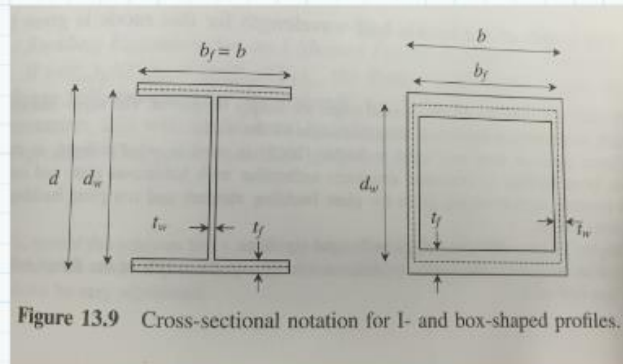


Figure 13.9 Cross-sectional notation for I- and box-shaped profiles.

(Bank L.C., 2006)

### Material and section properties (Strongwell, *COMPOSOLITE Brochure*, 2016):

$$E_L := 2.5 \cdot 10^6 \text{ psi} = 17.2368932 \text{ GPa}$$

$$E_T := 0.8 \cdot 10^6 \text{ psi} = 5.5158058 \text{ GPa}$$

$$\nu_L := 0.33$$

$$\nu_T := \nu_L \cdot \frac{E_T}{E_L} = 0.1056$$

$$G_{LT} := 0.425 \cdot 10^6 \text{ psi} = 2.9302718 \text{ GPa}$$

$$t_f := 4 \text{ mm}$$

$$t_w := 3 \text{ mm}$$

$$b_f := 84 \text{ mm}$$

$$d_w := 77 \text{ mm}$$

$$d := d_w + t_f = 81 \text{ mm}$$

$$I_x := 6.62 \cdot 10^6 \text{ mm}^4$$

Note: All equations used were taken from Bank, L.C., *Composites for Construction*, 2006

**Find orthotropic plate flexural rigidities for flange:**

$$D_{L_f} := \frac{E_L \cdot t_f^3}{12 \cdot (1 - \nu_L \cdot \nu_T)} = 0.0952493 \text{ kN} \cdot \text{m}$$

$$D_{T_f} := \frac{E_T \cdot t_f^3}{12 \cdot (1 - \nu_L \cdot \nu_T)} = 0.0304798 \text{ kN} \cdot \text{m}$$

$$D_{LT_f} := \frac{\nu_T \cdot E_L \cdot t_f^3}{12 \cdot (1 - \nu_L \cdot \nu_T)} = 0.0100583 \text{ kN} \cdot \text{m}$$

$$D_{S_f} := \frac{G_{LT} \cdot t_f^3}{12} = 0.0156281 \text{ kN} \cdot \text{m}$$

**Find orthotropic plate flexural rigidities for web:**

$$D_{L_w} := \frac{E_L \cdot t_w^3}{12 \cdot (1 - \nu_L \cdot \nu_T)} = 0.0401833 \text{ kN} \cdot \text{m}$$

$$D_{T_w} := \frac{E_T \cdot t_w^3}{12 \cdot (1 - \nu_L \cdot \nu_T)} = 0.0128587 \text{ kN} \cdot \text{m}$$

$$D_{LT_w} := \frac{\nu_T \cdot E_L \cdot t_w^3}{12 \cdot (1 - \nu_L \cdot \nu_T)} = 0.0042434 \text{ kN} \cdot \text{m}$$

$$D_{S_w} := \frac{G_{LT} \cdot t_w^3}{12} = 0.0065931 \text{ kN} \cdot \text{m}$$

### Using equations for box beams

#### 1. Local Buckling due to in-plane compression:

Find the critical stress in the flange:

$$\sigma_{ssf} := \frac{2 \cdot \pi^2}{t_f \cdot b_f^2} \cdot \left( \sqrt{D_{Lf} \cdot D_{Tf} + D_{LTf}} + 2 \cdot D_{Sf} \right) = 66.577679 \text{ MPa}$$

Buckle half-wave length:

$$a_{ssf} := b_f \cdot \sqrt[4]{\frac{E_L}{E_T}} = 111.6842138 \text{ mm}$$

Find the critical stress in the web:

$$\sigma_{ssw} := \frac{\pi^2}{t_w \cdot d_w^2} \cdot \left( 13.9 \cdot \sqrt{D_{Lw} \cdot D_{Tw}} + 11.1 \cdot D_{LTw} + 22.2 \cdot D_{Sw} \right) = 282.6716891 \text{ MPa}$$

Buckle half-wave length:

$$a_{ssw} := 0.707 \cdot d_w \cdot \sqrt[4]{\frac{E_L}{E_T}} = 72.3806776 \text{ mm}$$

Find which stress governs:

$$\frac{\sigma_{ssf}}{E_L} = 0.0038625$$

$$\frac{\sigma_{ssw}}{E_L} = 0.0163992$$

$$\frac{\sigma_{ssf}}{E_L} < \frac{\sigma_{ssw}}{E_L} \quad \text{The compression flange will buckle before one of the webs.}$$

Find the critical in-plane compressive stress:

$$k := \frac{4 \cdot D_{Tw}}{d_w} \cdot \left( 1 - \frac{\sigma_{ssf} \cdot E_L}{\sigma_{ssw} \cdot E_L} \right) = 510.6524901 \text{ N}$$

$$\zeta_{bf} := \frac{D_{Tf}}{k \cdot b_f} = 0.7105706$$

$$\xi_{bf} := \frac{1}{1 + 10 \cdot \zeta_{bf}} = 0.1233699$$

$$\sigma_{cr} := \frac{\pi^2}{b_f^2 \cdot t_f} \cdot \left( 2 \cdot \sqrt{(D_{Lf} \cdot D_{Tf}) \cdot (1 + 4.139 \cdot \xi_{bf})} + (D_{LTf} + 2 \cdot D_{Sf}) \cdot (2 + 0.62 \cdot \xi_{bf}^2) \right)$$

$$\sigma_{cr} = 75.3463364 \text{ MPa}$$

## 2. Web crushing and web buckling in the transverse direction:

$$\sigma_{ycrush} := 15000 \text{ psi} = 103.4213594 \text{ MPa}$$

At point load:

$$L_{eff} := 3 \text{ in} = 76.2 \text{ mm}$$

$$t_{bf} := \frac{1}{4} \text{ in} = 6.35 \text{ mm}$$

$$b_{eff} := b_f = 84 \text{ mm}$$

$$A_{eff} := (t_w + 2 \cdot t_f + 2 \cdot t_{bf}) \cdot L_{eff} = (1.80594 \cdot 10^3) \text{ mm}^2$$

$$F_{crush} := \sigma_{ycrush} \cdot A_{eff} = 186.7727698 \text{ kN}$$

$$\sigma_{ylocal} := \frac{2 \cdot \pi^2}{t_w \cdot b_{eff}^2} \cdot \left( \sqrt{D_{Lw} \cdot D_{Tw} + D_{LTw} + 2 \cdot D_{Sw}} \right) = 37.4499445 \text{ MPa}$$

$$F_{local} := \sigma_{ylocal} \cdot A_{eff} = 67.6323527 \text{ kN}$$

Find the approximate corresponding in-plane compressive stress that will be used in the moment curvature model:

$$M_{crush} := \frac{F_{local}}{2} \cdot 0.67 \text{ m} = 22.6568382 \text{ kN} \cdot \text{m}$$

$$y_{approx} := 50 \text{ mm}$$

$$\sigma_{crushbending} := \frac{-M_{crush} \cdot y_{approx}}{I_x} = -171.1241552 \text{ MPa}$$

+

**At support:**

$$L_{eff} := 3 \text{ in} = 76.2 \text{ mm}$$

$$t_{bf} := \frac{1}{4} \text{ in} = 6.35 \text{ mm}$$

$$b_{eff} := L_{eff} + \frac{d_w}{2} = 114.7 \text{ mm}$$

$$A_{eff} := (t_w + 2 \cdot t_f + 2 \cdot t_{bf}) \cdot L_{eff} = (1.80594 \cdot 10^3) \text{ mm}^2$$

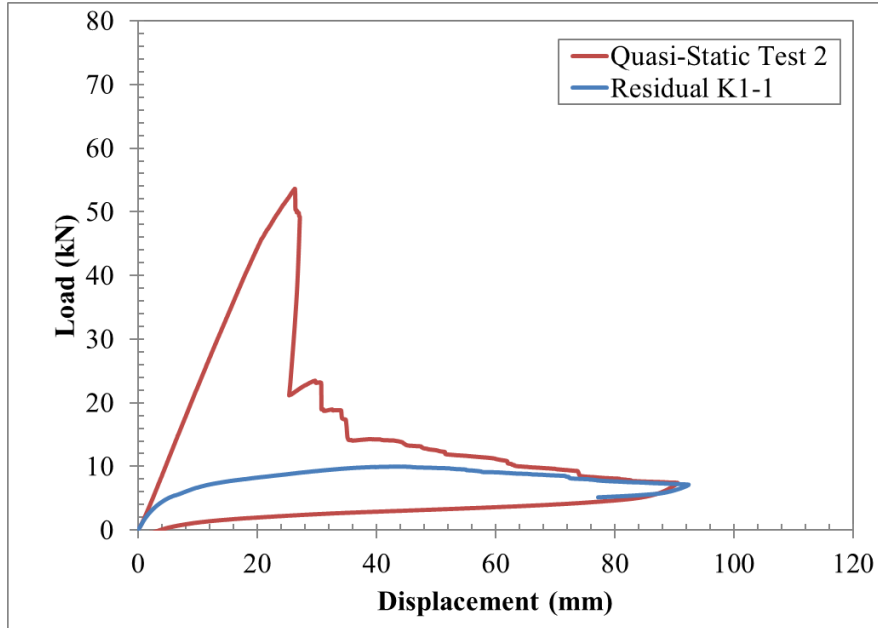
$$F_{crush} := \sigma_{ycrush} \cdot A_{eff} = 186.7727698 \text{ kN}$$

$$\sigma_{ylocal} := \frac{2 \cdot \pi^2}{t_w \cdot b_{eff}^2} \cdot \left( \sqrt{D_{Lw} \cdot D_{Tw}} + D_{LTw} + 2 \cdot D_{Sw} \right) = 20.0855123 \text{ MPa}$$

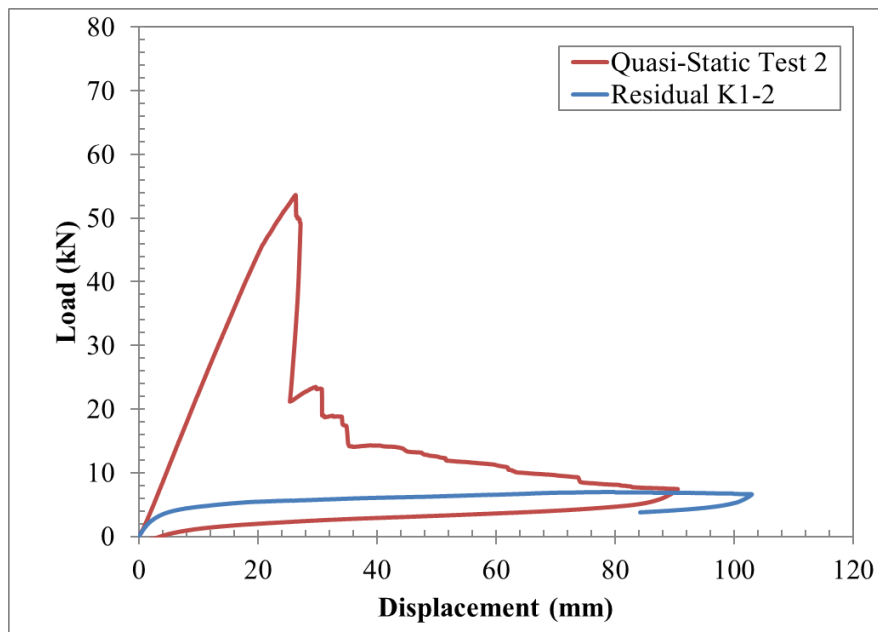
$$F_{local} := \sigma_{ylocal} \cdot A_{eff} = 36.2732302 \text{ kN}$$

**Appendix I**  
**Residual Strength Tests**

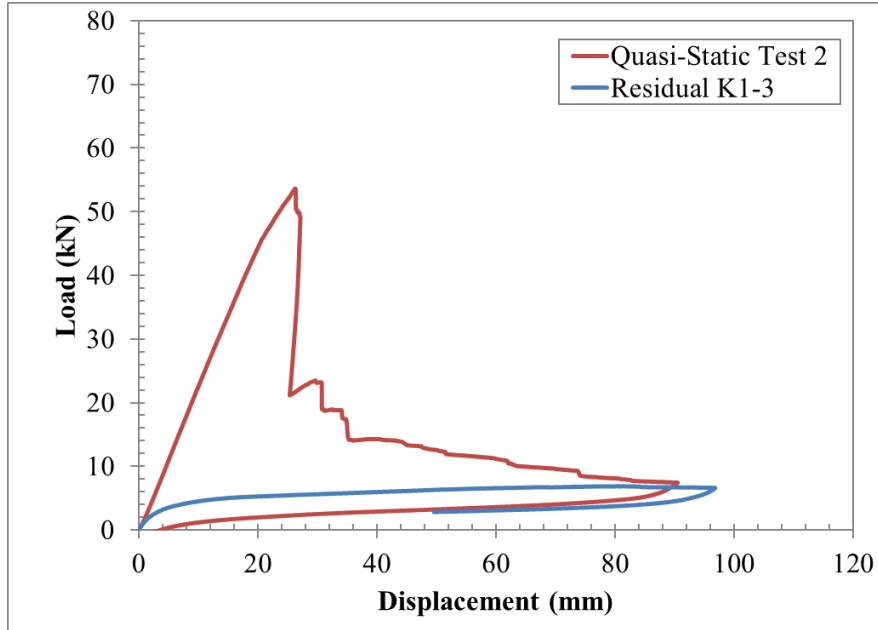
**Panel K1-1:**



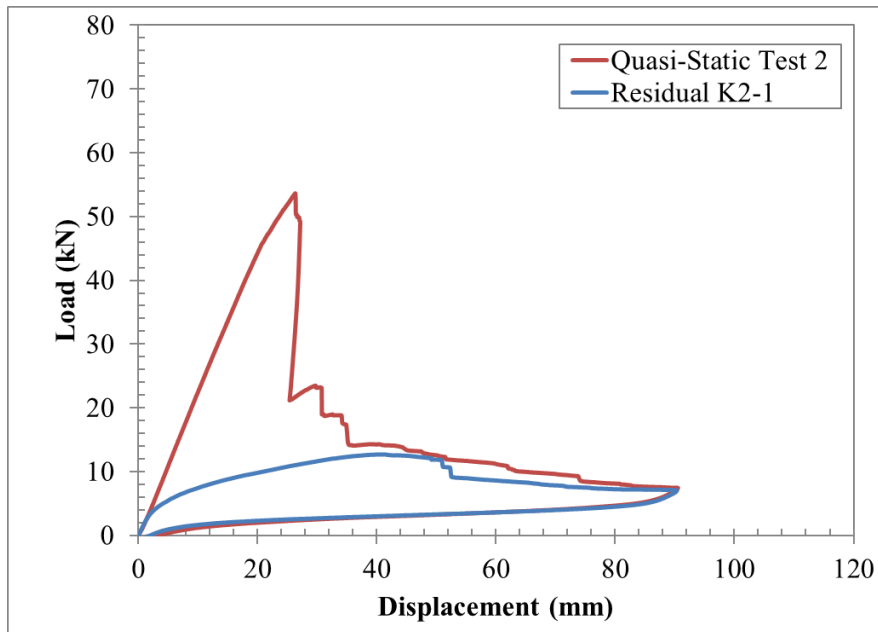
**Panel K1-2:**



**Panel K1-3:**

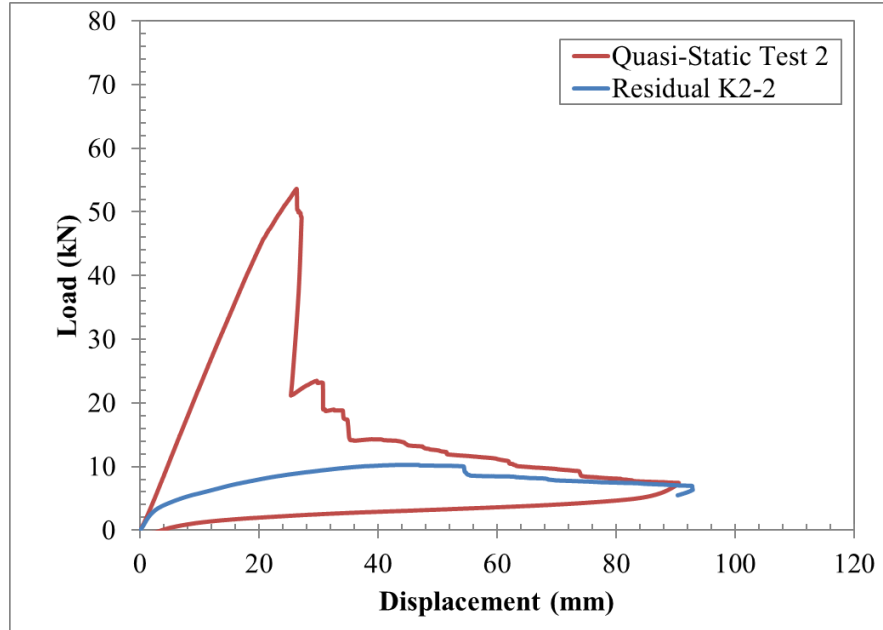


**Panel K2-1:**

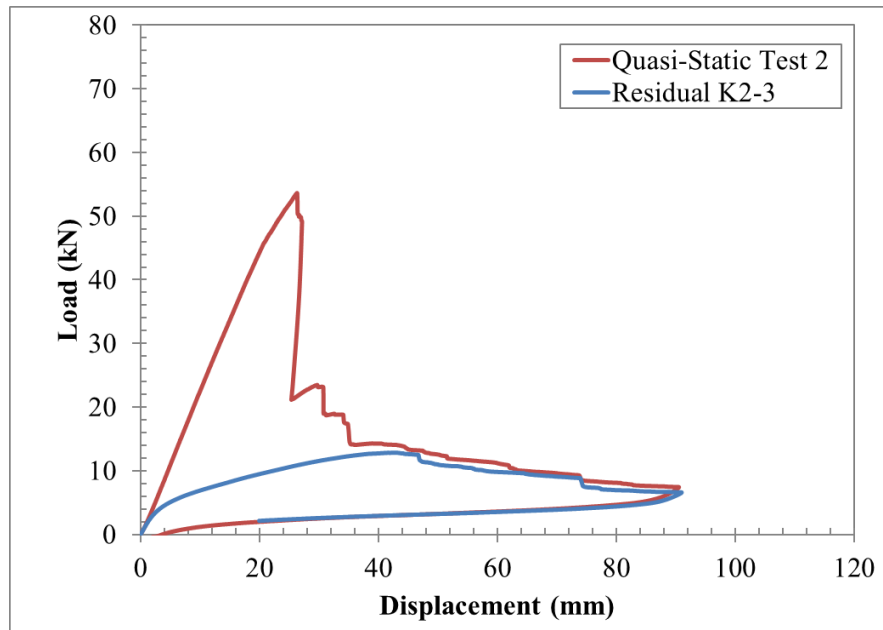




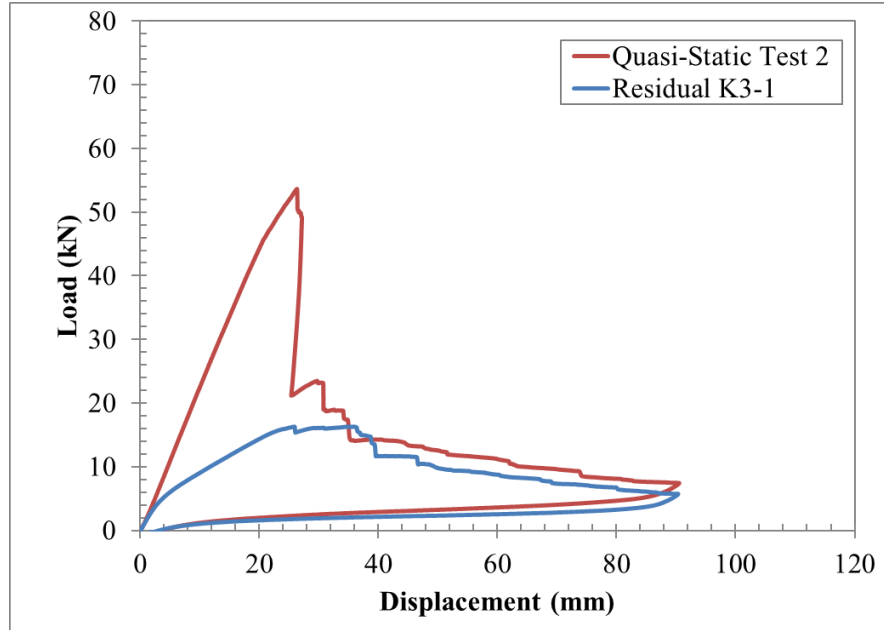
**Panel K2-2:**



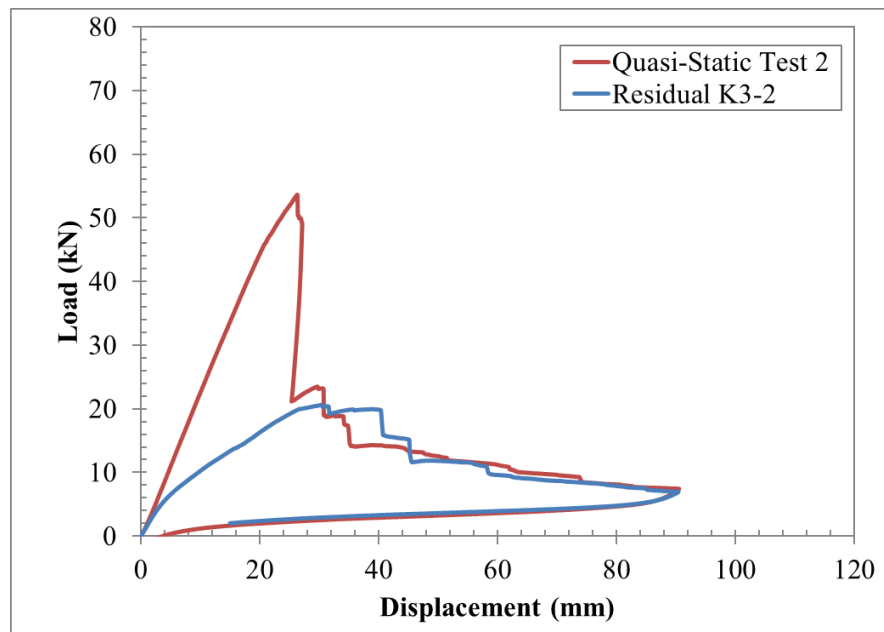
**Panel K2-3:**



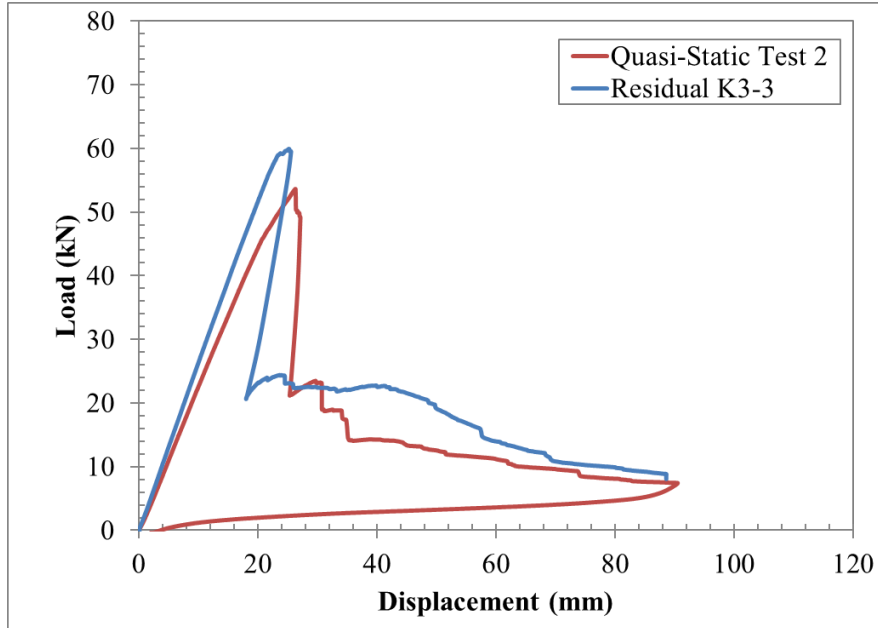
**Panel K3-1:**



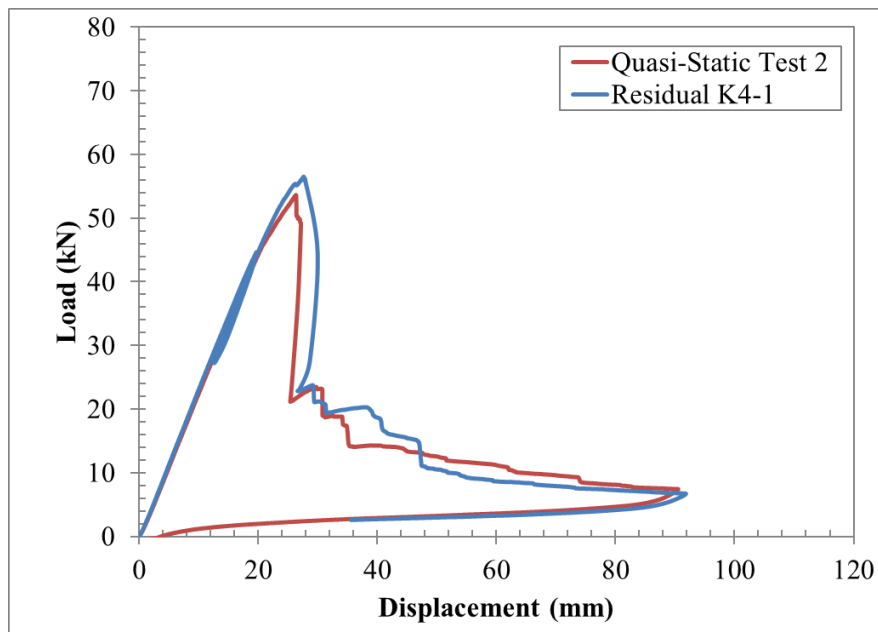
**Panel K3-2:**



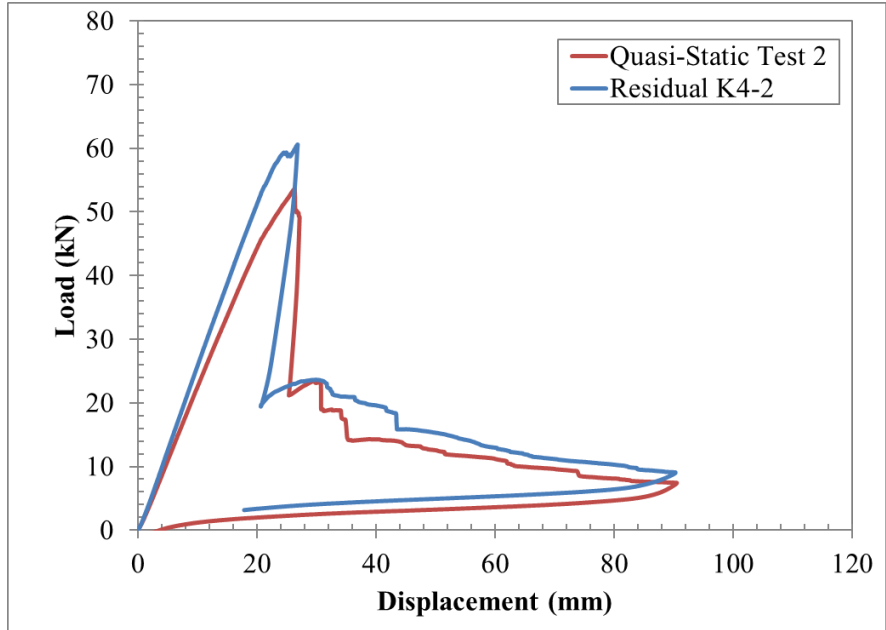
**Panel K3-3:**



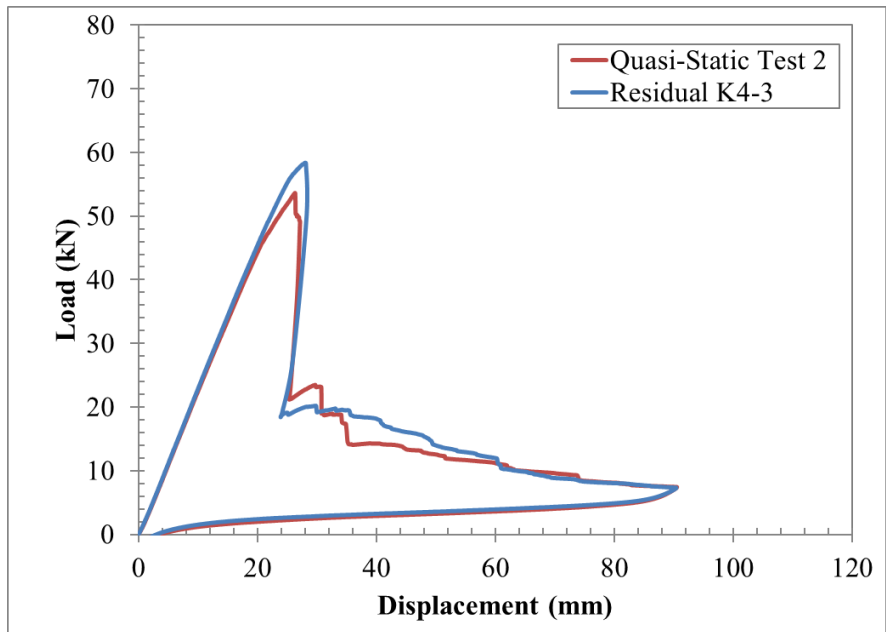
**Panel K4-1:**



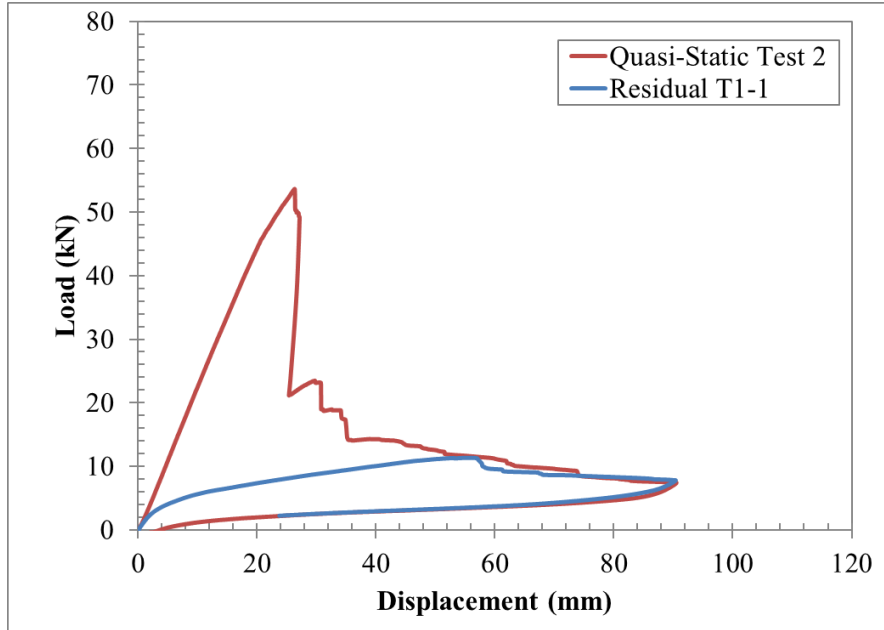
**Panel K4-2:**



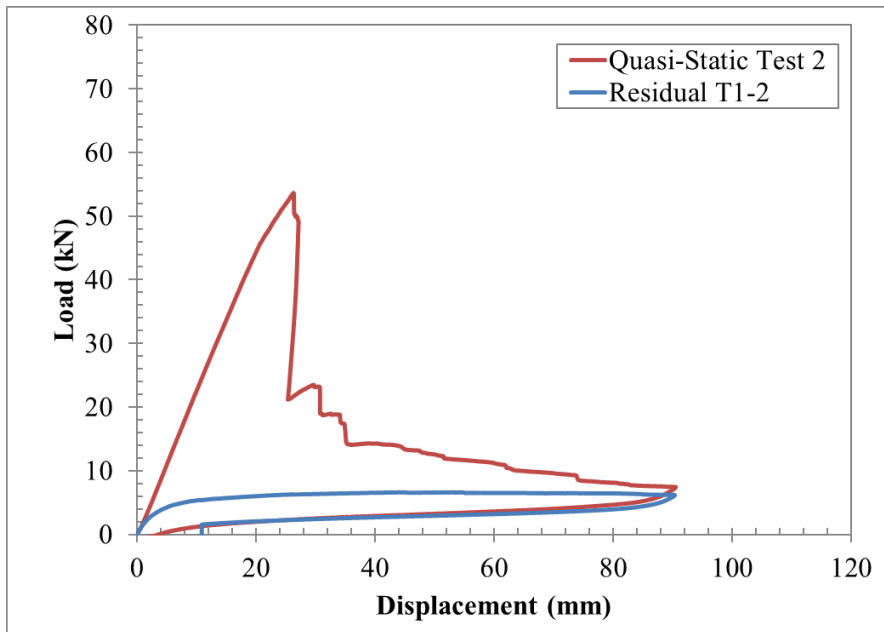
**Panel K4-3:**



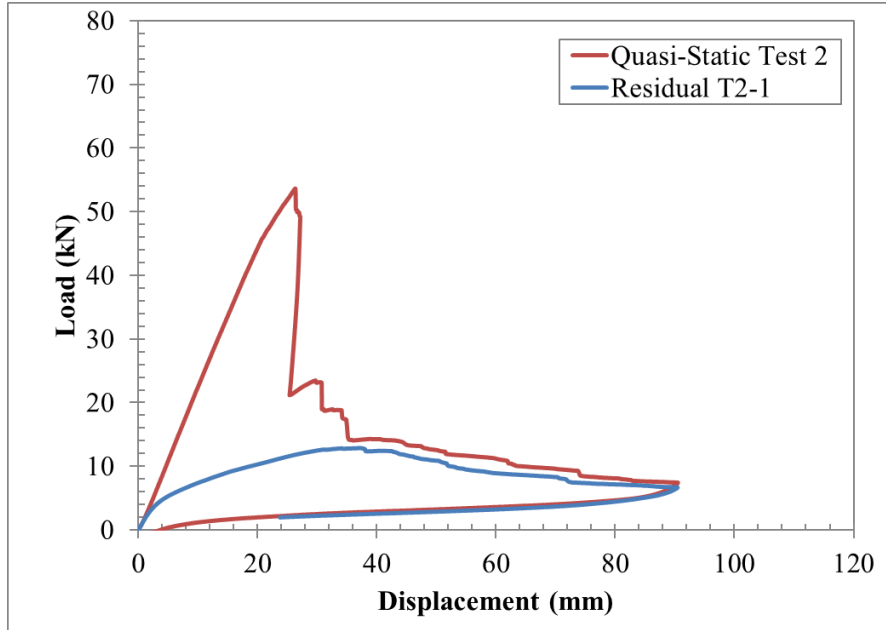
**Panel T1-1:**



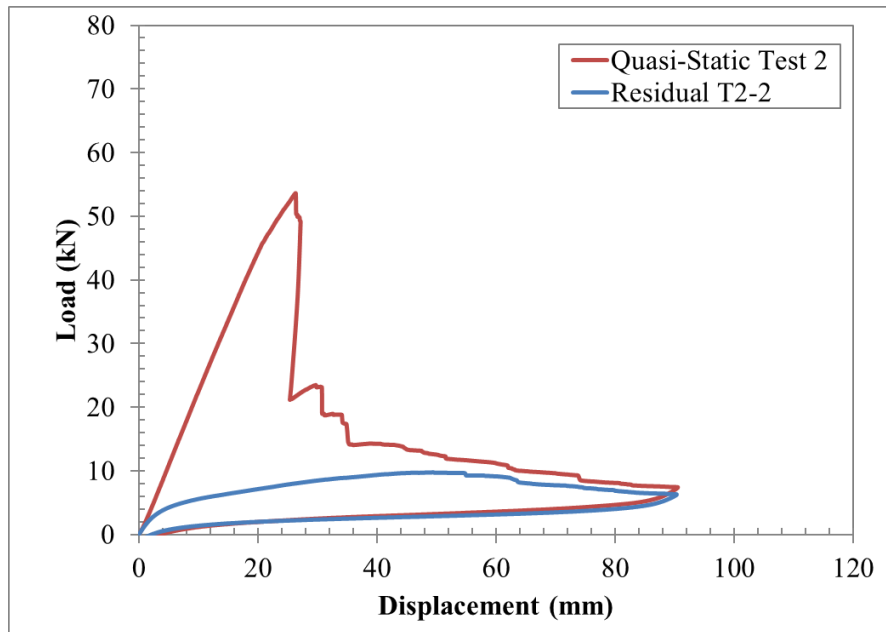
**Panel T1-2:**



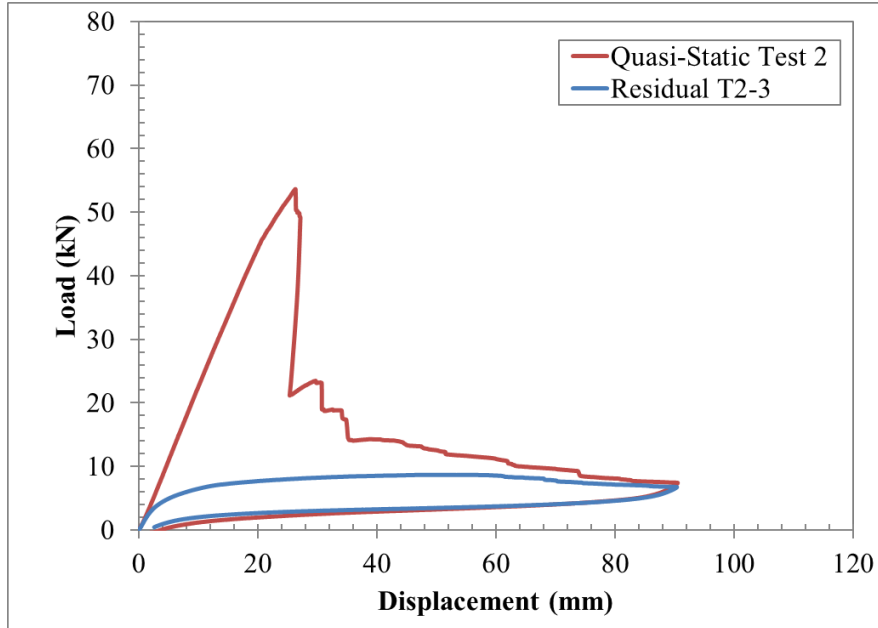
**Panel T2-1:**



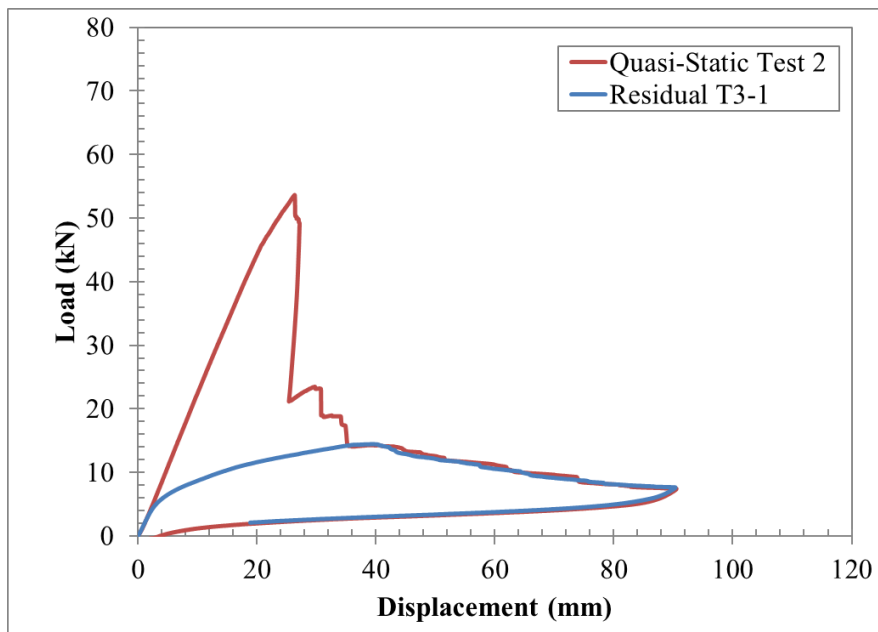
**Panel T2-2:**



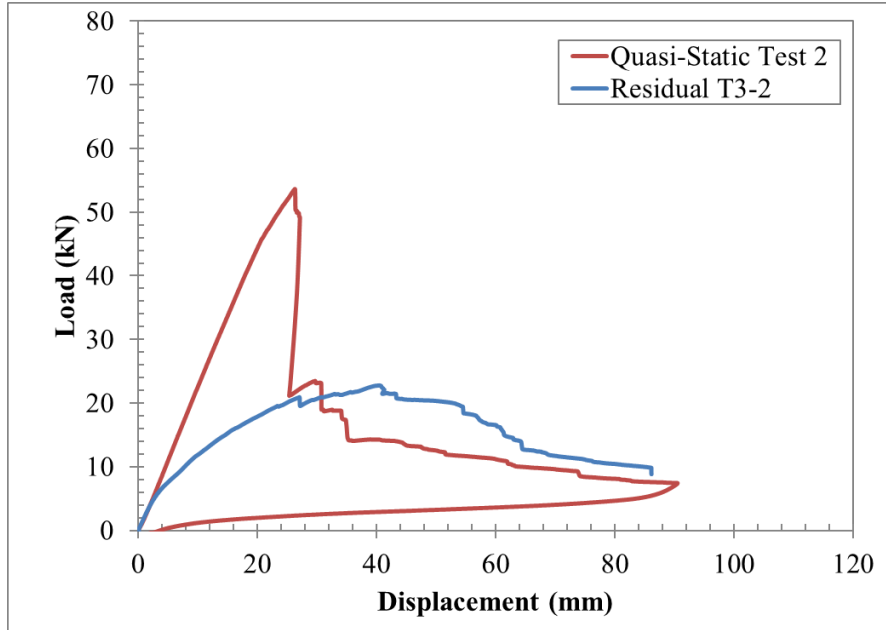
**Panel T2-3:**



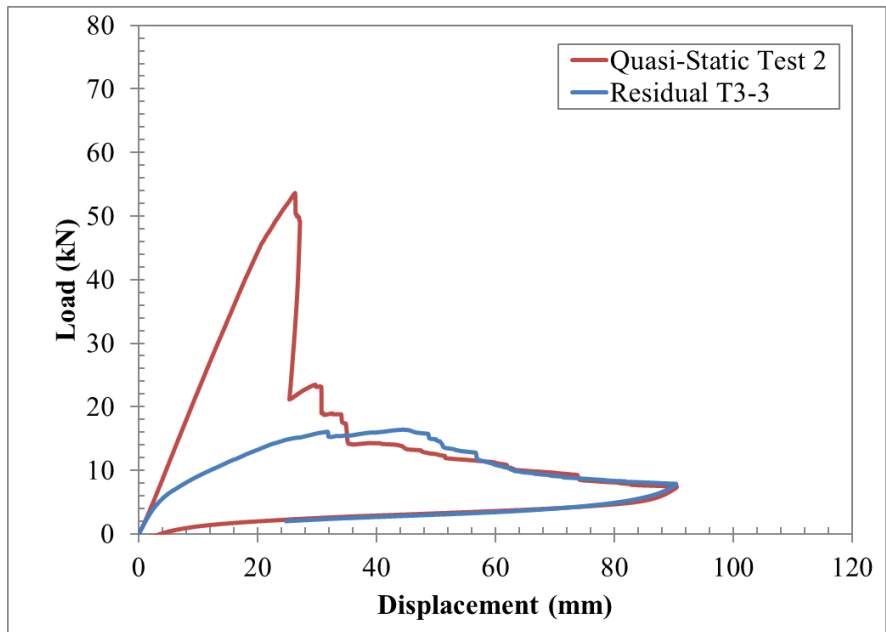
**Panel T3-1:**



**Panel T3-2:**

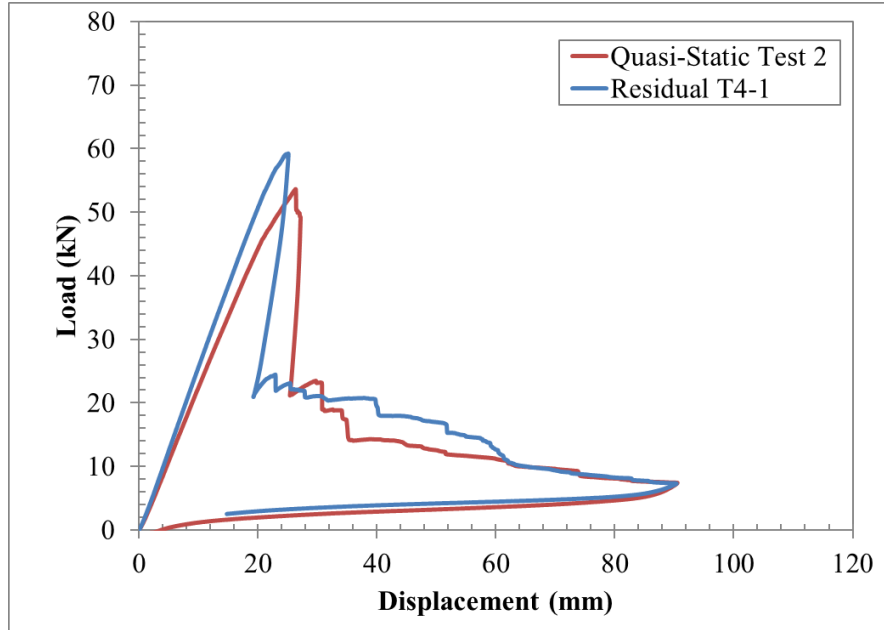


**Panel T3-3:**

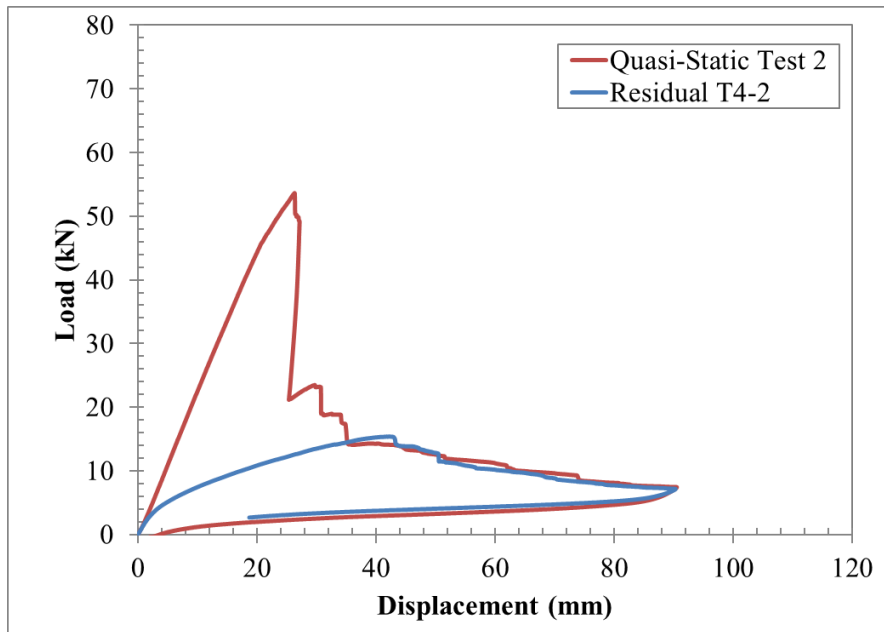




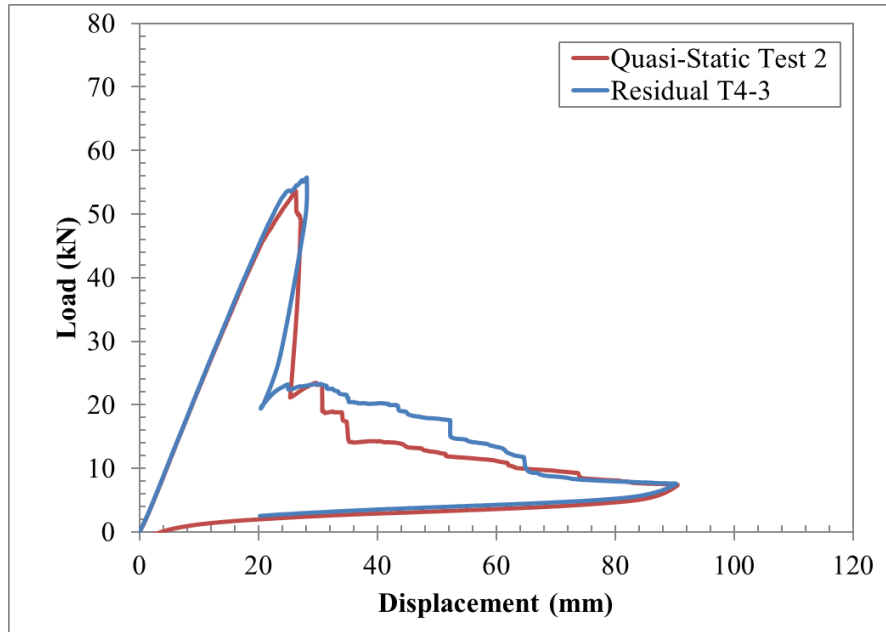
**Panel T4-1:**



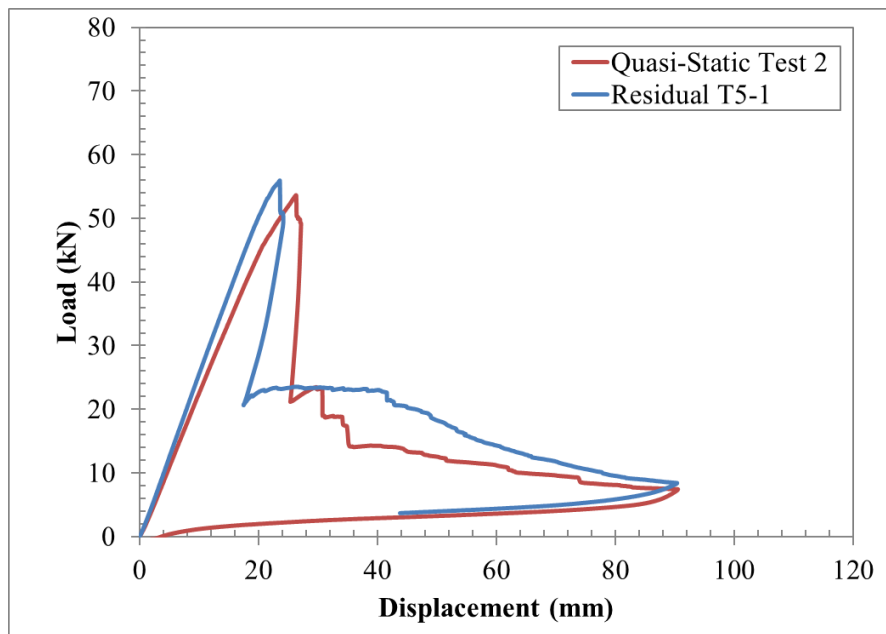
**Panel T4-2:**



**Panel T4-3:**



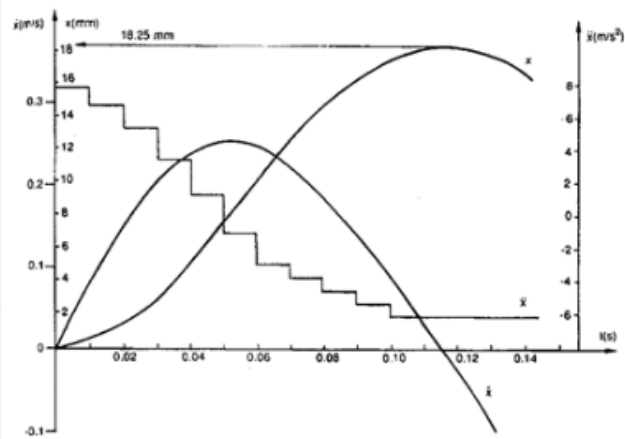
**Panel T5-1:**



**Appendix J**  
**Single Degree-of-Freedom Model Sample Calculations**

### **Single Degree-of-Freedom Model Calculations:**

The SDOF model is based off of the Smith and Hetherington (1994) method.



Graphical representation of the model (Smith and Hetherington, 1994)

### **Model Equations:**

$P_t(t_i)$  = Experimental load from impact hammer force ring

$R(y(t_i))$  = Resistance function calculated using the modelled moment-curvature relationship

$m_p$  = Total mass of the GFRP Panel

$m_e$  = Equivalent mass of the panel in SDOF model

$K_{LM}$  = Load-Mass equivalency factor

$a(t_i)$  = Modelled panel's acceleration

$v(t_i)$  = Modelled panel's velocity

$y(t_i)$  = Modelled panel's displacement

Equation of Motion:

Equivalency factors:

Using simply supported boundary conditions according to Cormie et al. (2012).  
Elastic factor was used prior failure and plastic factor was used post-failure.

Elastic:

$$K_{LM} := 0.49$$

Plastic:

$$K_{LM} := 0.33$$

$$m_p := 18.18 \text{ kg}$$

$$m_e := K_{LM} \cdot m_p$$

$$R(y(t_i - 1)) + m_e \cdot a(t_i) = P_t(t_i)$$

Note: the displacement from the previous time-step had to be taken to find the resistance function.

$$a(t_i) = \frac{P_t(t_i) - R(y(t_i - 1))}{m_e}$$

$$v(t_i) := \frac{(a(t_i - 1)) + a(t_i)}{2} \cdot ((t_i - 1) - t_i)$$

$$y(t_i) := \frac{(v(t_i - 1)) + v(t_i)}{2} \cdot ((t_i - 1) - t_i)$$

Panel K4-1:

SDOF Model						
F (kN)	R (kN)	t (s)	a (m/s <sup>2</sup> )	v (m/s)	y (m)	y (mm)
0.000	0.000	0.000	0.000	0.000	0.000	0.000
0.037	0.000	0.000	4.109	0.001	0.000	0.000
0.117	0.000	0.001	13.119	0.004	0.000	0.001
0.091	0.000	0.001	10.232	0.009	0.000	0.004
0.070	0.000	0.002	7.866	0.013	0.000	0.009
0.918	0.000	0.002	103.051	0.036	0.000	0.019
7.832	1.103	0.003	755.301	0.215	0.000	0.071
24.854	1.103	0.003	2665.927	0.928	0.000	0.309
42.602	1.103	0.003	4657.983	2.454	0.001	1.014
46.128	3.309	0.004	4806.202	4.425	0.002	2.447
35.026	7.170	0.004	3126.705	6.078	0.005	4.635
19.317	13.238	0.005	682.369	6.872	0.007	7.333
7.162	21.511	0.005	-1610.665	6.678	0.010	10.156
4.382	29.233	0.005	-2789.366	5.761	0.013	12.747
11.697	36.955	0.006	-2835.060	4.590	0.015	14.904
23.947	43.022	0.006	-2141.058	3.553	0.017	16.600
34.945	47.987	0.007	-1463.861	2.802	0.018	17.924
41.312	51.847	0.007	-1182.533	2.251	0.019	18.977
42.960	47.657	0.008	-527.174	1.894	0.020	19.841
43.365	48.643	0.008	-592.420	1.661	0.021	20.581
45.584	50.286	0.008	-527.816	1.428	0.021	21.225
49.038	51.272	0.009	-250.793	1.266	0.022	21.786
52.521	51.930	0.009	66.373	1.227	0.022	22.305
55.055	52.916	0.010	240.176	1.291	0.023	22.830
55.154	53.902	0.010	140.580	1.370	0.023	23.384
52.545	54.559	0.010	-226.053	1.353	0.024	23.952
49.298	56.202	0.011	-774.948	1.144	0.024	24.472
48.322	56.202	0.011	-884.539	0.798	0.025	24.877
51.260	57.188	0.012	-665.373	0.475	0.025	25.142

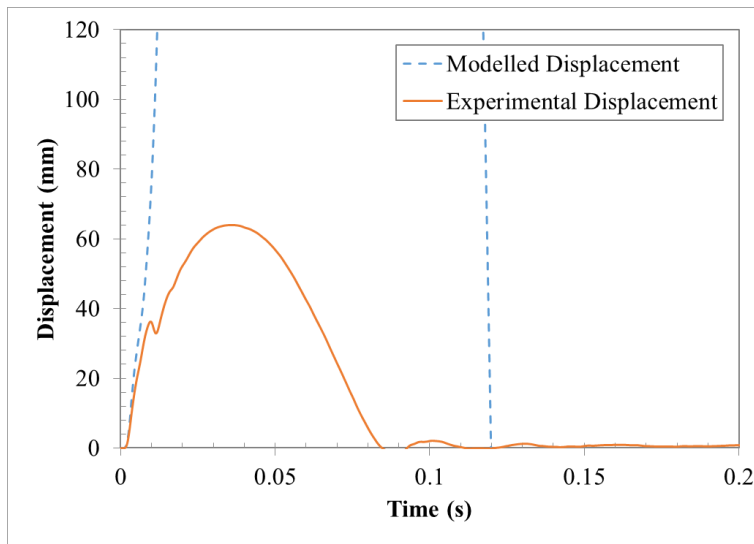
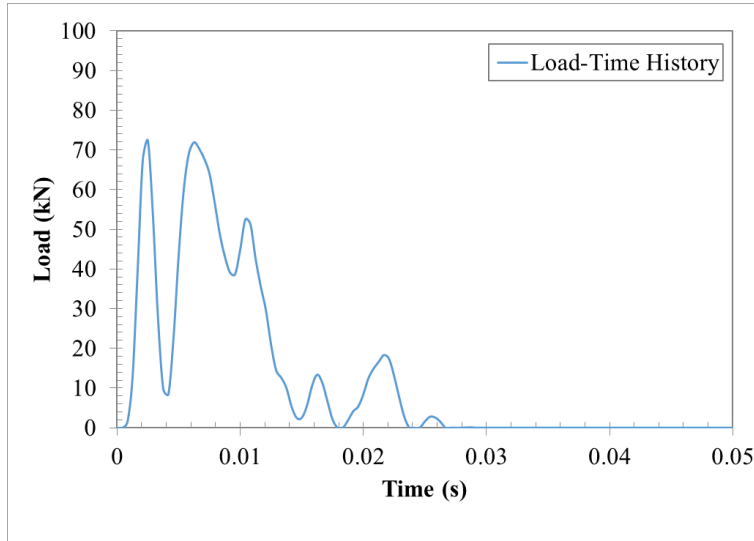
56.929	57.846	0.012	-102.931	0.315	0.025	25.307
61.817	58.174	0.013	408.824	0.379	0.025	25.451
63.197	58.503	0.013	526.887	0.574	0.026	25.650
60.796	58.503	0.013	257.427	0.737	0.026	25.923
56.439	58.832	0.014	-268.511	0.735	0.026	26.230
52.565	59.818	0.014	-814.066	0.510	0.026	26.489
50.987	60.146	0.015	-1028.118	0.126	0.027	26.622
52.300	60.475	0.015	-917.648	-0.280	0.027	26.590
55.195	60.475	0.015	-592.658	-0.594	0.026	26.407
57.266	60.146	0.016	-323.309	-0.785	0.026	26.120
56.908	59.489	0.016	-289.728	-0.913	0.026	25.766
54.144	58.503	0.017	-489.235	-1.075	0.025	25.352
50.418	58.503	0.017	-907.539	-1.366	0.025	24.844
47.693	57.188	0.018	-1065.825	-1.777	0.024	24.189
47.024	56.202	0.018	-1030.236	-2.214	0.023	23.357
47.746	54.559	0.018	-764.688	-2.588	0.022	22.357
48.322	52.916	0.019	-515.574	-2.855	0.021	21.223
47.592	51.272	0.019	-413.145	-3.048	0.020	19.994
45.461	48.972	0.020	-394.085	-3.216	0.019	18.689
43.042	46.671	0.020	-407.282	-3.383	0.017	17.314
41.454	50.193	0.020	-980.887	-3.672	0.016	15.844
40.679	45.780	0.021	-572.620	-3.996	0.014	14.246
39.820	41.368	0.021	-173.677	-4.151	0.013	12.549
38.161	36.404	0.022	197.284	-4.147	0.011	10.820
35.832	31.439	0.022	493.082	-4.003	0.009	9.122
33.344	26.475	0.023	771.003	-3.739	0.008	7.510
31.183	22.063	0.023	1023.652	-3.365	0.006	6.029
29.647	17.650	0.023	1346.601	-2.872	0.005	4.730
28.406	13.789	0.024	1640.650	-2.249	0.004	3.663
26.813	10.480	0.024	1833.315	-1.526	0.003	2.877
24.665	8.274	0.025	1839.907	-0.760	0.002	2.400
22.091	7.170	0.025	1674.766	-0.028	0.002	2.236
19.217	6.619	0.025	1414.065	0.615	0.002	2.359
16.409	7.170	0.026	1036.967	1.126	0.003	2.721
14.041	7.722	0.026	709.250	1.490	0.003	3.266
11.846	9.377	0.027	277.213	1.695	0.004	3.930

9.470	11.583	0.027	-237.186	1.704	0.005	4.638
6.954	13.238	0.028	-705.263	1.507	0.005	5.307
4.380	15.444	0.028	-1241.843	1.102	0.006	5.851
1.789	17.099	0.028	-1718.424	0.485	0.006	6.181
0.000	17.650	0.029	-1981.146	-0.286	0.006	6.223
0.000	18.202	0.029	-2043.057	-1.124	0.006	5.929
0.000	17.099	0.030	-1919.235	-1.950	0.005	5.289
0.000	15.444	0.030	-1733.502	-2.711	0.004	4.318
0.000	12.686	0.030	-1423.948	-3.368	0.003	3.051
0.000	8.825	0.031	-990.573	-3.871	0.002	1.543
0.000	4.413	0.031	-495.286	-4.181	0.000	-0.135

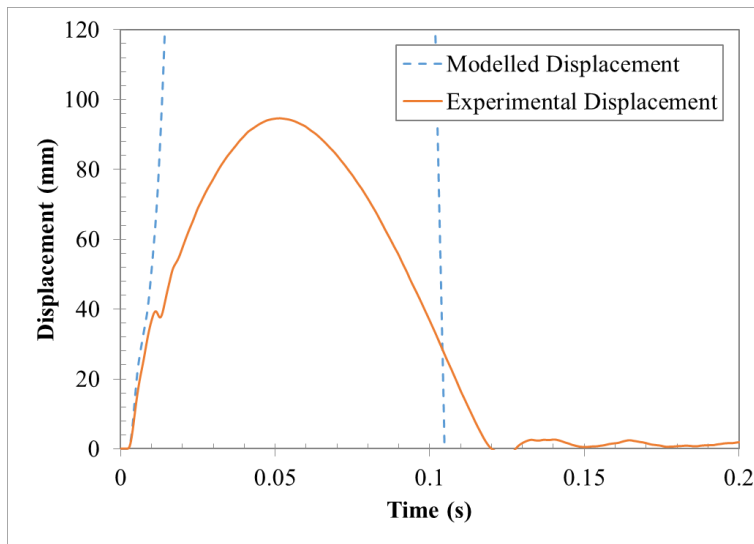
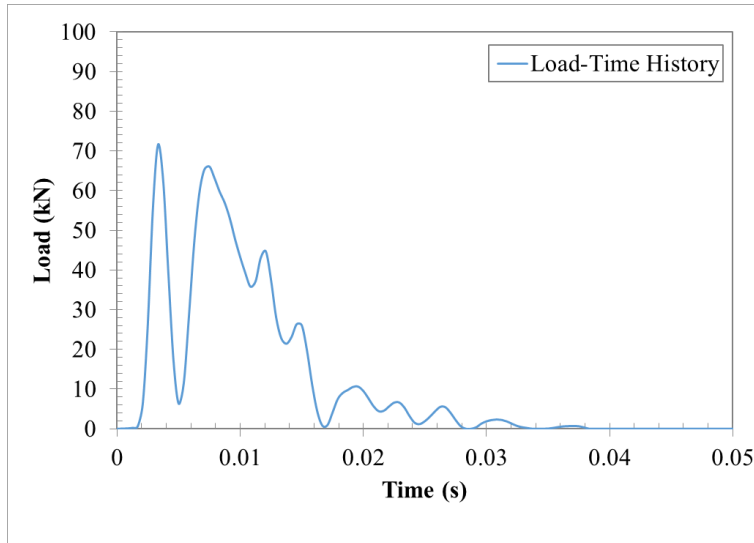


**Appendix K**  
**Comparison of Single Degree-of-Freedom Model with**  
**Experimental Results**

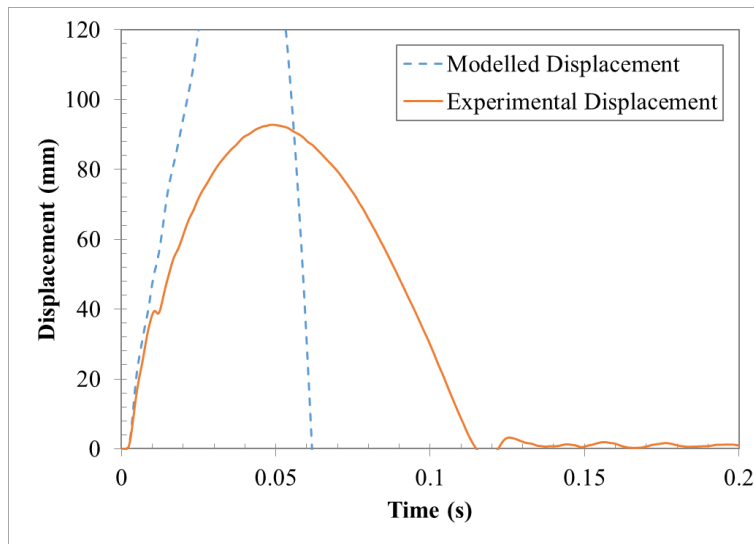
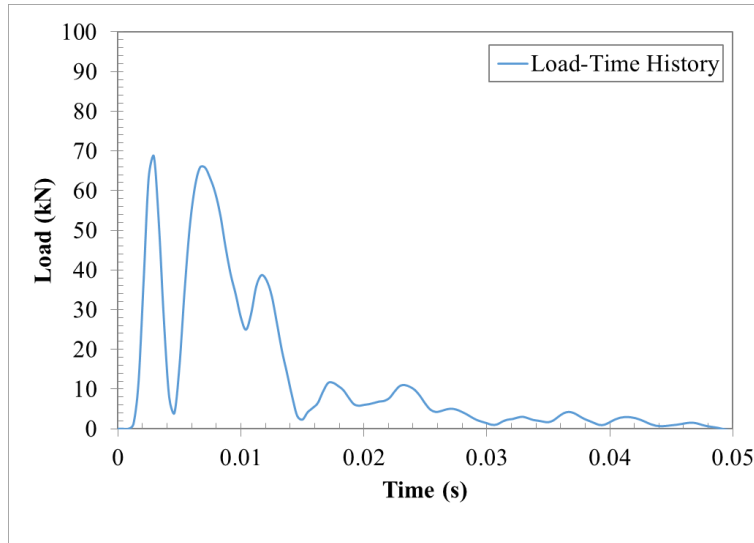
**Panel K1-1:**



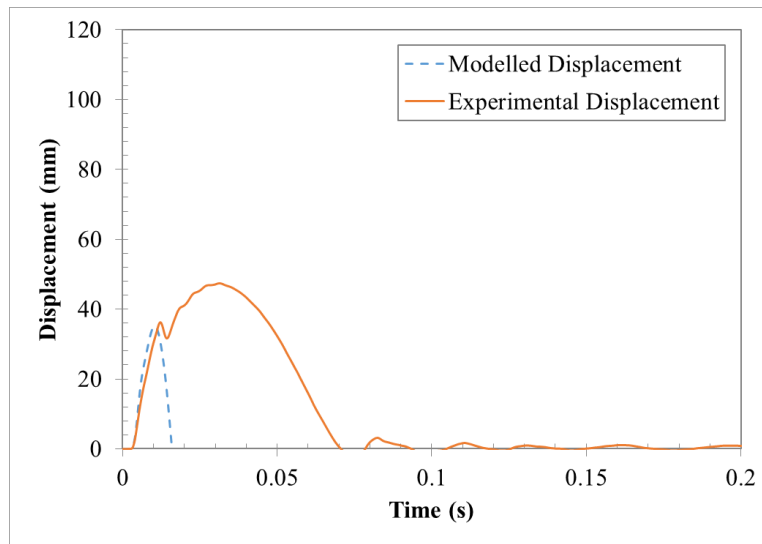
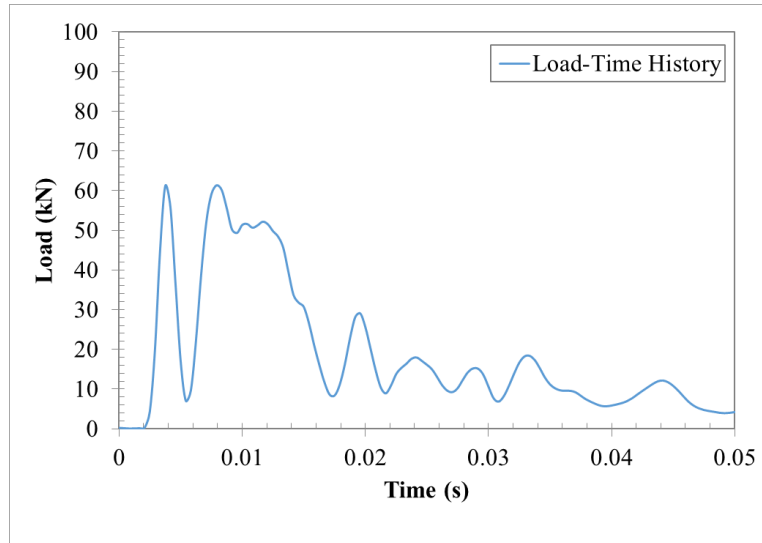
**Panel K1-2:**



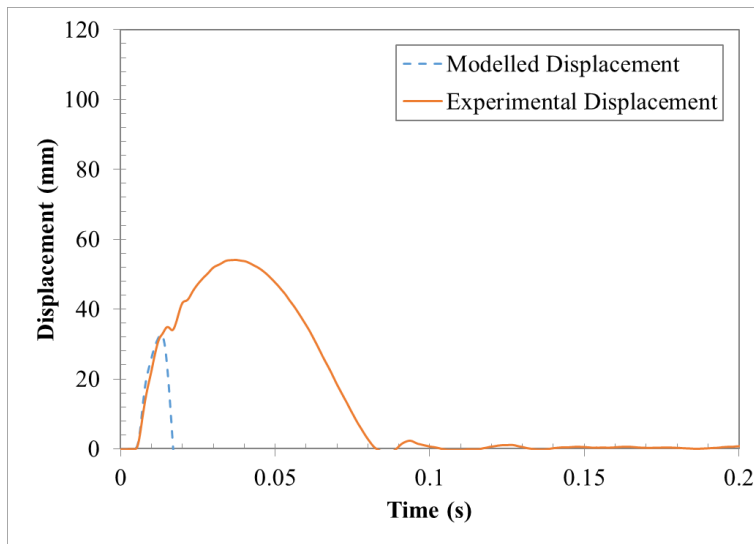
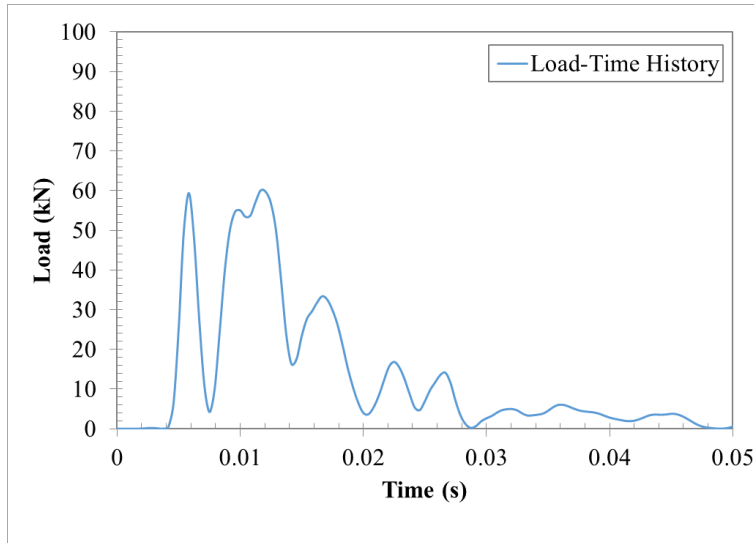
**Panel K1-3:**



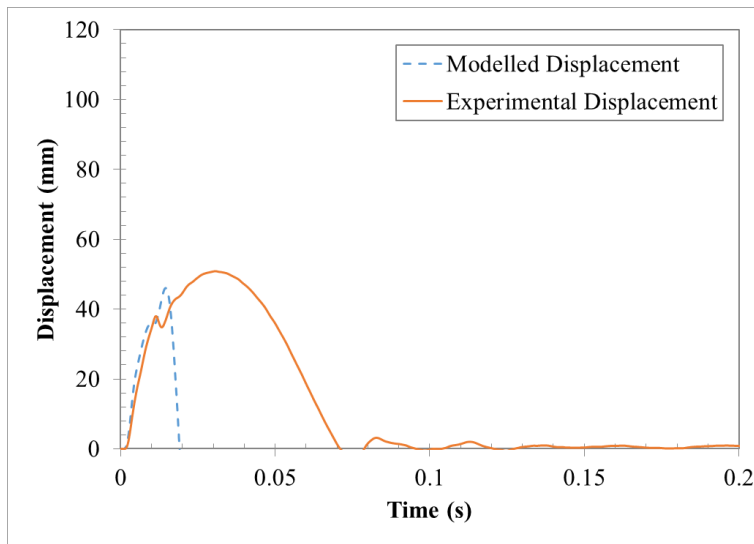
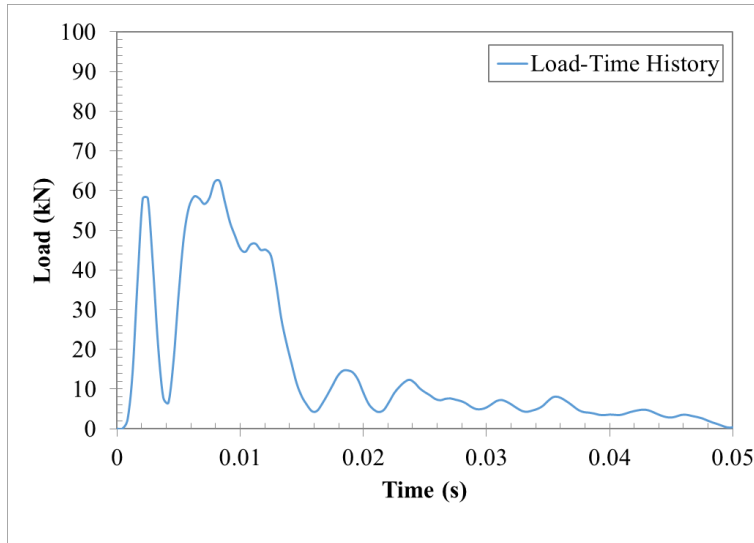
**Panel K2-1:**



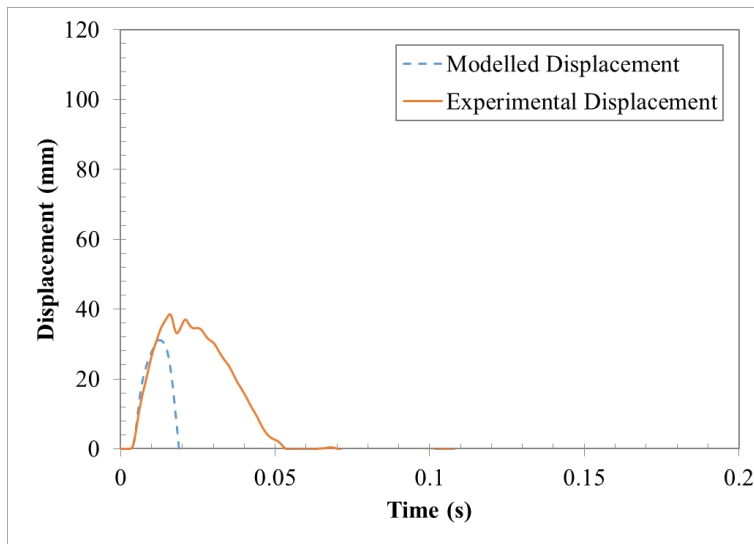
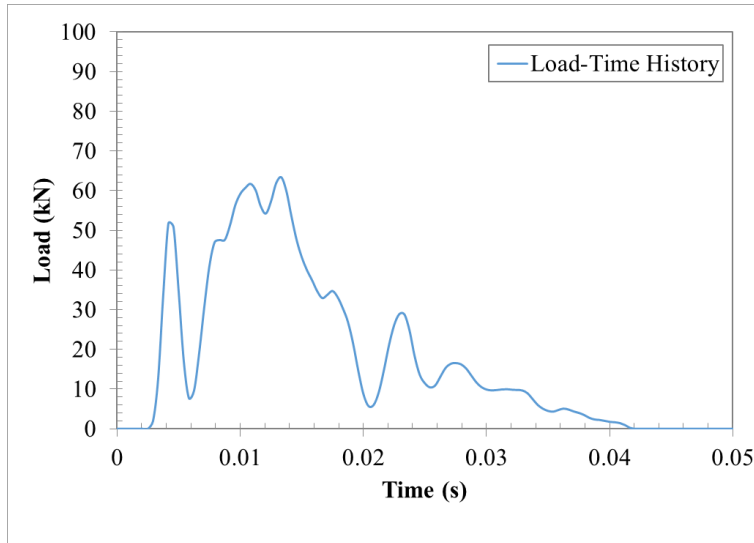
**Panel K2-2:**



**Panel K2-3:**

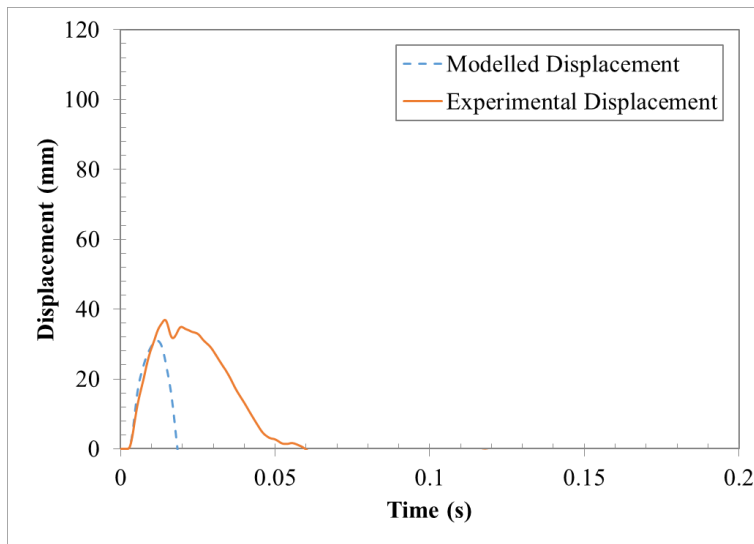
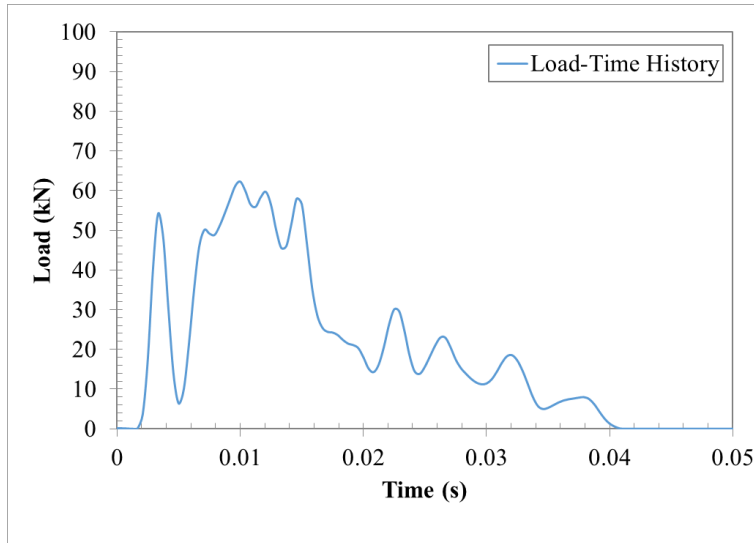


**Panel K3-1:**

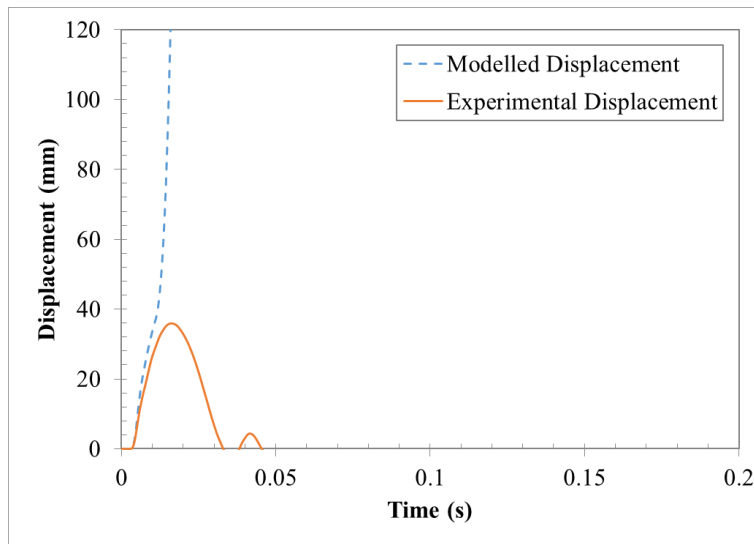
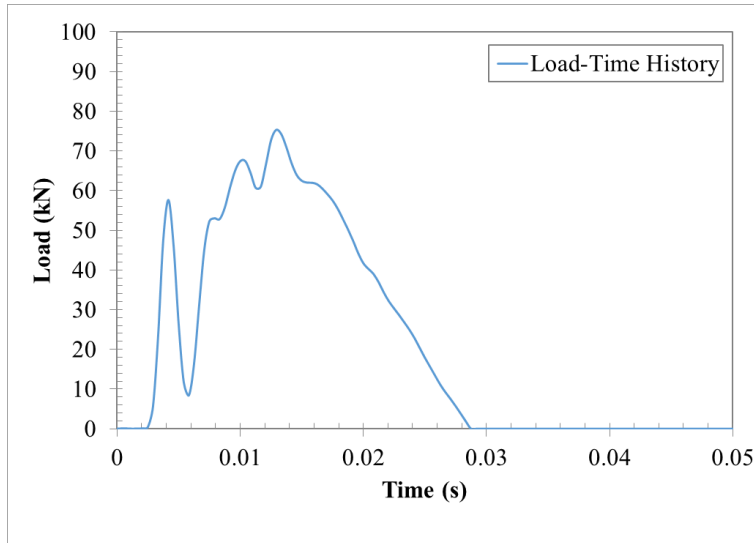




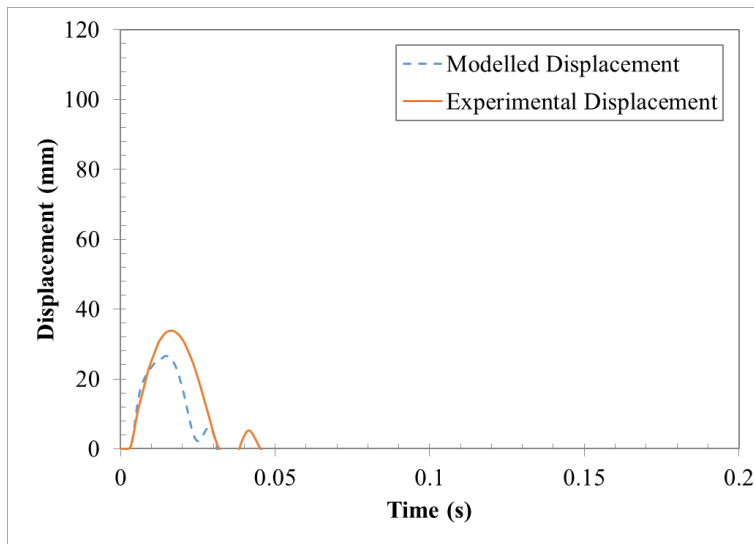
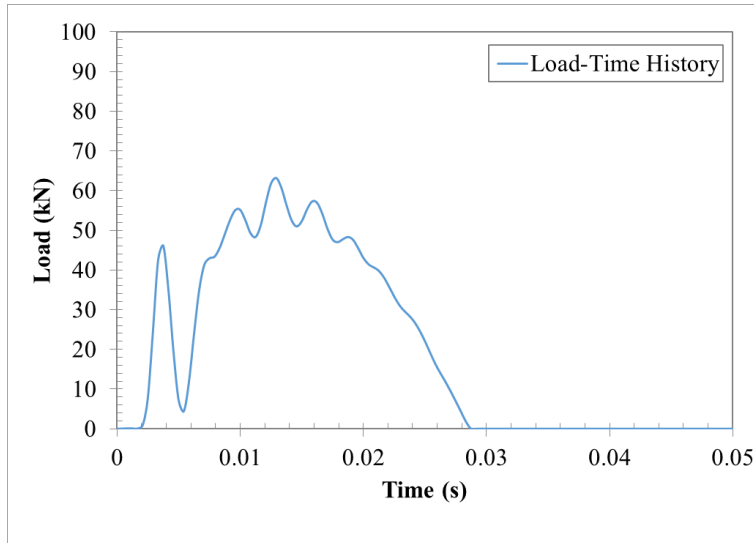
**Panel K3-2:**



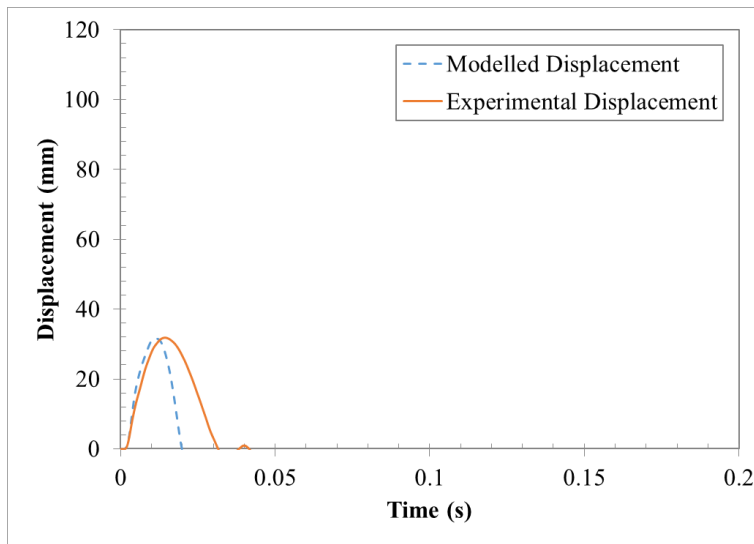
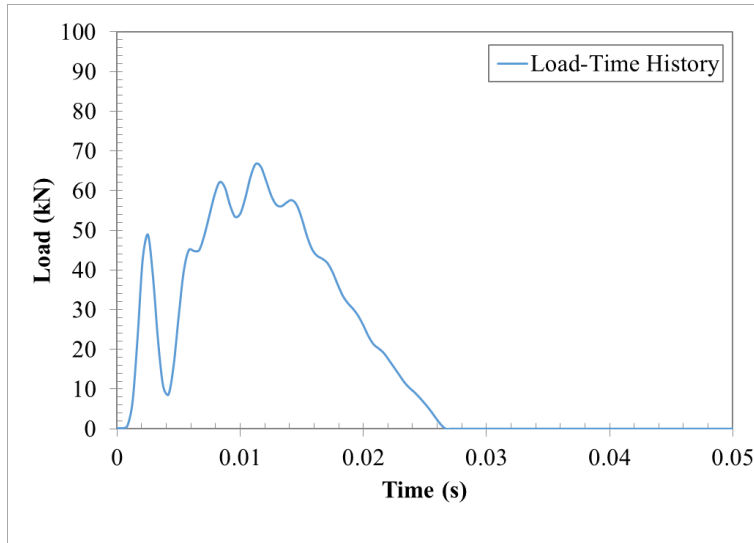
**Panel K3-3:**



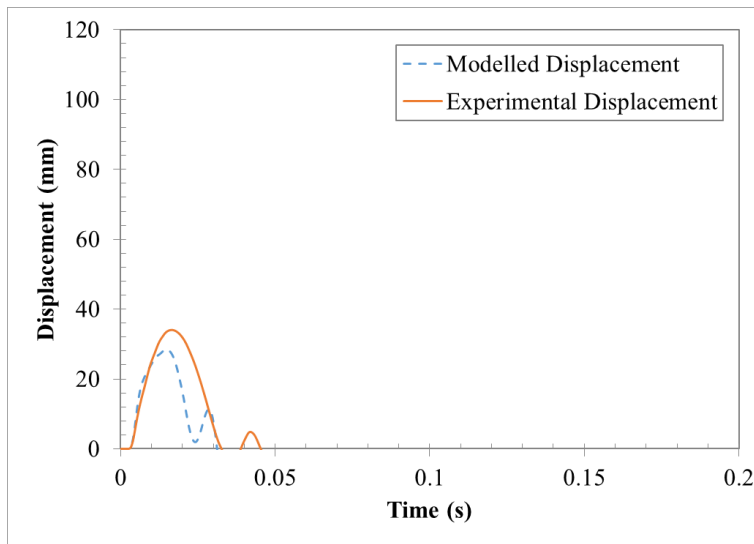
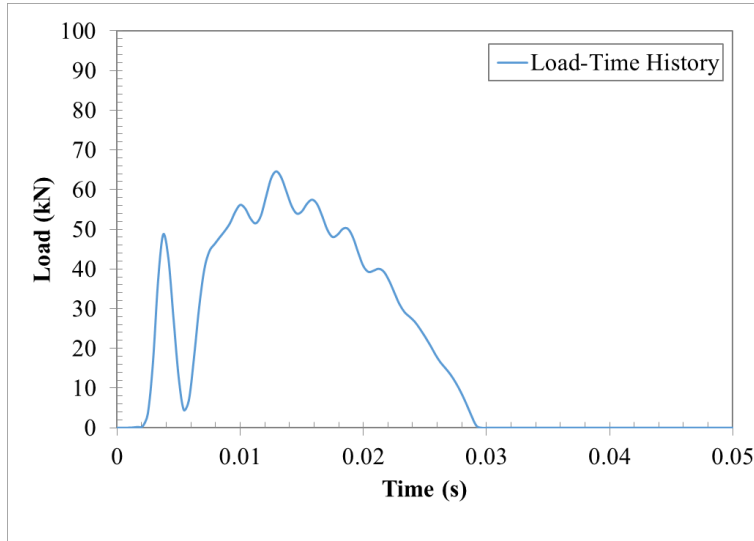
**Panel K4-1:**



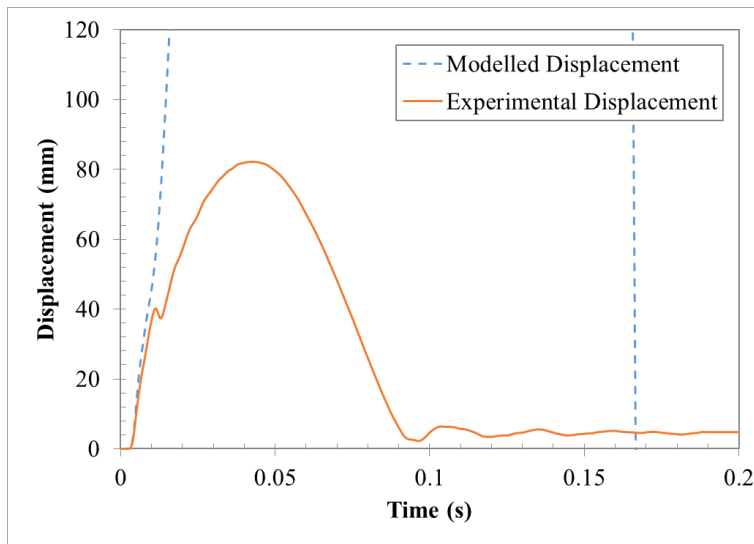
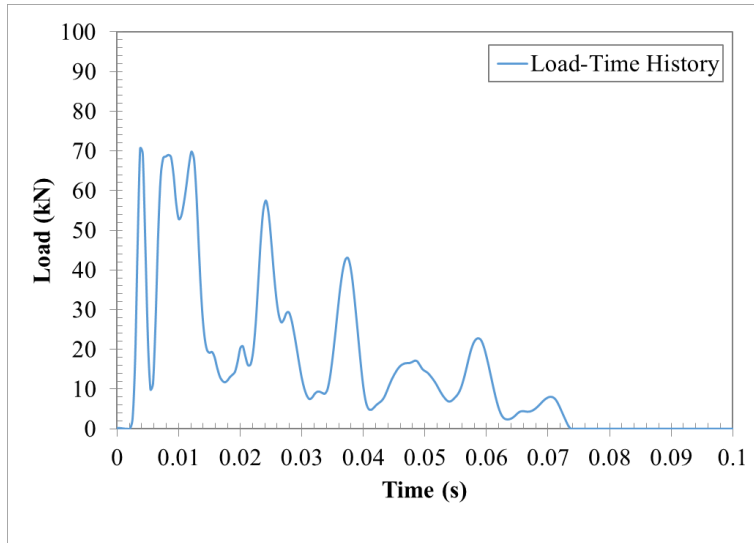
**Panel K4-2:**



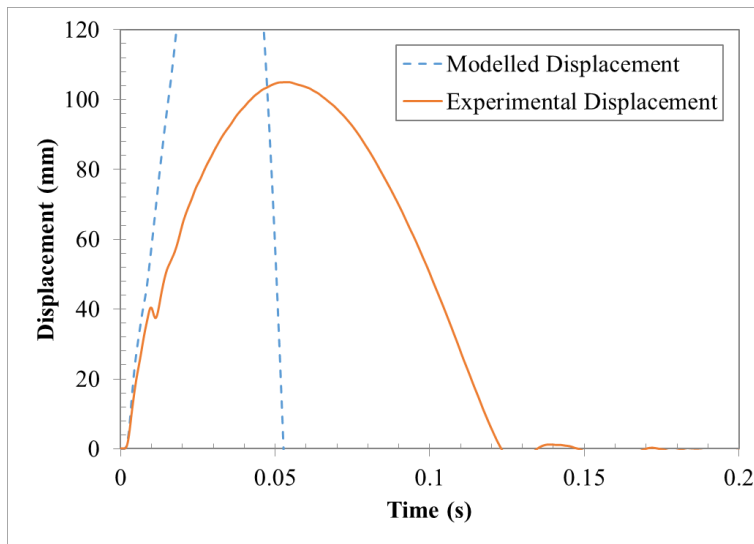
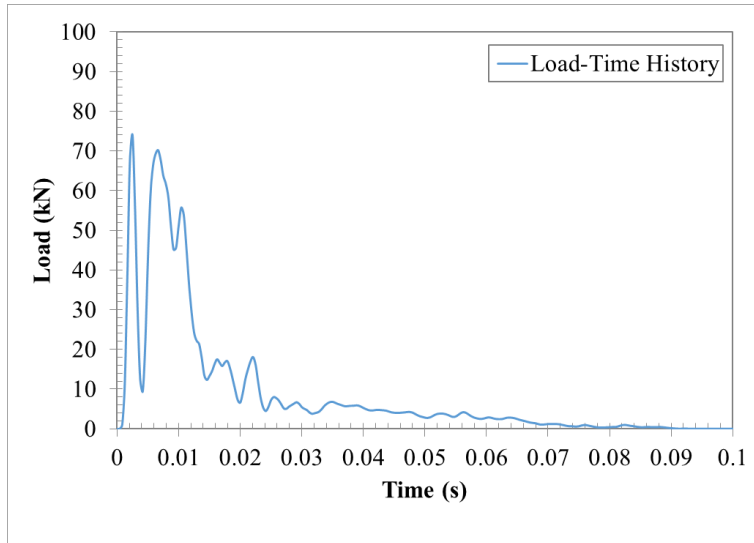
**Panel K4-3:**



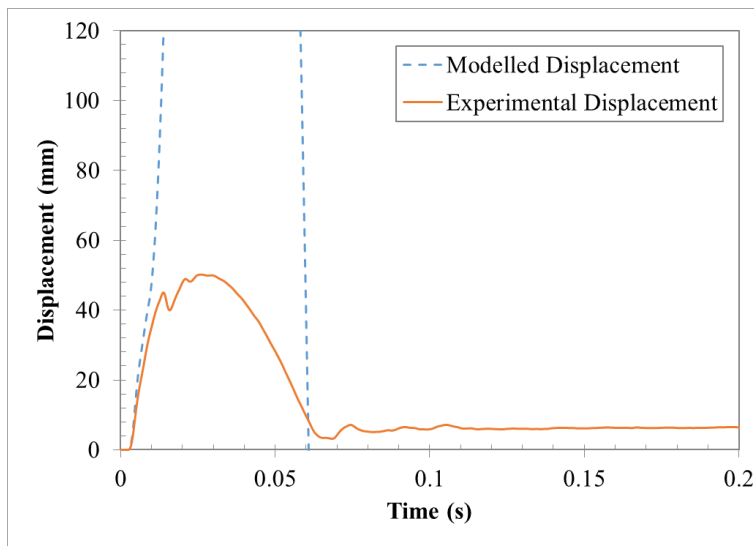
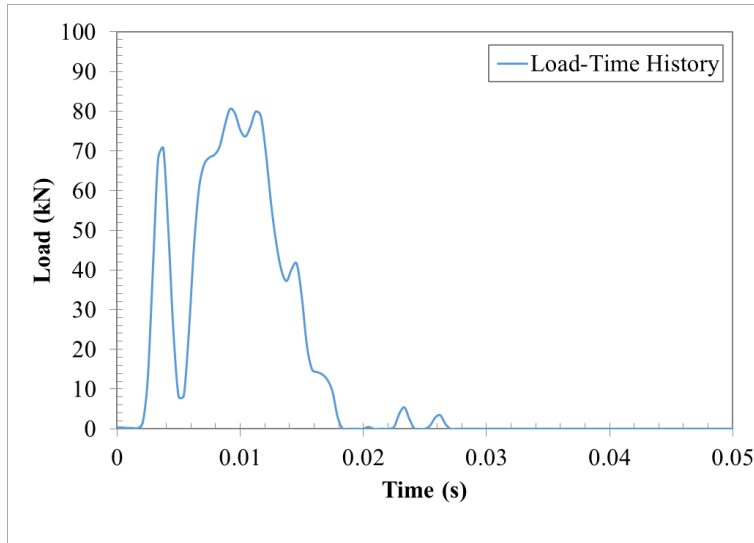
**Panel T1-1:**



**Panel T1-2:**

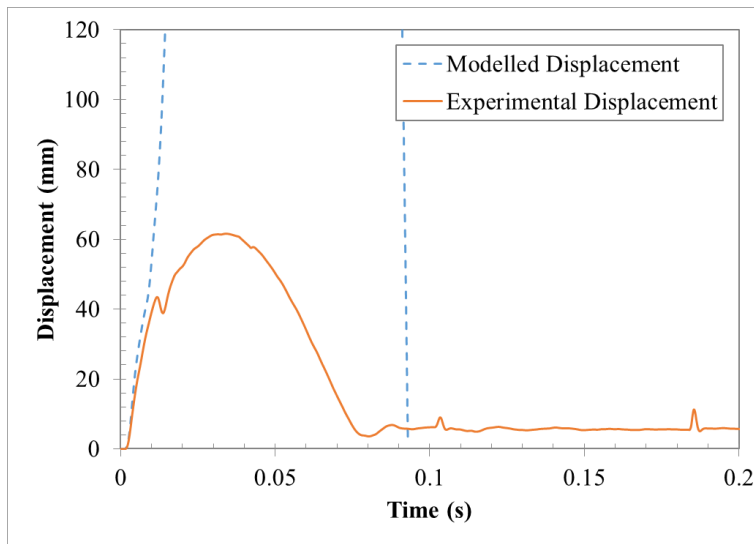
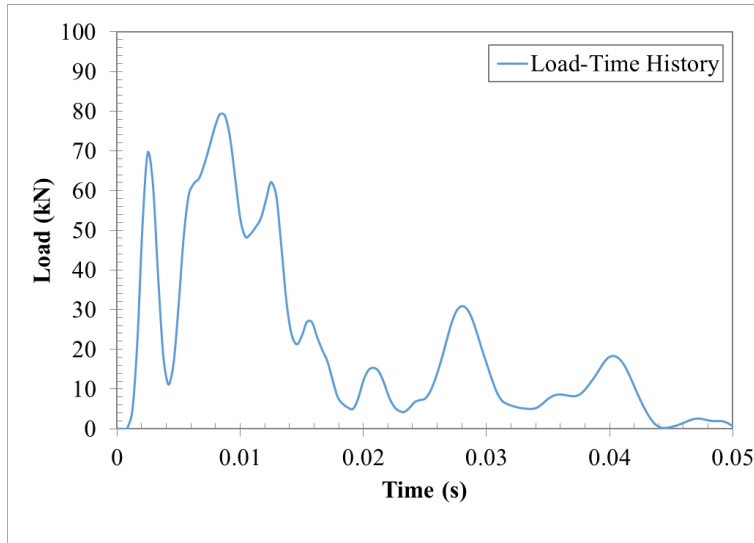


**Panel T2-1:**

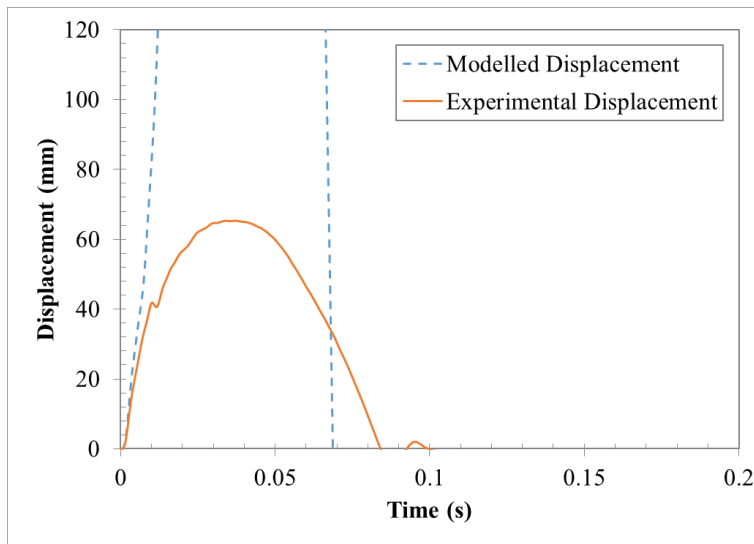
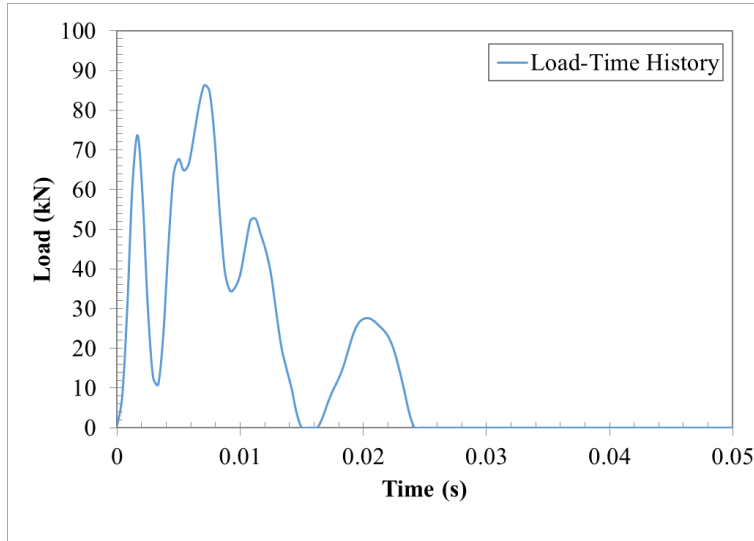




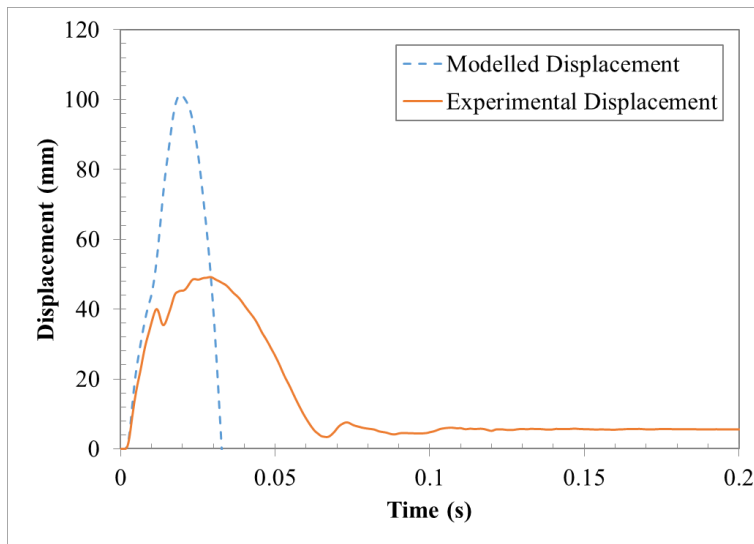
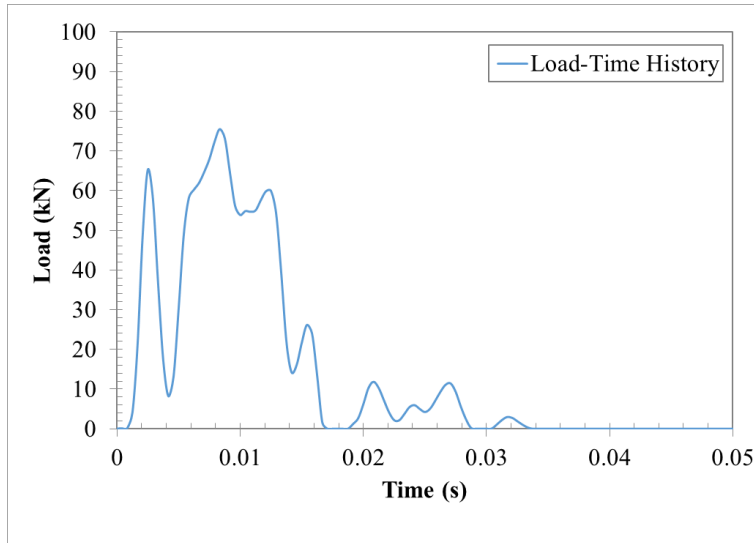
**Panel T2-2:**



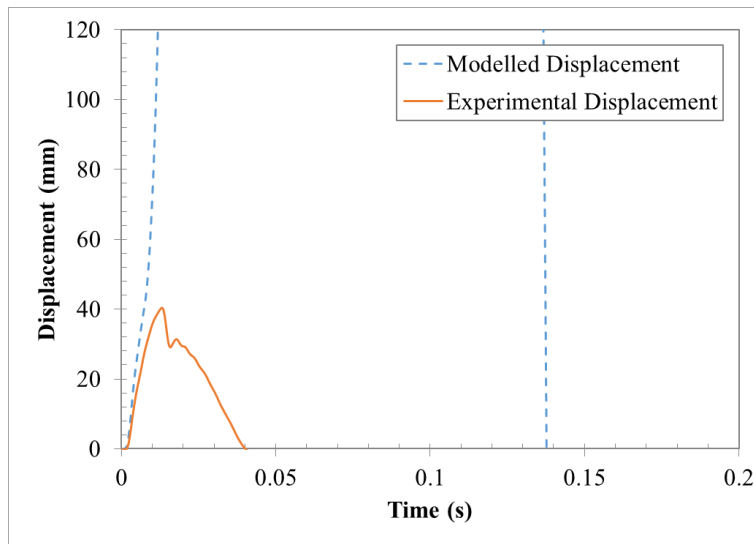
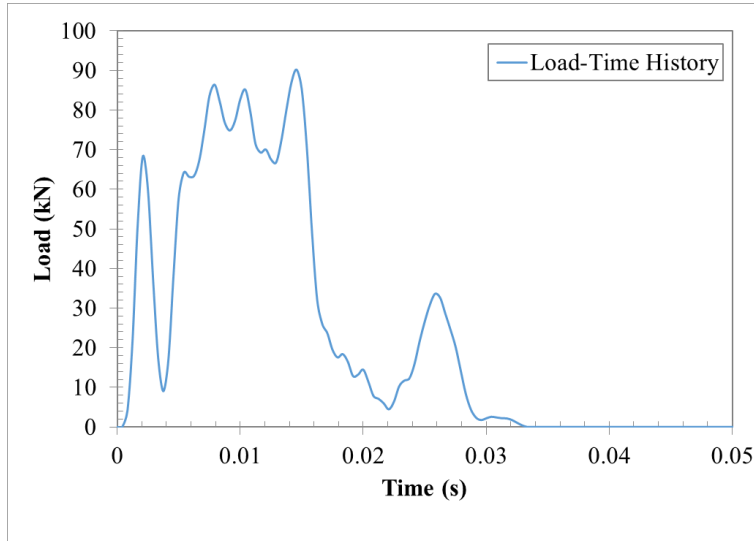
**Panel T2-3:**



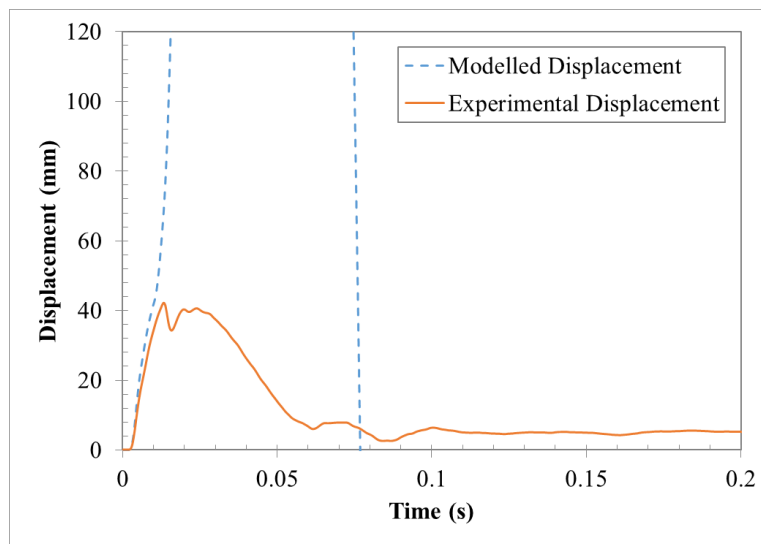
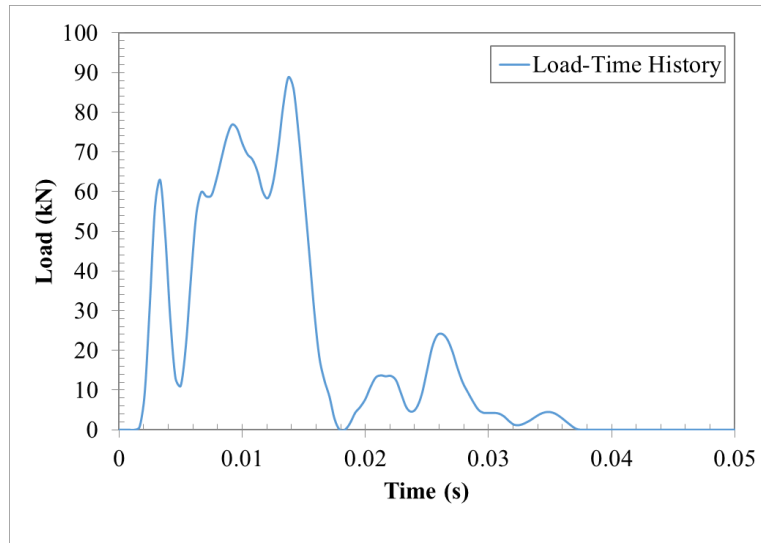
**Panel T3-1:**



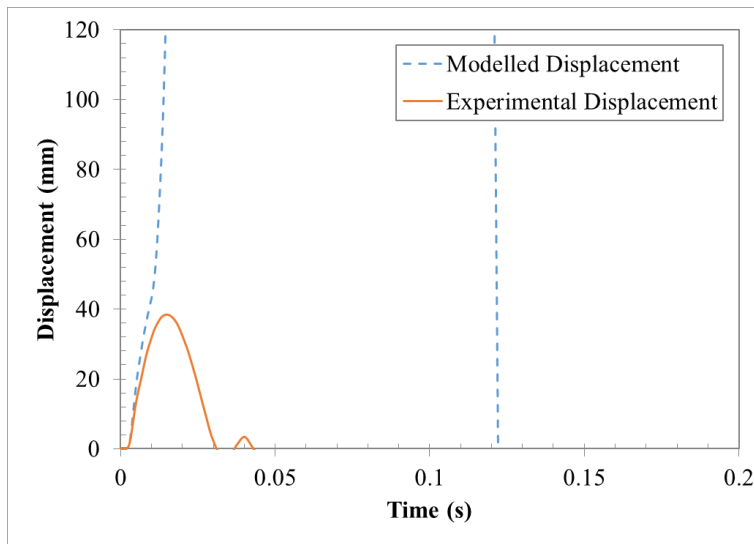
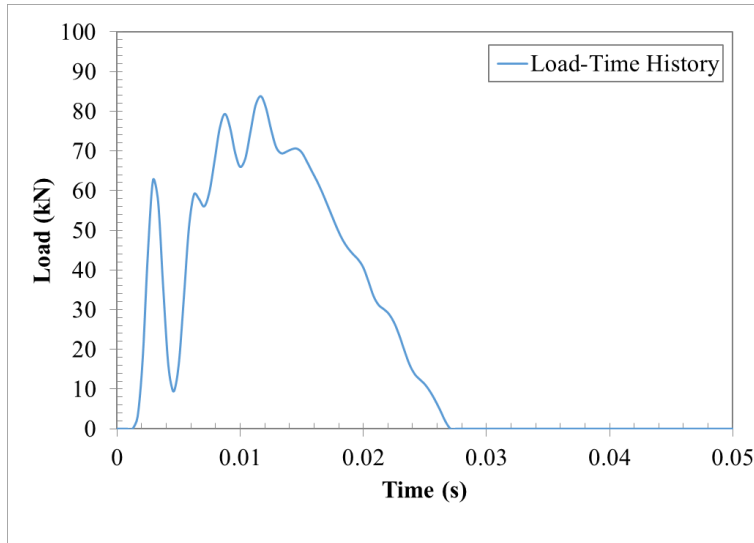
**Panel T3-2:**



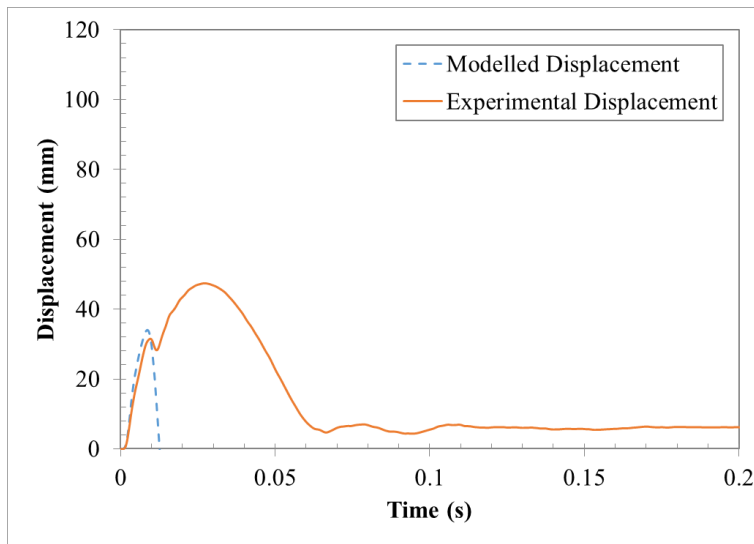
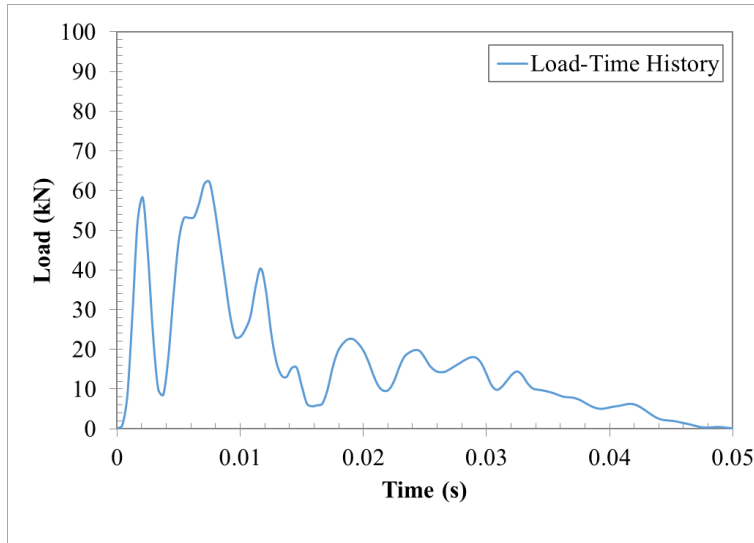
**Panel T3-3:**



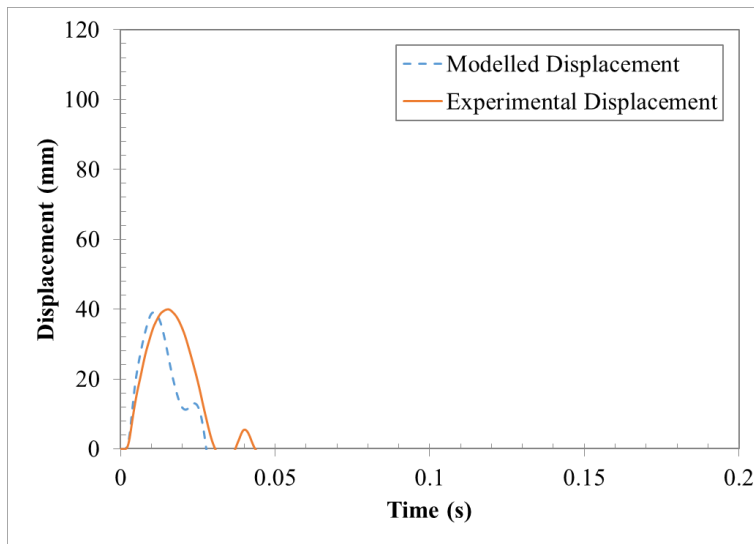
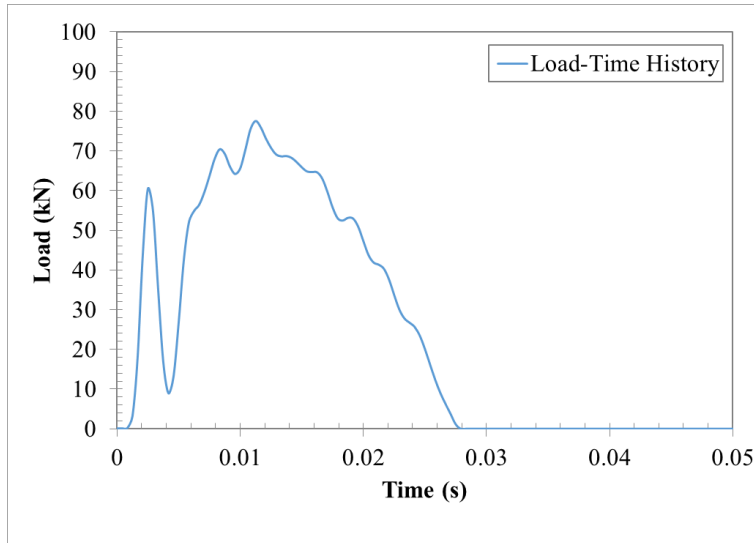
**Panel T4-1:**



**Panel T4-2:**



**Panel T4-3:**





**Panel T5-1:**

